Investigation of Magnetic, Spectroscopic, and Structural Properties of Molecular Metal Compounds

A Dissertation Presented for the

Doctor of Philosophy

Degree

The University of Tennessee, Knoxville

Alexandria Nicole Bone

May 2024

Copyright © 2024 by Alexandria Nicole Bone.

All rights reserved.

DEDICATION

To my husband and closest companion, Alan Fried.

I love you eternally.

ACKNOWLEDGEMENTS

I would like to acknowledge my advisor, Dr. Zi-Ling (Ben) Xue for his guidance and support throughout my graduate studies. His patience is matched only by his wisdom, and both were indispensable in my success as a doctoral student. I would like to thank my doctoral committee—Drs. David Jenkins, Tessa Calhoun, and Haidong Zhou—for their time, advice, and support. In addition, I would like to thank Dr. Viktor Nemykin and the staff and faculty of the Department of Chemistry at UTK for embracing and supporting me through a time of significant loss. I found a home in the Department of Chemistry not only for my work, but for myself.

I would like to thank several of our collaborators at Oak Ridge National Laboratory and the National High Magnetic Field Laboratory for their assistance and input: Drs. Mykhaylo Ozerov, Dmitry Smirnov, Andrey Podlesnyak, Yongqiang Cheng, Luke Daemen, Zheng Gai, and Xiaoping Wang. I extend thanks to Dr. Jason Haraldsen and Joseph Prescott of the University of North Florida and Joshua Telser at Roosevelt University for their assistance with computation.

I would like to thank the National High Magnetic Field Laboratory and Oak Ridge National Laboratories for use of several spectrometers and facilities, as well as the National Science Foundation for financial support of my research.

Additionally, I would like to thank past members of the Xue group: Dr. Duncan Moseley, Zhiming Liu, Chelsea Widener, Brian Kettell, and Dr. Pagnareach Tin for their research companionship, training, and support. I extend thanks to members who will graduate after me—Adam Hand, Michael Jenkins, Adiat Fakolujo, and Brandon Sanders. You are all brilliant chemists and I wish you luck in your future endeavors.

I could not have completed my graduate studies if not for the love and support of my friends and family—Dad, Mom, Robin, Grandma, Joe, Mary, Tim, Jeff, Monica, Josiah, Joy, Bonnie, Emily, and Graham. You all have been instrumental in my success as an individual and as a chemist; you never failed to meet my grief with love and understanding. Thank you to Sam and Linda Lewis, who ushered me into chemistry as a teenager. Thank you to my cats, Stevie and Esso, for always being my best gals. Special thanks to my parents, Michael Bone, Jeanie Bone, and Robin Bone, for I would not have gotten this far without them.

I would especially like to thank my late husband, Alan David Fried. Without the joy and love that you brought to every day of my graduate career, I never would have made it past my second year, much less to the graduation podium. I had the honor of accepting your posthumous Ph.D., and I can only hope that you are proud of me now. Thank you for your help with the synthetic portion of my Original Research Proposal. Thank you for believing in me. Thank you for leaving a legacy that I am proud to carry with me for the rest of my life. Consider this dissertation my greatest love letter to you.

ABSTRACT

Compounds exhibiting single-molecule magnetism (SMM) are of current interest for potential use in molecular data storage and quantum computing applications. However, rapid magnetic relaxation at desired operating temperatures currently limits the use of these materials, and a more thorough understanding of the magnetic and vibrational transitions that affect magnetic memory is required to inform SMM design. The primary focus of this dissertation is the study of magnetic and vibrational modes in molecular magnetic compounds via advanced spectroscopic techniques such as inelastic neutron scattering (INS), far-IR magneto-spectroscopy (FIRMS), and high-field, high-frequency electron paramagnetic resonance (HFEPR) to directly observe transitions among zero-field split (ZFS) states, spin-phonon couplings, and phonon modes. In many cases, DFT calculations are performed to support the spectroscopic studies. Notably, interesting magnetic interactions are directly revealed, such as the presence of an assembly excitation in *meso*-tetraphenylporphyrin compounds Fe(TPP)Cl and Mn(TPP)Cl (TPP^{2-} = *meso*-tetraphenylporphyrinate, Chapter II) and spin-phonon couplings in $Co(PPh_3)_2X_2$ (X = Cl, Br, I; Chapter III) compounds. In addition, structural and magnetic properties of Mn(TPP)Br, Mn(TPP)I (Chapter IV), and Fe(TPP)X (X = F, Cl, Br, I; Chapter V) are investigated. These studies aim to provide a more thorough understanding of magnetic transitions in transition metal compounds in order to develop SMM design criteria and reveal potential routes of magnetic relaxation.

TABLE OF CONTENTS

CHAPTER I INTRODUCTION 1

1.1. Molecular Magnetism 2

1.1.1. Energetic Structure and Anisotropy of Transition Metal Complexes 3

1.1.1.1. Fe(III) Porphyrin Complexes 6

1.1.1.2. Mn(III) Porphyrin Complexes 9

1.1.1.3. Tetrahedrally Coordinated Co(II) Complexes 11

1.1.2. Mechanisms of Magnetic Relaxation 15

1.2. Experimental Methods 21

1.2.1. Inelastic Neutron Scattering (INS) 21

1.2.2. Far-IR Magneto-Spectroscopy (FIRMS) 27

1.2.2. Raman Magneto-Spectroscopy (RaMS) 28

1.2.3. High-Field, High-Frequency Electron Paramagnetic Resonance (HFEPR) . 29

1.3. Current Dissertation 30

1.4. Chapter II 30

1.5. Chapter III 30

1.6. Chapter IV 31

1.7. Chapter V 31

CHAPTER II STUDIES OF INTERMOLECULAR INTERACTIONS IN METALLOPORPHYRINS M(TPP)Cl (M = Fe^{3+}, Mn^{3+}) VIA INELASTIC NEUTRON SCATTERING 32

2.1. Abstract 34

2.2. Previous INS Studies to Probe Intermolecular Interactions 34

2.3. Results and Discussion 37

2.3.1. INS Spectra of Fe(TPP)Cl (1) 39

2.3.2. INS Spectra of Mn(TPP)Cl (2) 42

2.3.3. Q-Dependence of Magnetic Transition in 1 and 2 44

2.3.4. Understanding the Q-Dependence of the INS Intensity 48

2.3. Experimental Methods 55

CHAPTER III SPECTROSCOPIC STUDIES OF MAGNETIC TRANSITIONS AND SPIN-PHONON COUPLINGS IN THE SINGLE-MOLECULE MAGNETS, $Co(PPh_3)_2X_2$ (X = Cl, Br, I) 58

3.1. Abstract 60

3.2. Results and Discussion 61

3.2.1. Experimental Determination of Magnetic and Phonon Transitions 61

3.2.1.1. INS 61

3.2.1.2. FIRMS 64

3.2.1.3. FD-FT THz EPR 73

3.2.1.3. HFEPR 76

3.2.2. LFT of the Co-X Series (X = Cl, Br, I) 77

3.2.2.1. LFT Background of the Co-X Series 77

3.2.2.2. Analysis of ZFS in Co-X by Ligand Field Theory 80

3.2.3. Experimental and Calculated Phonon Spectra and Studies of Spin-Phonon Couplings 81

3.2.3.1. Phonon Excitations in FIRMS, INS, and Raman Spectra, Calculated INS Spectra, and Computations of Phonon Excitations and Symmetries 82

3.2.3.2. Studies of Spin-Phonon Couplings in FIRMS Spectra 83

3.2.3.3. Calculated Spin Densities of Atoms in Co-X Complexes 88

3.3. Experimental Methods 91

CHAPTER IV STUDIES OF STRUCTURES AND MAGNETIC PROPERTIES OF METALLOPORPHYRINATES, Mn(TPP)X (X = Cl, Br, I) 95

4.1. Abstract 97

4.2. Results and Discussion 98

4.2.1. Crystal Structures of Mn-Br·CHCl3, 2·CH_2Cl_2, Mn-I·CHCl3, 3·$CDCl_3$ and Mn-I·1.5CHCl3 98

4.2.2. Hirshfeld Surface Analyses 104

4.2.3. Magnetic Susceptibility 111

4.2.4. HFEPR 114

4.2.5. INS 119

4.3. Experimental Methods 124

4.3.1. Synthesis of Mn-Br and Mn-I 124

4.3.2. Crystallization 124

4.3.3. Single Crystal X-Ray Diffraction 125

4.3.4. Hirshfeld Surface Calculations 127

4.3.5. Susceptbility Measurements 127

4.3.6. HFEPR Studies of Mn-Br·$CDCl_3$ and Mn-I·$CDCl_3$ 128

4.3.7. INS Studies of Mn-Br·CDCl3 and Mn-I·CDCl3 128

CHAPTER V STUDIES OF MAGNETIC AND PHONON MODES OF METALLOPORPHYRINATES Fe(TPP)X (X = F, Cl, Br, I) VIA INELASTIC NEUTRON SCATTERING 130
5.1. Abstract 131
5.2. Results and Discussion 131
5.2.1. INS, Phonon Animations, and Spin Densities of Fe-Cl and Fe-Cl-d_{28} 132
5.2.1.1. INS of Fe-Cl and Fe-Cl-d_{28} 132
5.2.1.2. Calculated Phonon Symmetries and Energies of Fe-Cl and Fe-Cl-d_{28} . 136
5.2.1.3. Phonon Movies of Fe-Cl and Fe-Cl-d_{28} 138
5.2.1.4. Spin Densities of Fe-Cl and Fe-Cl-d_{28} 141
5.2.2. INS of Fe-F, Fe-Br, and Fe-I 143
5.3. Experimental Methods 149
CHAPTER VI CONCLUSION AND RECOMMENDATIONS 151
REFERENCES 155
APPENDIX 181
Appendix A. Supporting Information for Chapter II 182
A.1. Fitting Using the Single-Molecule Model and the Average-Exchange Model 191
Appendix B. Supporting Information for Chapter III 199
B.1. Far-IR Magneto-Spectroscopy Studies 210
B.2. Magneto-Raman Studies 210
B.2.1. Experimental 210
B.2.2. Spectra 210

Appendix C. Supporting Information for Chapter IV 265

C.1. Crystallographic Data, Figures, Tables, and CShM Calculations 265

C.1.1. Crystallographic Data, Figures, and Tables 265

C.1.2. Results of the CShM Calculations by the SHAPE Program 275

C.1.3. Comparison of Contributions to the Hirshfeld Surface Areas for **Mn(TPP)Br** Molecules in Various Crystal Structures 284

C.1.4. Comparison of Contributions to the Hirshfeld Surface Areas for **Mn(TPP)I** Molecules in Various Crystal Structures 292

Appendix D. Supporting Information for Chapter V 301

VITA 312

LIST OF TABLES

Table 1.1. Axial and rhombic ZFS parameters for **Co-Cl**, **Co-Br**, and **Co-I** from previous studies 16

Table 1.2. *g*-Values for **Co-Cl** and **Co-Br** from previous studies 17

Table 3.1. Axial and rhombic ZFS parameters for **Co-Cl**, **Co-Br**, and **Co-I** 68

Table 3.2. *g*-values for **Co-Cl**, **Co-Br**, and **Co-I** 69

Table 3.3. Energies of phonons involved in spin-phonon couplings and the coupling constants of **Co-X** 70

Table 3.4. Calculated spin densities $\boldsymbol{\rho_s}$ of atoms in **Co-X** 89

Table 4.1. Selected bond lengths (Å) and angles (°) for **Mn-Br·CHCl$_3$** and **Mn-I·CHCl$_3$** at 100(2) K 100

Table 4.2. Comparison of structural features of Mn(TPP)X (X = Cl, Br, I) and Fe(TPP)X (X = Br, I) complexes 103

Table 4.3. Comparison of Hirshfeld areas, volumes, and void volumes 105

Table 4.4. ZFS parameters of Mn(TPP)X (X = Cl, Br, I) and Fe(TPP)X (X = Br, I) complexes 118

Table 5.1. Select calculated phonon energies/symmetries for **Fe-Cl** and **Fe-Cl-$\boldsymbol{d_{28}}$** 137

Table 5.2. Calculated spin densities $\boldsymbol{\rho_s}$ in **Fe-Cl** and **Fe-Cl-$\boldsymbol{d_{28}}$** 142

Table A.1. Peak parameters for Figure A.5 188

Table A.2. Peak parameters for Figure A.6 190

Table A.3. Fitting parameters for the effective-field and average-exchange models 194

Table B.1. Electronic Transitions (in cm^{-1}) for **Co-X** in Doped Single-Crystals of **Co/Zn-X** (X = Cl, Br, I)[49, 107] with Calculations from the AOM 226

Table B.2. Key Metrics for the AOM of the **Co-X** Series (X = Cl, Br, I) 227

Table B.3. LFT AOM parameters (in cm^{-1}) determined for the **Co-X** series (X = Cl, Br, I) 228

Table B.4. Calculated phonon modes in **Co-Cl** and their symmetries 229

Table B.5. Calculated phonon modes in **Co-Br** and their symmetries..... 237

Table B.6. Calculated phonon modes in **Co-I** and their symmetries 245

Table B.7. Calculated spin densities of atoms in **Co-Cl** and **Co-Br**..... 260

Table B.8. Calculated spin densities of atoms in **Co-I** 262

Table C.1. Crystallographic data for **Mn-Br·CHCl$_3$** and **Mn-Br·CH$_2$Cl$_2$**..... 265

Table C.2. Crystallographic data for **Mn-I·CHCl$_3$, Mn-I·CDCl$_3$** and **Mn-I·1.5CHCl$_3$** 267

Table C.3. Selected bond lengths (Å) and angles (°) for **Mn-Br·CH$_2$Cl$_2$** 269

Table C.4. Selected bond lengths (Å) and angles (°) for one molecule of **Mn-I** in **Mn-I·CDCl$_3$**..... 272

Table C.5. Selected bond lengths (Å) and angles (°) for **Mn-I·1.5CHCl$_3$**..... 274

Table C.6. CShM results for **Mn-Br·CHCl$_3$**, **Mn-Br·CH$_2$Cl$_2$**, and **Mn-Br·toluene**.... 276

Table C.7. CShM results for **Mn-I·CHCl$_3$**, **Mn-I·CDCl$_3$**, **Mn-I·1.5CHCl$_3$** and **Mn-I·toluene**..... 277

Table D.1. Calculated phonon modes of **Fe-Cl** and their symmetries 303

Table D.2. Calculated phonon modes of **Fe-Cl-*d*$_{28}$** and their symmetries..... 306

Table D.3. Spin densities, ρ_s, of individual atoms in **Fe-Cl**..... 310

LIST OF FIGURES

Figure 1.1. Double-well diagram representing the magnetic barrier for a transition metal-based system with $S = 3/2$ and $D < 0$ 5

Figure 1.2. (a) *d*-Orbital splitting diagram for d^5 **Fe-X** series with $S = 5/2$; (b) ZFS in **Fe-F** and **Fe-Cl** with $D > 0$ and $E = 0$; (c) ZFS in **Fe-Br** and **Fe-I** with $D > 0$ and $E \neq 0$ 7

Figure 1.3. ZFS in $S = 2$ complexes with (Left) 4-fold molecular and crystallographic symmetry and (Right) *no* 4-fold symmetry. 10

Figure 1.4. (Left) Diagram of **Co-X** (X = Cl, Br, I). (Right) Spin level diagram of the complexes in the case of $D < 0$. $D' = (D^2 + 3E^2)^{1/2}$ 12

Figure 1.5. Electronic states of quartet states of $3d^7$ Co^{2+} as a free-ion, in a tetrahedral (T_d) ligand field, in a tetragonally compressed ligand field (D_{2d}), and in a rhombic (C_{2v}) ligand field as in **Co-X** 14

Figure 1.6. Schematic representation of QTM (blue) and TA-QTM (red) mechanisms for magnetic relaxation. 18

Figure 1.7. Schematic diagram showing spin-lattice relaxation processes for SMMs 20

Figure 1.8. (a) Schematic of INS processes. $\boldsymbol{k_i}$ and $\boldsymbol{k_f}$ refer to the momenta of incoming and outgoing neutrons with energies of E_i and E_f, respectively. (b) Box diagram for a direct-geometry INS instrument. (c) Box diagram for an indirect-geometry INS instrument. 24

Figure 2.1. Structures of M(TPP)Cl (M = Fe, **Fe-Cl**; Mn, **Mn-Cl**). (Middle) ZFS pattern for **Fe-Cl** and (Right) ZFS pattern for **Mn-Cl** 38

Figure 2.2. (Top) INS spectra of **Fe-Cl** at 20 K collected with incident neutron energy of

E_i = 26.8 cm^{-1}. (Bottom) Deconvolution of Peak **A** into Peaks **A1** at 12.7(1) cm^{-1} and **A2** at 11.8(1) cm^{-1} for the data in the Q = 0.5–0.6 Å^{-1} range..... 41

Figure 2.3. (Top) INS spectrum of **Mn-Cl** at 20 K with E_i = 12.5 cm^{-1}. (Bottom) Expanded view of Peak **D** with the best energy resolution (largest peak separation = 0.0686 cm^{-1}). 43

Figure 2.4. (Top) Q-dependence of the two overlapping magnetic peaks. (Bottom) Q-dependence of Peak **D** at 6.9(1) cm^{-1} for **Mn-Cl** at 2 K with E_i = 42.3 cm^{-1} in Figure 2.3..... 47

Figure 2.5. (a) Visualization of the effective field with respect to the molecules surrounding one molecule at the center based on the crystal structures of **Fe-Cl** and **Mn-Cl** and intermolecular distances summarized in Figure A.7. (b) Illustration of the effective field produced by the intermolecular magnetic interactions..... 51

Figure 3.1. (Top) Variable-field INS spectra at DCS at 1.5-1.6 K; (Bottom) Bose-corrected forward-scattering VT INS spectra at VISION..... 62

Figure 3.2. Bose-corrected forward-scattering VT INS spectra on VISION: (Top) **Co-Br**. (Bottom) **Co-I** 63

Figure 3.3. FIRMS spectra of the complexes at 5 K and 0 and 17 T: (Left) **Co-Cl**, (Middle) **Co-Br**, (Right) **Co-I**..... 65

Figure 3.4. FIRMS maps (normalized transmission vs. field and energy/frequency): (Left) **Co-Cl**, (Middle) **Co-Br**, (Right) **Co-I** with HFEPR results superimposed..... 66

Figure 3.5. FIRMS plots of far-IR spectra normalized by average, which minimize

phonon features that do not change with magnetic field: (Top) **Co-Br**; (Bottom) **Co-I**, revealing simulations of spin-phonon couplings..... 72

Figure 3.6. FD-FT THz-EPR MDS at 5 K: (Top) **Co-Cl**, (Middle) **Co-Br**, (Bottom) **Co-I**..... 74

Figure 3.7. Electronic states of quartet states of $3d^7$ Co^{2+} as a free-ion, in a tetrahedral (T_d) ligand-field, in a tetragonally compressed ligand field (D_{2d}), and in a rhombic (C_{2v}) ligand-field as in **Co-X** 79

Figure 3.8. (Left) Schematic representation of an avoided crossing. Some of us have recently provided more detailed schematic views of the spin-phonon couplings in a Co(II) complex with axial anisotropy ($D < 0$).[95] (Right) FIRMS plot of **Co-Cl** spectra normalized by average, which minimizes phonon features that do not change with magnetic fields 84

Figure 4.1. ORTEP diagram of the structure of **Mn-Br** in the crystal of **Mn-Br·$CHCl_3$** 99

Figure 4.2. ORTEP diagram of Mn(TPP)I in **Mn-I·$CHCl_3$**..... 102

Figure 4.3. Two views of the Hirshfeld surface of **Mn-Br·$CHCl_3$** showing normalized close distances of the pro-molecule and neighboring molecules at 100(2) K..... 106

Figure 4.4. Hirshfeld fingerprint plots for **Mn-Br·$CHCl_3$**..... 107

Figure 4.5. Two views of the Hirshfeld surface of **Mn-I·$CHCl_3$** showing normalized close distances of the pro-molecule and neighboring molecules at 100(2) K 108

Figure 4.6. Hirshfeld fingerprint plots for **Mn-I·$CHCl_3$** 109

Figure 4.7. Variable-temperature DC susceptibility data under applied DC field of 0.5 T: (Top) **Mn-Br·$CHCl_3$**. (Bottom) **Mn-I·$CHCl_3$**..... 112

Figure 4.8. HFEPR spectra of Mn(TPP)Br·$CDCl_3$ (**Mn-Br·$CDCl_3$**, Top) and Mn(TPP)I·$CDCl_3$ (**Mn-I·$CDCl_3$**, Bottom) at 10 K and 321.6 GHz (black traces) and their powder-pattern simulations (colored traces) 115

Figure 4.9. 2-D field/frequency (energy) maps of turning points in HFEPR spectra of Mn(TPP)Br·$CDCl_3$ (**Mn-Br·$CDCl_3$**) (Top) and Mn(TPP)I·$CDCl_3$ (**Mn-I·$CDCl_3$**) (Bottom, black squares in each case) 117

Figure 4.10. INS spectra of **Mn-Br·$CDCl_3$** (Top) and **Mn-I·$CDCl_3$** (Bottom) at 1.7, 10 and 25 K. The *E* parameter leads to the splitting of the INS peaks. 121

Figure 5.1. VT-INS forward-scattered spectra of **Fe-Cl** with VASP-calculated phonon spectrum 133

Figure 5.2. VT-INS forward-scattered spectra of **Fe-Cl-d_{28}** with VASP-calculated phonon spectrum 135

Figure 5.3. Molecular structure of **Fe-Cl** with numbered carbon atoms (shown in grey) for discussion of phonon movies 139

Figure 5.4. Forward-scattered, Bose-corrected INS spectra of **Fe-F** showing magnetic transitions at 5-125 K (Top) and the full phonon spectrum at 5 K (Bottom) 144

Figure 5.5. Forward-scattered, Bose-corrected INS spectra of **Fe-Br** showing magnetic transitions at 5-125 K (Top) and the full phonon spectrum at 5 K (Bottom) 145

Figure 5.6. Forward-scattered, Bose-corrected INS spectrum of **Fe-I** at 5 K..... 146

Figure 5.7. Forward-scattered, Bose-corrected INS spectra of **Fe-X** series: X = F (black), Cl (red), Br (blue), and I (green) 147

Figure A.1. INS spectra of **Fe-Cl** with incident neutron energy of E_i = 42.3 cm^{-1}: (Top) 20 K; (Bottom) 2 K..... 183

Figure A.2. INS spectrum of **Fe-Cl** at 2 K with incident energy E_i = 26.8 cm^{-1}..... 184

Figure A.3. *Q*-dependence plot of the overlapping magnetic Peak A at ~12.7(1) cm^{-1} for **Fe-Cl** at 2 K with E_i = 26.8 cm^{-1} in Figure A.2..... 185

Figure A.4. (Top) INS spectrum of **Mn-Cl** at 2 K with E_i = 42.3 cm^{-1}. Each point in the plot contains the data over the entire available *Q* range. (Bottom) Peak **D** at *Q* = 1.7-1.8 $Å^{-1}$ with a Gaussian fit and baseline 186

Figure A.5. Example of the fitting of the magnetic peaks in **Fe-Cl** to determine the intensity of the peak at a *Q* value. Temperature = 2 K; E_i = 42.3 cm^{-1}; *Q* = 1.5-1.6 $Å^{-1}$ 187

Figure A.6. Example of fitting of the magnetic peaks in **Mn-Cl** to determine *Q*-dependence. Temperature = 2 K, E_i = 42.3 cm^{-1}; *Q* = 1.7-1.8 $Å^{-1}$ 189

Figure A.7. Tetragonal crystal structure of **Fe-Cl** at 20 K.[8] (Top) Unit cell lengths. (Bottom) Relevant distances in the structure 196

Figure A.8. Powder X-ray diffraction of **Fe-Cl** sample at 298 K (red) compared to pattern calculated from 100 K single-crystal X-ray data (black) 197

Figure A.9. Powder X-ray diffraction data of **Mn-Cl** sample at 298 K (red) compared to pattern calculated from 298 K single crystal X-ray data (black) 198

Figure B.1. Bose-corrected, forward-scattering variable-temperature INS spectra (5-5000 cm^{-1}) of **Co-Cl** (by VISION) with the VASP calculated INS spectrum 199

Figure B.2. Bose-corrected, forward-scattering variable-temperature INS spectra (5-5000 cm^{-1}) of **Co-Br** (by VISION) with the VASP calculated INS spectrum 200

Figure B.3. Bose-corrected, forward-scattering variable-temperature INS spectra (5-5000 cm^{-1}) of **Co-I** (by VISION) with the VASP calculated INS spectrum..... 201

Figure B.4. (Top) Far-IR transmittance spectra of **Co-Cl** at 0 and 17 T with assignments of phonon peaks based on the calculated *u* phonons in Table B.4. (Bottom) Plot of spectra normalized by average 204

Figure B.5. (Top) Far-IR transmittance spectra of **Co-Br** at 0 and 17 T with assignments of phonon peaks based on the calculated *u* phonons in Table B.5. (Bottom) Plot of spectra normalized by average 206

Figure B.6. (Top) Transmittance far-IR spectra of **Co-I** at 0 and 17 T. (Bottom) Plot of spectra normalized by average 208

Figure B.7. Plots of magnetic resonance absorptions (intensity vs. field and energy) calculated for **Co-Cl** (left), **Co-Br** (middle), and **Co-I** (right) 209

Figure B.8. Magneto-Raman spectra of **Co-Cl** at 5 K 212

Figure B.9. Magneto-Raman spectra of **Co-Br** at 5 K 213

Figure B.10. Magneto-Raman spectra of **Co-I** at 5 K 214

Figure B.11. Relative transmittance at 5 K in **Co-Br** upon changing the field from 0 to 7 T 215

Figure B.12. Two-dimensional maps (field vs. frequency/energy) of turning points in the HFEPR spectra of **Co-Cl** (top), **Co-Br** (middle), and **Co-I** (bottom) 216

Figure B.13. HFEPR spectra of loose (unrestrained) sample of **Co-Cl** at 815 GHz and 10 K (black trace), accompanied by a powder-pattern simulation using spin-Hamiltonian parameters in Table 1 (red trace) 217

Figure B.14. Optically-modulated HFEPR spectrum of a loose (unrestrained) sample of **Co-Br** at 830 GHz and 10 K (black trace), accompanied by a simulation using spin-Hamiltonian parameters as in Table 1 (red trace) 218

Figure B.15. Magnetically-modulated HFEPR spectrum of a **Co-Br** pellet at 473 GHz and 10 K, resulting in the conventional derivative shape of the resonances and its simulation using spin-Hamiltonian parameters as in Table 1 (red trace)..... 219

Figure B.16. Magnetically-modulated HFEPR spectrum of a **Co-Br** pellet at 98 GHz and 10 K, resulting in the conventional derivative shape of the resonances (black trace) and its simulation using spin-Hamiltonian parameters as in Table 1 (red trace)..... 220

Figure B.17. Magnetically-modulated HFEPR spectrum of a **Co-I** pellet at 473 GHz and 10 K, resulting in the conventional derivative shape of the resonances and its simulation using spin-Hamiltonian parameters: $D = -13.0$ cm^{-1}, $E = -2.14$ cm^{-1}, $\boldsymbol{g} = [2.23, 2.23, 2.32]$ 221

Figure B.18. Magnetically-modulated HFEPR spectrum of a **Co-I** pellet at 63 GHz and 10 K, resulting in the conventional derivative shape of the resonances and its simulation using spin-Hamiltonian parameters as in Table 1 except $g_z = 2.15$ .. 222

Figure B.19. (Top) Far-IR spectrum of **Co-Cl**. (Bottom) Raman spectrum of **Co-Cl** ... 223

Figure B.20. (Top) Far-IR spectrum of **Co-Br**. (Bottom) Raman spectrum of **Co-Br**... 224

Figure B.21. (Top) Far-IR spectrum of **Co-I**. (Bottom) Raman spectrum of **Co-I**..... 225

Figure B.22. Capped stick molecular structure representing **Co-Cl** and **Co-Br**..... 259

Figure B.23. Capped stick molecular structure of **Co-I**..... 261

Figure B.24. Correlation between the calculated spin densities on the Co(II) ions in **Co-X** and the ZFS *D*' parameters..... 263

Figure B.25. Powder X-ray diffraction of typical **Co-Cl**, **Co-Br**, and **Co-I** samples..... 264

Figure C.1. ORTEP diagrams of the two independent Mn(TPP)Br molecules in **Mn-Br·CH_2Cl_2** 268

Figure C.2. ORTEP diagram of the structure of one molecule of Mn(TPP)I in the crystal of **Mn-I·$CDCl_3$** 271

Figure C.3. ORTEP diagram of the structure of the molecule containing Mn2 in the crystal of Mn(TPP)I·1.5$CHCl_3$ (**Mn-I·1.5$CHCl_3$**) 273

Figure C.4. Qualitative MO diagram in a d^5 square pyramid complex with C_{4v} symmetry 278

Figure C.5. Two views of the Hirshfeld surface of the Mn1 (Top) and Mn2 (Bottom) molecules Mn(TPP)Br·CH_2Cl_2 (**Mn-Br·CH_2Cl_2**) showing normalized close distances of the pro-molecule and neighboring molecules at 100(2) K 279

Figure C.6. Hirshfeld fingerprint plots for **Mn-Br·CH_2Cl_2**: (Top) Molecule containing Mn1 atom; (Bottom) Molecule containing Mn2 atom..... 281

Figure C.7. Hirshfeld surface of Mn(TPP)Br·toluene (**Mn-Br·toluene**) showing normalized close distances of the pro-molecule and neighboring molecules at 100(2) K 282

Figure C.8. Hirshfeld fingerprint plots for **Mn-Br·toluene** 283

Figure C.9. Percentage contributions to the Hirshfeld surface areas for various intermolecular close contacts for Mn(TPP)Br (**Mn-Br**) molecules in various crystal structures..... 285

Figure C.10. Two views of the Hirshfeld surfaces of the Mn1 (Top) and Mn2 (Bottom) molecules **Mn-I·$CDCl_3$** showing normalized close distances of the pro-molecule and neighboring molecules at 100(2) K 286

Figure C.11. Hirshfeld fingerprint plots for **Mn-I·CDCl$_3$**: (Top) Molecule containing the Mn1 atom; (Bottom) Molecule containing the Mn2 atom 287

Figure C.12. Two views of the Hirshfeld surfaces of the Mn1 (Top) and Mn2 (Bottom) molecules **Mn-I·1.5CHCl$_3$** showing normalized close distances of the pro-molecule and neighboring molecules at 100(2) K..... 288

Figure C.13. Hirshfeld fingerprint plots for **Mn-I·1.5CHCl$_3$**: (Top) Molecule containing the Mn1 atom; (Bottom) Molecule containing the Mn2 atom..... 289

Figure C.14. Two views of the Hirshfeld surface of the Mn1 (Top) and Mn2 (Bottom) molecules of Mn(TPP)I·toluene (**Mn-I·toluene**) showing normalized close distances of the pro-molecule and neighboring molecules at 100(2) K..... 290

Figure C.15. Hirshfeld fingerprint plots for Mn(TPP)I·toluene (**Mn-I·toluene**): (Top) Molecule containing Mn1 atom; (Bottom) Molecule containing Mn2 atom..... 291

Figure C.16. Percentage contributions to the Hirshfeld surface areas for various intermolecular close contacts for Mn(TPP)I (**Mn-I**) molecules in various crystal structures..... 293

Figure C.17. **.** Variable-temperature DC susceptibility data under applied DC field of 0.5 T fitted for solvent-free samples: (Top) Mn(TPP)Br (**Mn-Br**). (Bottom) Mn(TPP)I (**Mn-I**)..... 294

Figure C.18. (Top) M-H plot for **Mn-Br·CHCl$_3$** at 1.8 K. (Bottom) AC susceptibility data (χ_M' = filled circles, χ_M'' = empty circles) for Mn(TPP)Br·CHCl$_3$ (**Mn-Br·CHCl$_3$**) with a DC field of 0.14 T and 2.74 Oe driving amplitude 296

Figure C.19. (Top) M-H plot for **Mn-I·1.5CHCl$_3$** at 1.8 K. (Bottom) AC susceptibility data (χ_M' = filled circles, χ_M'' = empty circles) for Mn(TPP)I·1.5CHCl$_3$ (**Mn-I·1.5CHCl$_3$**) with a DC field of 0.14 T and 2.74 Oe driving amplitude 298

Figure C.20. HFEPR spectra of **Mn-Br·CDCl$_3$** (Top) and **Mn-I·CDCl$_3$** (Bottom) at 10 K and 108 GHz and 112 GHz, respectively (black traces) and their powder-pattern simulations (colored traces) 299

Figure C.21. HFEPR spectra of **Mn-Br·CDCl$_3$** (Top) and **Mn-I·CDCl$_3$** (Bottom) at 10 K and 216 GHz and 220.8 GHz, respectively (black traces) and their powder-pattern simulations (colored traces) 300

Figure D.1. INS forward-scattered, Bose-corrected spectra of **Fe-Cl** at 5 K with VASP-calculated phonon spectrum (black)..... 301

Figure D.2. INS forward-scattered, Bose-corrected spectra of **Fe-Cl-*d*$_{28}$** at 5 K with VASP-calculated phonon spectrum (black)..... 302

Figure D.3. Molecular structure of **Fe-Cl** with labeled atoms to accompany Table D.3..... 309

Figure D.4. PXRD at 296 K of the samples of **Fe-Cl** (Top) and **Fe-Cl-*d*$_{28}$** (Bottom) used in INS and comparisons with that of calculated from single-crystal structure of **Fe-Cl**..... 311

LIST OF ATTACHMENTS

Phonon Movies for **Co-X** Series [$Co(PPh_3)_2X_2$_X=Cl,Br,I phonon animations.zip]

Phonon Movies of **Fe-Cl** and **Fe-Cl-d_{28}** [FeTPPCl and $FeTPPd_{28}Cl$ phonon animations.zip]

LIST OF ABBREVIATIONS

2-D or 2D	Two-dimensional
BM	Bohr magneton(s)
CASSCF	Complete active space self-consistent field
CIF	Crystallographic information file
CShM	Continuous shape measure calculations
DCS	Disc Chopper Spectrometer
DDN	Double precision d^n electronic configuration program (J. Telser)
DFT	Density functional theory
EPR	Electron paramagnetic resonance
FIRMS	Far-IR magneto-spectroscopy
FD	Frequency-domain
FD-FT THz EPR	Frequency-domain FT terahertz EPR
FT	Fourier transform
GGA	Generalized gradient approximation
HFEPR	High-frequency and -field EPR
INS	Inelastic neutron scattering
IR	Infrared
KD	Kramers doublet
LFT	Ligand-field theory
LMCT	Ligand-to-metal charge transfer
Ln	Lanthanide

MCD	Magnetic circular dichroism
MDS	Magnetic-field-division spectrum
QTM	Quantum tunneling of magnetization
Qubit	Quantum bit
SH	Spin-Hamiltonian
SIM	Single-ion magnet
SMM	Single-molecule magnet
SOC	Spin-orbit coupling
TA-QTM	Thermally-assisted quantum tunneling of magnetization
TM	Transition metal
TOF	Time-of-flight
VASP	Vienna *ab initio* simulation package
VISION	Vibrational Spectrometer
VT	Variable-temperature
ZFS	Zero-field split(ting)

LIST OF SYMBOLS

Λ	Spin-phonon coupling constant
D	Single-ion axial anisotropy parameter
E	Transverse or rhombic anisotropy parameter
g	g-factor or g-tensor
J	Total angular momentum
KD	Kramers doublet
k_f	Momenta of outgoing neutrons
k_i	Momenta of incoming neutrons
M_J	Total angular momentum quantum number
m_l	Magnetic quantum number
M_s or m_s	Spin quantum number
Q	Momentum transfer
S	Spin
U_{eff}	Effective energy barrier separating bistable magnetic states

LIST OF COMPOUNDS IN DISSERTATION

Fe-F	Fe(TPP)F (TPP^{2-} = *meso*-Tetraphenylporphyrinate)
Fe-Cl	Fe(TPP)Cl
Fe-Br	Fe(TPP)Br
Fe-I	Fe(TPP)I
Mn-Cl	Mn(TPP)Cl
Mn-Br	Mn(TPP)Br
Mn-I	Mn(TPP)I
Co-Cl	$Co(PPh_3)_2Cl_2$
Co-Br	$Co(PPh_3)_2Br_2$
Co-I	$Co(PPh_3)_2I_2$

CHAPTER I

INTRODUCTION

1.1. Molecular Magnetism

In 1993, Sessoli *et al.* reported a cluster compound—$[Mn_{12}O_{12}(AcO)_{16}(H_2O)_4]\cdot 2AcOH$, commonly known as Mn_{12}—with ground state spin $S = 10$ that exhibited long magnetic relaxation in the absence of an external magnetic field.[1] This magnet was the first of a class of materials coined "single-molecule magnets" (SMMs), which display hysteresis due to the electronic configuration(s) of individual spin centers rather than bulk magnetic ordering. In the decade that followed Sessoli's report, efforts to develop novel SMMs focused on similar transition metal clusters with high spin multiplicities.[2] In 2003, Ishikawa and coworkers forged a new branch of single-molecule magnetism with a seminal report on $[Pc_2Ln]^-\cdot TBA^+$ (Pc = phthalocyanine; $TBA^+ = N(n\text{-}Bu)_4^+$; Ln = Tb^{3+}, Dy^{3+}).[2] These lanthanide double-decker complexes exhibited hysteresis due to the electronic structure of a single lanthanide center and were aptly called single-ion magnets (SIMs). SMM and SIM systems have since garnered intense technological interest, as they are promising candidates for data storage (as binary bits) and quantum computing (as quantum bits, or qubits) applications. Compared to traditional bulk magnets, SIM-based computing offers a potential increase in storage density and processing speeds.[3-4]

One parameter for describing slow relaxation in SMM and SIM systems is U_{eff}, or the effective energy barrier between bistable spin states. A greater U_{eff} affords longer magnetic relaxation times, as the molecule is required to overcome a larger energy barrier to undergo spin reversal. The original approach to maximizing U_{eff} was to maximize the number of spin centers in a cluster compound; however, Ishikawa's $[Pc_2Ln]^-\cdot TBA^+$ far surpassed Mn_{12} in U_{eff} magnitude and retained slow relaxation at higher temperatures,

despite having only one spin center per molecule.[2] Ishikawa's work established a need for more complex design criteria to maximize hysteresis, which could only be achieved with deeper understanding of the energetic structures of SIM and SMM candidates, as well as the various pathways to magnetic relaxation.

1.1.1. Energetic Structure and Anisotropy of Transition Metal Complexes

In transition metal-, lanthanide-, and actinide-based SIMs, U_{eff} is a function of magnetic anisotropy, which arises when the energy of magnetization is dependent on the orientation of the magnetic moment.[5] How magnetic anisotropy is induced depends on the nature of the spin center, and is best described in terms of the perturbations that introduce anisotropy for different spin centers.

In general, for 3*d* transition metal (TM) complexes, magnetic states described by the quantum number *S* arise due to strong crystal field interactions. The resultant crystal field-split states are notated as ${}^{2S+1}L$ via the Russell-Saunders coupling scheme. In compounds with $S > ½$ and quenched orbital angular momenta, degenerate ${}^{2S+1}L$ states are split by a second-order spin-orbit coupling (SOC) interaction, leading to zero-field splitting (ZFS). In these complexes, ZFS defines the magnetic levels of interest according to the following spin-Hamiltonian (SH):

$$\widehat{H} = D\left[\hat{S}_z^2 - S(S+1)/3\right] + E\left(\hat{S}_x^2 - \hat{S}_y^2\right) + \mu_B g\hat{S}\cdot\hat{B} \qquad \text{(Eq. 1.1)}$$

where *D* and *E* are the respective axial and rhombic ZFS parameters described below, μ_B is a Bohr magneton, g is the electron spin g-factor, $\hat{S}$ is the spin operator, and $\widehat{B}$ is the magnetic induction vector.

The ZFS levels are defined by magnetic quantum number M_S, which ranges from zero to $\pm S$ in integer spin systems and from $\pm 1/2$ to $\pm M_S$ in half-integer spin systems. Axial ZFS parameter D and rhombic ZFS parameter E define the magnetic anisotropy of a given complex absent of an external magnetic field. The effective barrier to relaxation, U_{eff}, can be calculated using D for complexes with integer spins:

$$U_{eff} = \left(S^2 - \frac{1}{4}\right)|D| \qquad \text{(Eq. 1.2)}$$

and for complexes with half-integer spins:

$$U_{eff} = S^2|D| \qquad \text{(Eq. 1.3)}$$

According to Equations 1.2 and 1.3, in order to maximize U_{eff} and theoretically enhance slow magnetic relaxation in TM-based SIMs, a large absolute value of D is desired. D can be either positive or negative. Compounds with $D > 0$ exhibit easy-plane anisotropy, where the total spin is largely localized around the xy plane and the energy of the smallest M_S state (M_S = 0 or ½) is minimized. Conversely, when $D < 0$, the compound exhibits easy-axis anisotropy with the total spin localized along the z-axis, and energies of the $M_S = \pm S$ states are minimized. For most reported SIMs and SMMs, $D < 0$, as this configuration "forces" relaxation via several higher energy magnetic states in the absence of quantum tunneling, as shown by the double-well diagram in Figure 1.1. When $S > ½$, the direct transition from $-S \rightarrow +S$ is spin-forbidden ($\Delta S = 0, \pm 1$), thus promoting magnetic relaxation via traversal of the U_{eff} energy barrier. However, $D < 0$ is not a requisite condition for a TM-based SMM, and several SMMs with $D > 0$ have been reported.[6]

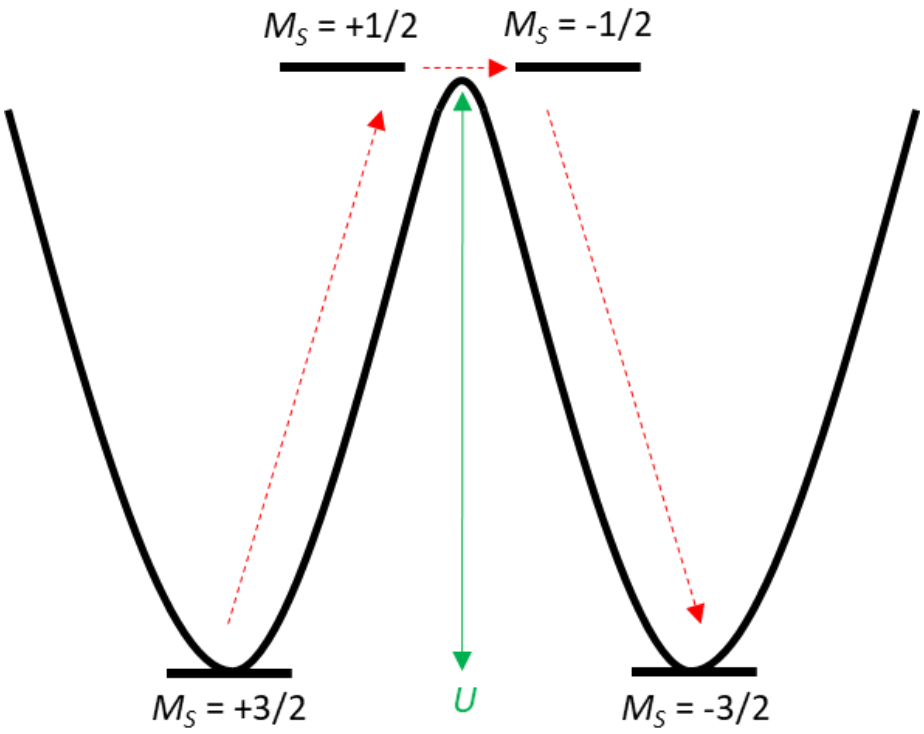


Figure 1.1. Double-well diagram representing the magnetic barrier for a transition metal-based system with $S = 3/2$ and $D < 0$. In the case of $D > 0$, energies of the $M_S = +1/2$ and -1/2 states are minimized. U represents the magnetic energy barrier (U_{eff} is the empirical equivalent of U, when additional relaxation mechanisms are considered). Dashed arrows indicate the ideal pathway for magnetic relaxation via spin-allowed $\Delta M_S = \pm 1/2$ transitions.

In cases of heavier 4*d* and 5*d* TM complexes, TM complexes with unquenched orbital angular momenta, and 4*f* complexes, strong spin-orbit coupling effects negate M_S as a good quantum number for magnetic states. As such, these SOC-defined states are represented by the total angular momentum quantum number, M_J. In these systems, ZFS parameters *D* and *E* do not strictly apply, though SMM behavior arises from a similar traversal of the U_{eff} barrier via several processes of magnetic relaxation (described in Section 1.1.3).

1.1.1.1. Fe(III) Porphyrin Complexes

The porphyrin backbone of *meso*-tetraphenylporphyrins Fe(TPP)X (TPP^{2-} = *meso*-tetraphenylporphyrinate, X = F, **Fe-F**; Cl, **Fe-Cl**; Br, **Fe-Br**; I, **Fe-I**) makes them suitable models for biologically active hemes.[7] **Fe-Cl** is a high-spin ($S = 5/2$) d^5 complex with molecular C_{4v} symmetry, leading to ZFS of the six-fold degenerate states into three doublets ($M_S = \pm 1/2, \pm 3/2, \pm 5/2$; Figure 1.2). The SH for **Fe-Cl** is given in Eq. 1.4:

$$\widehat{H}_S = D\left[\hat{S}_z^2 - S(S+1)/3\right] \qquad \text{(Eq. 1.4)}$$

where *D* is the axial ZFS parameter.

Splitting diagrams for the *d*-orbitals and six-fold degenerate magnetic states are shown in Figure 1.2. Due to the four-fold molecular symmetry and tetragonal *I*4 (space group No. 79) crystal symmetry,[8] theoretically $E = 0$ for **Fe-Cl**.[7, 9] The sign and value of *D*, determined by direct-geometry INS, is 6.33(8) cm^{-1}.[9] By high-frequency, high-field EPR (HFEPR), the experimental ZFS parameters are $D = 6.458(2)$ cm^{-1} and $E = 0.015(5)$ cm^{-1}.[10]

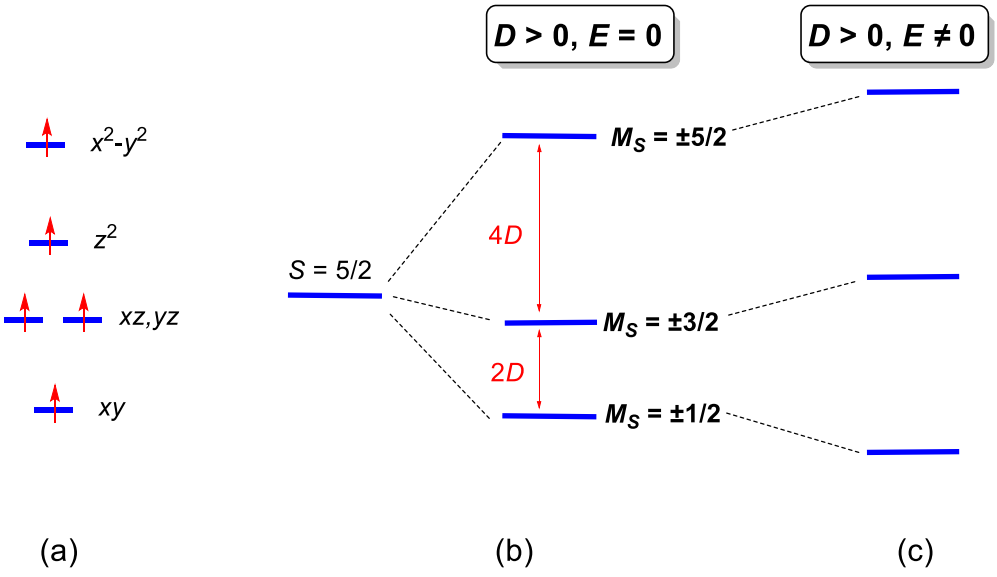


Figure 1.2. (a) *d*-Orbital splitting diagram for d^5 **Fe-X** series with $S = 5/2$; (b) ZFS in **Fe-F** and **Fe-Cl** with $D > 0$ and $E = 0$; (c) ZFS in **Fe-Br** and **Fe-I** with $D > 0$ and $E \neq 0$.

Fe-F, **Fe-Br** and **Fe-I**, like **Fe-Cl**, are d^5, $S = 5/2$ complexes with molecular four-fold symmetry. **Fe-F**, like **Fe-Cl**, crystallizes in the $I4$ space group and has both molecular and crystallographic four-fold symmetry ($E = 0$).[8] However, as both **Fe-Br** and **Fe-I** crystallize in a monoclinic space group ($P2_1/c$ and $P2_1/n$, respectively[11-12]), $E \neq 0$, and the SH (Eq. 1.5) includes the E parameter to account for ZFS properties:

$$\hat{H}_s = D\left[\hat{S}_z^2 - S(S+1)/3\right] + E\left[\hat{S}_x^2 - \hat{S}_y^2\right] \qquad \text{(Eq. 1.5)}$$

where D and E are the respective axial and rhombic ZFS parameters, and $\hat{S}$ is the spin operator.

As the covalent character of the Fe−X bond and the atomic SOC constant[10] increases from F to I, the D values increase accordingly; for **Fe-F**, $D = +4.49(9)$ cm^{-1}, for **Fe-Br**, $D = +8.8(2)$ cm^{-1}, and for **Fe-I**, $D = +13.4(6)$ cm^{-1} by INS.[7] By HFEPR, the ZFS parameters are $D = 9.03(5)$ cm^{-1}, $E = 0.047(5)$ cm^{-1} for **Fe-Br** and, for **Fe-I**, $D = 13.84$ cm^{-1}, $E = 0.07$ cm^{-1}.

Though the Fe(TPP)X (X = F, Cl, Br, I) series does not exhibit SMM behavior, there are several examples of 3*d* Fe(III) complexes with intermediate spin $S = 3/2$[13-14]—including a complex with an axial Fe−X bond and square pyramidal coordination geometry[14]—and spin-crossover ($S = 3/2 \leftrightarrow 5/2$) properties that behave as SMMs.[15] As such, insight into the magnetic, vibrational, and spin-phonon coupling properties of Fe(TPP)X (X = F, Cl, Br, I) is useful for modeling heme behavior as well as understanding the appearance of SIM-like behavior in similar Fe(III) complexes.

1.1.1.2. Mn(III) Porphyrin Complexes

Five-coordinate Mn(III) tetraphenylporphyrin complexes Mn(TPP)X (**Mn-X**; X = Cl, **Mn-Cl**; Br, **Mn-Br**; I, **Mn-I**) are paramagnetic d^4 complexes with spin $S = 1$ and quenched angular momenta. ZFS of these complexes is described by the SH in Eq. 1.5 in Section 1.1.1.1. For compounds with both 4-fold molecular and crystallographic symmetry, such as solvent-free **Mn-Cl**, the SH in Eq. 1.5 is simplified to Eq. 1.4. However, compounds in the Mn(TPP)X (X = Cl, Br, I) series are known to co-crystallize with various solvents in space groups with less than 4-fold crystallographic symmetry.[16-19]

For d^4 Mn(III), $S = 2$ complexes, the splitting diagrams for five degenerate states are shown in Figure 1.3. When $D > 0$, in the case of easy-plane anisotropy, ZFS affords a $M_S = 0$ ground state. In the case of easy-axis anisotropy, when $D < 0$, ZFS gives $M_S = \pm 2$ ground states. In the absence of 4-fold symmetry in either the molecule or crystal structure, $x \neq y$, and the rhombic ZFS parameter $E \neq 0$, leading to splittings shown in Figure 1.3. For an easy-plane ($D > 0$) compound, transitions between the ground $M_S = 0$ and either first excited $M_S = -1$ or second excited $M_S = +1$ state ($\Delta M_S = \pm 1$) are magnetically allowed. For an easy-axis ($D < 0$, $E = 0$) compound inside a magnetic field, the transition from the ground $M_S = -2$ to the first excited $M_S = +2$ state ($\Delta M_S = +4$) is forbidden, as magnetically-allowed transitions have $\Delta M_S = 0$ or ± 1.

Complexes with spin quintet ($S = 2$) ground states and 4-fold molecular and crystallographic symmetries, such as solvent-free **Mn-Cl**, have been historically considered 'EPR-silent' using the criterion of not giving an EPR signal on a spectrometer operating at conventional frequency (generally X-band, e.g., 9.5 GHz). However, when

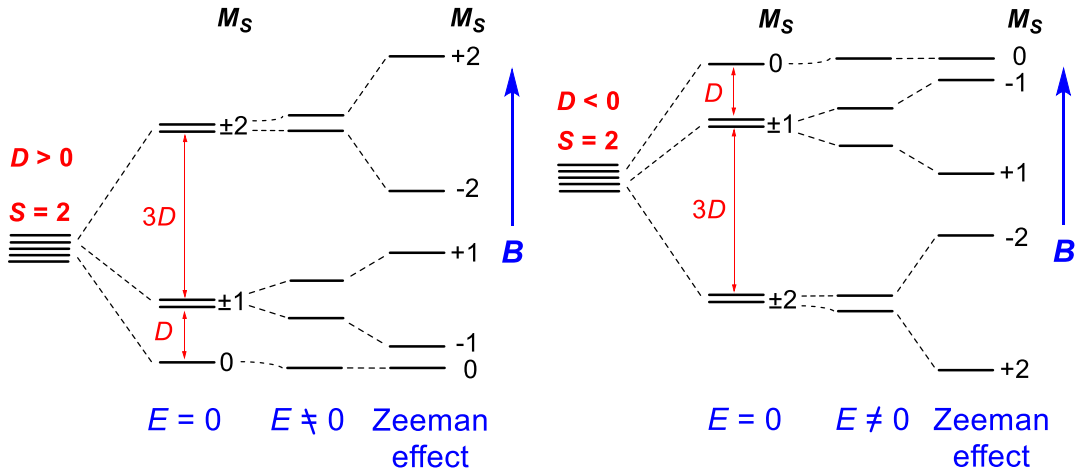


Figure 1.3. ZFS in $S = 2$ complexes with (Left) 4-fold molecular and crystallographic symmetry and (Right) *no* 4-fold symmetry. Zeeman effect inside a magnetic field (B) further splits the sublevels.

either molecular or crystallographic symmetry deviates from 4-fold, the rhombic ZFS parameter $E \neq 0$, leading to state mixing. In particular, it makes a nominally forbidden transition between the $M_S = |+2\rangle$ and $|-2\rangle$ levels partially allowed. Given the generally small energy difference between these levels, this results in a frequent observation of that transition in X-band at low field. Examples of Mn(III) coordination complexes exhibiting such X-band low-field EPR signals are Mn(salen) complexes such as Mn(salen)Cl [salen = (*R*,*R*)-(−)-N,N'-bis(3,5-di-tert-butylsalicylidene)-1,2-cyclohexanediamine],[20-21] $Mn(acac)_3$ (acac = acetylacetonate),[22] and corrole Mn(tpfc) [tpfc = 5,10,15-tris(pentafluorophenyl)corrole trianion.[23] However, HFEPR has been utilized to determine the ZFS parameter for solvent-free **Mn-Cl** ($D \approx -2.3$ cm^{-1})[24-26] that agrees with *D* values from INS [$D = -2.24(2)$ cm^{-1}].[9]

Though **Mn-Cl** co-crystallized with benzene in the lattice [$D = -2.2(0.1)$ cm^{-1}][27] exhibits slow magnetic relaxation,[28] the magnetic properties of **Mn-Br** and **Mn-I** with various lattice solvents have not been thoroughly investigated.

1.1.1.3. Tetrahedrally Coordinated Co(II) Complexes

In tetrahedrally coordinated, d^7 Co(II) complexes, such as the $Co(PPh_3)X_2$ (**Co-X**; X = Cl, **Co-Cl**; Br, **Co-Br**; I, **Co-I**) described in Chapter III, the ligand field affords the high-spin ($S = 3/2$) electronic ground state $^4A_2$. In paramagnetic complexes with $S \geq 1$ and quenched orbital angular momentum, ZFS of electronic states arises due to second-order SOC, splitting the $^4A_2$ state into two levels: $M_S = \pm 1/2$ and $M_S = \pm 3/2$ (Figure 1.4).[29-45] Lowering the symmetry to D_{2d} and further to C_{2v} results in $^4B_1$ and $^4A_2$ electronic ground states (Figure 1.5), respectively, affording an axial ZFS parameter *D* that is highly

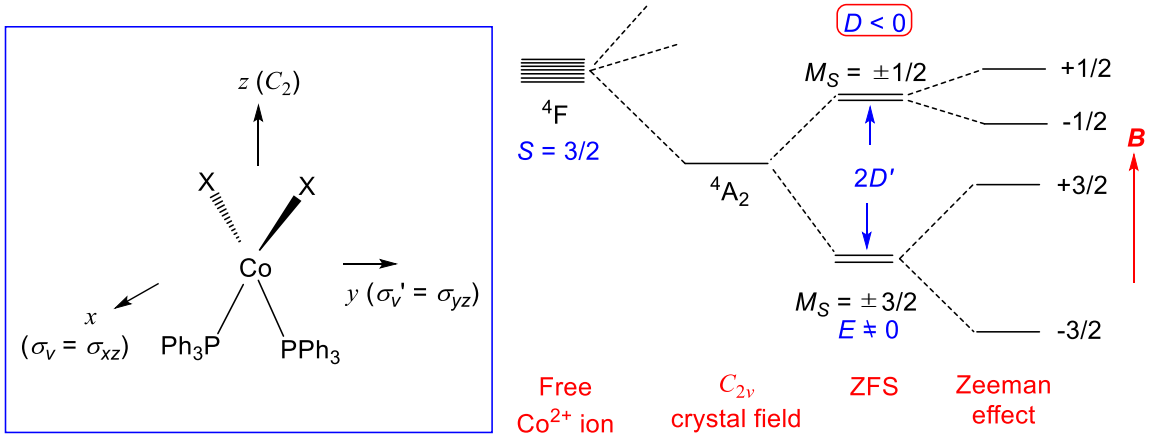
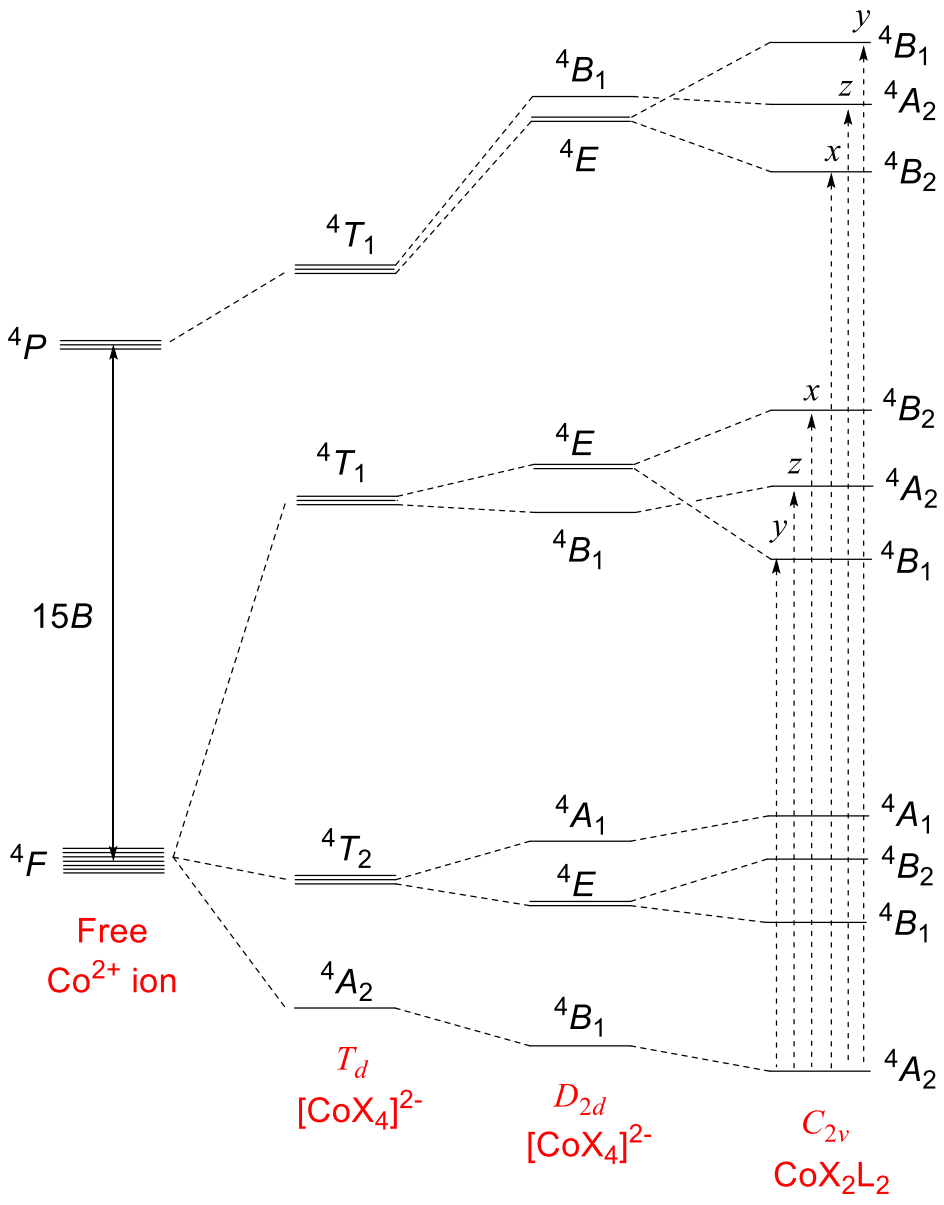


Figure 1.4. (Left) Diagram of **Co-X** (X = Cl, Br, I). (Right) Spin level diagram of the complexes in the case of $D < 0$. $D' = (D^2 + 3E^2)^{1/2}$. It should be pointed out that the $M_S = \pm 1/2$ and $M_S = \pm 3/2$ are nominal labels for the levels, as the zero-field $|\pm 1/2\rangle$ and $|\pm 3/2\rangle$ levels are mixed when $E \neq 0$, as found for **Co-X**.[46-47] For excited electronic states of the complexes involved in second-order SOC, contributing to ZFS, see Figure 1.5.

Figure 1.5. Electronic states of quartet states of $3d^7$ Co^{2+} as a free-ion, in a tetrahedral (T_d) ligand field, in a tetragonally compressed ligand field (D_{2d}), and in a rhombic (C_{2v}) ligand field as in **Co-X**. This figure is based on one derived for $NiX_2(PPh_3)_2$.[48] The electronic transitions are also indicated, together with their polarization, fully for the C_{2v} case,[49] and partially for the D_{2d} case.[50-51] Inclusion of spin-orbit coupling (not shown) would split each of the quartets into two degenerate levels, affording the observed ZFS. This effect is shown graphically in Figure 3e of the paper by Sundararajan *et al.*[52]


^4P
^4F
15B
Free
Co^{2+} ion
$^4T_1$
$^4T_2$
$^4A_2$
^4E
$^4B_1$
$^4A_1$
T_d
$[CoX_4]^{2-}$
D_{2d}
$[CoX_4]^{2-}$
C_{2v}
CoX_2L_2
y
z
x

sensitive to the difference in energy between ground and excited states. The energy difference between the two $M_S = \pm 1/2$ and $M_S = \pm 3/2$ levels can be described by the SH in Eq. 1.5 in Section 1.1.1.1.

ZFS of the **Co-X** series has been studied extensively via terahertz time-domain EPR,[53] HFEPR,[54] magnetic circular dichroism (MCD),[54] and magnetic susceptibility[55-56] techniques. Values derived from these studies are listed in Tables 1.1 and 1.2. Prior to the current work, **Co-Cl** was determined to have $D = -14.76$ cm^{-1} by THz time-domain EPR[53] and HFEPR,[54] $D = -14(3)$ cm^{-1} by MCD,[54] and $D = -11.6$ cm^{-1} by magnetometry.[56] **Co-Br** was determined to have $D = -13.90$ cm^{-1} by THz time-domain EPR[53] and $D = -12.5$ cm^{-1} by magnetometry,[56] and for **Co-I**, $D = -36.9$ cm^{-1} by magnetometry.[55] AC susceptibility studies of **Co-X** show that, under an external DC magnetic field, **Co-Cl**,[57] **Co-Br**,[58] and **Co-I**[55] all exhibit slow magnetic relaxation. However, only **Co-Br** and **Co-I** exhibit SMM behavior in zero field, as quantum tunneling of the magnetization (QTM) causes rapid magnetic relaxation of **Co-Cl** when the transitions are not suppressed by an external field.[55, 57-58]

1.1.2. Mechanisms of Magnetic Relaxation

A long relaxation time (ideally years to decades) is required for the practical application of SIMs for data storage and computing. After perturbation of the molecule by a magnetic field, relaxation occurs via quantum tunneling of the magnetization (QTM) or by exchanging energy with the lattice. QTM, shown schematically in Figure 1.6, occurs between ground M_S or M_J levels, where the magnetization undergoes a transition directly from $M_J = +J$ to $M_J = -J$ (or $M_S = -S$ to $M_S = +S$). Thermally-assisted QTM (TA-

Table 1.1. Axial and rhombic ZFS parameters for **Co-Cl**, **Co-Br**, and **Co-I**

Complex	**Method**	D **(cm^{-1})**	$\lvert E \rvert$ **(cm^{-1})**[a]	$\lvert E/D \rvert$	$D' = (D^2 + 3E^2)^{1/2}$ **(cm^{-1})**	**Ref.**
Co-Cl	THz time-domain EPR	−14.76	1.61	0.109	15.0	53
	HFEPR	−14.76(2)	1.141(8)	0.0773(5)	14.89(2)	54
	MCD	−14(3)	0.96(20)	0.08(2)	14(3)	54
	Magnetometry	−11.6	2.43	0.21	12.3	56
Co-Br	THz time-domain EPR	−13.90	0.96	0.069	14.0	53
	Magnetometry	−12.5	0.70	0.056	12.6	56
Co-I	Magnetometry	−36.9				55

[a] Sign of E values in cited references is positive. The sign was not determined in the current work. Absolute signs are placed to all values here.

Table 1.2. *g*-Values for **Co-Cl** and **Co-Br**

Complex	Method	g_x	g_y	g_z	Ref.
Co-Cl	THz time-domain EPR	2.20	2.18	2.23	53
	HFEPR	2.166(4)	2.170(4)	2.240(5)	54
	MCD	2.15(5)	2.16(4)	2.17(3)	54
	Magnetometry	2.215		2.265	56
Co-Br	THz time-domain EPR	2.10	2.10	2.22	53
	Magnetometry	2.006		2.164	56

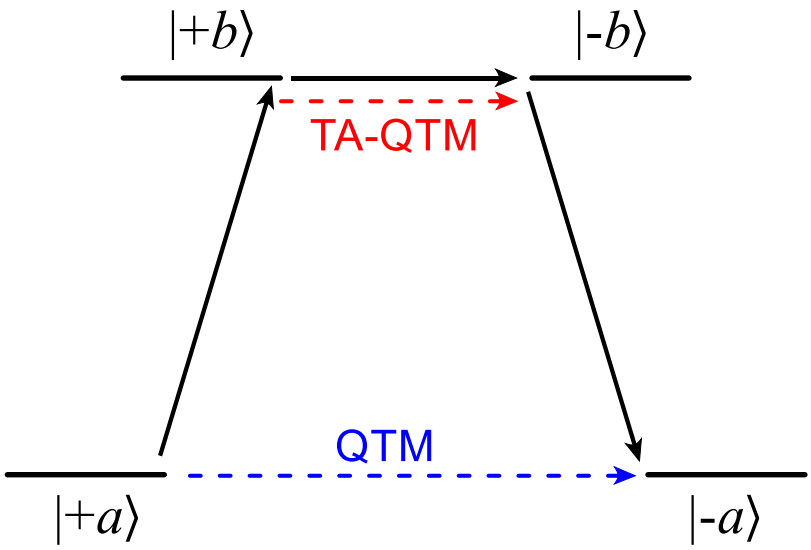


Figure 1.6. Schematic representation of QTM (blue) and TA-QTM (red) mechanisms for magnetic relaxation. Black arrows represent the slow relaxation process. In the TA-QTM mechanism, tunneling occurs between magnetic states of equal energy and opposite sign after the system absorbs a phonon to populate an excited state. In this representation, TA-QTM occurs via the first excited state shown; however, TA-QTM can also occur through higher-energy magnetic states.

QTM) occurs when phonons are absorbed to populate excited states, followed by QTM between $\pm M_S$ or $\pm M_J$ states of equal energies and opposite sign before the molecule relaxes to the ground sublevel.[59] The probability of QTM increases with energy barrier height and particle mass, and is promoted in the presence of a transverse magnetic field (in transition metal complexes, when $E \neq 0$) and with hyperfine coupling (when spin-active nuclei couple to the magnetic moment).[59]

There are three primary sources of spin-lattice relaxation: the direct process, the Orbach process, and the Raman process, all of which are represented in Figure 1.7. The direct process is a one-phonon process, where the system undergoes relaxation from one microstate to another (from $|2\rangle$ to $|1\rangle$ in Figure 1.7), and the excess energy is taken up by the lattice as a phonon. Direct relaxation dominates at lower temperatures in the liquid helium regime, but does not have a significant effect at practical operating temperatures for SIMs.[5, 60] The Raman process is a two-phonon process involving a virtual state above the phonon cutoff, or the energy of the highest allowed phonon frequency. When the system relaxes, the excess energy is taken up by a superposition of two phonons with a difference in energy that matches that released by the system during relaxation. In the Orbach process, the spin system starts in a low-lying crystal field excited state, and absorption of a phonon induces a transition to a higher-energy crystal field state (from $|2\rangle$ to $|3\rangle$ in Figure 1.7). The system then relaxes to the ground state (from $|3\rangle$ to $|1\rangle$) and emits a phonon. The spin-lattice relaxation mechanisms are described in Eq. 1.7:

$$\tau^{-1} = AH^{n_1}T + CT^{n_2} + \tau_0^{-1} \exp\left(\frac{-U_{eff}}{k_B T}\right) \qquad \text{(Eq. 1.7)}$$

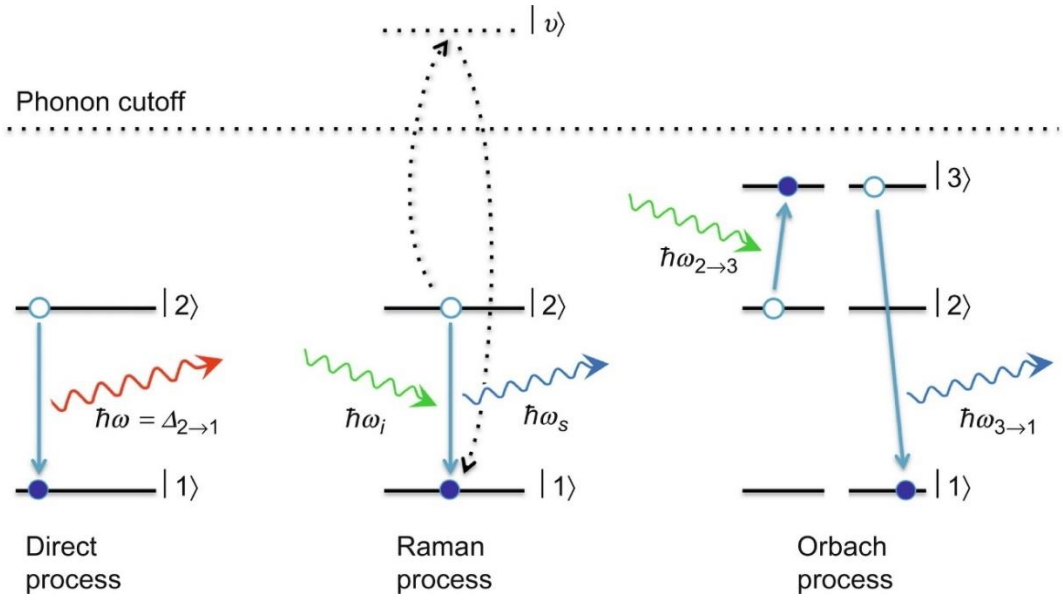


Figure 1.7. Schematic diagram showing spin-lattice relaxation processes for SMMs.[61] Adapted with permission from Ref. 61.

where *A*, *C*, and τ_0 are parameters that contain the spin-phonon coupling matrix element and the speed of sound, *H* is the magnetic field, and *T* is the temperature.

The terms on the right side of Eq. 1.7 correspond to the direct, Raman, and Orbach processes, respectively. It is evident from Eq. 1.7 that the three processes exhibit distinct temperature dependences, and thus are more or less prominent within specific temperature regimes. Magnetic susceptibility data can be fitted using Eq. 1.7 to estimate U_{eff}; however, such indirect AC susceptibility techniques are insufficient for direct observation of the U_{eff} barrier (or *D*' in transition metal complexes). As such, additional experimental techniques are necessary to directly and unambiguously quantify the magnetic separations of SMMs.

1.2. Experimental Methods

1.2.1. Inelastic Neutron Scattering (INS)

Inelastic neutron scattering (INS) is a major spectroscopic technique to directly probe magnetic excitations and vibrational modes in chemical compounds.[62] Because neutrons are spin-active (spin = 1/2) particles, they are able to interact with electrons to promote magnetic transitions. Additionally, incident neutrons are scattered by atomic nuclei in the sample, promoting vibrational transitions (*i.e.*, phonons) when energy transfer occurs (*i.e.*, in an *inelastic* process). The magnetic scattering cross section for identical magnetic ions with localized electrons scattering unpolarized neutrons is given in Eq. 1.8:

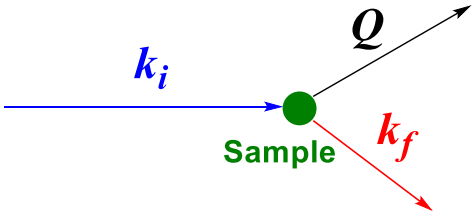
$$\frac{d^2\sigma}{d\Omega d\omega} = (\gamma r_0)^2 \frac{k_f}{k_i}\left[\frac{1}{2} gF(Q)^2 e^{-2W(Q)} \sum_{\alpha,\beta}\left(\delta_{\alpha\beta} - \frac{Q_\alpha \cdot Q_\beta}{Q^2}\right) S^{\alpha\beta}(Q,\omega)\right] \quad \text{(Eq. 1.8)}$$

where σ = neutron cross-section; γ = gyromagnetic ratio; r_0 = classical radius of an electron; g = Landé g-factor; $F(\boldsymbol{Q})$ = dimensionless magnetic form factor defined as the Fourier transform of the normalized spin density associated with magnetic ions; $\boldsymbol{Q}$ = scattering vector; $e^{-2W(\boldsymbol{Q})}$ = Debye-Waller factor caused by thermal motion; $S^{\alpha\beta}(\boldsymbol{Q},\omega)$ = magnetic scattering function; $\left(\delta_{\alpha\beta} - \frac{\boldsymbol{Q}_\alpha \boldsymbol{Q}_\beta}{Q^2}\right)$ = polarization factor which implies neutrons can only couple to magnetic moments or spin fluctuations perpendicular to $\boldsymbol{Q}$; $\eta\omega$ = energy change experienced by the sample; and ω = angular frequency of the neutron.

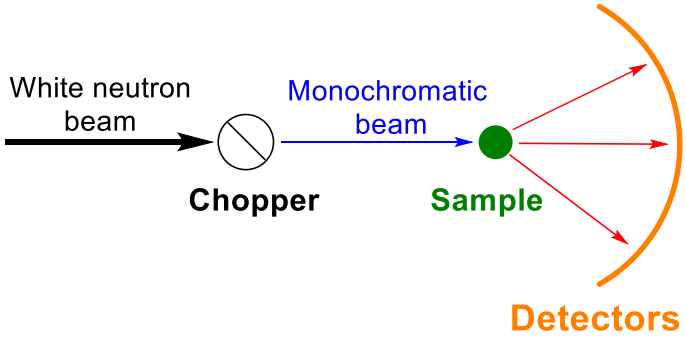
In INS experiments, a monochromatic neutron beam (with incident energy E_i) is scattered by either unpaired electrons or atomic nuclei in the sample, causing an energy transfer to give outgoing neutrons with energy E_f. Two types of INS instruments are utilized in this dissertation: direct-geometry and indirect-geometry instruments (Figure 1.8). In direct-geometry INS, E_i of the incident neutrons is selected and fixed, and E_f of outgoing neutrons are measured via time-of-flight (TOF) to determine ΔE.[62] This configuration also allows for scanning a broad range of the scattering vector $\boldsymbol{Q}$, which is the resultant vector from the addition of incoming ($\boldsymbol{k_i}$) and outgoing ($\boldsymbol{k_f}$) momentum vectors (Figure 1.8), to evaluate $\boldsymbol{Q}$-dependence of magnetic and phonon modes.[62] The scattering vector $\boldsymbol{Q}$ of a transition is a unique parameter among spectroscopies, as it provides critical information about the nature of the transition: i.e., as the magnitude of $\boldsymbol{Q}$ increases, the intensities of magnetic transitions decrease, while the intensities of vibrational transitions increase.[9, 62-63] As a result, the Q-dependence of peak intensities can be used to distinguish among magnetic and phonon transitions in SMMs. It is worth noting that, unlike far-IR magneto-spectroscopy (FIRMS) and EPR techniques, this is a

Figure 1.8. (a) Schematic of INS processes. $\boldsymbol{k_i}$ and $\boldsymbol{k_f}$ refer to the momenta of incoming and outgoing neutrons with energies of E_i and E_f, respectively. $\boldsymbol{Q} = \boldsymbol{k_i} - \boldsymbol{k_f}$ is the scattering vector (also known as the momentum transfer vector). $Q = |\boldsymbol{Q}|$ is the length of $\boldsymbol{Q}$. In INS, there is a momentum/energy transfer between the incoming neutrons and the sample. Thus, $E_i \neq E_f$. (b) Box diagram for a direct-geometry INS instrument. Since the outgoing neutrons reach different detectors at various scattering angles, as represented by the three red arrows in the scheme, different Q values for any E_f reflect the scattering angles of the outgoing neutrons. In other words, outgoing neutrons with the same energy E_f may reach detectors with various angles [i.e., different Q], thus giving the Q-dependence of the E_f, or an absorption peak, in INS. (c) Box diagram for an indirect-geometry INS instrument. Scattering angles are shown at 45° (forward scattering) and 135° (back-scattering).

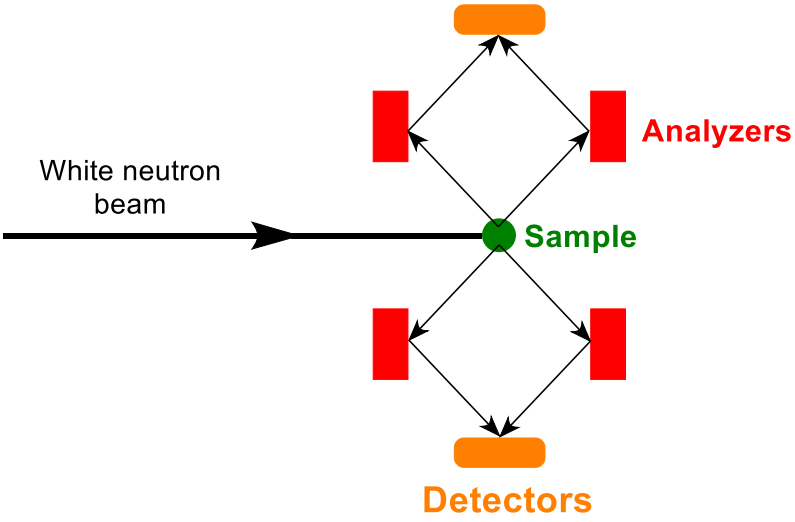
A


Q
k_i
k_f
Sample

B


White neutron beam
Monochromatic beam
Chopper
Sample
Detectors

C


Analyzers
White neutron beam
Sample
Detectors

zero-field technique.

Another unique feature of INS is that, in metal dimers/clusters, the *Q*-dependence of magnetic transitions gives direct information about the *intra*molecular configuration of the metal ions in the molecules.[64-66] For a magnetic transition from the ground spin state to an excited spin state *S* in the metal dimers/clusters, its peak intensity in INS is given by:

$$I \sim A\, F^2(Q)\, \mathfrak{M}\, [1 - \frac{\sin(QR)}{QR}] \qquad \text{(Eq. 1.9)}$$

where $F(Q)$ is the magnetic scattering factor (also known as the magnetic form factor)[67] which is the Fourier transform of the spin density in the crystal lattice of the sample; $F^2(Q)$ is the intensity of the magnetic scattering factor, which decreases with Q increase; $\mathfrak{M}$ is a matrix element[64] about the interferences between/among the metal ions, giving the oscillatory behavior of the peak intensity with Q[64, 66, 68] as a direct picture of the metal-metal distance(s) in the dimer/cluster;[69] R is the metal-metal distance in the dimer/cluster; $A = \exp\left(-\frac{E(S)}{k_B T}\right)\exp(-2W)$, in which $E(S)$ is the energy of the spin state S; k_B is Boltzmann constant; and exp(-2W) is the Debye-Waller factor about the reduction of scattering from atomic vibrations.

It is evident from Eq. 1.9 that, in the case of two paramagnetic metal ions separated by distance R, peaks arising from magnetic interactions among the ions in the cluster would exhibit an oscillatory, sinusoidal relationship. Several cases of this appear in the literature and are described in more detail in Chapter II of this dissertation. In Chapter II, this sinusoidal Q-dependence for magnetic interactions among paramagnetic

metal centers is exploited to investigate *inter*molecular interactions in **Fe-Cl** and **Mn-Cl** compounds.

For indirect-geometry INS, which is utilized in the vibrational measurements collected at the Vibrational Spectrometer (VISION) at Oak Ridge National Laboratory in Oak Ridge, TN, E_f of the scattered neutrons is fixed (via crystal diffraction and/or filters) and the incident neutrons with energy E_i can be parsed and measured using a monochromator or TOF.[62] Selecting E_i via the latter technique affords a high spectral resolution over a wide energy transfer range;[62] VISION can measure magnetic and vibrational transitions from 10 to 8000 cm^{-1}. In addition, since phonons are bosons that follow the Bose-Einstein distribution, and electrons are fermions that follow the Boltzmann distribution, Bose-correction can be applied to the INS data to distinguish among magnetic and phonon transitions. Essentially, Bose-correction is a data processing method that corrects for the temperature-dependence of phonon modes; therefore, if spectra are measured via INS under varying temperature, magnetic transitions will display changes in intensity relative to the temperature-dependent Boltzmann population(s) of the magnetic states, and phonon transitions will maintain relatively constant intensities. In addition, calculations with the Vienna *ab initio* Simulation Package (VASP) to predict energies, intensities, and symmetries of phonon modes is coupled with experimental INS data to further validate the nature of magnetic transitions, as a magnetic transition present in the data will be absent from the simulated phonon spectrum.

1.2.2. Far-IR Magneto-Spectroscopy (FIRMS)

Far-IR magneto-spectroscopy (FIRMS) is a direct technique for accurately determining energies of magnetic and phonon transitions in magnetic transition metal complexes.[70] ZFS transitions are IR-allowed, as they are magnetic dipole transitions, although they are generally weaker than *u*-symmetric (IR-active) phonons.[70] The absorption cross-section of a single transition between an initial and final state ($|i_n\rangle$ and $|i_f\rangle$, respectively) is described in Eq. 1.10:[71]

$$\alpha_n(\nu) = \frac{4\pi^2 e^2 N_o}{h m_e^2 c^3} \nu \rho(\nu - \nu_n) \left| \langle f_n | \hat{k} \times \hat{\pi} \cdot \hat{S} | i_n \rangle \right|^2 \qquad \text{(Eq. 1.10)}$$

where N_o is the concentration of paramagnetic ions, h is Planck's constant, m_e is the mass of an electron, c is the speed of light, ρ is a lineshape function, and ν_n is the energy difference between eigenvalues of both states. Unit vectors $\hat{k}$ and $\hat{\pi}$ correspond respectively to the directions of propagation and electric field polarization of the incident light, and $\hat{S}$ is the spin operator.

To account for the thermal population of initial and final states at any given temperature, one must multiply $\alpha_n(\nu)$ by $P_n(T)$, defined in Eq. 1.11 as:[71]

$$P_n(T) = \frac{\exp\left(-\frac{E_{i_n}}{kT}\right) - \exp\left(-\frac{E_{f_n}}{kT}\right)}{\sum_i \exp\left(-\frac{E_i}{kT}\right)} \qquad \text{(Eq. 1.11)}$$

where E_i is the eigenvalue of the SH for state $|i\rangle$.

To determine the total absorption coefficient [$\alpha(\nu)$] of a single particle, the product of Eqs. 1.10 and 1.11 is summed across all possible ZFS transitions:[71]

$$\alpha(\nu) = \Sigma_n \alpha_n(\nu) P_n(T) \quad \text{(Eq. 1.12)}$$

For powder samples (as opposed to single crystals or crystal arrays), $\alpha(\nu)$ must be averaged over all orientations (x, y, z).

In practice, FIRMS is used to directly observe IR-active magnetic transitions by varying the external magnetic field. While phonons do not shift in energy with increasing field (except where spin-phonon coupling interactions are present), magnetic transitions do and can be distinguished from phonon modes. Magnetic dipole transitions also occur in molecular lanthanide complexes among the crystal-field-split magnetic states. However, as molecular lanthanide compounds often support high coordination numbers and have consequently low symmetries, state-mixing often obfuscates the IR-active magnetic and phonon transitions in lanthanide SMMs, and interpretation of FIRMS data requires additional *ab initio* calculations.

1.2.3. Raman Magneto-Spectroscopy (RaMS)

Raman magneto-spectroscopy (RaMS) can also be used to identify and quantify the energy barrier(s) between magnetic states and observe Raman-active (*i.e.*, *g*-symmetric) phonons, though there are significantly fewer studies utilizing Raman compared to FIRMS to determine magnetic separations.[6, 72] One potential explanation for this is the current ambiguity of Raman selection rules for magnetic transitions. Since the selection rules for electronic Raman transitions are $\Delta J \leq 2$, $\Delta L \leq 2$, and $\Delta S = 0$, a change in the orbital component from one energy state to the next must occur for a transition to be allowed. As such, transitions among magnetic states in compounds that exhibit first-order SOC (*e.g.*, lanthanide- or 4*d*/5*d*-based compounds) should be Raman-allowed.[73]

ZFS transitions in transition metal complexes that exhibit second-order SOC are vanishingly small in Raman spectroscopy, though ZFS transitions have been observed via coupling with Raman-active phonons.[6]

1.2.4. High-Field, High-Frequency Electron Paramagnetic Resonance (HFEPR)

EPR is a common technique to investigate magnetic transitions in paramagnetic complexes. In EPR measurements, the Zeeman effect is exploited under varying magnetic field so that the separation in energy between two magnetic states is equal to a fixed frequency. The magnetic transition in HFEPR is described by:

$$\Delta E = \hbar\nu = g\mu_B B_0 \qquad \text{(Eq. 1.13)}$$

where ν is applied frequency, g is the g-tensor, μ_B is a Bohr magneton, and B_0 is the applied magnetic field.

The g-tensor is a proportionality constant related to magnetic anisotropy; g of a free electron is 2.002.

For many metal complexes, however, ZFS is too large in energy to be measured via conventional EPR spectroscopy (X-band: 0.3 cm^{-1}, Q-band: 1.2 cm^{-1}). HFEPR operates in the sub-THz frequency range and is thus suitable for determining ZFS in metal complexes and SMM candidates. In this work, HFEPR is used to determine the magnitude and sign of ZFS parameters D and E, as well as the g_x-, g_y-, and g_z-tensors of several transition metal complexes.

1.3. Current Dissertation

In this dissertation, several unique spectroscopic techniques are utilized to investigate magnetic and vibrational properties of molecular magnetic materials. These studies reflect and progress the overall goals of the molecular magnetism community: (a) to determine how phonon transitions assist in relaxing spin (*i.e.*, collapsing magnetic memory), (b) to investigate intermolecular magnetic interactions in SMM systems with presumed "isolated" spin centers, and (c) to investigate how systematic changes in the first coordination sphere of SMMs (*e.g.*, increasing covalency of an M−X bond) affects ZFS parameters and spin-phonon coupling behavior. In addition, this work showcases several unique spectroscopic techniques for directly measuring magnetic and vibrational transitions in paramagnetic molecular complexes.

1.4. Chapter II

The *Q*-dependences of magnetic transitions in two M(TPP)Cl (M = Mn^{3+}, Fe^{3+}) complexes were studied via direct-geometry INS at the Cold Neutron Chopper Spectrometer (CNCS) at ORNL in Oak Ridge, TN. The oscillatory *Q*-dependences were fit to a new model combining the Heisenberg spin-spin exchange (from intermolecular magnetic interactions) with the single-molecule excitation to reliably reproduce the distance between metal centers and determine the energies of intermolecular magnetic interactions.

1.5. Chapter III

A series of cobalt complexes, $Co(PPh_3)_2X_2$ (X = Cl, Br, I), were investigated via FIRMS to reveal spin-phonon coupling as avoided crossings between magnetic and *u*-

symmetry phonon transitions. INS, coupled with VASP and Phonopy calculations, gives the phonon spectra, symmetries, and visual representations/movies. Magnetic transitions among ZFS levels of the $S = 3/2$ electronic ground state were probed by INS, HFEPR, FIRMS, and frequency-domain FT terahertz EPR (FD-FT THz-EPR) to give magnetic excitation spectra, ZFS parameters D and E, and g-values. Ligand field theory (LFT) was used to analyze earlier electronic absorption spectra and give calculated ZFS parameters that reflect the empirical ones. Finally, DFT was used to calculate spin densities in the series, showing that larger spin density localized on Co(II) corresponds with larger ZFS splitting.

1.6. Chapter IV

Manganese tetraphenylporphyrin halide complexes, Mn(TPP)X (X = Br, I), co-crystallized with no/various solvents in the lattice were synthesized. Crystal structures of novel compounds were determined by single-crystal X-ray diffraction and investigated via Hirshfeld surface analysis. Magnetic properties of the complexes were studied by direct-current (DC) and alternating current (AC) susceptibility, HFEPR, and INS to reveal a trend in ZFS properties within the Mn(TPP)X series.

1.7. Chapter V

Phonon spectra of Fe(TPP)X (X = F, Cl, Br, I) and the fully deuterated chloro-analog, Fe(TPP-d_{28})Cl, have been investigated by INS supported with VASP phonon and spin density calculations. It is shown that deuteration of the chloro-analog affords a 3.2(2)-fold increase in the intensity of the $M_S = \pm 1/2 \rightarrow \pm 3/2$ transition at 5 K. The vibrational spectra of the protio series are compared.

CHAPTER II

STUDIES OF INTERMOLECULAR MAGNETIC INTERACTIONS IN METALLOPORPHYRINS M(TPP)Cl (M = Fe^{3+}, Mn^{3+}) VIA INELASTIC NEUTRON SCATTERING

This chapter is based on the following paper:

Alexandria N. Bone, Joseph A. Prescott, Andrey A. Podlesnyak, Jason T. Haraldsen, Zi-Ling Xue, Probing Intermolecular Magnetic Interactions in Metal Complexes by Inelastic Neutron Scattering. *In Preparation*.

The author participated in collecting experimental data (via remote instrument access, due to the COVID-19 pandemic). A. Podlesnyak performed on-site data collection. The author processed all data, and results were interpreted with contributions from Z. Xue, A. Podlesnyak, and J. Haraldsen. J. Prescott performed all fitting processes with support from J. Haraldsen.

2.1. Abstract

The performance of single-molecule magnets and qubits is limited by intermolecular magnetic interactions causing relaxations, loss of data, and shortened coherence times. However, few experimental techniques exist to directly probe these essential interactions. We have found that inelastic neutron scattering (INS) reveals the interactions in M(TPP)Cl (M = Fe^{3+}, **Fe-Cl**; Mn^{3+}, **Mn-Cl**; TPP^{2-} = *meso*-tetrapheylporphyrinate) as oscillatory *Q*-dependences of magnetic transition intensities. *Q* (length of the vector of neutron momentum transfer ***Q***) reflects scattering angles of the outgoing neutrons leaving the sample. In addition, INS spectra unexpectedly show the magnetic transition from interactions of a molecule with its neighbors (as an assembly) in **Fe-Cl**, in addition to a peak from a single-molecule magnetic excitation. In **Mn-Cl**, the peak of the assembly (from the intermolecular interactions) overlaps with the single-molecule excitation. A new model, combining the Heisenberg spin-spin exchange (from the intermolecular magnetic interactions) with the single-molecule excitation, has been developed to analyze the oscillatory *Q*-dependence, providing an understanding of the interactions. The unique oscillatory *Q*-dependence, magnetic excitation of the assembly, and the advanced model to successfully analyze the INS results are novel. The current work demonstrates that INS is a unique, direct technique to probe the critical intermolecular magnetic interactions.

2.2. Previous INS Studies to Probe *Intra*molecular Interactions

The *Q*-dependence of magnetic transitions has been used to probe *intra*molecular magnetic interactions within metal dimers/clusters. Furrer and Güdel have reported that,

in the perdeuterated ammonia hydroxide Cr^{3+} dimer $[(D_3N)_5Cr(OD)Cr(ND_3)_5]Cl_5$ consisting of antiferromagnetic coupling, *Q*-dependence of magnetic peak intensities reveals directly the intramolecular $Cr^{3+}\cdots Cr^{3+}$ magnetic interactions.[64-66] Podlesnyak and coworkers have used the technique to probe the magnetic transition in the solid $La_{1-x}Sr_xCoO_3$ ($x = 0.002$) with holes introduced by the substitution of Sr^{2+} for La^{3+}, demonstrating that the oscillatory behavior of the magnetic peak intensity is caused by the formation of an octahedral cluster consisting of one Co^{3+} ion bridged by O^{2-} ligands to six other Co^{3+} ions.[74] Haraldsen *et al.* have extensively analyzed neutron scattering and magnetic observables for spin clusters and molecular magnets consisting of two, three, and four spin centers in various spatial arrangements.[69, 75] The use of this technique to study magnetic excitations in cluster compounds was reviewed recently by Furrer and Waldmann.[66] In the INS study of the Ni^{2+} dimer $[Ni_2(D_2NC_2H_4ND_2)_4(\mu\text{-}Br)_2]Br_2$ with intramolecular exchange coupling, Stebler and coworkers found that the experimental *Q*-dependence of INS intensities deviated from the expected dependence based on intramolecular exchange coupling.[76] The authors attributed the deviation to the presence of intermolecular coupling between molecules. In investigating magnetic properties of nickelocene $Ni(\eta^5\text{-}C_5H_5)_2$ and $Ni(\eta^5\text{-}C_5D_5)_2$ ($\eta^5\text{-}C_5H_5$ = cyclopentadienyl; $\eta^5\text{-}C_5D_5$ = perdeutero-cyclopentadienyl) with two unpaired electrons by Baltzer and coworkers, magnetic susceptibility measurements confirmed the presence of a predominantly ferromagnetic coupling of a molecule to its nearest neighbors.[63] The INS data of $Ni(\eta^5\text{-}C_5D_5)_2$, giving the axial zero-field splitting (ZFS) parameter *D*, appeared to show an oscillatory behavior in the magnetic peak intensity with *Q*. However, the small number of data points (four) at each temperature (8 and 50 K) and data errors make its oscillatory

nature uncertain. Therefore, the authors did not address if there was an oscillatory behavior in the INS data.[63] Gransbury and coworkers recently probed an octahedral high-spin Co^{2+} complex, $[Co(Me_3\text{-tpa})(dbsq\bullet)](PF_6)$ [$dbsq\bullet^-$ = 3,5-di-tert-butylsemiquinonate radical; Me_3tpa = tris[(6-methyl-2-pyridyl)methyl]amine)] containing a semiquinonate radical ligand with an unpaired electron, by several techniques including INS.[77] The work showed a dominant *intra*molecular, ferromagnetic exchange between the Co^{2+} ion and the radical ligand within the $[Co(Me_3\text{-tpa})(dbsq\bullet)]^+$ cation. For the magnetic peak in INS, its intensity vs *Q*-dependence does not fit the predicted plot based on the intramolecular interactions.[77] The authors attributed the lack of oscillations in the *Q*-dependence to the unpaired electrons distributed across the Co-dbsq• unit. Using an average-exchange model involving an interaction distance within the range of those between two Co-semiquinonate sub-units, an essentially flat line calculated from the model fits the experimental *Q*-dependence data well.[77] EPR of $[Zn(Me_3\text{-tpa})(dbsq\bullet)](PF_6)$, a Zn^{2+} analog of $[Co(Me_3\text{-tpa})(dbsq\bullet)](PF_6)$**,** indicated the presence of intermolecular interactions.

In this study, we aim to explore whether INS could be used directly to probe *inter*molecular magnetic interactions. That is, whether the *Q*-dependence in INS reveals magnetic interactions among molecules in a solid. Metalloporphyrin compounds M(TPP)Cl (M = Fe^{3+}, **Fe-Cl**;[7, 9-10, 78-81] Mn^{3+}, **Mn-Cl**[9, 82-83]) have been chosen in the current study for the following: (1) The complexes contain one metal ion as the magnetic center in each molecule *free of intramolecular magnetic interactions*; (2) Principal magnetic transitions at 12.65(8) cm^{-1} and 6.70(3) cm^{-1} for **Fe-Cl** and **Mn-Cl**,

respectively, are outside of phonon peaks mainly at ≥16 cm^{-1},[9] thus avoiding phonon interferences to the magnetic transitions and making **Fe-Cl** and **Mn-Cl** attractive for probing the *Q*-dependence. (3) **Mn-Cl** has demonstrated single-molecule magnet (SMM) properties.[28] Probing the intermolecular interactions in SMMs may help understand their magnetic relaxations. For molecular compounds here, phonons refer to external (intermolecular or lattice) and internal (intramolecular) vibrational modes in the solid.[84] Internal and external modes often couple as they originate from the same governing equations. Thus, we do not distinguish external and internal modes in the current work and refer to all vibrations as phonons.

2.3. Results and Discussion

Fe-Cl and **Mn-Cl** have C_{4v} molecular symmetry (Figure 2.1-Left) in the tetragonal crystal system.[8, 16] Thus, $x = y$ in crystalline solids of **Fe-Cl** and **Mn-Cl**, making $E = 0$ for both complexes. For d^5, high spin ($S = 5/2$) **Fe-Cl**, the six-fold ($2S + 1 = 6$) degenerate state is split by ZFS into three doublets (known as Kramers doublets or KDs): $M_S = \pm 1/2, \pm 3/2$, and $\pm 5/2$. It has the rhombic magnetic anisotropy ($D > 0$), making $M_S = \pm 1/2$ the lowest in energy and $M_S = \pm 3/2, \pm 5/2$ first and second excited states, respectively, with the splitting pattern of the levels shown in Figure 2.1-Middle. For d^4, high spin ($S = 2$) **Mn-Cl**, the five-fold ($2S + 1 = 5$) degenerate state is split by ZFS into three levels: $M_S = 0, \pm 1$, and ± 2. It has the uni-axial magnetic anisotropy ($D < 0$), making $M_S = \pm 2$ the lowest in energy and $M_S = \pm 1, 0$ the first and second excited states, respectively, with the splitting pattern shown in Figure 2.1-Right.

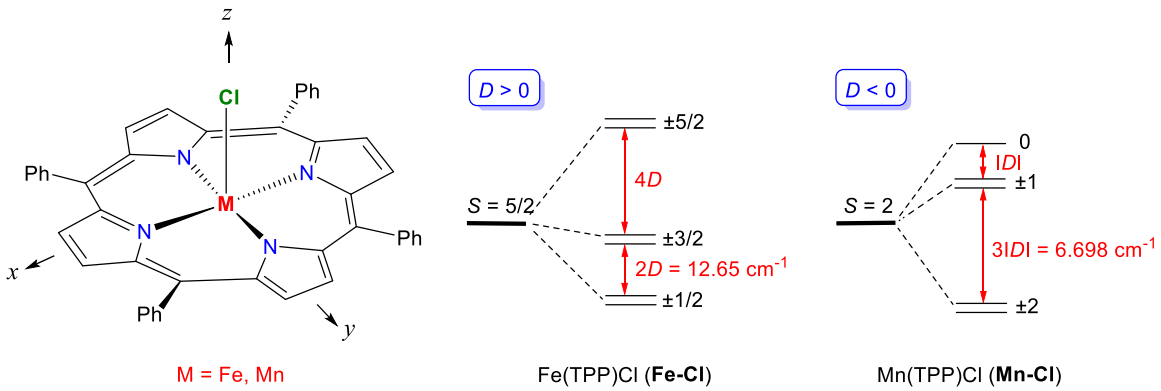


Figure 2.1. (Left) Structures of M(TPP)Cl (M = Fe, **Fe-Cl**; Mn, **Mn-Cl**). (Middle) ZFS pattern for **Fe-Cl** and (Right) ZFS pattern for **Mn-Cl**.[9]

2.3.1. INS Spectra of Fe-Cl

The splitting of the three ZFS levels (*i.e.*, the *D* values) in both **Fe-Cl** and **Mn-Cl** were determined by INS using the Cold Neutron Chopper Spectrometer (CNCS)[85] instrument in 2013, when CNCS was at an early stage of its operation at the newly constructed Spallation Neutron Source (SNS), Oak Ridge National Laboratory (ORNL).[9] For **Fe-Cl** at the low temperature of 2 K, the ground doublet $M_S = \pm 1/2$ is occupied, leading to the transition to $M_S = \pm 3/2$ at 12.65(8) cm^{-1} in INS.[9] At the higher temperature of 20 K, both $M_S = \pm 1/2$ and the first excited state $M_S = \pm 3/2$ are partially occupied,[9] giving two excitations: $M_S = \pm 1/2 \rightarrow \pm 3/2$ at 12.65(8) cm^{-1} and $M_S = \pm 3/2 \rightarrow \pm 5/2$ at 25.3(3) cm^{-1} for **Fe-Cl**. One particularly remarkable feature of the INS experiments is that they were conducted with H-containing samples of **Fe-Cl** and **Mn-Cl**, primarily because SNS provides the most intense pulsed neutron beams in the world for scientific research and development, overcoming the large background noise in neutron scattering from H-containing samples. It should be pointed out that both the SNS neutron source[86] and the CNCS spectrometer[87] have been undergoing several upgrades since the 2013 experiments, including a more powerful neutron source. The upgrades have resulted in a significant overall improvement in the performance of CNCS, including an increased neutron flux by nearly an order of magnitude, a higher signal/noise level, and much better resolution of the spectrometer.[87] Features of the CNCS spectrometer were reviewed in 2011[85] and upgrades by 2016 were reported.[87] Additional upgrades to CNCS have been made since 2016.

We have recently used the upgraded CNCS spectrometer to re-take the INS spectra of **Fe-Cl** with the initial aim of observing new features, including the *Q*-dependence of magnetic transitions in the complex. At 20 K, the first doublet $M_S = \pm 1/2$ and the second doublet $M_S = \pm 3/2$ in **Fe-Cl** (Figure 2.1-Middle) are partially occupied. In the INS spectrum of **Fe-Cl** collected at 20 K with the incident neutron energy of E_i = 26.8 cm^{-1} (Figure 2.2-Top), two magnetic peaks at 12.7(1) cm^{-1} (Peak **A**) and –12.7(2) cm^{-1} (Peak **B**) correspond, respectively, to $M_S = \pm 1/2 \rightarrow \pm 3/2$ excitation and $M_S = \pm 3/2 \rightarrow \pm 1/2$ relaxation in **Fe-Cl**. In the latter, the outgoing neutrons gain ~12.7 cm^{-1} energy in the process, giving Peak **B** at –12.7(2) cm^{-1}. The observations are consistent with partial occupation of the second magnetic doublet $M_S = \pm 3/2$ doublet at 20 K.

It is important to note that the magnetic transition at 12.7(1) cm^{-1} (Peak **A**) in Figure 2.2-Top features a shoulder peak centered at 11.8(1) cm^{-1} (Peak **A2**), giving the overlapping peak. Deconvolution of Peak **A** for the data in one *Q* range is given in Figure 2.2-Bottom. Peak **A2** indicates the excitation of an assembly, as described in more detail below. The assembly here refers to that formed by several molecules around a central molecule through intermolecular magnetic interactions. They differ from a cluster compound containing several metal ions bound together by ligands through chemical bonds with intramolecular magnetic interactions among the metal ions in Eq. 2.1:

$$I \sim A\, F^2(Q)\, \mathfrak{M}\, [1 - \frac{\sin(QR)}{QR}] \qquad \text{(Eq. 2.1)}$$

where $F(Q)$ is the magnetic scattering factor (also known as the magnetic form factor)[67] which is the Fourier transform of the spin density in the crystal lattice of the sample; $F^2(Q)$ is the intensity of the magnetic scattering factor, which decreases with *Q* increase;

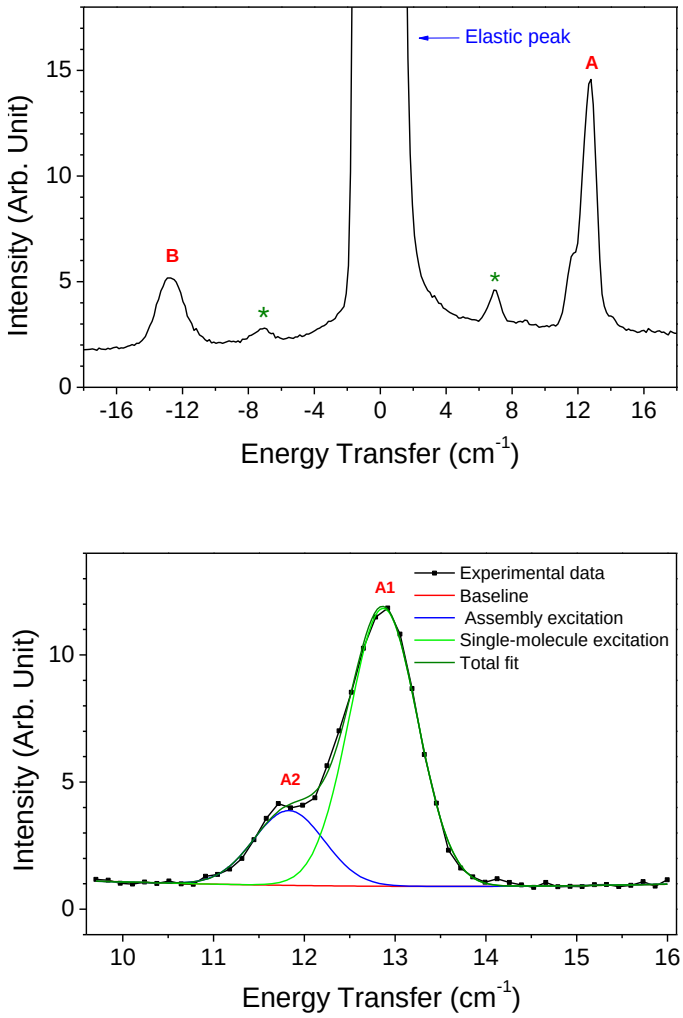


Figure 2.2. (Top) INS spectra of **Fe-Cl** at 20 K collected with incident neutron energy of E_i = 26.8 cm^{-1}. Each point in the plot contains data over the entire available Q range. Peak **A:** $M_S = \pm 1/2 \rightarrow \pm 3/2$ excitation; Peak **B**: $M_S = \pm 3/2 \rightarrow \pm 1/2$ relaxation in Figure 2.1-Middle. (Bottom) Deconvolution of Peak **A** into Peaks **A1** at 12.7(1) cm^{-1} and **A2** at 11.8(1) cm^{-1} for the data in the Q = 0.5–0.6 Å^{-1} range. *: Lattice phonons which are observable due to the improved neutron flux and resolution of the upgraded CNCS compared to the spectrometer in 2013.[9]

$\mathfrak{M}$ is a matrix element[64] about the interferences between/among the metal ions, giving the oscillatory behavior of the peak intensity with Q[64, 66, 68] as a direct picture of the metal-metal distance(s) in the dimer/cluster;[69] R is the metal-metal distance in the dimer/cluster; $A = \exp\left(-\frac{E(S)}{k_B T}\right)\exp(-2W)$, in which $E(S)$ is the energy of the spin state S; k_B is Boltzmann constant; and exp(-2W) is the Debye-Waller factor about the reduction of scattering from atomic vibrations.

When the incident neutron energy was increased to E_i = 42.3 cm^{-1} for **Fe-Cl** at 20 K, three magnetic transitions (Peaks **A**, **B,** and **C**) were observed (Figure A.1-Top in Appendix A). The new Peak **C** at 25.7(2) cm^{-1} corresponds to the $M_S = \pm 3/2 \rightarrow M_S = \pm 5/2$ transition (Figure 2.1-Middle). In the experiment with E_i = 26.8 cm^{-1} in Figure 2.2-Top, Peak **C** was too close to E_i to be observed. The observation of Peak **C** is in good agreement with the expected energy of the $M_S = \pm 3/2 \rightarrow \pm 5/2$ excitation, where the two levels are separated by $4D \approx 25.5$ cm^{-1}.[9] When the sample temperature is at 2 K, only the ground doublet $M_S = \pm 1/2$ is populated, leading to the $M_S = \pm 1/2 \rightarrow M_S = \pm 3/2$ transition (Figure 2.1-Middle). Indeed, INS spectrum at 2 K with E_i = 42.3 cm^{-1} (Figure A.1-Bottom) only shows this first transition as Peak **A**.

2.3.2. INS Spectra of Mn-Cl

For **Mn-Cl** with D = –2.24(3) cm^{-1},[9] the separation of the ground $M_S = \pm 2$ state to the first excited $M_S = \pm 1$ state is $3|D| = \sim 6.7$ cm^{-1} (Figure 2.1-Right).

In the INS spectra of **Mn-Cl** collected at 20 K with E_i = 12.5 cm^{-1} (Figure 2.3-Top), four peaks are observed: –6.92(5), –2.30(4), 2.30(3), and 6.92(2) cm^{-1}.[9] At 20 K,

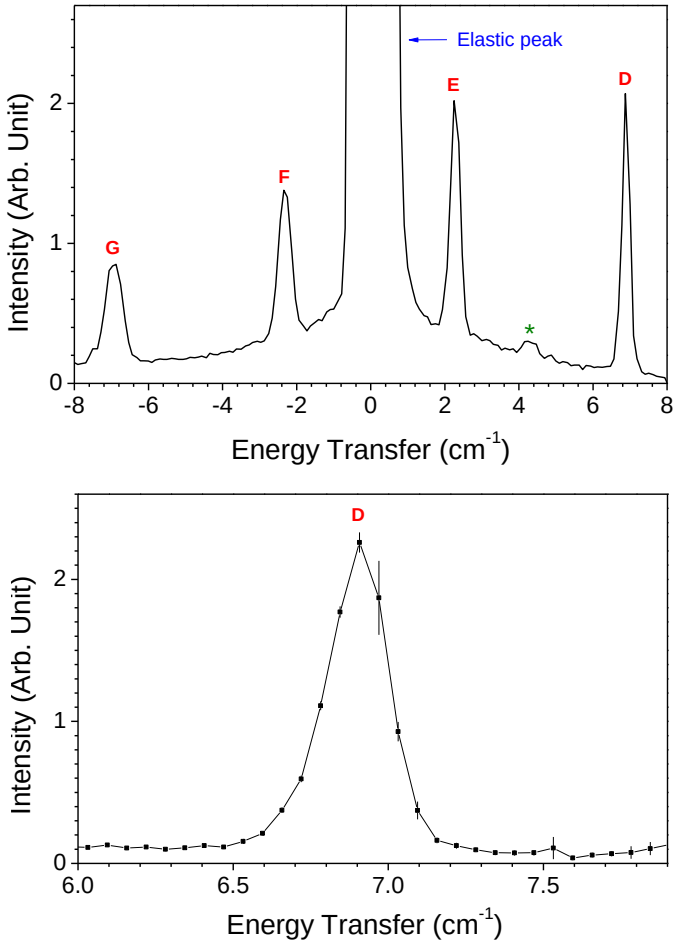


Figure 2.3. (Top) INS spectrum of **Mn-Cl** at 20 K with E_i = 12.5 cm^{-1}. Each point in the plot contains the data over the entire available Q range. The peaks in the plot correspond to the following transitions: Peak **D**, $M_S = \pm 2 \rightarrow \pm 1$; Peak **E**, $M_S = \pm 1 \rightarrow 0$; Peak **F**, $M_S = 0 \rightarrow \pm 1$; Peak **G**, $M_S = \pm 1 \rightarrow \pm 2$, as shown in Figure 2.1-Right; *: Lattice phonon. (Bottom) Expanded view of Peak **D** with the best energy resolution (largest peak separation = 0.0686 cm^{-1}).

all three levels (M_S = ±2; ±1 and 0) are partially occupied. The peaks at 6.92(2) cm^{-1} (Peak **D**) and 2.30(3) cm^{-1} (Peak **E**) correspond to the respective M_S = ±2 → ±1 and M_S = ±1 → 0 excitations. That is, molecules of **Mn-Cl** at M_S = ±2 and M_S = ±1 gain energy from the incident neutrons to excite to the M_S = ±1 and M_S = 0 states, respectively. On the other hand, the peaks at –6.92(5) cm^{-1} (Peak **G**) and –2.30(4) cm^{-1} (Peak **F**) are from the M_S = ±1 → ±2 and M_S = 0 → ±1 relaxations, respectively. That is, in the scattering process, molecules of **Mn-Cl** at the excited states M_S = 0 and M_S = ±1 give energy to the incident neutrons and relax to the respective M_S = ±1 and M_S = ±2 levels.[9]

2.3.3. Q-Dependence of Magnetic Transition in Fe-Cl and Mn-Cl

As pointed out in Figures 2.2-2.3 and Figure A.1 captions, each INS spectrum in the figures contains data from all detectors with different scattering angles in the spectrometer. In other words, the spectrum reflects the INS data integrated over all scattering angles (i.e., the entire available Q range).

One feature of the INS process is that the larger the incident neutron energy E_i, the larger the span of scattered neutron angles (i.e., the broader the Q-range).[84] However, large E_i reduces the spectral resolution and increases background noise. On balance, INS experiments with E_i = 42.3 cm^{-1} for **Fe-Cl** at 2 K were conducted in part to give a sufficient Q-range. However, at this E_i, the overlapping Peaks **A1** and **A2** could not be resolved (Figure A.1-Bottom). The Q-dependence was evaluated with the combined Peak **A** at E_i = 42.3 cm^{-1} in the Q = ~0.5–2.5 Å^{-1} range. The lowest possible temperature of 2 K was chosen to place all molecules at the ground M_S = ±1/2 state, making the transition from this state to M_S = ±3/2 (Peak **A**) the strongest with the enhanced signal/noise ratio.

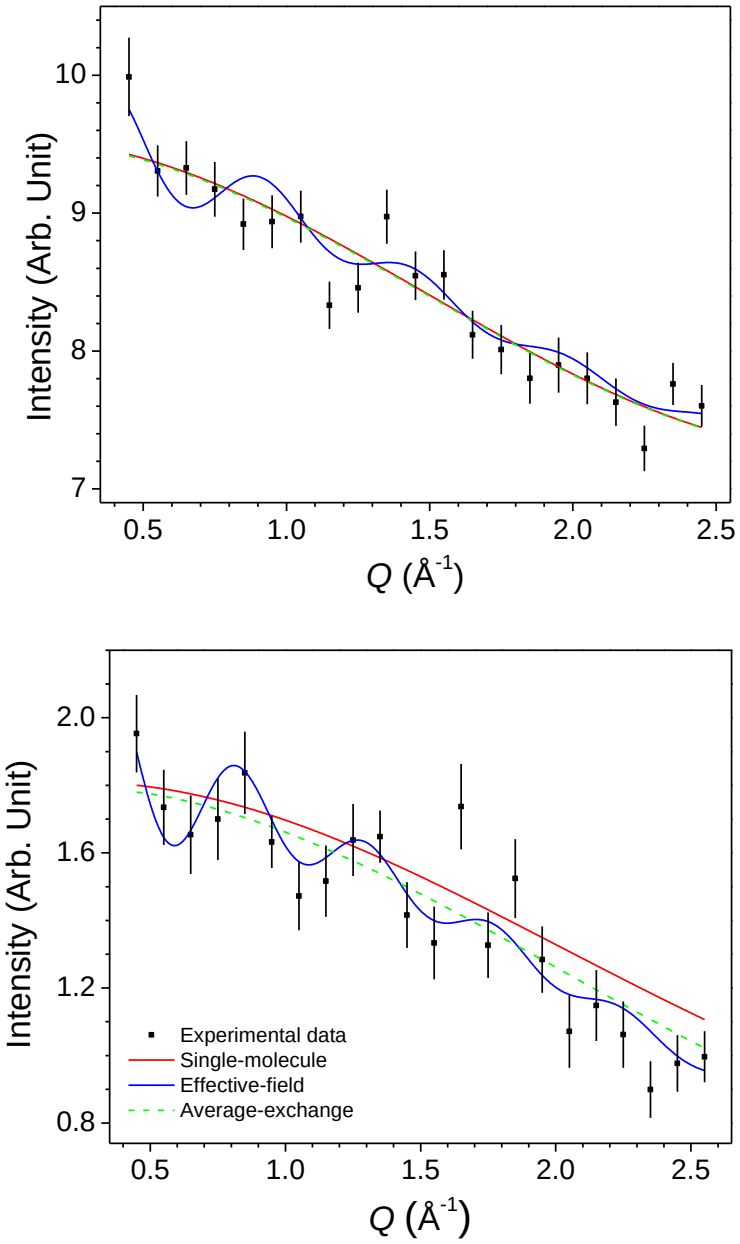
Peak **A** at 12.7(2) cm^{-1} in Figure A.1-Bottom (E_i = 42.3 cm^{-1}) with different Q values were analyzed. For each Q value, data in the next 0.075 $Å^{-1}$ Q range (called Q-cut) were integrated as the intensity for the Q value. The analysis gives peak intensities at different Q values in Figure 2.4. This plot shows the oscillation of peak intensities vs. different Q values.

With smaller E_i = 26.8 cm^{-1} (and thus with a smaller Q range) at 2 K, deconvoluted Peaks **A1** and **A2** were observed (Figure A.2). Intensities of overlapping Peak **A** vs Q plot in Figure A.3 for the smaller Q = ~0.5–1.6 $Å^{-1}$ range also show oscillation. These oscillations of the magnetic peak intensities vs Q indicate the presence of intermolecular interactions in the solid of **Fe-Cl**. In comparison, the standard response of magnetic excitations of monomeric (i.e., single-molecule) metal complexes is a simple decay with Q increase, as shown in the red fit in Figure 2.4-Top.

For **Mn-Cl**, INS experiments with E_i = 42.3 cm^{-1} at 2 K (Figure A.4) were conducted for a good Q-range. The lowest possible temperature of 2 K increases the population of molecules at the ground $M_S = \pm 2$ state, making the transition from this state to $M_S = \pm 1$ (Peak **D**) the strongest for enhanced signal/noise ratio for the peak intensity.

Peak **D** at 6.9(1) cm^{-1} in Figure A.4 with different Q values were analyzed. At each Q value, data in a Q-cut of 0.1 $Å^{-1}$ were integrated to give the peak intensity for the Q value. Thus, the analysis gives different peak intensities at different Q values ranging from ~0.4–2.6 $Å^{-1}$ in Figure 2.4-Bottom. Oscillation of peak intensities vs. different Q values is evident in the plot, indicating the presence of intermolecular interactions in the solid of **Mn-Cl**. The energy of Peak **D** at 6.9(1) cm^{-1} for **Mn-Cl** is smaller than Peak **A** at

Figure 2.4. (Top) *Q*-dependence of the two overlapping magnetic peaks. Peak **A** at ~12.7(2) cm^{-1} for **Fe-Cl** at 2 K with E_i = 42.3 cm^{-1} in Figure A.1-Bottom. Each point (with error bar) represents a *Q*-cut of 0.075 $Å^{-1}$. (Bottom) *Q*-dependence of Peak **D** at 6.9(1) cm^{-1} for **Mn-Cl** at 2 K with E_i = 42.3 cm^{-1} in Figure 2.3. Each point (with error bar) represents a *Q*-cut of 0.1 $Å^{-1}$. Fits by single-molecule, effective-field, and average-exchange models are shown and discussed below. The fits by the single-molecule and average-exchange models, discussed in Appendix A, do not capture the oscillations observed in the experimental data. In comparison, the fits by the effective-field model do show the oscillations for both **Fe-Cl** and **Mn-Cl**.


Intensity (Arb. Unit)
10
9
8
7
0.5
1.0
1.5
2.0
2.5
Q (Å-1)
Intensity (Arb. Unit)
2.0
1.6
1.2
0.8
Experimental data
Single-molecule
Effective-field
Average-exchange
0.5
1.0
1.5
2.0
2.5
Q (Å-1)

~12.7(2) cm^{-1} for **Fe-Cl**. The lower energy in **Mn-Cl** makes its Q = ~0.4–2.6 $Å^{-1}$ range in Figure 2.4-Bottom slightly larger than the Q = ~0.5–2.5 $Å^{-1}$ range in Figure 2.4-Top for the Fe^{3+} complex **Fe-Cl** (with the same E_i = 42.3 cm^{-1}).

The results in the current work indicate that both S = 5/2 **Fe-Cl** and S = 2 **Mn-Cl** exhibit *inter*molecular interactions in the solid state. To our knowledge, the oscillation behaviors have not been reported.

2.3.4. Understanding the Q-Dependence of the INS Intensity

The Q-dependent intensities of magnetic Peak **A** at 12.7(2) cm^{-1} for **Fe-Cl** and Peak **D** at 6.92(2) cm^{-1} for **Mn-Cl** reveal an oscillatory nature, indicating a deviation from the standard response of single-molecule magnetic excitations of a simple decay with increasing Q. These oscillations indicate the presence of intermolecular magnetic interactions. Since there is little energy variation with Q in the incident neutrons, it can be assumed that the excitations by the assembly must be responsible for the additional Q-dependence of the excitation intensity. The assumption is supported by the presence of the distinct shoulder Peak **A2** in Figure 2.2 for **Fe-Cl**. As the analysis below indicates, in **Mn-Cl**, the single-molecule and assembly excitations are on top of each other to give Peak **D** in Figure 2.3-Top.

The oscillations (of the peak intensities vs. Q) in Figure 2.4-Top and -Bottom are indicative of a spatial dependence on Q, as Eq. 2.1 shows. Since, unlike dimers or clusters, monomers M(TPP)Cl (**Fe-Cl** and **Mn-Cl**) have no intramolecular metal-metal distance (i.e., R in Eq. 2.1), intensities of their single-molecule magnetic excitations should simply follow a decay (with *no* oscillation) of intensities of the magnetic form

factor $F^2(Q)$ as Q increases. Therefore, to analyze the Q-dependence of the magnetic peaks, we fit the INS data using:

$$S(Q) = \xi_0 F^2(Q)\left[f + (1-f)S(Q)_{eff}\right] + S(Q)_{back} \qquad \text{(Eq. 2.2)}$$

where $S(Q)$ is the overall magnetic scattering function in the fit. The experimental $S(Q)$ is given in Eq. A.1 (in Appendix A); ξ_0 is a scaling factor to adjust for the overall neutron flux; $F^2(Q)$ is the intensity of the magnetic form factor $F(Q)$; f is the fractional contribution of the magnetic excitation in a single molecule; $S(Q)_{eff}$ is the structure factor from the intermolecular magnetic interactions (also known as exchange interactions) using an effective-field model discussed below; $S(Q)_{back}$ is a background correction.

In Eq. 2.2, there are two contributions to the magnetic scattering function (after the background correction $S(Q)_{back}$). The first part, $\xi_0 F^2(Q)f$, reflects contributions from the magnetic excitation of a single molecule. As discussed above, for M(TPP)Cl (**Fe-Cl** and **Mn-Cl**) with a single metal ion containing unpaired electrons, this first part in Eq. 2.2 does *not* have oscillation in the INS intensity vs. Q. The second part, $\xi_0 F^2(Q)[(1-f)S(Q)_{eff}]$, shows contributions from the magnetic interactions of this molecule with other surrounding molecules. A good model for the second part is expected to give a fit showing the oscillation in INS intensity vs. Q. Since the oscillation is from the second part, but not the first part, of Eq. 2.2, the relative contributions from the single molecule and the intermolecular magnetic interactions to the overall magnetic scattering function $S(Q)$ are essential to how well the oscillation is shown in the fit by the model.

The development of the second part in Eq. 2.2 is given below. The intermolecular interactions in **Fe-Cl** and **Mn-Cl**, addressed by $S(Q)_{eff}$ in the second part of Eq. 2.2, are weak and complex, as a molecule may interact with molecules with different (M···M) distances and angles in the crystal. However, since the magnetic interactions are weak, we can assume they are approximately equal in the model, allowing us to build an effective field for the interactions around the molecule at the center (shown in Figure 2.5). This model provides a general method for understanding the *Q*-dependences of the magnetic excitations.

The effective-field model produces a center-sphere for the intermolecular magnetic interactions, and the structure factor (in the second part of Eq. 2.2) is given for any spin *S* by:

$$S(Q)_{eff} = \xi_1 \frac{2S(S+1)}{3}\left[1 - \frac{\sin(Q\,R_{eff})}{Q\,R_{eff}}\right] \qquad \text{(Eq. 2.3)}$$

where R_{eff} is the distance between the central molecule and the sphere or the radius of the sphere in the effective-field model in Figure 2.5;[69] ξ_1 is a fitting parameter that provides the amount of contributions other than the sphere of the effective field in Figure 2.5 to the structure factor, $S(Q)_{eff}$.

In essence, this model makes the interactions from surrounding molecules into a sphere around the central molecule. When ξ_1 = 1.00 (or 100%), all contributions are from the effective field in Figure 2.5. Deviation of ξ_1 from 1.00 indicates that magnetic interactions (with the central molecule) other than the sphere are present. In other words, interactions *not* from the sphere of the effective field in Figure 2.5 may also contribute to

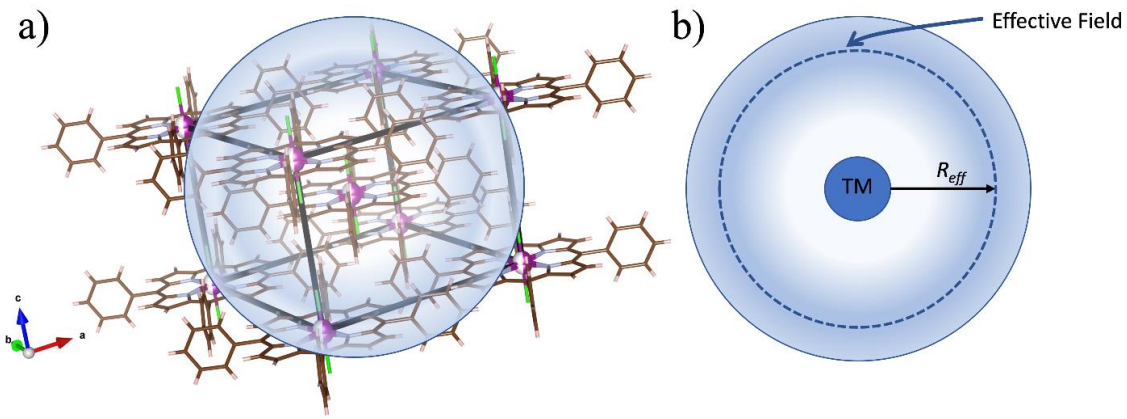


Figure 2.5. (a) Visualization of the effective field with respect to the molecules surrounding one molecule at the center based on the crystal structures of **Fe-Cl** and **Mn-Cl** and intermolecular distances summarized in Figure A.7. (b) Illustration of the effective field produced by the intermolecular magnetic interactions. Here, the effective field is a spherical average of all the interactions with the central metal atom.

the intermolecular magnetic interactions, and the sphere of the effective field in Figure 2.5 alone does not reflect all intermolecular magnetic interactions.

One key feature of Eq. 2.3 is that its $1 - \frac{\sin(Q\,R_{eff})}{Q\,R_{eff}}$ part simulates the $1 - \frac{\sin(QR)}{QR}$ part in Eq. 2.1 for the experimental INS peak intensity from *intra*molecular magnetic interactions in metal dimers. That is, the magnetic interaction of the central molecule with the field from neighboring molecules in the model has a similarity to that in Eq. 2.1 between two metal ions in dimeric molecules (with the M···M distance R), including showing the oscillatory features from the *inter*molecular magnetic interactions. The effective-field model we have developed here offers the structure factor $S(Q)_{eff}$ to analyze the experimental spatial dependence of Q, while assessing the overall nature of the interactions from both the sphere in Figure 2.5 and the interactions not included in the sphere.

Figure 2.4 shows the best fits of the calculated intensity of the magnetic peak vs. Q obtained by the model. Except for the $Q < 1.0$ Å^{-1} region for **Fe-Cl**, the effective-field model provides a good overall fit to the INS data of both Peak **A** in **Fe-Cl** and Peak **D** in **Mn-Cl**, while also capturing the oscillatory nature of the experimental data in Figure 2.4.

Two other models were also considered with details given in Appendix A: (1) Single-molecule model, treating $f = 1.00$ (or 100%) in Eq. 2.2. That is, $S(Q) = \xi_0 F^2(Q)$ with contributions *only* from the first part in Eq. 2.2 and *no* intermolecular magnetic contributions. In essence, this model does not include any intermolecular magnetic interaction and the fit is expected to show only magnetic scattering factor $F^2(Q)$ in Eq. 2.1 decreasing with Q increase. (2) Average-exchange model, in which all intermolecular

magnetic interactions to one molecule are averaged. Here, $S(Q)_{eff}$ in Eq. 2.2 is replaced by $S(Q)_{av}$ given in Eq. A.2 in Appendix A. The fits for **Fe-Cl** by either single-molecule or average-exchange models, also given in Figure 2.4-Top, show the decrease of the peak intensities with Q increase. However, neither model captures the oscillatory nature of the experimental data. Thus, the effective-field model in Eqs. 2.2-2.3 developed in the current work best explains the oscillations. In other words, combining the single-molecule model (first part in Eq. 2.2) with the effective field (second part in Eq. 2.2 given in Eq. 2.3) captures the oscillations in the experimental data.

It should be noted that, for **Fe-Cl**, the fit from the effective-field model in Figure 2.4-Top shows deviation from the experimental oscillation, even though the overall trend is similar. The variation is due to the separation of the single-molecule Peak **A1** and assembly Peak **A2** (from intermolecular interactions). The overall magnetic scattering function $S(Q)$ in Eq. 2.2 models essentially an overlapping peak of a single molecule and the assembly. When these two peaks are separated in **Fe-Cl**, as shown in Figure 2.2, deviations of the fit from experimental data may occur. However, there is an oscillation in the fit in Figure 2.4-Top, and the model does provide the proper intermolecular distance comparable to those observed in the crystal structure of **Fe-Cl**, discussed below.

On the contrary, the fit to the oscillations observed for the Mn compound **Mn-Cl** in Figure 2.4-Bottom is much better. This is not surprising as the peak of the assembly (from the intermolecular interactions) overlaps with the single-molecule excitation into Peak **D** in Figure 2.3, giving a higher percentage of the assembly contributions to the overall intensity than in **Fe-Cl**. The analyses of the fits by the effective-field model support that we are observing both a single-molecule excitation in concert with an

excitation from intermolecular interactions (i.e., assembly) for both compounds. The conclusion is unclear when analyzing either of the two compounds alone. However, experimental results of both **Fe-Cl** and **Mn-Cl** and analyses by the model together make the conclusion much more evident.

Table A.3 provides a list of the parameters R_{eff}, ξ_1, and f obtained from fittings by the effective-field model. R_{eff}, the distance of the central molecule from the sphere in Figure 2.5, is an important parameter representing the distances in the intermolecular magnetic interactions. The R_{eff} values of 11.84 Å for **Fe-Cl** and 13.22 Å for **Mn-Cl** are within intermolecular distances of ~10.69 Å and ~13.48 Å in the crystal structures of **Fe-Cl** and **Mn-Cl** (Figure A.7).[8, 16]

The parameter ξ_1 in Eq. 2.3, representing contributions by the interactions *not* represented by the sphere, is slightly smaller ($\xi_1 = 0.96$) for **Fe-Cl** than ($\xi_1 = 0.99$) for **Mn-Cl**, suggesting that **Mn-Cl** has more characteristics of the center-sphere interaction with little contributions from magnetic interactions outside of the sphere. For **Fe-Cl**, ξ_1 value shows a larger deviation from 1.00, suggesting slightly higher contributions of magnetic interactions outside the sphere and less contributions from the center-sphere in Figure 2.5. The difference between **Fe-Cl** and **Mn-Cl** may be in part the result of the extra d electron in the $S = 3/2$, d^5 Fe^{3+} complex **Fe-Cl** than $S = 2$, d^4 Mn^{3+} complex **Mn-Cl**, given that the two complexes are isostructural in the crystals.

Furthermore, $f = 0.54$ for **Mn-Cl** is smaller than $f = 0.95$ for **Fe-Cl**, suggesting that there is a larger percentage of the assembly contribution (and smaller percentage of the single-molecule contribution) in **Mn-Cl** than in **Fe-Cl**. This is consistent with the fact

that, for **Mn-Cl**, the assembly peak and the single-molecule peak directly overlap as Peak **D** in Figure 2.3, both contributing to the peak intensity. In contrast, for **Fe-Cl**, the assembly Peak **A2** at 11.8(1) cm^{-1} in Figure 2.2-Bottom is shifted from the single-molecule Peak **A1** by ~1 cm^{-1}.

From the analyses using the effective-field model, we can conclude that these molecular solids exhibit both single-molecule and intermolecular magnetic excitations. Using a simple spin model presented earlier,[69] the coupling constants *J* between the molecule at the center and effective field in Figure 2.5 are calculated to be ~11.8 cm^{-1} and ~6.92 cm^{-1} for the Fe^{3+} and Mn^{3+} compounds, respectively. Since the first INS excitation of a symmetric dimeric compound is approximately equal to *J*, the excitations from intermolecular magnetic interactions for **Fe-Cl** and **Mn-Cl** are estimated to be ~11.8 cm^{-1} and ~6.92 cm^{-1}, respectively. These values are the same as Peak **A2** in Figure 2.2-Bottom and Peak **D** in Figure 2.3, supporting the assignment of Peaks **A2** and **D** discussed earlier. The weak nature of dipole-dipole interactions among the molecules of **Fe-Cl** and **Mn-Cl** explains why the size of *J* is relatively small.

2.4. Experimental Methods

Powders of Fe(TPP)Cl (**Fe-Cl**, ≥98%) and Mn(TPP)Cl (**Mn-Cl**, 97%) were purchased from Arctom (Westlake Village, California, USA) and Ambeed (Arlington Heights, Illinois, USA), respectively, and used as received without further purification. Single-crystal X-ray diffraction data of Fe(TPP)Cl (**Fe-Cl**) at 20(2), 142(2), and 293(2) K indicates that the solid sample assumes the tetragonally symmetric *I*4 space group.[8, 88] Powder X-ray diffraction data of the microcrystalline sample of **Fe-Cl** at 296 K (Figure

A.8), which was used in current studies, is in good agreement with that simulated from the single-crystal data at 20-293 K.[8] Single crystals of Mn(TPP)Cl (**Mn-Cl**) are isomorphous with **Fe-Cl**,[16] and the powder X-ray diffraction pattern of the solid sample of **Mn-Cl** (Figure A.9 at 296 K) used in the current work corresponds with the 4-fold symmetric *I*4 space group. Earlier INS studies at zero field performed by some of us suggest that both **Fe-Cl** and **Mn-Cl** retain the 4-fold crystal symmetry at temperatures as low as 1.5 K.[9] The powder X-ray diffraction data were collected on an Panalytical Empyrean theta-theta diffractometer with a Cu $K\alpha_1$ (1.5406 Å) source and a zero-background Si plate.

For the measurements on the time-of-flight (TOF) Cold Neutron Chopper Spectrometer (CNCS),[85, 87] samples of **Fe-Cl** (5 g) and **Mn-Cl** (2 g) were sealed in respective aluminum cans and placed in the sample environment containing an 8 T vertical cryomagnet. Placing the magnet into the sample environment blocks ~70% of the instrument detectors. In the current work, only the zero-field data were used. Measurements were performed with incident neutron energies of E_i = 12.5, 26.8, and 42.3 cm^{-1} at 2 and 20 K. The data were collected for 6-10 hours each. The data under magnetic fields is not discussed further here, as the signal/noise ratio was prohibitively low due to the short measurement times and blocking of instrument detectors by the magnet.

Reduction of the TOF data was done using the Mantid[89] and DAVE[90] software packages. Peak intensities vs. *Q*-dependence (Figure 2.4) were prepared by taking the intensities at 12.7(1) cm^{-1} for **Fe-Cl** and 6.92(2) cm^{-1} for **Mn-Cl** in the accessible *Q*-

range. For each Q value, intensities in the next 0.075 $Å^{-1}$ or 0.1 $Å^{-1}$ Q range were integrated as the intensity for the Q value.

Examples of the fitting of the magnetic peaks to determine the peak areas, including error analyses, are given in Figures A.5 and A.6.

CHAPTER III

SPECTROSCOPIC STUDIES OF MAGNETIC TRANSITIONS AND SPIN-PHONON COUPLINGS IN THE SINGLE-MOLECULE MAGNETS $Co(PPh_3)_2X_2$ (X = Cl, Br, I)

This chapter is based on the following paper:

Alexandria N. Bone, Chelsea N. Widener, Duncan H. Moseley, Zhiming Liu, Zhengguang Lu, Yongqiang Cheng, Luke L. Daemen, Mykhaylo Ozerov, Joshua Telser, Komalavalli Thirunavukkuarasu, Dmitry Smirnov, Samuel M. Greer, Stephen Hill, J. Krzystek, Karsten Holldack, Azar Aliabadi, Alexander Schnegg, Kim R. Dunbar, Zi-Ling Xue, Applying Unconventional Spectroscopies to the Single-Molecule Magnets, $Co(PPh_3)_2X_2$ (X = Cl, Br, I): Unveiling Magnetic Transitions and Spin-Phonon Coupling. *Chem. Eur. J.* **2021**, *27*, 11110-11125. https://doi.org/10.1002/chem.202100705

The author processed and interpreted experimental FIRMS and Raman results, as well as results of calculations (performed by Yongqiang Cheng) of the phonons, INS spectra, far-IR spectrum of $Co(PPh_3)_2Cl_2$, and spin densities. In addition, the author generated phonon animations and assigned symmetries of the calculated phonons. Results from HFEPR performed by S. M. Greer, J. Krzystek, and S. Hill, LFT by J. Telser, and FT-FD THz-EPR by K. Holldack, A. Aliabadi, and A. Schnegg are included for a complete presentation of the studies.

INS studies of $Co(PPh_3)_2X_2$ (X = Cl, Br, I) are reported in the thesis of Zhiming Liu[182] and are presented here for completeness.

3.1. Abstract

Large separation of magnetic levels and slow relaxation in metal complexes are desirable properties of single-molecule magnets (SMMs). Spin-phonon coupling (interactions of magnetic levels with phonons) is ubiquitous, leading to magnetic relaxation and loss of memory in SMMs and quantum coherence in qubits. Direct observation of magnetic transitions and spin-phonon coupling in molecules is challenging. We have found that far-IR magnetic spectra (FIRMS) of $Co(PPh_3)_2X_2$ (**Co-X**; X = Cl, Br, I) reveal rarely observed spin-phonon couplings as avoided crossings between magnetic and *u*-symmetry phonon transitions. Inelastic neutron scattering (INS) gives phonon spectra. Calculations using VASP and phonopy programs give phonon symmetries and movies. Magnetic transitions among zero-field split (ZFS) levels of the $S = 3/2$ electronic ground state were probed by INS, high-frequency and -field EPR (HFEPR), FIRMS, and frequency-domain FT terahertz EPR (FD-FT THz EPR), giving magnetic excitation spectra and determining ZFS parameters (D, E) and g values. Ligand-field theory (LFT) was used to analyze earlier electronic absorption spectra and give calculated ZFS parameters matching those from experiments. DFT calculations also gave spin densities in **Co-X**, showing that the larger Co(II) spin density in a molecule, the larger its ZFS magnitude. The current work reveals dynamics of magnetic and phonon excitations in SMMs. Studies of such couplings in the future would help to understand how spin-phonon coupling may lead to magnetic relaxation and develop guidance to control such coupling.

3.2. Results and Discussion

3.2.1. Experimental Determination of Magnetic and Phonon Transitions

3.2.1.1. INS

For **Co-Cl**, both variable-field (with a 10 T magnet) and VT INS studies were conducted. The former gave spectra in Figure 3.1-Top with low signal-to-noise ratio of the peaks, as the magnet blocked many detectors. A comparison of the spectra at 0 and 10 T shows that the peak at 29.7(2) cm^{-1} at 0 T disappears at 10 T, indicating its magnetic nature [i.e., $2D' = 29.7(2)$ cm^{-1}]. VT INS spectra of **Co-Cl** at 5, 30, 60, and 90 K are presented in Figure 3.1-Bottom. At zero applied field, only one magnetic transition from the $M_S = \pm 3/2$ ground level to the $M_S = \pm 1/2$ excited level is expected in the INS spectra. After Bose-correction of the VT INS spectra to make the intensities of phonon peaks relatively constant, the intensity of the magnetic transition should decrease with increasing temperature, as the $M_S = \pm 1/2$ excited level is increasingly thermally populated at the expense of the $M_S = \pm 3/2$ ground level. Figure 3.1-Bottom shows that the magnetic transition at 5 K by VT INS is at $2D' = 29.5(2)$ cm^{-1}. The sign of the D parameter, as those of **Co-Br** and **Co-I** below, was based on the HFEPR results, as the INS results cannot determine the sign.

For **Co-Br** and **Co-I**, VT INS studies were similarly conducted and the spectra are given in Figure 3.2. Magnetic transitions of **Co-Br** and **Co-I** area clearly observed at $2D' = 27.6(4)$ cm^{-1} and 27.3(0.3) cm^{-1}, respectively.

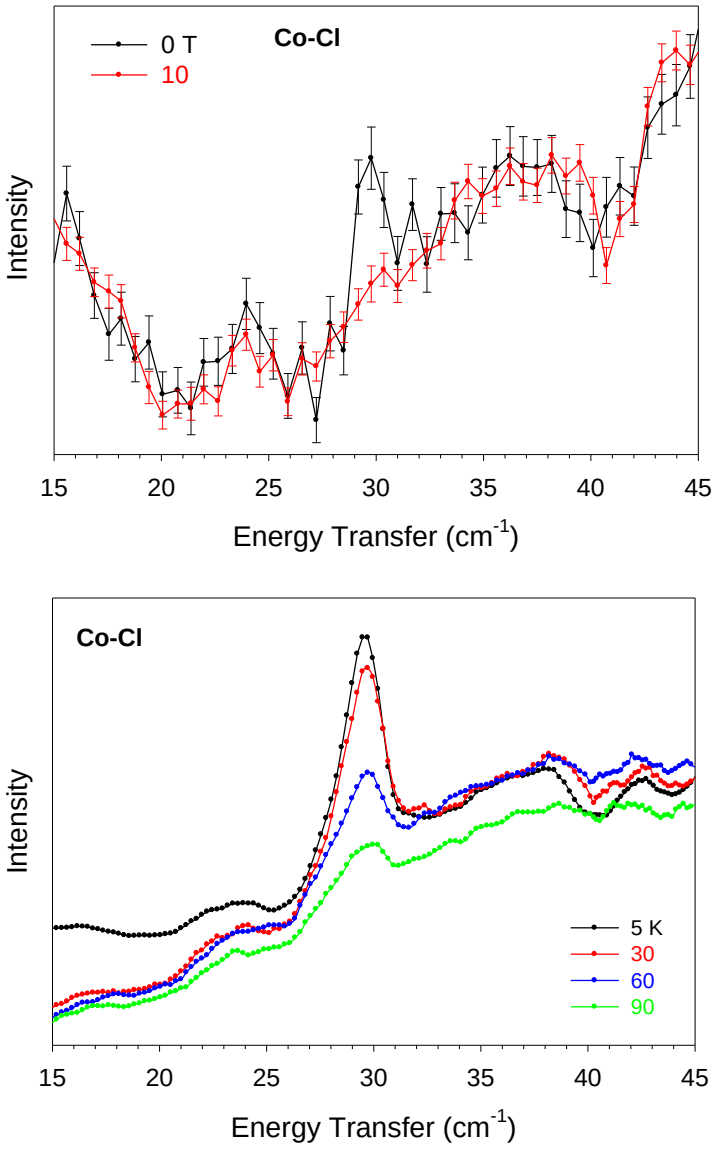


Figure 3.1. (Top) Variable-field INS spectra at DCS at 1.5-1.6 K; (Bottom) Bose-corrected forward-scattering VT INS spectra at VISION. Figure B.1 in Appendix B shows additional VT INS spectra of **Co-Cl**, revealing phonon excitations and their symmetry assignments.

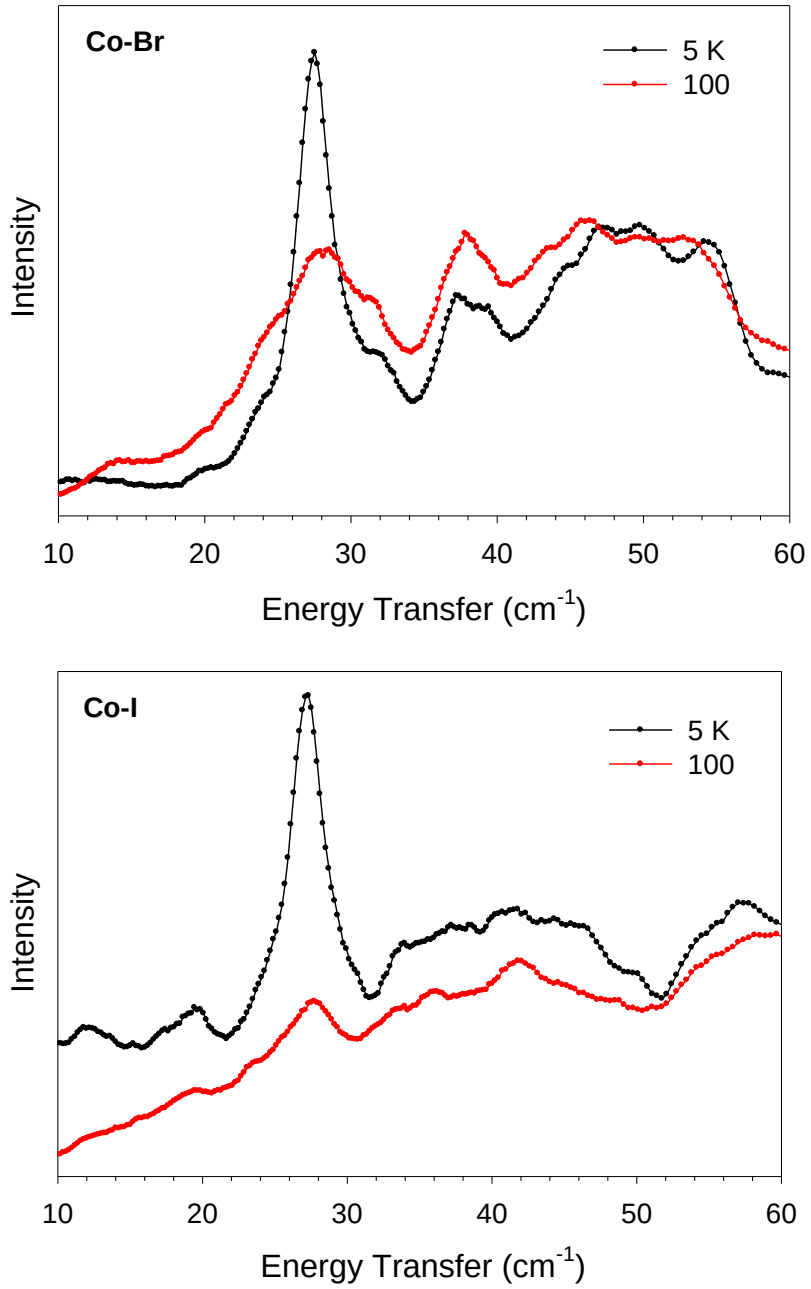


Figure 3.2. Bose-corrected forward-scattering VT INS spectra on VISION: (Top) **Co-Br**. (Bottom) **Co-I**. Additional VT INS spectra of **Co-Br** and **Co-I** by VISION revealing phonon excitations are given in Figures B.2 and B.3 in Appendix B, respectively.

3.2.1.2. FIRMS

Magnetic transitions (at 0 T) between the two ZFS sublevels (e.g., M_s = -3/2 → -1/2 and M_s = +3/2 → +1/2) in **Co-X** are magnetic-dipole-allowed by symmetry and selection rules (ΔM_s = 0, ±1).[70-71] In C_{2v} local symmetry around the Co(II) ion, the magnetic dipole moment operators have B_2, B_1, and A_2 symmetries as the rotations R_x, R_y, and R_z, respectively. In the double group C_{2v}', both M_s = ±3/2 and ±1/2 levels are represented by $E_{1/2}$.[91-92] Thus, the magnetic transitions are observable in far-IR. Frequency-domain spectroscopy (i.e., FIRMS) using high magnetic fields, revealing how the Zeeman effect changes the transitions between ZFS levels, is ideal to probe magnetic transitions in addition to studying IR-active phonon excitations.[6, 70-71, 93-104] In the present S = 3/2, D < 0 case, the M_s = +3/2 level can be excited to the M_s = +1/2 level and spin-Hamiltonian parameters can then be extracted from the spectra.

Transmittance of **Co-Cl**, **Co-Br**, and **Co-I** at 0 and 17 T in Figure 3.3 reveals the changes caused by the external magnetic fields with additional FIRMS spectra and assignments of phonon symmetries for **Co-Cl** and **Co-Br** in Figures B.4-B.6 in Appendix B. Transmission spectra normalized by the average are shown as a function of magnetic fields in Figure 3.4. The largest transmission changes are presented in the blue color and are proportional to the intensity of the transitions between the levels split under magnetic field, while the yellow color corresponds to regions lacking magnetic-dependent spectral features. The magnetic resonance absorption is most intense at 0 T, allowing *direct* determination of the energy gap between the ±3/2 and ±1/2 levels from FIRMS spectra as follows: **Co-Cl**, 29.85(13) cm^{-1}; **Co-Br**, 27.62(11) cm^{-1}; and **Co-I**, 27.38(15) cm^{-1} (Figure 3.4). The intensity of the magnetic absorption decreases and spreads out in high magnetic

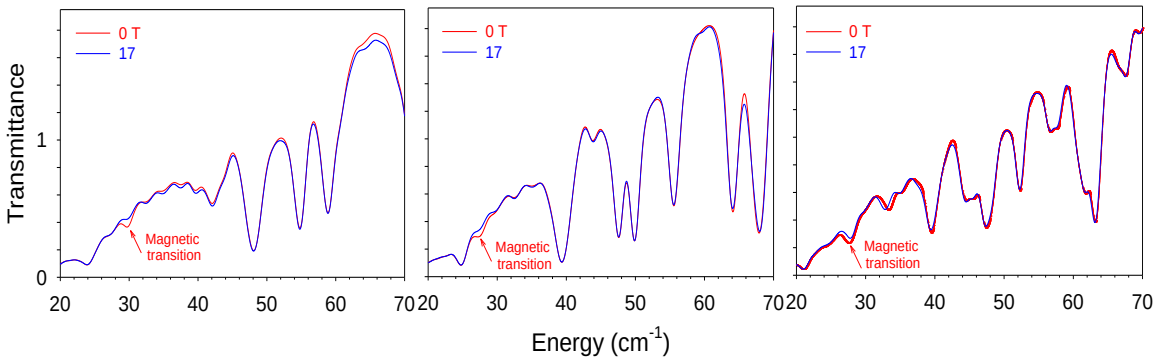


Figure 3.3. FIRMS spectra of the complexes at 5 K and 0 and 17 T: (Left) **Co-Cl**, (Middle) **Co-Br**, (Right) **Co-I**. Assignments of the phonon peaks in **Co-Cl** and **Co-Br** are given in Figures B.4-B.6. The phonons in **Co-I** could not be assigned.

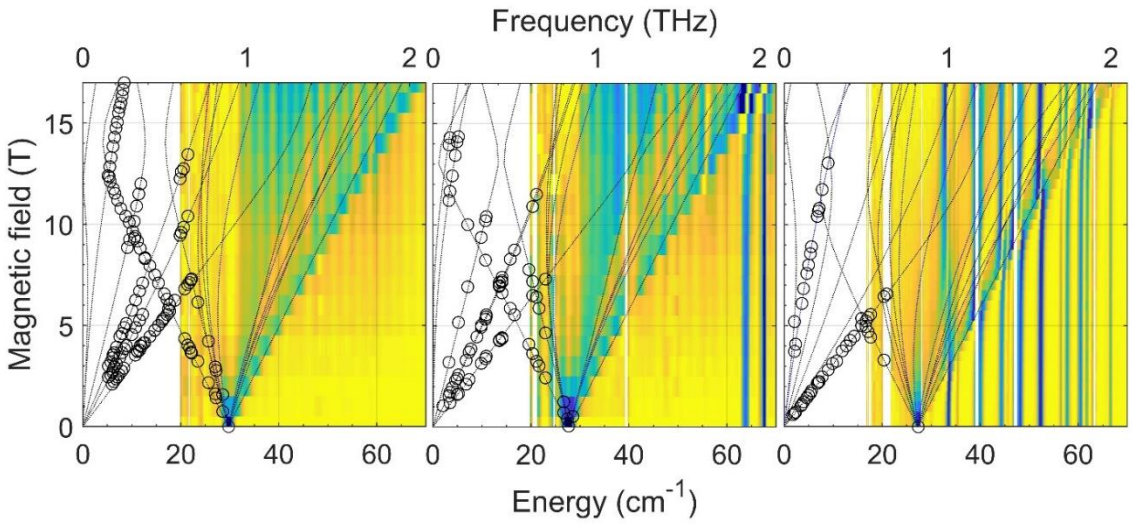


Figure 3.4. FIRMS maps (normalized transmission vs. field and energy/frequency): (Left) **Co-Cl**, (Middle) **Co-Br**, (Right) **Co-I** with HFEPR results superimposed. The color trend from blue to yellow corresponds to a decrease of the magnetic absorption. The lines are simulations of turning points in the powder spectra that assume the (best-fitted) spin-Hamiltonian parameters in Tables 3.1-3.2. The circles correspond to the observed HFEPR resonances, except for the zero-field resonance in **Co-I** obtained from FIRMS spectra. The equidistant vertical stripes are due to instrumental artifacts, while the white regions correspond to the spectral ranges without reliable data. Spin-phonon couplings in the FIRMS plots normalized by average are presented below in Figure 3.5 (for **Co-Br** and **Co-I**) and Figure 3.8 (for **Co-Cl**).

fields, because the intensity and the frequency of the transitions are defined by the direction of the magnetic field relative to the magnetic anisotropy ***D***- and ***g***-tensors using microcrystalline samples with random orientations. The black lines in Figure 3.4 show *calculated* field dependences of turning points[105] in the powder spectra. While the low-energy turning points are revealed in HFEPR spectra (shown as circles in Figure 3.4), turning points with energies larger than 2*D*' show up in FIRMS maps (black lines). The maps are consistent with $D < 0$, and these results are in excellent agreement with calculated powder spectra of magnetic absorption (Figure B.7) using the spin-Hamiltonian parameters from HFEPR in Tables 3.1-3.2, thus confirming the HFEPR determination of the parameters. One additional finding from Figure 3.3-Right is that, for **Co-I**, the phonon at 33.3(1) cm^{-1} (phonon **B** in Figure 3.5-Bottom and Table 3.3 below) is coupled to the magnetic transition even at 0 T, pushing each other apart. At 17 T, when the magnetic transition (peak **A** in Figure 3.5-Bottom) is shifted away after several avoided crossings, it is no longer coupled to this phonon. In fact, the original peak of magnetic transition, **A**, has become the phonon (through the coupling during the avoided crossing with **B**) and now "returned" to a new position (at 32.8 cm^{-1} to the left of the original position of **B** at 0 T).

Magneto-Raman spectra of **Co-Cl**, **Co-Br**, and **Co-I** under 0-14 T magnetic fields (Figures B.8-B.10) do not reveal the magnetic transitions in these complexes. Phonon features of the Raman spectra of **Co-X** at 0 T are discussed below.

Table 3.1. Axial and rhombic ZFS parameters for **Co-Cl**, **Co-Br**, and **Co-I**

Complex	Method	D (cm^{-1})	$\lvert E \rvert$ (cm^{-1})[b]	$\lvert E/D \rvert$	$D' = (D^2 + 3E^2)^{1/2}$ (cm^{-1})	Ref.[c]
Co-Cl	Variable-field INS				14.9(2)	*
	VT INS				14.7(2)	*
	FIRMS				14.93(13)	*
	FD-FT THz-EPR				14.97(5)	*
	THz time-domain EPR	−14.76	1.61	0.109	15.0	53
	HFEPR	−14.76(2)	1.141(8)	0.0773(5)	14.89(2)	*, 54
	MCD	−14(3)	0.96(20)	0.08(2)	14(3)	54
	Magnetometry	−11.6	2.43	0.21	12.3	56
	Calculated[a]				14.91	*
Co-Br	VT-INS				13.8(6)	*
	FIRMS				13.81(11)	*
	FD-FT THz-EPR				13.75(5)	*
	THz time-domain EPR	−13.90	0.96	0.069	14.0	53
	HFEPR	−13.82(2)	0.29(1)	0.02	13.83(2)	*
	Magnetometry	−12.5	0.70	0.056	12.6	56
	Calculated[a]				13.86	*
Co-I	VT-INS				13.7(3)	*
	FIRMS				13.69(15)	*
	FD-FT THz-EPR				13.6(1)	*
	HFEPR	−13.13(10)	2.11(5)	0.16	13.63(10)	*
	Magnetometry	−36.9				55
	Calculated[a]				13.63	*

[a] LFT does not provide separate D and E components, only the splitting of the ground state spin quartet into two doublets (or levels). Half of this splitting is what is provided. Calculated g_{eff} values indicate a negative sign of ZFS. The parameters described in Table B.3 were used, with ζ = 459 cm^{-1} (**Co-Cl**), ζ = 338 cm^{-1} (**Co-Br**), and ζ = 355 cm^{-1} (**Co-I**).

[b] Sign of E values in cited references is positive. The sign was not determined in the current work. Absolute signs are placed to all values here.

[c] Values determined in the current work are notated with an asterisk (*).

Table 3.2. *g*-Values for **Co-Cl**, **Co-Br**, and **Co-I**

Complex	Method	g_x	g_y	g_z	Ref.[a]
Co-Cl	FD-FT THz-EPR	2.3	2.3	2.15	*
	THz time-domain EPR	2.20	2.18	2.23	53
	HFEPR	2.166(4)	2.170(4)	2.240(5)	*, 54
	MCD	2.15(5)	2.16(4)	2.17(3)	54
	Magnetometry	2.215		2.265	56
Co-Br	FD-FT THz-EPR	2.3	2.3	2.13	*
	THz time-domain EPR	2.10	2.10	2.22	53
	HFEPR	2.24(1)	2.15(1)	2.24(2)	*
	Magnetometry	2.006		2.164	56
Co-I	FD-FT THz-EPR	2.2(1)	2.2(1)	2.0(1)	*
	HFEPR	2.28(4)		2.36(2)	*

[a] Values determined in the current work are notated with an asterisk (*).

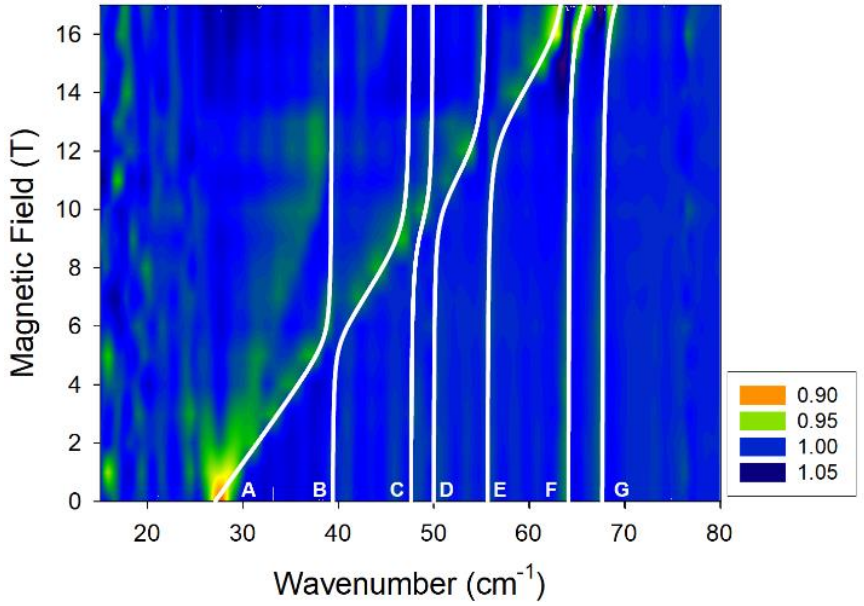
Table 3.3. Energies of phonons involved in spin-phonon couplings and the coupling constants

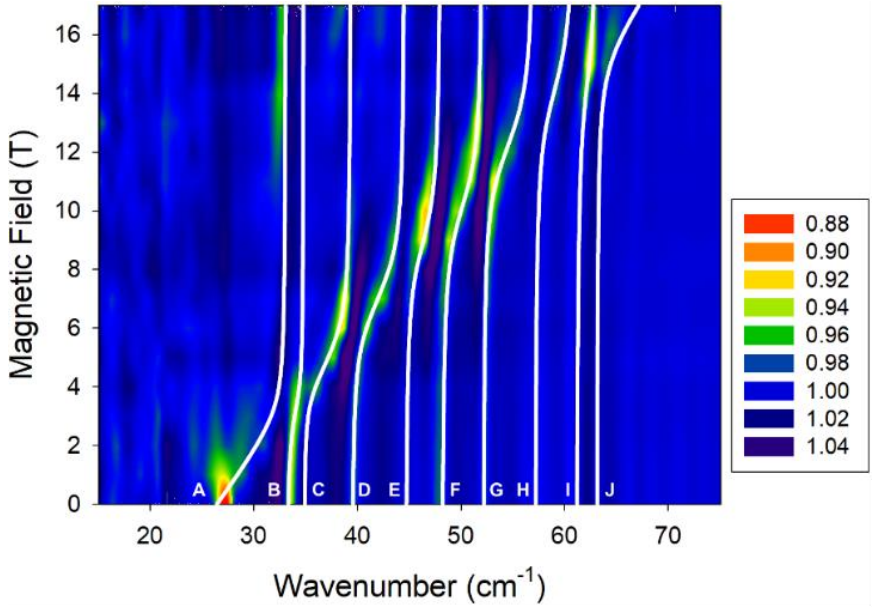
Co-Cl				
Phonon	**B**	**C**	**D**	**E**
Phonon peak (cm^{-1})	42.2(1)	48.1(3)	54.8(2)	58.9(3)
Λ (cm^{-1})	1.3(2)	1.3(1)	1.3(2)	1.4(3)

Co-Br						
Phonon	**B**	**C**	**D**	**E**	**F**	**G**
Phonon peak (cm^{-1})	39.5(3)	47.5(1)	50.0(1)	55.6(2)	64.0(2)	68.1(2)
Λ (cm^{-1})	1.0(3)	1.3(4)	1.1(3)	1.5(3)	1.4(4)	1.8(4)

Co-I									
Phonon	**B**	**C**	**D**	**E**	**F**	**G**	**H**	**I**	**J**
Phonon peak (cm^{-1})	33.3(1)	35.3(1)	39.5(2)	44.1(1)	47.7(2)	52.3(2)	56.7(1)	61.0(2)	63.0(1)
Λ (cm^{-1})	1.3(2)	0.9(3)	1.5(3)	1.6(2)	1.8(2)	1.6(3)	1.8(3)	2.0(4)	1.1(3)

Figure 3.5. FIRMS plots of far-IR spectra normalized by average, which minimize phonon features that do not change with magnetic field: (Top) **Co-Br**; (Bottom) **Co-I**, revealing simulations of spin-phonon couplings. The color trend from red to blue corresponds to a decrease of absorption. The white lines show the results of the spin-phonon coupling model using a 7 × 7 matrix for **Co-Br** and a 10 × 10 matrix for **Co-I**, which are similar to those of the 5 × 5 matrix in Eq. 3.3 and are given in Appendix B. Figure 3.5-Left (**Co-Br**) and -Right (**Co-I**) are also given in Figures B.5-Bottom and B.6-Bottom, respectively, without the white simulation lines here to more clearly show the avoided crossings.


Magnetic Field (T)
Wavenumber (cm-1)
A
B
C
D
E
F
G
0.90
0.95
1.00
1.05


Magnetic Field (T)
Wavenumber (cm-1)
A
B
C
D
E
F
G
H
I
J
0.88
0.90
0.92
0.94
0.96
0.98
1.00
1.02
1.04

3.2.1.3. FD-FT THz-EPR

Figure 3.6 depicts FD-FT THz-EPR of **Co-X** at 0-7 T with a spectral resolution of 0.5 cm^{-1}. Division by a reference spectrum measured under identical conditions, but with a field offset, leads to FD-FT THz-EPR magnetic-field-division spectra (MDS) containing only the field-dependent components of the spectrum. Magnetic resonances in MDS are similar to those in first-derivative EPR spectra. Field-independent phonons are cancelled by this technique. However, in the case of spin-phonon couplings, phonons shift in an applied magnetic field and therefore lead to peaks of magnetic transitions similar to EPR resonances. Discrimination between magnetic transitions originating from EPR resonances and spin-phonon coupled peaks requires the comparison with simulated spectra using the spin-Hamiltonian in Equation 1.1 in Chapter I. In Figure 3.6, EPR spectra simulated with Eq. 1.1 are plotted alongside measured spectra. Field vs. frequency plots in Figure 3.6 are equivalent to Figure 3.4, but allow for more convenient comparison of measured and simulated spectra.

The simulations were performed with the *EasySpin* program and its extensions for frequency-domain EPR.[101] Very good estimates of 2*D*' can be directly obtained from the zero-field FD-FT THz-EPR spectrum. However, more accurate *D*' and *g* values are available from simulations of MDS at different external magnetic fields, giving the SH parameters for **Co-X** in Tables 3.1-3.2. Simulations of the spectra can also provide estimates of *E*. However, these values are usually less accurate than those from HFEPR.[106] Thus, the *E* parameters from FD-FT THz-EPR are not given in Table 3.1.

A very good match between experiment and simulation was achieved for **Co-Cl**. No indication of spin-phonon coupling is found in the spectral window. Similarly, good

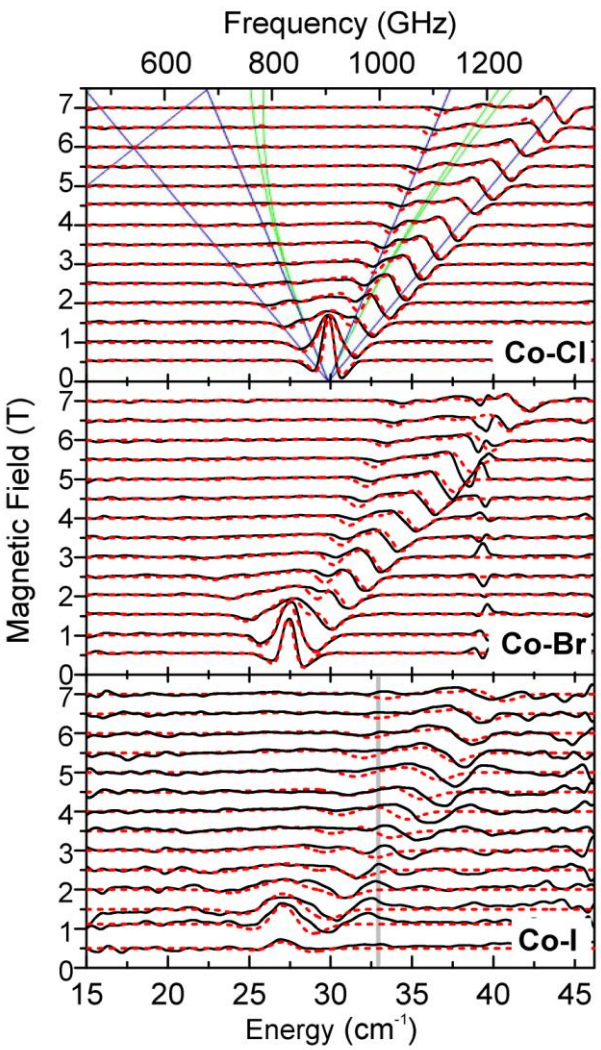


Figure 3.6. FD-FT THz-EPR MDS at 5 K: (Top) **Co-Cl**, (Middle) **Co-Br**, (Bottom) **Co-I**. Spectra are plotted as offset to corresponding magnetic field. Experimental spectra (black) are overlaid on spin-only simulations (dashed red; simulation parameters available in Tables 3.1-3.2). In the top panel, simulated transition energies for magnetic fields parallel (blue) and perpendicular (green) to the z-axis of the ZFS tensor are shown. The red shaded bar in the lower panel marks the transition energy of a phonon at 33 cm^{-1}.

agreement was found for **Co-Br**. However, a distortion around 39.5 cm^{-1} is observed, originating from a strong (phonon) absorption (see Figures 3.3 and B.11 for a view of the phonon). For MDS spectra of **Co-Br** between 5.5 T and 6.5 T, a partial overlap with this absorption leads to a deviation of the simulated and measured spectrum. However, despite the high quality of the data, no clear assignment of spin-phonon coupling is possible in this case. Interestingly, spectra of both **Co-Cl** and **Co-Br** show low energy phonon modes at ~25 cm^{-1}, which are very close to the zero-field EPR peaks (see Figure 3.3). Yet, neither of these modes appears to couple to the magnetic resonance (or the coupling is too weak to be observed here), when they overlap with the magnetic transitions at elevated fields, and therefore does not alter the MDS of **Co-Cl** and **Co-Br**.

Spectra of **Co-I**, on the contrary, show pronounced spin-phonon coupling between 2.5 T and 5.5 T, leading to clear deviations between calculated and experimental MDS [see dashed spectra in Figure 3.6-Bottom simulated with Eq. 1.1 (without spin-phonon coupling)]. While experimental spectra and simulations match very well below 2 T and above 5.5 T, spectra in the intermediate field range exhibit an additional splitting, which is not reproduced by the SH simulations. The splitting of the magnetic resonance by spin-phonon coupling is most obvious in the 3 T MDS of **Co-I**, where the predicted magnetic resonance (without spin-phonon coupling) overlaps with the phonon at 33 cm^{-1} (phonon **B** in Figure 3.5-Bottom and Table 3.3), as discussed earlier in Figure 3.3-Right. The experimental MDS clearly reveals two minima centered around 33 cm^{-1}, which originate from an avoided crossing of the Co(II) spin resonance and phonon **B**.[107]

3.2.1.4. HFEPR

Co-Cl was the subject of an earlier detailed HFEPR and MCD study.[54] In the current work, we have confirmed the previous results and added spectra at several high frequencies to the 2-D field vs. frequency map of turning points[105] (Figure 3.4-Left and Figure B.12-Top), which were unavailable earlier.[54] One such spectrum, obtained at 815 GHz, which is just below the frequency (~890 GHz) of the transition between the M_s = ±3/2 and M_s = ±1/2 levels as determined at zero field by FIRMS and FD-FT THz EPR, is shown in Figure B.13.

Co-Br generated a very good HFEPR response, similarly to **Co-Cl**. Three representative HFEPR spectra (Figures B.14-B.16) are shown in Appendix B. Figure B.14 gives an optically modulated spectrum recorded at the frequency corresponding almost exactly to the zero-field transition frequency (~830 GHz) between the M_s = ±3/2 and M_s = ±1/2 levels. Figure B.15 shows a conventional, magnetically modulated spectrum at 473 GHz, while Figure B.16 displays a spectrum at a low frequency of 98 GHz, where it is possible to observe all three turning points of the intra-Kramers M_s = -3/2 → +3/2 transition. The full 2-D map of HFEPR turning points in **Co-Br** is shown in Figure 3.4-Middle and Figure B.12-Middle.

The HFEPR response of **Co-I** was weaker than those of the other two congeners. In particular, most of the observed resonances originated from the intra-Kramers M_s = -3/2 → +3/2 transition within the m_s = ±3/2 doublet. Only in one narrow frequency region (ca. 500 GHz) were we able to record resonances belonging to the inter-Kramers M_s = -3/2 → +1/2 transition, which are informative with regard to ZFS (Figure B.17). Figure B.18 shows a spectrum at the low end of available frequencies (63 GHz) which turned

out to be the only frequency at which we were able to observe all three turning points of the intra-Kramers M_s = -3/2 → +3/2 transition. As a result, a least-square fit to the 2-D field vs. frequency map (Figure 3.4-Right and Figure B.12-Bottom) yielded lower accuracy in the spin-Hamiltonian parameters of **Co-I** than those for **Co-Cl** and **Co-Br**.

Least-square fits of the spin-Hamiltonian parameters to the 2-D field vs. frequency maps for the three complexes resulted in the following values: D = -14.76(2), $|E|$ = 1.141(8) cm^{-1} for **Co-Cl**; D = -13.82(2), $|E|$ = 0.29(1) cm^{-1} for **Co-Br**; and D = -13.13(10), $|E|$ = 2.11(5) cm^{-1} for **Co-I** (Table 3.1), along with most g (g_x, g_y, g_z) values listed in Table 3.2.

3.2.2. LFT of the Co-X Series (X = Cl, Br, I)

3.2.2.1. LFT Background of the **Co-X** Series

As is typical for roughly tetrahedral open-shell complexes, electronic absorption spectra of the **Co-X** (X = Cl, Br, I) series are rich and informative, and the complete series was thoroughly studied many years ago. For **Co-Cl**, Simo and Holt provided a comprehensive analysis of the single-crystal electronic absorption of Co-doped $Zn(PPh_3)_2Cl_2$ (**Co/Zn-Cl**).[107] Tomlinson et al. did the same for Co-doped $Zn(PPh_3)_2Br_2$ (**Co/Zn-Br**) and $Zn(PPh_3)_2I_2$ (**Co/Zn-I**).[49] In **Co-X** with C_{2v} point group symmetry, the molecular z axis lies along the C_2 axis (i.e., bisecting the X-Co-X and P-Co-P bond angles as shown in Figure 1.4 in Chapter 1), the x axis lies in the X-Co-X plane (σ_v), and the y axis lies in the P-Co-P plane (σ_v'). The spectroscopic results are summarized in Table B.1 in SI, which corrects a minor discrepancy between the analysis described by Tomlinson *et al.* and data in a table in their paper.[49] In C_{2v} point group symmetry, the

ground electronic state of **Co-X** is $^4A_2$, derived from the parent $^4A_2(F)$ term in T_d symmetry ($e^4t_2^3$ in strong-field notation). The quartet excited states are $^4T_2(F)$ ($e^3t_2^4$), $^4T_1(F)$ ($e^2t_2^5$), and $^4T_1(P)$ ($e^3t_2^4$) in T_d symmetry and each splits into $^4A_1$ (for $^4T_2$) or $^4A_2$ (for $^4T_1$), $^4B_1$, and $^4B_2$ states. The electronic transition $^4A_2 \rightarrow {}^4A_1$ is symmetry forbidden, but $^4A_2 \rightarrow {}^4A_2$ is allowed with *z* polarization, $^4A_2 \rightarrow {}^4B_1$ is allowed with *y* polarization, and $^4A_2 \rightarrow {}^4B_2$ is allowed with *x* polarization. Transitions to the states derived from $^4T_2$ would be in the mid-IR region and thus very difficult, although not impossible,[51, 108] to observe. Transitions to those derived from $^4T_1(F, P)$ are in the visible region and all were observed experimentally with their polarization assignments.[49, 107] These states are given in Figure 3.7, which also shows the descent in symmetry for a Co(II) from the free-ion to a hypothetical, tetrahedral $[CoX_4]^{2-}$ complex,[109] to a hypothetical tetragonally compressed $[CoX_4]^{2-}$ complex, to the $CoX_2(PPh_3)_2$ system which has C_{2v} symmetry.

These results can then be used with a ligand-field theory (LFT) analysis using the Angular Overlap Model (AOM) to provide a quantitative comparison among the three complexes. The above geometrical model is employed, with the experimental bond angles ∠X-Co-X and ∠P-Co-P in each case, as given in Table B.2.

Use of the AOM satisfactorily fitted the experimental data given in Table B.1. As simplifying assumptions, the two halide ligands and the two phosphine ligands were held equivalent. Both ligand types were constrained to have cylindrical π-interactions; donating for X and accepting for P. The fit values for **Co-Cl** and **Co-Br** can be compared to those determined by Davies et al.,[110] who used single-crystal magnetic susceptibility data in combination with the same literature electronic absorption data as was used here. As shown in Table B.3, the two analyses are in reasonable agreement, the chief

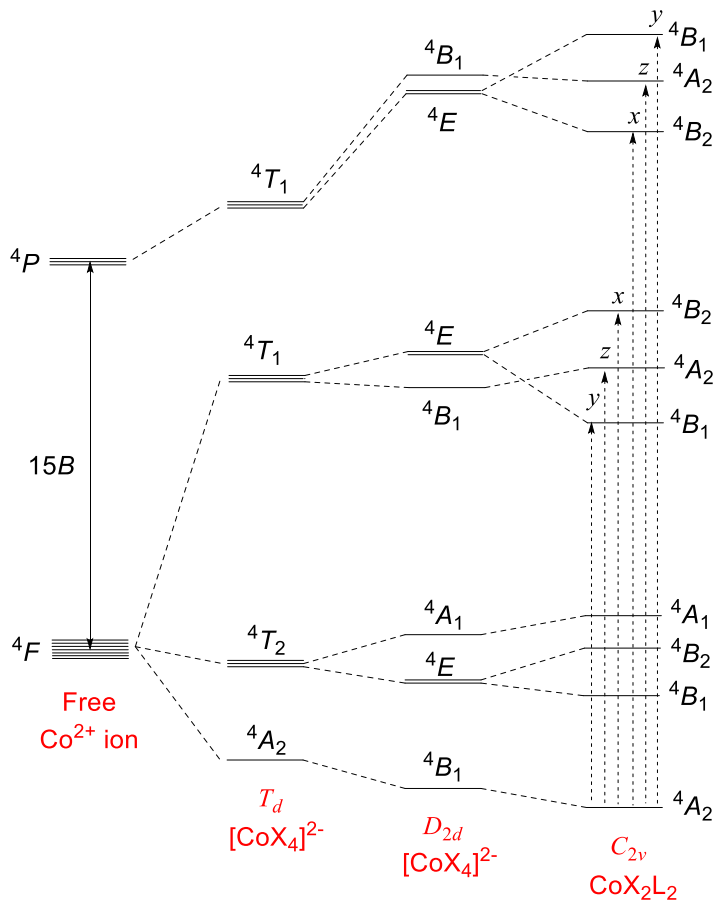


Figure 3.7. Electronic states of quartet states of $3d^7$ Co^{2+} as a free-ion, in a tetrahedral (T_d) ligand-field, in a tetragonally compressed ligand field (D_{2d}), and in a rhombic (C_{2v}) ligand-field as in **Co-X**. This figure is based on one derived for Ni(II) ($3d^8$) as in $NiX_2(PPh_3)_2$.[48] The electronic transitions are also indicated, together with their polarization, fully for the C_{2v} case,[49] and partially for the D_{2d} case, which is relevant to the discussion of previous work.[49, 107] Inclusion of spin-orbit coupling (not shown) would split each of the quartets into two degenerate levels, affording the observed ZFS. This effect is shown graphically in Figure 3e of the paper by Sundararajan *et al.*[52] and in tabular format in the Supporting Information of the paper by Bone *et al.*[113]

difference being that in the present work the π-acidity of the PPh_3 ligands is proposed to be greater. As also evident in Table B.3, the σ- and π-donor strength of the halide ligands in **Co-X** decreases in the order $Cl^- > Br^- > I^-$, in agreement with the spectrochemical series.[111] The values determined here, and previously,[110] for the Racah interelectronic repulsion parameter *B* are ~60% of the free-ion value,[112] which is plausible for a highly covalent compound. The complete output listing of the electronic states and orbital descriptions (using the Ligfield software[114]) for each of the **Co-X** series is given in Tables S7-S9 of the Supporting Information of the work by Bone *et al.*[113]

The results show that inclusion of the Racah *C* parameter, so that *C*/*B* = 4.26, the free-ion ratio,[112] gives a plethora of doublet excited states well above the quartet states, but there are relatively lower lying doublet states in the ranges of 9500–12 500 cm^{-1} and 14 000–17 500 cm^{-1} above the ground state [i.e., close to quartet states derived from $^4T_1(F, P)$]. These doublet excited states might contribute to ZFS and possibly to the observed absorption bands. For a more tractable depiction of the doublet states, Table S12 of the published work[113] gives the complete d^7 electronic states for a hypothetical $[CoX_4]^{2-}$ ion with ideal T_d symmetry.

3.2.2.2. Analysis of ZFS in Co-X by Ligand Field Theory

Spin-orbit coupling can be included into the above LFT-AOM analysis to reproduce experimental ZFS parameters (Table S11 in SI of Ref. 113 by Bone *et al.*). Davies et al. used ζ = 500 cm^{-1}, which is only slightly lower than the free-ion value (533 cm^{-1}).[115] We find that, for **Co-Cl**, use of ζ = 459 cm^{-1} (86% of the free-ion value, perhaps more realistic than 94% used earlier) exactly reproduces the experimental ZFS

parameters (Tables 3.1-3.2 in comparison to those from HFEPR). It is not possible to de-convolute this splitting into D and E components, nor to their sign. The spin expectation value of each of the levels of the ground state quartet does not readily afford the spin-only values of $M_S = \pm 1/2, \pm 3/2$ (Tables S7b, S8b, S9b, S10, and S11 in Ref. 113), e.g., for **Co-Cl**, $M_S = \pm 0.14$ and $M_S = \pm 0.85$ (Table S7b in Ref. 113). However, inclusion of an applied field [300 mT, as in conventional, X-band EPR; using the locally written (J. Telser) program DDN] sheds light on this situation, as shown for the electronic states of the lowest spin quartet state for a hypothetical $[CoX_4]^{2-}$ ion with D_{2d} symmetry (Table S10 in Ref. 113) and for the real **Co-X** complexes with C_{2v} symmetry (Table S11 in Ref. 113). These cases give observed g_{eff} values for **Co-Cl** as follows: $g_{x(\text{max})} = 6.96$, $g_{y(\text{min})} = 0.57$, $g_{z(\text{mid})} = 0.91$ (Table S11a in Ref. 113). The assignment to x, y, and z components of $\boldsymbol{g}_{\text{eff}}$ is a consequence of the chosen AOM coordinate system, but in general for $S = 3/2$, observed g_{eff} values in which one is large and two are very small (for intrinsic $g = 2.00$, $\boldsymbol{g}_{\text{eff}} = [6, 0, 0]$[116]) are characteristic of $D < 0$, as is the case for **Co-Cl**.[117] Smaller values of ζ (~65% of the free-ion value; see Table 3.1) exactly reproduce the experimental ZFS for **Co-Br** and **Co-I**, again with negative sign, as demonstrated by their $\boldsymbol{g}_{\text{eff}}$ components (Tables S11b and S11c in Ref. 113, respectively). The origin of the ZFS in **Co-X** is discussed in Supporting Information of the paper by Bone *et al.*[113]

3.2.3. Experimental and Calculated Phonon Spectra and Studies of Spin-Phonon Couplings

Crystals of **Co-Cl** [$P2/c$, No. 13, 293(2) and 295 K],[57, 118] **Co-Br** ($P2/c$, 295 K),[118] and **Co-I** [$P2_1/c$, No. 14, 110(2) K][55] in the current work are all monoclinic with C_{2h}

crystallographic lattice symmetry. Thus, phonon modes of their crystalline solids have one of the four symmetries: A_g, B_g, A_u, and B_u.[119] Phonons of the A_u and B_u modes are IR-active, while those of A_g and B_g modes are Raman-active.

Phonon modes of the three complexes, energies of the modes, and INS spectra were obtained by VASP and phonopy calculations.[120] Spin-phonon coupling simulations were conducted for the avoided crossings in FIRMS spectra using Hamiltonians in Eqs. 3.1 and 3.3 below.

3.2.3.1. Phonon Excitations in FIRMS, INS, and Raman Spectra, Calculated INS Spectra, and Computations of Phonon Excitations and Symmetries

Accurate phonon calculations are a critical step to understand the atomic displacements leading to spin-phonon coupling in SMMs. In the most general sense, the atomic displacement pattern associated with a specific vibrational mode can change the bond length and angle, resulting in changes of electronic and magnetic structure. Different vibrational modes at different frequencies can affect the electronic and magnetic structure differently. The DFT phonon calculations of the INS spectra were conducted using the reported single-crystal structures of the three complexes (Table B.2) with two goals: (1) Determine the symmetries of phonon modes and their energies; (2) Give calculated INS spectra to compare with the experimental ones. The lattice symmetry for all three crystal structures is C_{2h}, which was used to assign symmetries to each phonon mode. The calculated phonon modes and their energies for **Co-Cl**, **Co-Br**, and **Co-I** are given in Tables B.4-B.6 in Appendix B. In addition, the DFT calculations gave calculated INS spectra in Figures B.1, B.2, and B.3 for comparison with the experimental

INS spectra of the three compounds. It is noted that, unlike (optical) far-IR and Raman spectroscopies, there are no symmetry-based INS selection rules. Thus, all phonon modes are active. Overall, there is a good match between experimental (by VISION at 5 K) and calculated INS in the region above 150 cm^{-1}. However, low-energy modes are difficult to calculate accurately. It should be pointed out that the current calculations do not account for any peaks of magnetic origin or spin-phonon coupling. In addition, the VASP and phonopy[120] calculations, while giving phonons (and their symmetries and energies) and spin densities discussed below, are not able to address spin-phonon coupling in the solids. Spin-phonon couplings in other SMMs, particularly their roles in magnetic relaxation, have been the subject of recent computations or modeling studies.[121-125]

Far-IR and Raman spectra of the three complexes recorded at 0 T and 5 K, revealing IR- (*u*-symmetry) and Raman-active (*g* symmetry) phonons, are given in Appendix B (**Co-Cl**, Figure B.19; **Co-Br**, Figure B.20; **Co-I**, Figure B.21). Since spin-phonon couplings, discussed below, involve some of the IR-active phonons and were observed in FIRMS, animations of the A_u and B_u phonons near the peaks of the magnetic transition around 20-75 cm^{-1} (14, 16, and 31 movies for **Co-Cl**, **Co-Br**, and **Co-I**, respectively) have been made based on the VASP and phonopy calculations and are provided in the Appendix. These animations show atomic displacements with contributions from both external and internal modes.

3.2.3.2. Studies of Spin-Phonon Couplings in FIRMS Spectra

Multiple phonons were found to be involved in spin-phonon couplings with the magnetic transition in FIRMS spectra of **Co-Cl** (Figures 3.8 and B.4), leading to avoided

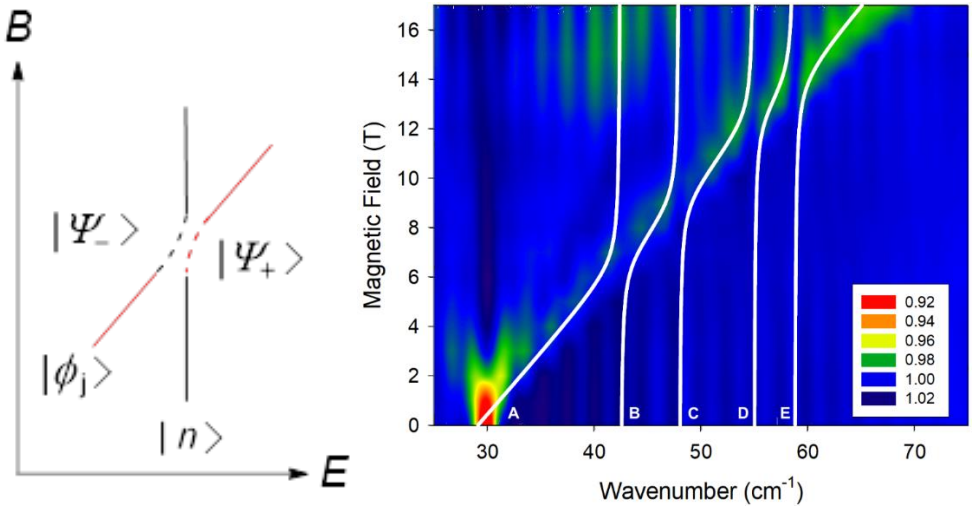


Figure 3.8. (Left) Schematic representation of an avoided crossing. Some of us have recently provided more detailed schematic views of the spin-phonon couplings in a Co(II) complex with axial anisotropy ($D < 0$).[95] (Right) FIRMS plot of **Co-Cl** spectra normalized by average, which minimizes phonon features that do not change with magnetic fields. The color trend from red to blue corresponds to absorption decrease. The white lines show the results of the spin-phonon coupling model using a 5 × 5 matrix in Eq. 3.3 below. Figure 3.8-Right is also shown in Figure B.4-Bottom in Appendix B without the white lines to more clearly reveal the avoided crossings. The blue shifting transition is from the lowest magnetic level to the highest magnetic level of the ground spin quartet and corresponds to a specific direction of the external field with respect to the spin coordinate system (i.e., a turning point). These levels are not well-defined by M_s quantum numbers due to the mixing.[46-47]

crossings (also known as non-crossings or anticrossings). An avoided crossing is, in essence, the result of interactions between two states/levels of the same symmetries, leading to two new states/levels from mixing of the two original states/levels, as shown in Figure 3.8-Left.[126] When 1*s* orbitals from two H atoms interact to form σ bonding and σ* antibonding orbitals, it is essentially an avoided crossing of two 1*s* orbitals. Spin-phonon coupling here reflects how a vibration (with a periodic motion of the atoms in a molecule) affects the magnetic levels in Figure 1.4. Recently, a vibronic model was used to account for similar couplings of vibrations in $Co(acac)_2(H_2O)_2$ ($S = 3/2$) with the $M_s = \pm 1/2, \pm 3/2$ levels.[6]

In the FIRMS spectra of **Co-Cl** (Figures 3.8-Right and B.4-Bottom), when a magnetic (spin) peak (**A**) is close to a phonon peak (**B**) with the same symmetry (i.e., both excitations belong to the same irreducible representation in the C_{2h} point group), the two couple, causing the peak of the magnetic transition to take on the characteristic of the phonon peak and vice-versa. That is, the two coupled peaks carry both magnetic and phonon features.[6] The avoided crossings are observed as peak **A** is blue-shifted by the increasing magnetic field. In Figure 3.8-Right and more clearly in Figure B.4-Bottom without the white lines, peak **B** progressively picks up more magnetic features as the magnetic field increases, until it becomes the peak of the magnetic transition undergoing a blue-shift itself, while peak **A** turns into a phonon peak. Peak **B** continues the blue-shift until encountering another phonon (**C**) with the same symmetry. At this point, **B** and **C** undergo new spin-phonon coupling, resulting in another avoided crossing. This process is repeated with two additional phonon peaks **D** and **E**. It should be pointed out that there might be spin-phonon couplings involving additional phonons. However, if they exist,

they are not easily identified in Figure 3.8-Right. The observations of the spin-phonon couplings between magnetic transitions and IR-active *u*-symmetry phonons here are in contrast with the spin-phonon couplings in $Co(acac)_2(H_2O)_2$ and its isotopologues,[6] in which the couplings were observed with Raman-active *g* phonons.

For the 2-*D* FIRMS map in Figure 3.8-Right, a simplified Hamiltonian for the coupling between the magnetic excited level $|\phi_j\rangle$ and *one* phonon excited state $|n\rangle$ is given by the following 2 × 2 matrix in Eq. 3.1:[6]

$$H = \begin{pmatrix} E_{sp} & \Lambda \\ \Lambda & E_{ph} \end{pmatrix} \qquad \text{(Eq. 3.1)}$$

in which E_{sp} and E_{ph} are expected energies of the magnetic and phonon excitations, respectively, and Λ is a spin-phonon coupling constant.

Solving the matrix gives two eigenvalues $E_{\pm}$ (with the associated avoided crossing peaks $|\Psi_{\pm}\rangle$) in the secular Eq. 3.2:

$$\begin{vmatrix} E_{sp} - E_{\pm} & \Lambda \\ \Lambda & E_{ph} - E_{\pm} \end{vmatrix} = 0 \qquad \text{(Eq. 3.2)}$$

During the spin-phonon coupling, $|\Psi_+$ shifts to higher E_+, while $|\Psi_-$ shifts to lower E_- in the avoided crossing, as shown in Figure 3.8-Left. Equations 3.1 and 3.2 give a model to understand spin-phonon coupling in the FIRMS map and calculate the coupling constants Λ.

This model can be expanded to a 5 × 5 matrix in Equation 3.3 involving the couplings of the magnetic transition with all four phonons **B**, **C**, **D**, and **E** simultaneously. Eq. 3.3 ignores interactions (couplings) among phonons, as the off-diagonal elements

between any two phonons are set to be 0. The ZFS peak (E_{sp}) was modeled every 0.5 T from 0 to 17 T for the transmittance peak, giving the coupling constants Λ_1-Λ_4 of 1.3(1)-1.4(3) cm^{-1} in Table 3.3. If the spectra are instead fit using multiple 2 × 2 matrices in Eq. 3.1, the coupling constants are not appreciably different. It should be pointed out that **B**, **C**, **D**, and **E** are those phonons in the crystalline solid of **Co-Cl** that are observed to undergo spin-phonon couplings, even though there are additional IR-active phonons in the 30-80 cm^{-1} region, as listed in Table B.4.

$$H = \begin{pmatrix} E_{sp} & \Lambda_1 & \Lambda_2 & \Lambda_3 & \Lambda_4 \\ \Lambda_1 & E_{ph1} & 0 & 0 & 0 \\ \Lambda_2 & 0 & E_{ph2} & 0 & 0 \\ \Lambda_3 & 0 & 0 & E_{ph3} & 0 \\ \Lambda_4 & 0 & 0 & 0 & E_{ph4} \end{pmatrix} \quad \text{(Eq. 3.3)}$$

Spin-phonon couplings are also observed in FIRMS maps of **Co-Br** (Figure 3.5-Top) and **Co-I** (Figure 3.5-Bottom) and also in Figures B.5-Bottom and Figure B.6-Bottom, respectively, without the white lines of spin-phonon couplings. Six phonons in the crystalline solid of **Co-Br** are noticed to couple with the magnetic transition, giving rise to avoided crossings as the latter blue-shifts due to the Zeeman effect (IR-active, *u*-symmetry phonons **B-G** in the 30-80 cm^{-1} region, Table B.5). Simulations using a 7 × 7 matrix (Eq. B.1 in SI) give the coupling constants of 1.0(3)-1.8(4) cm^{-1} in Table 3.3. For a crystalline solid of **Co-I**, nine phonons (**B-J** in Figure 3.5-Bottom) are shown to couple to the magnetic transition leading to several avoided crossings, as peak **A** moves to higher energy with increasing external magnetic field. Simulations using a 10 × 10 matrix (Eq. B.2 in SI) give the coupling constants of 0.9(3)-2.0(4) cm^{-1} in Table 3.3.

3.2.3.3. Calculated Spin Densities of Atoms in **Co-X** Complexes

The DFT calculations using VASP also give spin densities, ρ_s, in **Co-X**, as summarized in Table 3.4 with detailed lists for each atom in Tables B.7-B.8 in SI. Although the VASP calculations here are not of high-level, they provide a quantitative scale, revealing how the spin is dispersed onto X, P, C and peripheral H atoms in the molecules.[127] VASP partitions electrons according to the Wigner-Seitz radius a_e in Eq. 3.4:[128]

$$a_e = (3/4\pi n_e)^{1/3} \qquad \text{(Eq. 3.4)}$$

where n_e is the particle density of electrons; a_e is the radius "occupied" by one atom in a sample, and each atom is considered as a sphere.

This method does not include spin densities in bonds between atoms. Therefore, the total spin densities (sums of those on all atoms) of 2.80, 2.78 and 2.75 for **Co-Cl**, **Co-Br** and **Co-I**, respectively, are smaller than 3 (= 3 unpaired electrons) on the molecules. The results in Table 3.4 show that the unpaired electron densities are transferred from the central Co(II) ions to ligand atoms, although the metal ions retain 2.59, 2.57 and 2.55 unpaired electrons (>92% of total spin in each of the three compounds, not counting the spin densities between bonds), respectively. That the spin density is mostly on the Co(II) ion in **Co-X** is consistent with the above simple LFT that describes the complexes as pure d^7 systems, i.e., as having nearly "innocent" ligands. This is in contrast to the case of a diiodide complex of Mn(III) (d^4, $S = 2$) wherein a valence tautomer that can be described as $[Mn^{II}I^{\bullet}]^{2+}$, as opposed to the innocent $[Mn^{III}I^{-}]^{2+}$, leads to unusual ZFS.[129] Among ligand atoms, the halides X carry very small, yet the highest spin densities (6.01×10^{-2} to

Table 3.4. Calculated spin densities ρ_s of atoms in **Co-X**

Atom	**Co-Cl**	**Co-Br**	**Co-I**
Co	2.585	2.570	2.553
X	6.69×10^{-2} (**Cl**)	6.85×10^{-2} (**Br**)	6.01×10^{-2} to 6.39×10^{-2} (**I**)
P	2.06×10^{-2}	1.92×10^{-2}	1.55×10^{-2} to 1.94×10^{-2}
C	-2.02×10^{-4} to -6.38×10^{-4} 1.21×10^{-4} to 2.98×10^{-3}	-1.50×10^{-4} to -5.36×10^{-4} 3.90×10^{-4} to 2.93×10^{-3}	-6.62×10^{-6} to -1.04×10^{-3} 4.40×10^{-8} to 5.07×10^{-3}
H	-1.77×10^{-5} to -5.65×10^{-5} 2.40×10^{-7} to 8.40×10^{-5}	-1.89×10^{-5} to -4.92×10^{-5} 1.21×10^{-6} to 9.47×10^{-5}	-2.70×10^{-6} to -4.10×10^{-5} 5.85×10^{-6} to 8.85×10^{-5}
Total	**2.797**	**2.783**	**2.747**

6.85×10^{-2}), followed by the P atoms (1.55×10^{-2} to 2.06×10^{-2}). These densities are positive, as those of *some* C and H atoms of the phenyl groups in the PPh_3 ligands (Tables B.7 and B.8), indicating that spins on the α atoms in the molecules are parallel to those on the Co(II) ion. Other C and H atoms, however, have negative spin densities, i.e., the spin densities on these atoms have opposite polarization to that on the Co(II) ion, X, and P atoms.

The results here are consistent with NMR studies of paramagnetic compounds, which show ligand resonances are typically shifted by electron spin densities on the ligand atoms.[130-132] The signs of $\boldsymbol{\rho_s}$ in Table 3.4 indicate that both spin delocalization and polarization mechanisms, which are used as a model to explain spin delocalization in paramagnetic molecules,[130-131] likely account for the transfer of spin densities in **Co-X**.

It is interesting to note that the slight decrease of spin density on the Co(II) ion from **Co-Cl** (2.585), **Co-Br** (2.570), to **Co-I** (2.553) parallels the drop of D' from 14.89(2), to 13.83(2), and to 13.63(10) cm^{-1} (HFEPR results) for the three complexes, as shown in Figure B.24 in Appendix B. For $Co(acac)_2(H_2O)_2$, also a SMM,[6, 127, 133] but with only light atom (Period 2) donor ligands, the calculated spin density of 2.81 (by the same VASP program) on its Co(II) ion and D' of 57 cm^{-1} are both larger than those of **Co-X**. At least among these four Co(II) complexes, the larger spin density on a metal ion is, the larger ZFS in the complex is. It should be pointed out that the number of complexes here [four including $Co(acac)_2(H_2O)_2$] is limited, and different DFT programs may give different calculated spin densities. Studies of more compounds are needed to see if there is a correlation between the spin densities and magnitudes of ZFS. In addition, the VASP calculations here are not able to address spin-phonon coupling,[121-125] as indicated earlier.

Thus, additional studies are needed to understand how the spin density affects ZFS in a complex and how the lattice and molecular motions (i.e., phonons) that are coupled to the magnetic excited levels impact the spin density.

3.3. Experimental Methods

Compounds of **Co-Cl**, **Co-Br**, and **Co-I** were prepared by literature methods. Powder X-ray diffraction of typical **Co-Cl**, **Co-Br**, and **Co-I** are given in Figure B.25.

Variable-field INS data were collected at the Disc Chopper Spectrometer (DCS) at the NIST Center for Neutron Research (NCNR). A powder sample of **Co-Cl** (2 g) was measured in the 1.5-1.6 K range at 0 T with E_i = 73 cm^{-1}, and at 10 T with E_i = 54 cm^{-1}, in order to compare the results of variable-temperature and variable-field INS. All data were processed on DAVE.[90] Variable-temperature INS spectra were collected on the Vibrational Spectrometer (VISION) at the Spallation Neutron Source (SNS), ORNL. For each measurement, approximately 0.2 g of the powder sample was sealed in an aluminum can. The aluminum can was then fixed on the end of the sample holder and placed inside the neutron beam. VISION has two detector banks, forward- and back-scattering, providing data for low and high |$\boldsymbol{Q}$| scattering, respectively.[62] As an indirect-geometry INS spectrometer,[62] data of low scattering angles, including magnetic scattering, are more intense in the forward-scattering detectors at VISION.

The far-IR setups with applied magnetic fields at the National High Magnetic Field Laboratory (NHMFL, Tallahassee, Florida) in the USA (FIRMS) and at the electron storage BESSY II in Germany (FD-FT THz-EPR) have been used. The two groups practicing it in the current work, however, use different magnet configurations (vertical-

bore or split-coil) and process the data differently. FIRMS spectra were collected at NHMFL using a Bruker Vertex 80v Fourier-transform infrared (FT-IR) spectrometer coupled with a 17.5 T vertical-bore superconducting magnet. The experimental setup is equipped with a mercury lamp and a composite silicon bolometer (Infrared Laboratories), as an incoherent (sub)-THz radiation source and detector, respectively. The THz radiation propagates in free-space inside the optical beamline, connecting the output of the spectrometer and top of the sample probe. The radiation then passes through the brass lightpipe over a distance of 2.5 m from room temperature to the field center. The probe and beamline are evacuated to eliminate strong parasitic absorptions of the air. The samples are mulls of *n*-eicosane and powder (~2 mg) of each complex. Both the sample and the bolometer were cooled by low-pressure helium gas to ~5 K. The spectrum of the THz radiation transmitted through the samples was measured between 10 and 720 cm^{-1} (0.3–21.6 THz) with a resolution of 0.3 cm^{-1} (9 GHz), acquisition time of 3 min, and 5 kHz scanner speed.

FD-FT THz-EPR experiments were performed at the THz beamline of the BESSY II storage ring and employed a 10 T split-coil superconducting magnet (Oxford-Spectromag 4000) equipped with wedged *z*-cut quartz windows in transmission geometry. The temperature was varied between 2 K and 300 K and the field from 0 to 7 T. To vary the temperature, we either used an Oxford-Optistat cryostat with quartz windows in transmission geometry or, for magnetic measurements, a variable-temperature insert in the magnet. The FT-IR spectrometer was a Bruker IFS125 HR with its internal Hg-source (Q202) and set to 0.5 cm^{-1} resolution (0.2 cm^{-1} for absorbance measurements in the Appendix B), 40 kHz scanner frequency, 100 sweeps and an IR-

Labs 4.2 K/Si-bolometer (and a 1.6 K one for temperature-dependent measurements shown in Figure B.25). The acquisition time for a single raw spectrum was 3 min and transmittance data presented in Figures B.24 and B.27 in Appendix B were measured in 10 min.

Errors in $2D'$ values were obtained as described below: (1) For INS spectra, they were estimated to be 10% of the full width at half maximum (FWHM) of the peaks of magnetic transitons in baseline-corrected spectra (0 T) in the 20-40 cm^{-1} range. (2) For FIRMS and HFEPR spectra, the errors were obtained from simulations of the spectra. (3) For FD-FT THz-EPR spectra, they were obtained from visual inspection of the agreement between experimental and simulated spectra.

Experimental details of the Raman spectroscopic studies and results are given in Appendix B.

HFEPR was performed using the EMR facility at NHMFL. The facility operates a transmission spectrometer described elsewhere,[134] which was modified by the use of Virginia Diodes Inc. (VDI, Charlottesville, VA, USA) sources, generating sub-THz radiation in the 50–640 GHz frequency range. In some experiments requiring higher frequencies (>700 GHz), backward-wave oscillators were used as sources of sub-THz radiation. The spectrometer is associated with a 15/17 T warm-bore superconducting magnet. The samples were measured both "as is" which allowed them to orient (torque) in the magnetic field, or as pellets mixed with *n*-eicosane. About 30–60 mg of the powder samples were used in each measurement. HFEPR spectra were typically collected at 5–10 K.

In the calculations of phonons for **Co-Cl**, **Co-Br**, and **Co-I**, geometry optimizations were performed on the single-crystal X-ray structures of the compounds (Table B.2).[55, 57, 118] The optimized structure at 0 T was used for the phonon calculations. Spin-polarized, periodic DFT calculations were performed using VASP to generate the force constants on the supercell (284 atoms) created by Phonopy.[120] Phonopy was further used to produce phonon frequencies and polarization vectors (also gives irreducible representations). Then, OCLIMAX[135] calculates INS spectra using VISION parameters (and generating 0 K spectra). Jmol was used to create the phonon movies shown in the Appendix.

The unpaired electron spin density was calculated using VASP on the optimized structure. Spin-polarized, periodic DFT calculations were performed using VASP with the Projector Augmented Wave (PAW)[136-137] method and the local density approximation (GGA)[138] + *U* (*U* = 4.4 eV)[136, 139-140] exchange correlation functional. The energy cut off was 800 eV for the plane-wave basis of the valence electrons. The total energy tolerance for electronic structure minimization was 10^{-8} eV. The optB86b-vdW, a non-local correlation functional that approximately accounts for dispersion interactions, was applied.[141] For the structure relaxation, a $1 \times 2 \times 1$ Monkhorst-Pack mesh was used. Wigner-Seitz radii (Å): H = 0.370; C = 0.863; P = 1.233, Cl = 1.111, Br = 1.164, I = 1.487, Co = 1.302.

CHAPTER IV

STUDIES OF STRUCTURES AND MAGNETIC PROPERTIES OF METALLOPORPHYRINATES Mn(TPP)X (X = Cl, Br, I)

This chapter is based on the following paper:

Alexandria N. Bone, Shelby E. Stavretis, J. Krzystek, Zhiming Liu, Qiang Chen, Zheng Gai, Xiaoping Wang, Carlos A. Steren, Xian B. Powers, Andrey A. Podlesnyak, Xue-Tai Chen, Joshua Telser, Haidong Zhou, Zi-Ling Xue, Manganese tetraphenylporphyrin bromide and iodide. Studies of structures and magnetic properties. *Polyhedron* **2020**, *182*, 114488. https://doi.org/10.1016/j.poly.2020.114488

The author grew crystals of **Mn-Br·$CHCl_3$**, **Mn-Br·CH_2Cl_2**, and **Mn-I·$CHCl_3$**, performed and interpreted all DC and AC susceptibility measurements, conducted X-ray single-crystal diffraction studies of **Mn-Br·$CHCl_3$**, **Mn-Br·CH_2Cl_2**, **Mn-I·$CHCl_3$**, and **Mn-I·1.5$CHCl_3$**, and performed CShM and Hirshfeld surface calculations with X. Wang. Results from HFEPR performed by J. Krzystek and J. Telser, as well as results of X-ray single-crystal diffraction of **Mn-I·$CHCl_3$** and INS performed by S. Stavretis, are included for a complete presentation of the studies.

4.1. Abstract

Manganese tetraphenylporphyrin bromide and iodide Mn(TPP)X (X = Br, **Mn-Br**; I, **Mn-I**; TPP^{2-} = *meso*-tetraphenylporphyrinate) are synthetic analogs of Mn(III) geoporphyrins. Crystal structures of **Mn-Br** and **Mn-I** with chloroform in the lattices, $Mn(TPP)Br\cdot CHCl_3$ (**Mn-Br·CHCl$_3$**), $Mn(TPP)I\cdot CHCl_3$ (**Mn-I·CHCl$_3$**), $Mn(TPP)I\cdot CDCl_3$ (**Mn-I·CDCl$_3$**) in a different space group from **Mn-I·CHCl$_3$**, $Mn(TPP)I\cdot 1.5CHCl_3$ (**Mn-I·1.5CHCl$_3$**), and **Mn-Br** with dichloromethane in the lattice, $Mn(TPP)Br\cdot CH_2Cl_2$ (**Mn-Br·CH$_2$Cl$_2$**), have been determined by single-crystal X-ray diffraction at 100 K or 298 K. Hirshfeld surface analyses of the crystal structures of **Mn-Br·CHCl$_3$**, **Mn-Br·CH$_2$Cl$_2$**, **Mn-I·CHCl$_3$**, **Mn-I·CDCl$_3$** and **Mn-I·1.5CHCl$_3$** have been performed. Surprisingly the Mn(III)–Br and Mn(III)–I bonds in Mn(TPP)X (**Mn-Br** and **Mn-I**) are about 0.2 Δ (8%) longer than Fe(III)–Br and Fe(III)–I bonds in $S = 5/2$ Fe(TPP)X (X = Br, **Fe-Br**; I, **Fe-I**), although both Mn(III) and Fe(III) ions have the same radii. Magnetic properties of **Mn-Br** and **Mn-I** have been studied by direct current (DC) and alternating current (AC) susceptibility measurements, high-field electron paramagnetic resonance (HFEPR), and inelastic neutron scattering (INS). With four unpaired electrons in Mn(TPP)X (X = Br, **Mn-Br**; I, **Mn-I**), the bromide complex **Mn-Br** in **Mn-Br·CDCl$_3$** possesses easy-axis anisotropy, as the chloride analog Mn(TPP)Cl (**Mn-Cl**), with the axial (D) and rhombic (E) zero-field splitting parameters of D = –1.091 (3) cm^{-1} and $|E|$ = 0.087(2) cm^{-1}. The iodide complex **Mn-I** in **Mn-I·CDCl$_3$** becomes easy-plane with D = +1.30(1) cm^{-1} and $|E|$ = 0.010(5) cm^{-1}. Axial ZFS parameters D change from –2.24(2) cm^{-1} in **Mn-Cl**, reported earlier, to –1.091(3) cm^{-1} in

Mn-Br and +1.30(1) cm^{-1} in **Mn-I**.

4.2. Results and Discussion

4.2.1. Crystal Structures of Mn-Br·$CHCl_3$, Mn-Br·CH_2Cl_2, Mn-I·$CHCl_3$, Mn-I·$CDCl_3$ and Mn-I·1.5$CHCl_3$

Crystallographic data of the five structures are given in Tables C.1 and C.2 along with their CIF files in Appendix C. Crystal structures of **Mn-Br·$CHCl_3$** and **Mn-I·$CHCl_3$** are discussed below. ORTEP drawings of three other structures, Mn(TPP)X in **Mn-Br·CH_2Cl_2**, **Mn-I·$CDCl_3$** and **Mn-I·1.5$CHCl_3$**, are given in Figures C.1, C.2 and C.3, respectively with their selected bond lengths and angles in Tables C.3, C.4 and C.5, respectively. Continuous shape measure (CShM) calculations using the SHAPE program[142-143] were performed on all five structures as well as **Mn-Br·toluene** and **Mn-I·toluene**[144] to analyze the degree of deviation from ideal geometry, and results are provided in Tables C.6 and C.7.

Crystals of **Mn-Br·$CHCl_3$** adopt the monoclinic space group $P2_1/n$. An ORTEP diagram of the molecule is given in Figure 4.1. Selected bond lengths and angles for **Mn-Br·$CHCl_3$** are included in Table 4.1. The penta-coordinated Mn^{III} center adopts a distorted square pyramidal geometry with the Mn−Br and four Mn−N bonds in axial and equatorial positions, respectively. In the equatorial plane, the linear N1−Mn1−N3 bonds are slightly elongated [with bond lengths of 2.018(2) and 2.014(2) Å, respectively] than the other N2−Mn1−N4 bonds [bond lengths of 2.001(2) and 2.008(2) Å, respectively]. CShM calculations performed on the solvent-containing structures of Mn(TPP)Br (**Mn-Br**) [**Mn-Br·$CHCl_3$**, **Mn-Br·toluene** and two independent **Mn-Br** molecules in **Mn-**

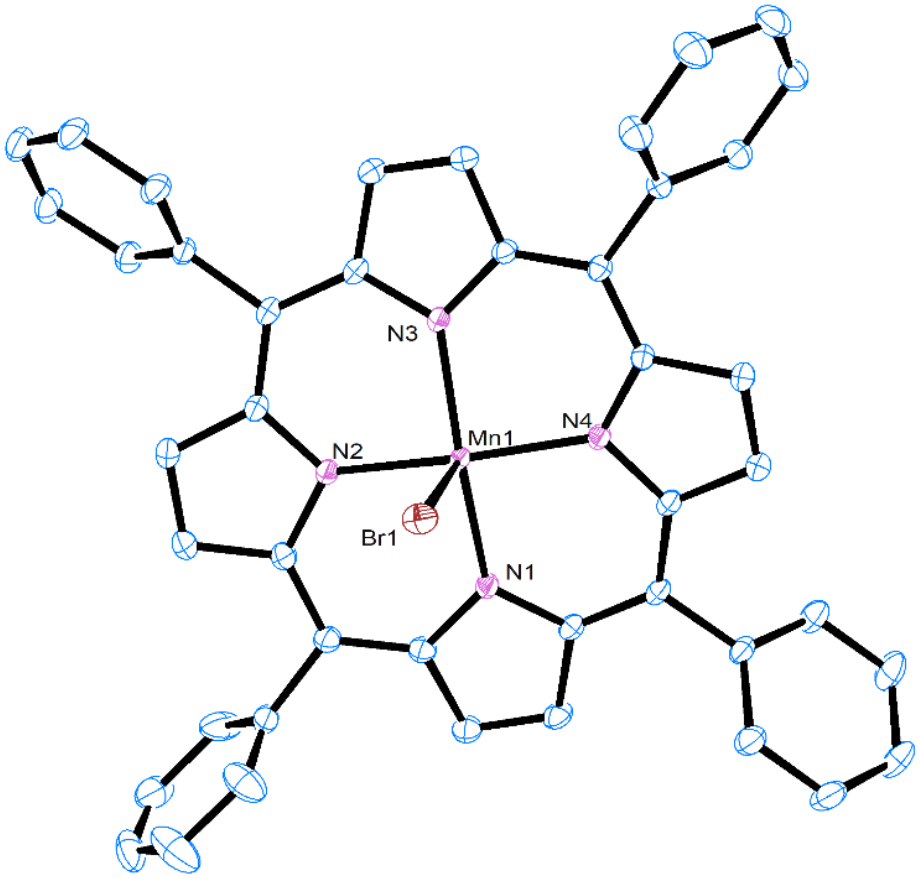


Figure 4.1. ORTEP diagram of the structure of **Mn-Br** in the crystal of **Mn-Br·CHCl$_3$**. $CHCl_3$ in the lattice and H atoms are omitted.

Table 4.1. Selected bond lengths (Å) and angles (°) for **Mn-Br·CHCl$_3$** and **Mn-I·CHCl$_3$** at 100(2) K.

Mn-Br·CHCl$_3$		**Mn-I·CHCl$_3$**	
Atoms	Length (Å) or angle (°)	Atoms	Length (Å) or angle (°)
Mn1—Br1	2.5363(5)	Mn1—I1	2.7494(4)
Mn1—N1	2.018(2)	Mn1—N1	2.0162(18)
Mn1—N2	2.001(2)	Mn1—N2	2.0148(18)
Mn1—N3	2.014(2)	Mn1—N3	2.0101(18)
Mn1—N4	2.008(2)	Mn1—N4	2.0126(18)
N1—Mn1—Br1	94.60(6)	N1—Mn1—I1	99.36(5)
N2—Mn1—Br1	90.88(7)	N2—Mn1—I1	93.99(5)
N3—Mn1—Br1	100.72(6)	N3—Mn1—I1	96.32(5)
N4—Mn1—Br1	100.77(6)	N4—Mn1—I1	97.16(5)
N1—Mn1—N2	89.98(9)	N1—Mn1—N2	89.42(7)
N2—Mn1—N3	88.73(8)	N2—Mn1—N3	89.27(7)
N3—Mn1—N4	89.37(8)	N3—Mn1—N4	89.06(7)
N4—Mn1—N1	88.81(8)	N4—Mn1—N1	89.21(7)
N1—Mn1—N3	164.64(9)	N1—Mn1—N3	164.32(8)
N2—Mn1—N4	168.35(9)	N2—Mn1—N4	168.83(8)

Br·CH$_2$Cl$_2$ (Table C.6)] show that Mn(TPP)Br molecules in all three analogs exhibit only slight distortion from square pyramidal geometry. Comparison of the Mn−Br bond length here with that of Fe−Br in Fe(TPP)Br (**Fe-Br**) is given below.

Mn-I crystallized in layered pentane/$CHCl_3$ solution at 23 °C to give crystals of **Mn-I·CHCl$_3$** (monoclinic space group $P2_1/n$). An ORTEP diagram of the molecule is given in Figure 4.2 with selected bond lengths and angles for **Mn-I·CHCl$_3$** in Table 4.1. The structure shares features with its bromo analog **Mn-Br·CHCl$_3$** discussed earlier, as comparisons in Table 4.1 show. CShM calculations of all four structures of **Mn-I** [**Mn-I·CHCl$_3$**, **Mn-I·CDCl$_3$**, **Mn-I·1.5CHCl$_3$** and **Mn-I·toluene**] by the SHAPE program[142-143] (Table C.7) show slight deviations of the Mn(TPP)I molecules in all structures from the square pyramid.

Five-coordinate Mn(III) and Fe(III) ions have identical radii of 0.72 Δ.[145] Yet, both Mn−Br and Mn−I bonds in Mn(TPP)X (**Mn-Br** and **Mn-I**) in the crystals (bond lengths of 2.490-2.536 Δ and 2.730-2.784 Δ, respectively) are about 0.2 Δ (or 8%) longer than Fe−Br and Fe−I bonds (bond lengths of 2.348 Δ and 2.554 Δ, respectively) in Fe(TPP)X (X = Br, **Fe-Br**; X = I, **Fe-I**),[11-12] as a comparison in Table 4.2 below shows. This is surprising, as Fe(TPP)X (**Fe-Br** and **Fe-I**) have higher spin (S = 5/2) than Mn(TPP)X (**Mn-Br** and **Mn-I**, S = 2), and the extra d electron in the former resides in an antibonding orbital, as a qualitative MO diagram for the square pyramid complex with C_{4v} symmetry in Figure C.4 shows. The Fe−X bonds in Fe(TPP)X are expected to be longer (not shorter) than the Mn−X bonds in M(TPP)X. Extensive studies of octahedral spin crossover complexes[146] and metalloporphyrins[147] have shown that high-spin

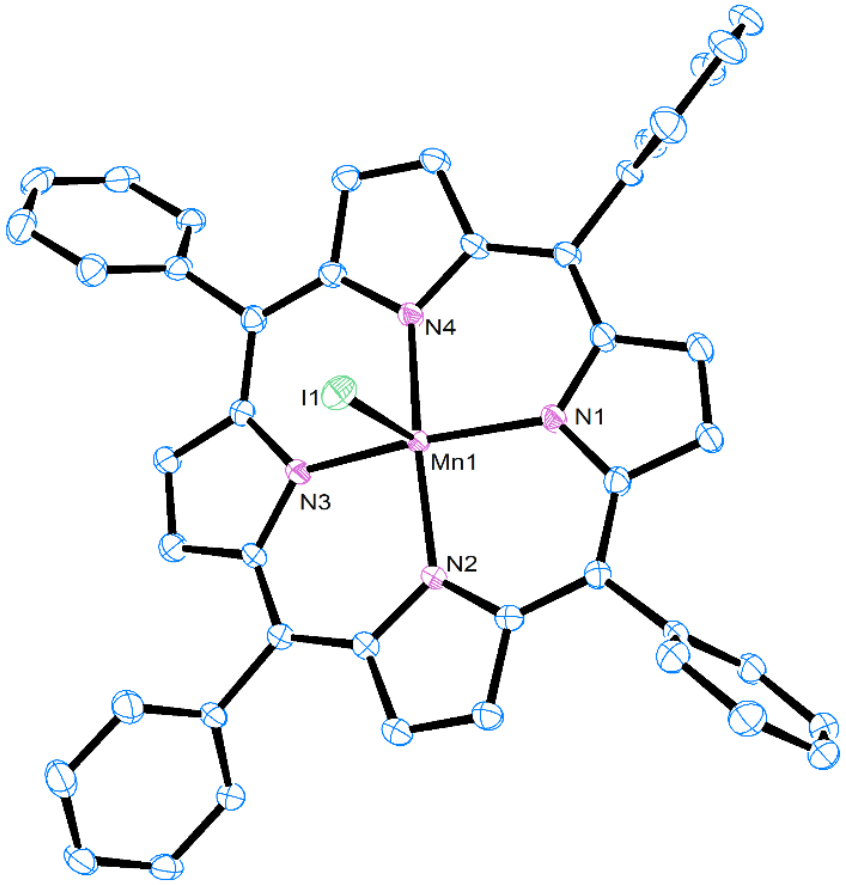


Figure 4.2. ORTEP diagram of Mn(TPP)I in **Mn-I·CHCl$_3$**. $CHCl_3$ and H atoms are omitted.

Table 4.2. Comparison of structural features of Mn(TPP)X (X = Cl, Br, I) and Fe(TPP)X (X = Br, I) complexes[a]

Complex	Temp. (K)	Space Group	Molecules per unit cell	M ion	M–X bond length (Å)[b]	Distance from M to TPP^{2-} plane (Å)[c]	Distance from X to TPP^{2-} plane (Å)[d]
Mn(TPP)Cl (**Mn-Cl**)	293(2)		2	Mn	The reported structure[16] is isomorphous to that of disordered Fe(TPP)Cl.[8-9]		
Mn-Br·$CHCl_3$	100(2)	$P2_1/n$	4	Mn1	2.536	0.236	2.760
Mn-Br·CH_2Cl_2	100(2)	$P2_1/n$	8	Mn1	2.525	0.244	2.762
				Mn2	2.520	0.264	2.775
Mn-Br·toluene	298[144]	$P2_1/m$	2	Mn	2.490	0.295	2.785
Mn-I·$CHCl_3$	100(2)	$P2_1/n$	4	Mn1	2.749	0.235	2.983
Mn-I·$CDCl_3$	293(2)	$P2_1/c$	8	Mn1	2.744	0.232	2.969
				Mn2	2.748	0.225	2.972
Mn-I·1.5CHCl3	100(2)	$P\bar{1}$	4	Mn1	2.742	0.213	2.954
				Mn2	2.784	0.259	3.041
Mn-I·toluene	298[144]	$P\bar{1}$	4	Mn1a	2.767	0.239	3.006
				Mn1b	2.730	0.252	2.979
Fe(TPP)Br (**Fe-Br**)	295[11]	$P2_1/c$	4	Fe1	2.348	0.489	2.837
Fe(TPP)I (**Fe-I**)	293[12]	$P2_1/n$	4	Fe1	2.554	0.459	3.013

[a] Unless cited, the data are from the current work.

[b] Four significant figures of the bond lengths are used here, and estimated standard deviations (esd) are not listed. For the precise bond lengths, see tables listing bond lengths of the structures of the original publications.

[c] The distances here are from the metal ions to the centers of the least-square planes defined by the four N atoms of the TPP^{2-} ligands.

[d] The distances here are from the halide atoms to the centers of the least-square planes defined by the four N atoms of the TPP^{2-} ligands.

complexes have more elongated M−L bonds than low-spin complexes as a result of adding electrons to antibonding $d_{x^2-y^2}$ and/or d_{z^2} orbitals, although the comparison here involves complexes of the same metal ions. Another difference between the structures of Mn(TPP)X and its iron(III) analogs Fe(TPP)X is that the former have smaller distances between the Mn(III) ions and the center of the TPP^{2-} ligand [0.236-0.295 Δ for Mn(TPP)Br (**Mn-Br**) and 0.213-0.259 Δ for Mn(TPP)I (**Mn-I**)] than those [0.489 Δ for Fe(TPP)Br (**Fe-Br**) and 0.459 for Fe(TPP)I (**Fe-I**)] in the latter. In fact, the X^-–TPP^{2-} (center) distances of 2.760-2.785 Δ in **Mn-Br** and 2.954-3.041 Δ in **Mn-I** are similar to 2.837 Δ in **Fe-Br** and 3.013 Δ in **Fe-I**, as shown in Table 4.2. In other words, the shorter Fe−X bond lengths are compensated by the longer Fe−TPP^{2-} (center) distances. Temperatures, affecting crystal structures, are known to change Hirshfeld surfaces and volumes.[8] However, Hirshfeld surfaces and volumes of Mn(TPP)X (surfaces and volumes are 637.8-656.7 $Δ^2$ and 816.6-845.8 $Δ^3$ for **Mn-Br**; 648.7-662.3 $Δ^2$ and 826.6-858.0 $Δ^3$ for **Mn-I**) with different solvents and temperatures [100(2) or 293-298 K] are similar to those of Fe(TPP)X at 293-295 K with no solvent, as shown in Table 4.3 and discussed below. The average lengths of the Mn−N bonds in Mn(TPP)X [between the Mn(III) ions and N atoms in the TPP^{2-} ligands] are similar at 2.002-2.010 Δ. The Mn−N bonds are slightly shorter than 2.066-2.069 Δ of the Fe−N bonds in Fe(TPP)X.

4.2.2. Hirshfeld Surface Analyses

Hirshfeld surface analyses and fingerprint plots of **Mn-Br·$CHCl_3$** (Figures 4.3-4.4) and **Mn-I·$CHCl_3$**, Figures. 4.5-4.6) are discussed below, with the analyses of

Table 4.3. Comparison of Hirshfeld areas, volumes, and void volumes

Complex	Temp. (K)	Space Group	Molecules per unit cell	M ion	Hirshfeld area (Å^2)	Hirshfeld volume (Å^3)	Void volume in the cell volume (%)
Mn-Cl	293(2)		2	Mn	The reported structure[16] is isomorphous to that of disordered Fe(TPP)Cl.[8-9] For Hirshfeld analysis of the disorder in the structure of Fe(TPP)Cl, see Ref. 8.[8]		
Mn-Br·CHCl$_3$	100(2)	$P2_1/n$	4	Mn1	643.0	819.6	12.22
Mn-Br·CH$_2$Cl$_2$	100(2)	$P2_1/n$	8	Mn1	655.7	821.6	11.66
				Mn2	637.8	816.6	
Mn-Br·toluene	298[144]	$P2_1/m$	2	Mn	656.7	845.8	15.79
Mn-I·CHCl$_3$	100(2)	$P2_1/n$	4	Mn1	662.3	849.2	14.12
Mn-I·CDCl$_3$	293(2)	$P2_1/c$	8	Mn1	654.0	850.6	14.63
				Mn2	648.7	846.0	
Mn-I·1.5CHCl$_3$	100(2)	$P\bar{1}$	4	Mn1	656.5	834.8	12.61
				Mn2	651.4	826.6	
Mn-I·toluene	298[144]	$P\bar{1}$	4	Mn1a	657.8	852.0	14.56
				Mn1b	659.4	858.0	

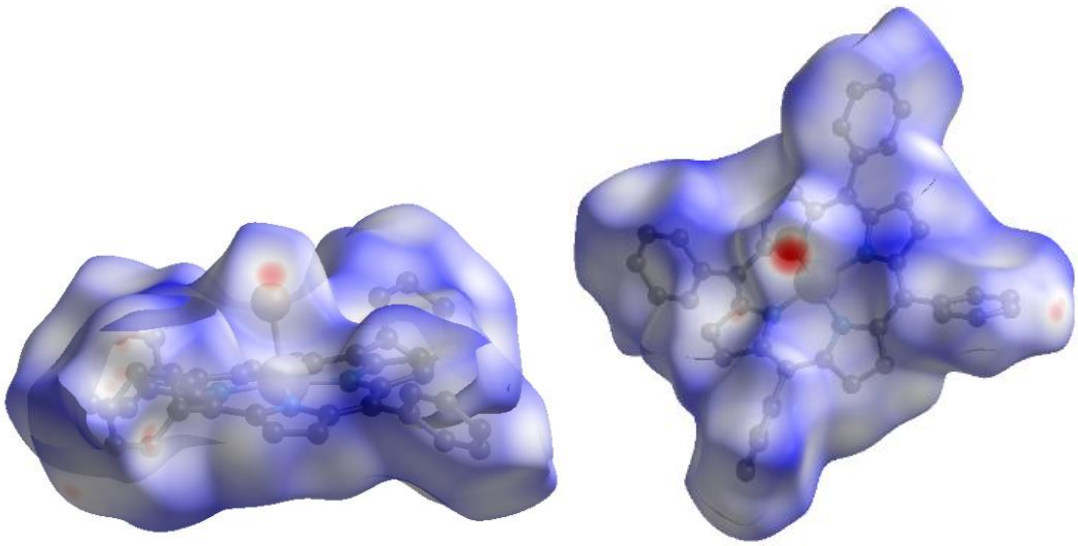


Figure 4.3. Two views of the Hirshfeld surface of **Mn-Br·CHCl$_3$** showing normalized close distances of the pro-molecule and neighboring molecules at 100(2) K.[148] The red-white-blue coloring scheme demonstrates decreasing contacts. Sites of close contacts are shown in red dots. Semi-transparent view reveals the enclosed molecule. Hereafter the same below for the coloring scheme, sites of close contacts and semi-transparent view.

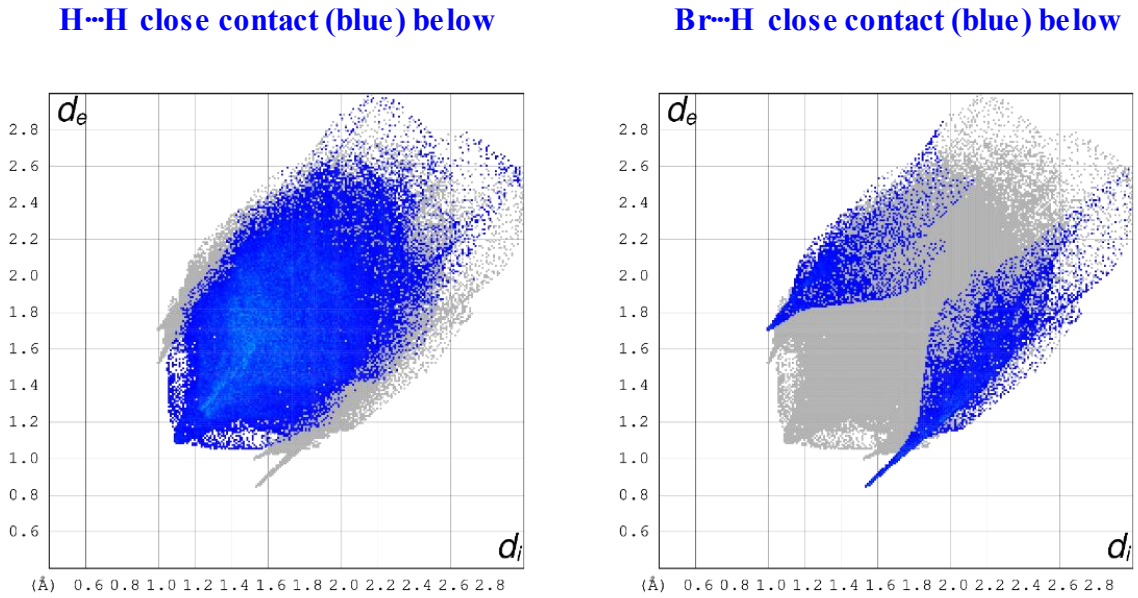


Figure 4.4. Hirshfeld fingerprint plots for **Mn-Br·CHCl$_3$.** The closest contacts correspond to the minimum $d_i + d_e$ values in each plot, hereafter the same below. d_i and d_e are distances from the Hirshfeld surface to the nearest atom *interior* and *exterior* to the surface, respectively.[149]

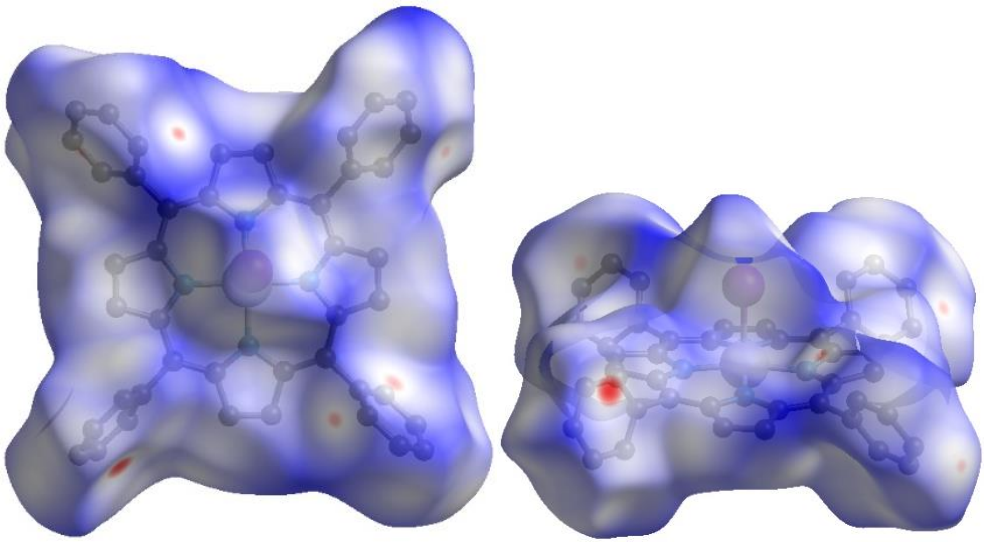
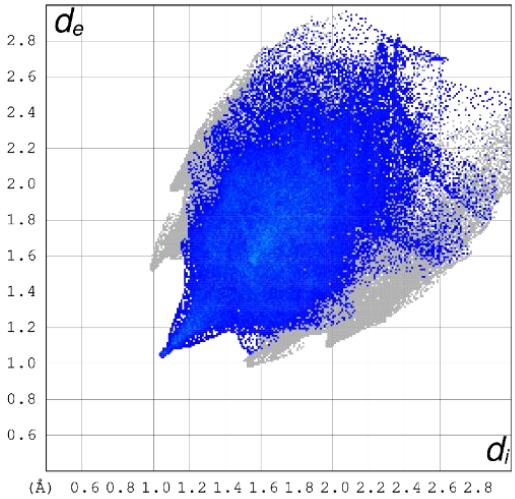


Figure 4.5. Two views of the Hirshfeld surface of **Mn-I·CHCl$_3$** showing normalized close distances of the pro-molecule and neighboring molecules at 100(2) K.[148]

H···H close contact (blue) below



I···H close contact (blue) below

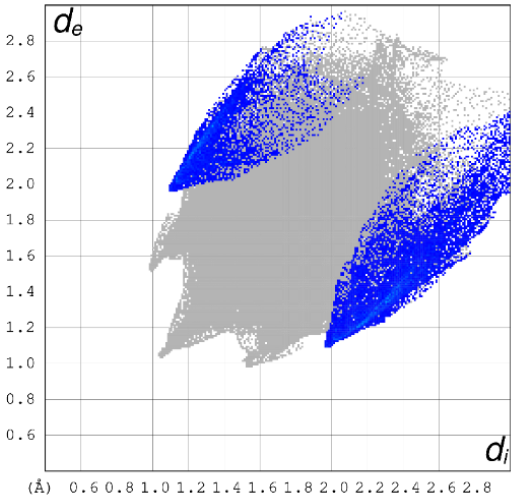


Figure 4.6. Hirshfeld fingerprint plots for **Mn-I·CHCl$_3$.**

Mn-Br·CH_2Cl_2 (Figures C.5-C.6), **Mn-I·$CDCl_3$** (Figures C.10-C.11) and **Mn-I·1.5$CHCl_3$** (Figures C.12-C.13) given in Appendix C. We have conducted Hirshfeld surface analyses of the reported structures of **Mn-Br·toluene** (Figures C.7-C.8) and **Mn-I·toluene** (Figures C.14-C.15). The results are provided in Appendix C. Views of the Hirshfeld surfaces for these structures (e.g., Figures 4.3 and 4.5) show that they all have sites of close contacts (red spots). In addition to a comparison of structure features, percentage contributions to the Hirshfeld surface areas for various intermolecular close contacts for **Mn-Br** and **Mn-I** molecules, respectively, in various crystal structures.

Hirshfeld analyses of the single molecule in the unit cell of Mn(TPP)Br·$CHCl_3$ (**Mn-Br·$CHCl_3$**) in the $P2_1/n$ space group (100 K) give areas and volumes 643.0 Δ^2 and 819.6 Δ^3 (Figure 4.3, Table 4.3), respectively, that are similar to those (637.8-655.7 Δ^2 and 816.6-821.6 Δ^3, Figure C.5, Table 4.3) of the two independent molecules in the unit cell of **Mn-Br·CH_2Cl_2** which is also in the $P2_1/n$ space group (100 K). The two structures also have similar percent void volumes (12.22% and 11.66% for **Mn-Br·$CHCl_3$** and **2·CH_2Cl_2**, respectively). Hirshfeld fingerprint plots in Figures 4.4 and C.6 for **Mn-Br·$CHCl_3$** and **Mn-Br·CH_2Cl_2**, respectively, emphasize close intermolecular interactions. For both structures with different solvent molecules, the H···H and H···Br close contacts involving **Mn-Br** in **Mn-Br·$CHCl_3$** (Figure 4.4) and the Mn1 molecule in **Mn-Br·CH_2Cl_2** (Figure C.6-Top) are fairly similar to each other and to those in **Mn-Br·toluene** at 298 K (Figure C.8) containing non-halogen solvent toluene. The molecules of Mn1 and Mn2 in **Mn-Br·CH_2Cl_2** form pairs of Mn1...Mn1 and Mn2...Mn2 dimers in which the Mn-Br bonds point inwards with each other in each of the dimer units. Br1 in the molecule of Mn1 has close contact to the terminal H atoms on a phenyl ring of the

adjacent Mn1 molecule. In the molecule of Mn2, one of the phenyl groups is facing Br2 with much longer Br2…H(phenyl) distances. The difference in the Hirshfeld fingerprint plots for the Br···H close contacts in Figure C.6 reflects the packing difference of Mn1 and Mn2 molecules in **Mn-Br·CH_2Cl_2**.

Although both Hirshfeld surfaces and fingerprint plots for the structures of **Mn-I·$CHCl_3$** ($P2_1/n$) and **Mn-I·1.5$CHCl_3$** ($P\bar{1}$) determined at 100(2) K reveal sites of close contacts (Figures 4.5 and C.12) and similar H···H and I···H close contacts (Figures 4.6 and C.13), the Hirshfeld surface area (662.3 Δ^2) and volume (849.2 Δ^3) in **Mn-I·$CHCl_3$** are slightly larger than those (651.4-656.5 Δ^2 and 826.6-834.8 Δ^3) of both independent Mn(TPP)I (**Mn-I**) molecules in **Mn-I·1.5$CHCl_3$** (Table 4.3). Structures of both Mn(TPP)I·$CDCl_3$ (**Mn-I·$CDCl_3$** in $P2_1/c$) and **Mn-I·toluene** ($P\bar{1}$)[144] were determined at room temperatures. Since the D atom in $CDCl_3$ has the same electron density as an H atom, the D atom was refined as an H atom. The two independent molecules in the unit cells of both crystals show sites of close contacts (Figures C.10 and C.14). Although the patterns of fingerprint plots for the two are similar, the minimum $d_i + d_e$ I···H/D values of about 2.6-2.7 Δ in **Mn-I·$CDCl_3$** (Figure C.11), indicating the closest I···H/D contacts, are smaller than about 3.0-3.1 Δ in **Mn-I·toluene** (Figure C.15).

4.2.3. Magnetic Susceptibility

DC magnetic susceptibility χ versus temperature T for Mn(TPP)Br·$CHCl_3$ (**Mn-Br·$CHCl_3$**) measured between 2 and 300 K in an applied magnetic field of 0.5 T is given as a plot of $\chi_M T$ versus T in Figure 4.7-Top, yielding effective magnetic moment $\mu_{eff} \approx 5.2$ BM. Volatile $CHCl_3$ molecules in the lattice are expected to be partially (or completely)

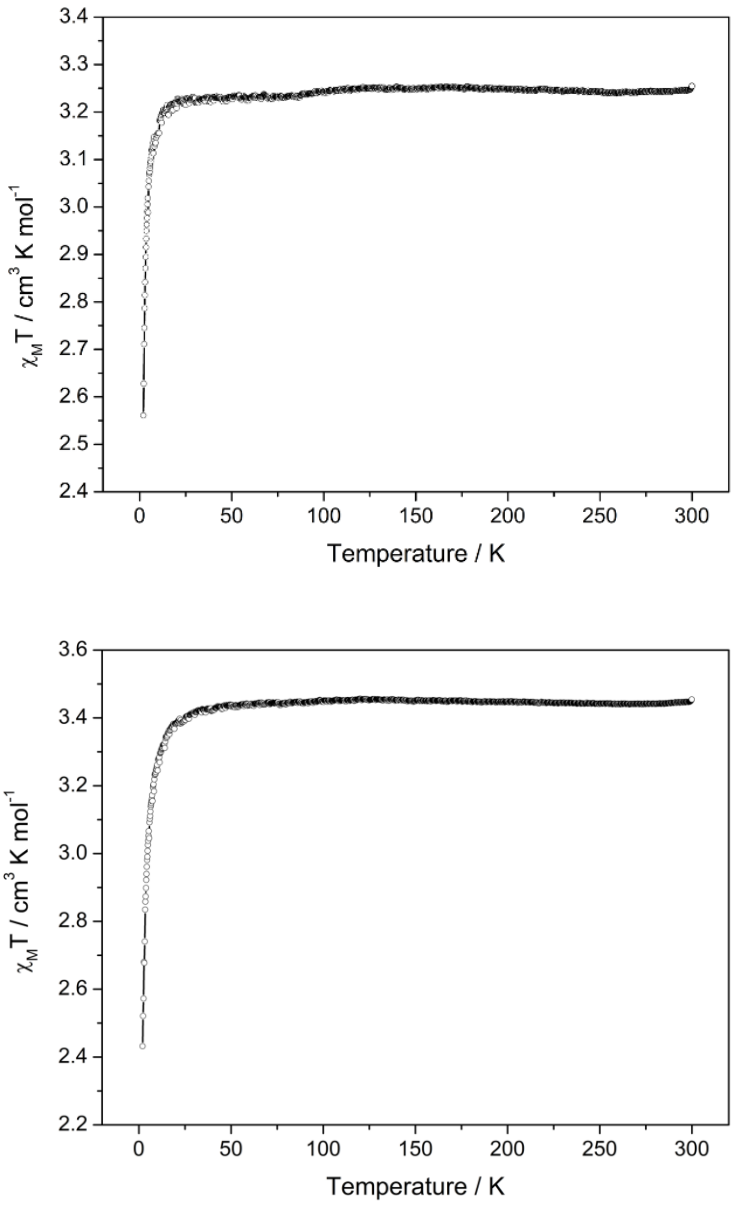


Figure 4.7. Variable-temperature DC susceptibility data under applied DC field of 0.5 T: (Top) **Mn-Br·CHCl$_3$**. (Bottom) **Mn-I·CHCl$_3$.** Fits are included to guide the eye.

removed before and/or in the measurements, as the experiments were conducted under vacuum (~5 torr). If the same data were processed for solvent-free **Mn-Br** as shown in Figure C.17-Top, they gave effective magnetic moment $\mu_{eff} \approx 4.6$ BM. For a spin-only, $S = 2$ complex, $\mu_{eff} = 4.9$ BM is expected. Thus, $\mu_{eff} \approx 5.2$ and 4.6 BM calculated for **Mn-Br·CHCl$_3$** and solvent-free **Mn-Br**, respectively, are about 7% higher and lower than 4.9 BM. The discrepancies here suggest that a significant portion of the solvent $CHCl_3$ molecules in the lattice was removed under vacuum (5 torr) during the measurements. Upon cooling below 20 K, $\chi_M T$ exhibits a sharp decrease from a constant 3.259 $cm^3 \cdot K \cdot mol^{-1}$ to 2.561 $cm^3 \cdot K \cdot mol^{-1}$ at 2 K. This decrease is likely due to ZFS of the Mn(III) ion in the complex, as observed for **Mn-Cl**.[28] An M-H plot of **Mn-Br·CHCl$_3$** is given in Figure C.18-Top. No frequency-dependent out-of-phase signals (χ_M'') were observed with the AC frequency of 1-1488.1 Hz at 1.8 K using 0 or 0.14 magnetic field (Figure C.18-Bottom), suggesting that **Mn-Br·CHCl$_3$** does not exhibit SMM properties.

DC susceptibility data of **Mn-I·CHCl$_3$** give plots such as those in Figure 4.7-Bottom for data at 0.5 T, yielding $\mu_{eff} \approx 5.5$ BM. However, if the same data were processed for solvent-free **Mn-I** (Figure C.17-Bottom), $\mu_{eff} \approx 4.9$ BM. The results suggest that nearly all $CHCl_3$ molecules in **Mn-I·CHCl$_3$** were removed before or during the measurements. Like **Mn-Br·CHCl$_3$**, **Mn-I·CHCl$_3$** exhibits a decrease in $\chi_M T$ from 3.454 $cm^3 \cdot K \cdot mol^{-1}$ to 2.432 $cm^3 \cdot K \cdot mol^{-1}$ upon cooling below 50 K; this may also be attributed to the ZFS of the Mn(III) complex. An M-H plot of **Mn-I·1.5CHCl$_3$** is given in Figure C.19-Top. AC susceptibility measurements of **Mn-I·1.5CHCl$_3$** show no slow magnetic relaxation (Figure C.19-Bottom).

4.2.4. HFEPR

HFEPR response of **Mn-Br·CDCl$_3$** represents powder spectra of an $S = 2$ spin species with moderate negative ZFS on the order of -1 cm^{-1}. Figure 4.8-Top shows a typical spectrum recorded at 10 K, and at the highest end of frequencies used, 322 GHz, along with its simulations. Two more spectra, recorded at lower frequencies, are shown in Figure C.20-Top and Figure C.21-Top in Appendix C. Although the spectra show a presence of more than one species, spin-Hamiltonian parameters for the dominant species could be well established using tunable-frequency EPR methodology,[150] as shown in Figure 4.9-Top. Spin-Hamiltonian parameters obtained from computer fits, and used in the simulations, are collected in Table 4.4. From a visual comparison of the single-frequency spectra and the two cases of simulations for each of them, one for $D < 0$, and the other $D > 0$, it is apparent that D is *negative* in **Mn-Br·CDCl$_3$**.

HFEPR response of **Mn-I·CDCl$_3$** is very different from that of **Mn-Br·CDCl$_3$**. Figure 4.8-Bottom shows a typical spectrum recorded at 10 K, and at the same frequency as the bromide analog, 322 GHz, along with its simulations. Two more spectra, recorded at lower frequencies, are shown in Figure C.20-Bottom and Figure C.21-Bottom in Appendix C. Although the quality of the spectra is somewhat lower than that of **Mn-Br·CDCl$_3$**, and there is noticeable presence of a minority spin species, it is beyond doubt that the sign of D in **Mn-I·CDCl$_3$** is *positive*. In addition, both single-frequency spectra and the 2-D field vs. frequency (energy map) (Figure 4.9-Bottom) show that the g-values in **Mn-I·CDCl$_3$** (1.93-1.97) are markedly lower than 1.99-2.01 which are the usual numbers found in Mn coordination complexes at any oxidation state.

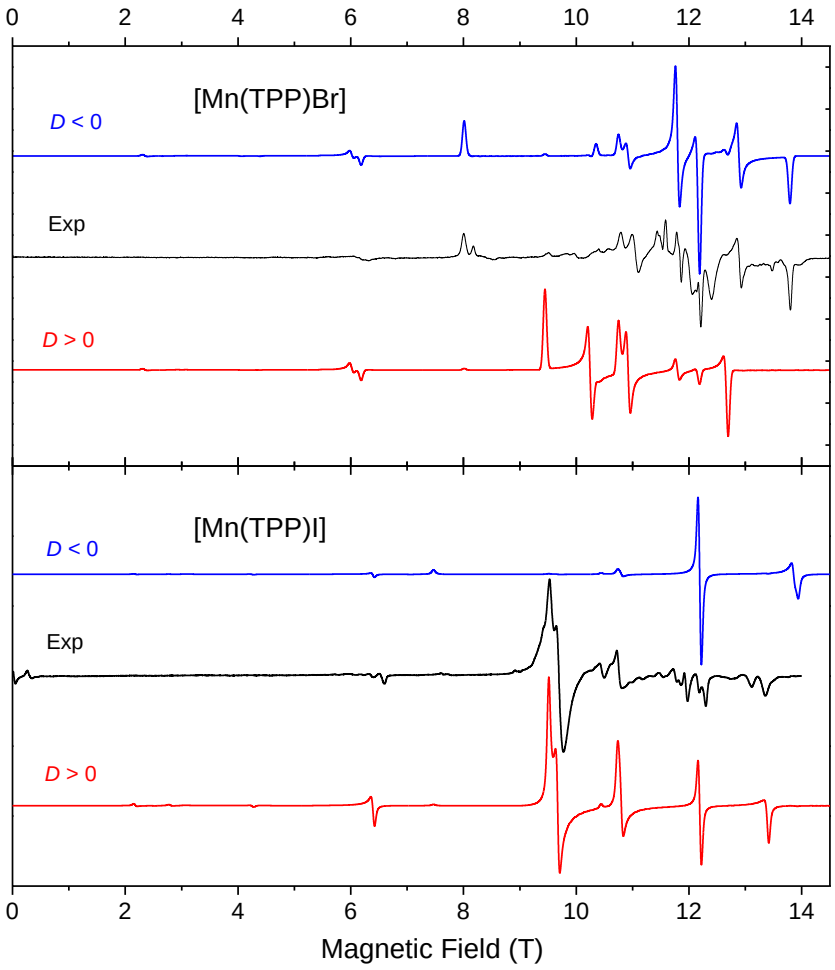


Figure 4.8. HFEPR spectra of Mn(TPP)Br·$CDCl_3$ (**Mn-Br·$CDCl_3$**, Top) and Mn(TPP)I·$CDCl_3$ (**Mn-I·$CDCl_3$**, Bottom) at 10 K and 321.6 GHz (black traces) and their powder-pattern simulations (colored traces). The spin-Hamiltonian parameters used in simulations were the same as in Table 4.4 for **Mn-Br·$CDCl_3$** and slightly adjusted for **Mn-I·$CDCl_3$**: D = +1.34 cm^{-1}, E = +0.013 cm^{-1} (E/D = 0.01); g = [1.965(5), 1.971(10), 1.930(5)]. Blue traces: $D < 0$; red traces: $D > 0$. Two near-zero field resonances in the spectrum of **Mn-I·$CDCl_3$** indicate a minority spin species with ZFS on the order of 4 cm^{-1}, typical for octahedrally-coordinated Mn(III) ions.

Figure 4.9. 2-D field/frequency (energy) maps of turning points in HFEPR spectra of Mn(TPP)Br·$CDCl_3$ (**Mn-Br·$CDCl_3$**) (Top) and Mn(TPP)I·$CDCl_3$ (**Mn-I·$CDCl_3$**) (Bottom, black squares in each case). The curves are simulations using spin-Hamiltonian parameters as in Table 4.4. Red curves: turning points with magnetic field parallel to the *x* axis of the ZFS tensor; blue: $B_0 \parallel y$; black: $B_0 \parallel z$. Off-axis turning points, of which there are several depending on frequency, are not plotted as they were not used in the fits. The vertical dashed lines represent frequencies, at which spectra shown in Figure 4.8-Top, Figure C.20-Top, and Figure C.21-Top for **Mn-Br·$CDCl_3$** and Figure 4.8-Bottom, Figure C.20-Bottom and Figure C.21-Bottom for **Mn-I·$CDCl_3$** are collected.

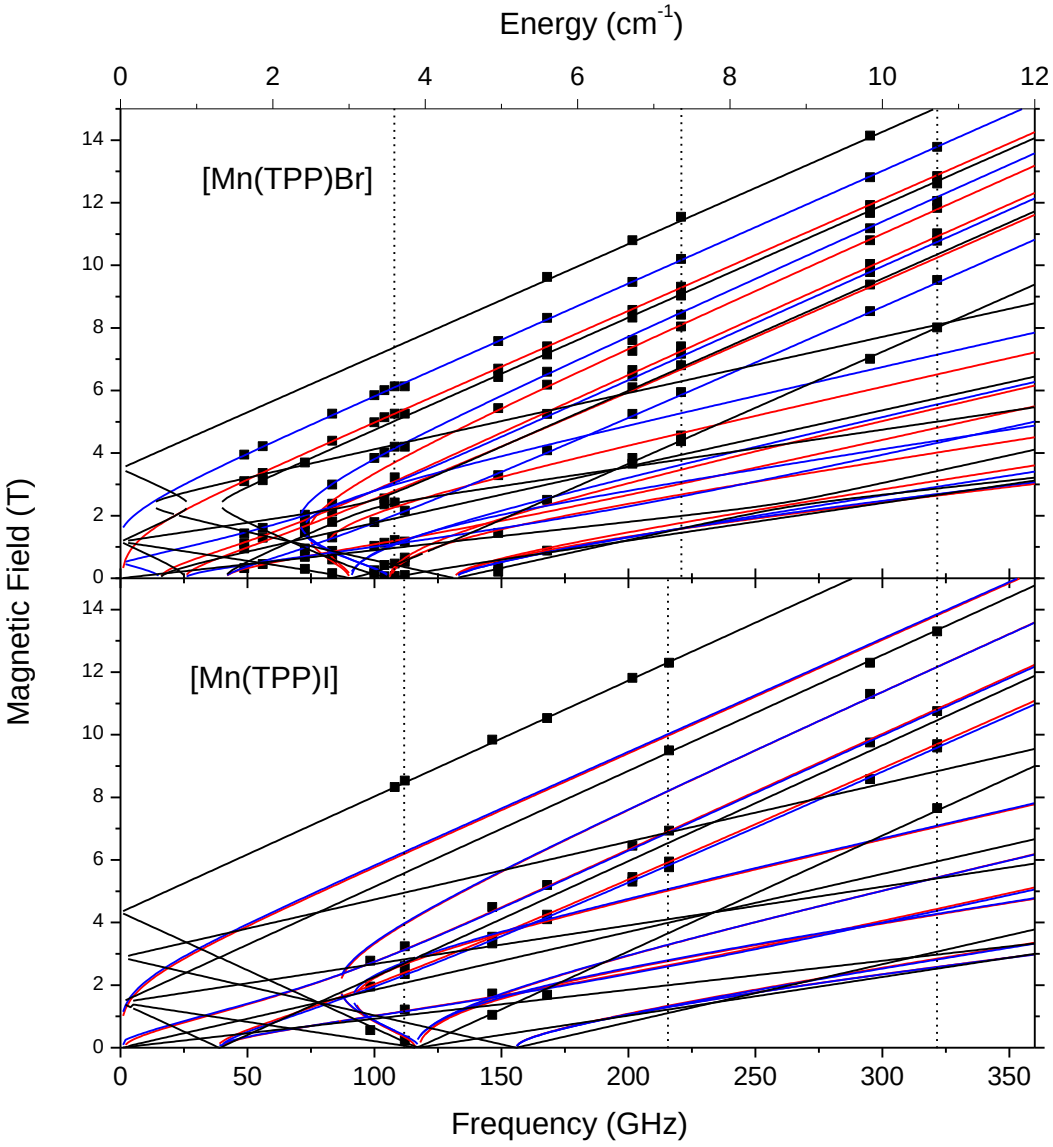

Energy (cm-1)
0
2
4
6
8
10
12
[Mn(TPP)Br]
[Mn(TPP)I]
Magnetic Field (T)
0
2
4
6
8
10
12
14
0
50
100
150
200
250
300
350
Frequency (GHz)

Table 4.4. ZFS parameters of Mn(TPP)X (X = Cl, Br, I) and Fe(TPP)X (X = Br, I) complexes

Complex	Technique	D (cm^{-1})	$\|E\|$ (cm^{-1})	g parameters	Ref. No.
Mn-Cl	HFEPR	-2.290(5)		$g_{\|\|}$ = 1.98(2) $g_{\perp}$ = 2.005(3)	25
	INS[a]	-2.24(3)			9
Mn-Br·$CDCl_3$	HFEPR	-1.091(3)	0.087(2)	g_x = 1.996(4) g_y = 1.985(5) g_z = 1.994(2)	
Mn-I·$CDCl_3$	HFEPR	+1.30(1)	0.010(5)	g_x = 1.965(5) g_y = 1.971(10) g_z = 1.930(5)	
Fe-Br	INS	+8.8(2)	0.1(2)		7
Fe-I	INS	+13.4(6)	0.3(6)		7

[a] Magnetic susceptibility measurements of Mn(TPP)Cl·benzene (**Mn-Cl·benzene**)[27], Mn(TPP)Cl·2benzene (**Mn-Cl·2benzene**)[151] and Mn(TPP)Cl·H_2O (**Mn-Cl·H_2O**)[27] gave D = -2.2(2), -2.3(5), and -2.3(2) cm^{-1}, respectively. The g values for **Mn-Cl·benzene** and **Mn-Cl·H_2O** are 2.01(1) and 2.00(1), respectively.[27]

While molecules of **Mn-Br** and **Mn-I** have 4-fold symmetry, crystals of Mn(TPP)Br·$CHCl_3$ (**Mn-Br·CHCl$_3$**, $P2_1/n$) and Mn(TPP)I·$CDCl_3$ (**Mn-I ·CDCl$_3$**, $P2_1/c$) do not have 4-fold symmetry. Although the structure of **Mn-Br·CDCl$_3$** used for the HFEPR studies was not directly determined, it is expected to be in a monoclinic space group. Since in monoclinic unit cells, $x \neq y$, additional ZFS occurs, as shown in Eq. 1.5 in Chapter I. Thus, in addition to axial ZFS parameters D, both **Mn-Br·CDCl$_3$** and **Mn-I·CDCl$_3$** have rhombic ZFS parameters E, as observed in the HFEPR spectra.

4.2.5. INS

In neutron scattering processes, the incident neutrons are scattered from interactions with either atomic nuclei or unpaired electrons in the sample.[62, 152-153] The cross section of magnetic scattering, from the interactions between neutron spins and electron spins, corresponds to the number of neutrons scattered per second due to the magnetic interaction into a solid angle $d\Omega$ with energy transfer between $\eta\omega$ and $\eta(\omega + d\omega)$ divided by the flux of the incident neutrons. If unpolarized neutrons are scattered from identical magnetic ions with localized electrons, the magnetic scattering cross section for spin-only scattering is expressed by Eq. 4.1:[7, 152, 154]

$$\frac{d^2\sigma}{d\Omega d\omega} = (\gamma r_0)^2 \frac{k_f}{k_i}\left[\frac{1}{2} gF(Q)^2 e^{-2W(Q)} \sum_{\alpha,\beta}\left(\delta_{\alpha\beta} - \frac{Q_\alpha \cdot Q_\beta}{Q^2}\right) S^{\alpha\beta}(Q,\omega)\right] \quad \text{(Eq. 4.1)}$$

where σ = neutron cross section; γ = gyromagnetic ratio; r_0 = classical radius of an electron; g = Landé g-factor; $F(\boldsymbol{Q})$ = dimensionless magnetic form factor defined as the Fourier transform of the normalized spin density associated with magnetic ions; $e^{-2W(\boldsymbol{Q})}$ = Debye-Waller factor caused by thermal motion; $S^{\alpha\beta}(\boldsymbol{Q},\omega)$ = magnetic scattering

function; $\left(\delta_{\alpha\beta} - \frac{\boldsymbol{Q}_\alpha \boldsymbol{Q}_\beta}{Q^2}\right)$ = polarization factor which implies neutrons can only couple to magnetic moments or spin fluctuations perpendicular to $\boldsymbol{Q}$; $\eta\omega$ = energy change experienced by the sample; ω = angular frequency of neutron.

Some neutrons transfer energies with the sample during the scattering process, thus changing both their direction and energy in what is thus inelastic neutron scattering (INS). There are two types of INS instruments, *direct-geometry* and *indirect-geometry* time-of-flight (TOF) spectrometers. Their features and use for coordination chemistry research have been reviewed.[62] In a direct-geometry spectrometer, the selected incident energy E_i is fixed (monochromatic) and final energy E_f is measured by TOF to determine the energy transfer (E_i - E_f).[62, 152] CNCS used in the current work is a direct-geometry instrument.[62, 84-85, 155-156]

The variable-temperature INS spectra of Mn(TPP)Br·$CDCl_3$ (**Mn-Br·$CDCl_3$**) in Figure 4.10-Top confirm that its *D* value is negative, as for Mn(TPP)Cl (**Mn-Cl**).[9] The easy-axis ZFS ($D < 0$) was identified for **Mn-Br·$CDCl_3$** based on temperature dependence of the neutron energy loss (right) side of the spectra. The peaks centered around +3.3 cm^{-1} (= ~3*D*) are present at low temperatures while the peaks at about +0.8 to +1.4 cm^{-1} (= ~*D*) become stronger as the temperature is increased to 25 K. This is expected for an easy-axis ($D < 0$) system, as shown in Figure 1.3-Right in Chapter I. The multiple peaks around +3.3 cm^{-1} are consistent with the presence of rhombic parameter *E* for **Mn-Br·$CDCl_3$**. From the INS data, if $E = 0$, $D = -1.07$ cm^{-1}. This is close to the parameters from HFEPR: $D = -1.091(3)$ cm^{-1} and $|E| = 0.087(2)$ cm^{-1} discussed above.

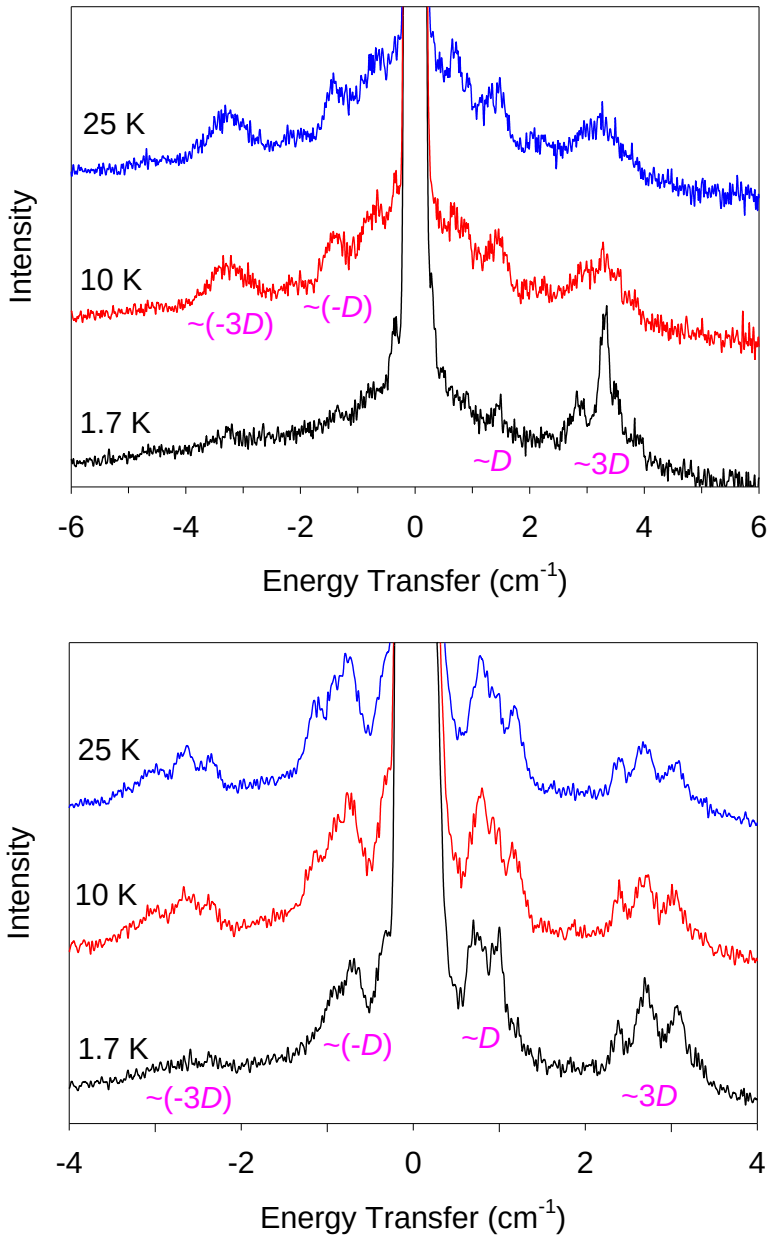


Figure 4.10. INS spectra of **Mn-Br·CDCl$_3$** (Top) and **Mn-I·CDCl$_3$** (Bottom) at 1.7, 10 and 25 K. The *E* parameter leads to the splitting of the INS peaks.

Variable-temperature INS spectra of **Mn-I** in **Mn-I·CDCl$_3$** (Figure 4.10-Bottom) point to an easy-plane ($D > 0$) compound based on the neutron energy gain (left) side of the spectra. The peaks around –0.8 to –1.1 cm^{-1} [= ~(-D)] are present at low temperatures while the peaks around –2.4 to –3.3 cm^{-1} [= ~(-3D)] become stronger as the temperature is increased to 25 K. This is expected for an easy-plane ($D > 0$) system (Figure 1.3-Left). At lower temperatures of 1.7 and 10 K, most molecules are at the $M_S = 0$ and ±1 states. Relaxation from the $M_S = \pm 1$ states to $M_S = 0$ state gives the peaks around –0.8 to –1.1 cm^{-1}. When the temperature is at 25 K, more molecules are at the $M_S = \pm 2$ states which relax back to the $M_S = \pm 1$ states, making the higher energy peaks around –2.4 to –3.3 cm^{-1} stronger. The multiple INS peaks, such as those around ~D and ~3D, are consistent with the presence of rhombic parameter E for **Mn-I·CDCl$_3$**. If $E = 0$, the INS spectra gave $D \approx 0.90$ cm^{-1}. Although the value is close $D = 1.30$ cm^{-1} and $E = 0.01$ cm^{-1} by HFEPR discussed above, the result also demonstrates that E, although small, is critical here.

It is interesting to point out the trend in D values for **Mn-Cl**, **Mn-Br**, and **Mn-I**: −2.24, −1.09, and +1.30 cm^{-1}, respectively.[9] The degree of axial anisotropy decreases from the chloride to the bromide analog. Such decreases of axial anisotropy from chloride to bromide analogs have been reported in other Mn(III) chlorides and bromides such as Mn(Me$_2$dbm)X (X = Cl, Br; Me$_2$dbm$^-$ = anion of 4,4'-dimethyldibenzoylmethane) and Mn(OEP)X (X = Cl, Br; OEP^{2-} = 2,3,7,8,12,13,17,18-octaethylporphinate).[157] A qualitative summary of the studies is given here. For the Mn(III) chloride and bromide complexes such as Mn(OEP)X, the second-order spin-orbital couplings of the four

unpaired electrons in the ground electronic quintet state are with the excited electronic states from d-d transitions in the Mn(III) ion.[25, 157-158] Such ZFS generates easy-axis (D < 0) ZFS states, as the equatorial ligand field between the Mn(III) ion and the four N atoms of the OEP^{2-} ligand dominates the spin-orbital couplings. Since both Cl^- and Br^- complexes have the same equatorial ligand OEP^{2-}, the axial ligand field (along the Mn–X axis) determines the magnitude of the $|D|$. This decrease in $|D|$ is primarily due to a weaker axial ligand field for the Br^- complex than its Cl^- analog.[157] We think the decrease in $|D|$ from **Mn-Cl** to **Mn-Br** is similar to those in Mn(Me_2dbm)X and Mn(OEP)X.

How is it that the iodide analog **Mn-I** becomes an easy-plane (D > 0) complex? Such a change from easy-axis (D < 0) to easy-plane (D > 0) between metal halide analogs has been reported in Mn(III) complexes *trans*-[Mn(cyclam)Br_2]Br (cyclam = 1,4,8,11-tetraazacyclotetradecane) and *trans*-[Mn(cyclam)I_2]I.[129] The positive D value for the iodide analog here is attributed to the presence of ligand-to-metal charge transfer (LMCT) from the lone pair electrons on I^- ions (in *trans*-[Mn(cyclam)I_2]$^-$) to a 3d orbital of the Mn(III) ion, generating low-lying excited electronic LMCT states with atomic iodine character. The second-order spin-orbital interactions of the four unpaired electrons in the ground electronic quintet state of *trans*-[Mn(cyclam)I_2]$^-$ are primarily mediated by spin-orbit coupling, which is very large for iodine, with the excited electronic LMCT states, leading to the unique easy-plane (D > 0) zero-field splitting (ZFS) states.[129] In other words, ZFS in **Mn-Cl** and **Mn-Br** are mainly the results of ligand fields on the metal ions, while ZFS in **Mn-I** reflects the participation of LMCT.

4.3. Experimental Methods

4.3.1. Synthesis of Mn-Br and Mn-I

Mn-Br and **Mn-I** were prepared by the literature procedure from the exchange reactions between Mn(TPP)(acetate), which was obtained from the reaction of $Mn(CH_3CO_2)_2$ with H_2TPP, and NaX (X = Br, I) in mixed $CHCl_3$-water.[159] $Mn(CH_3CO_2)_2{\cdot}(H_2O)_4$ (99+%) from Acros Organics, H_2TPP from Frontier Scientific, NaBr (Fisher Scientific, Certified ACS), NaI (Fisher Scientific), N,N-dimethylformamide (Fisher Scientific, Certified ACS) and $CHCl_3$ (Fisher Scientific, Certified ACS) were used as received. Deionized water was obtained in house.

We also prepared Mn(TPP)F by the reported method.[159] However, repeated attempts to purify the product by crystallization failed to yield crystals of Mn(TPP)F. Unlike Mn(TPP)X (X = Cl, **Mn-Cl**; Br, **Mn-Br**; I, **Mn-I**), Mn(TPP)F was found to have low solubility in solvents we tested, including $CHCl_3$ and CH_2Cl_2. Mn(TPP)F may have a polymeric structure, as some other fluoride-bridged complexes.[160] It was not studied further in the current work.

4.3.2. Crystallization

$CHCl_3$ (Fisher Scientific, Certified ACS), CH_2Cl_2 (Fisher Scientific, Certified ACS), pentane (Fisher Scientific, Certified ACS) and $CDCl_3$ (Cambridge Isotope Laboratories, 99.8% deuterium) were used in the crystallization.

Complex **2** was dissolved in either $CHCl_3$ or $CDCl_3$ and crystals of **Mn-Br·CHCl₃** or **Mn-Br·CDCl₃** grew from concentrated solutions at 23 °C.

Crystals of **Mn-Br·CHCl$_3$** were dissolved in a minimal amount of CH_2Cl_2. The solution was left open to air at -33 °C, and crystals of **Mn-Br·CH$_2$Cl$_2$** were harvested from the concentrated solution after several days.

Crystals of **Mn-I·1.5CHCl$_3$** were dissolved in a minimal amount of $CHCl_3$ and layered with pentane. Slow mixing of the solvents at room temperature over five days afforded dark green crystals of **Mn-I·CHCl$_3$** suitable for single-crystal X-ray analysis.

Newly prepared **3** was dissolved in $CDCl_3$ and crystals of **Mn-I·CDCl$_3$** were obtained from the concentrated solution at 23 °C.

Impure crystals of **Mn-I·1.5CHCl$_3$** were dissolved in $CHCl_3$ and stored at either -33 or 23 °C for recrystallization. Dark green, plate-like crystals of **Mn-I·1.5CHCl$_3$** suitable for X-ray analysis were harvested from the concentrated solution.

4.3.3. Single Crystal X-ray Diffraction

Single-crystal X-ray diffraction studies of **Mn-Br·CHCl$_3$**, **Mn-Br·CH$_2$Cl$_2$**, **Mn-I·CHCl$_3$** and **Mn-I·1.5CHCl$_3$** were conducted on a Bruker D8 Venture diffractometer equipped with a Photon 100 detector (Mo K_α radiation, $\lambda = 0.71073$ Å). For data collection, a suitable crystal was coated in Paratone oil, mounted on a Mitegen loop, and placed in a cold stream of nitrogen (100 K) generated by an Oxford Cryostream low-temperature apparatus. Frames were collected using the Apex 3 program. The diffraction data were reduced using Bruker SAINT and corrected for absorption with the SADABS multiscan program. The molecular structures were solved with SHELXT and refined with SHELXL-2015.

Single-crystal X-ray diffraction data for **Mn-I·CDCl$_3$** were collected on a Bruker ASX Smart 1000 diffractometer with a CCD area detector (Mo K_α radiation, $\lambda = 0.71073$ Å). A suitable crystal was mounted on a goniometer and the data were collected at 293(2) K. Frames were collected using the Apex2 program. Data were reduced using Bruker SAINT and corrected for absorption with the SADABS multiscan program. The molecular structure was solved with SHELXS and refined with SHELXL-2014.

Mn-Br·CH$_2$Cl$_2$ crystallizes in the space group $P2_1/n$. There are two Mn(TPP)Br molecules and two CH_2Cl_2 solvent molecules located in general positions of the monoclinic cell. The molecules of **Mn-Br** form pairs of closely packed Mn(TPP)Br dimers. One of the two CH_2Cl_2 molecules in the cavities is disordered in two positions with a site-occupancy ratio of 0.751(4) : 0.249(4).

Mn-I·CDCl$_3$ crystallizes in the space group $P2_1/c$. There are two Mn(TPP)I and two solvent molecules located in the asymmetric unit of the monoclinic cell. One of the $CDCl_3$ molecules is disordered in three positions with a site-occupancy ratio of 0.328(3) : 0.368(3) : 0.304(3).

Mn-I·1.5CHCl$_3$ crystallizes in the space group P-1. There are two Mn(TPP)I molecules located in the asymmetric unit of the triclinic cell. All three chloroform molecules were found disordered in two positions. One displayed about 9.5 degree rotation of the chlorine atoms along the C-H bond with a refined occupancy ratio of 0.814(4) : 0.186(4). Another one showed a displacement less than 1 Å from the main component with 0.325(2) site occupancy. The third chloroform molecule was found disordered around the center of inversion with a site-occupancy ratio of 0.519(1) : 0.481(1).

4.3.4. Hirshfeld Surface Calculations

Hirshfeld surfaces were calculated using CrystalExplorer (version 17) software from the crystal-structure coordinates supplied in the format of crystallographic information file (CIF).[161] The X-ray CIF files of **Mn-Br·CHCl$_3$** (CCDC 1977356), **Mn-Br·CH$_2$Cl$_2$** (CCDC 1977357), **Mn-I·CHCl$_3$** (CCDC 1977355), **Mn-I·CDCl$_3$** (CCDC 1977353) and **Mn-I·1.5CHCl$_3$** (CCDC 1977354) from the current work and **Mn-Br·toluene** (CCDC 1168698)[144] and **Mn-I·toluene** (CCDC 1168699)[144] in the literature were used. Hirshfeld surfaces were calculated at an isovalue of 0.5 e au^{-3}. Void volumes were calculated using an isovalue of 0.002 e au^{-3}.[162] To perform calculations on disordered structures of **Mn-Br·CH$_2$Cl$_2$**, **Mn-I·CDCl$_3$**, and **Mn-I·1.5CHCl$_3$**, atomic coordinates with minor partial site occupancies were removed, and the CIF files were regenerated with only atomic coordinates and U^{ij} displacement parameter values.

4.3.5. Susceptibility Measurements

Measurements of DC susceptibilities of **Mn-Br·CHCl$_3$**, **Mn-I·CHCl$_3$** and Mn(TPP)F were conducted at the University of Tennessee on a Quantum Design MPMS SQUID VSM (Magnetic Property Measurement System Superconducting Quantum Interference Device Vibrating Sample Magnetometer) at the temperature range of 2-300 K within an applied external DC magnetic field of 0.5 T.

Measurements of AC susceptibilities of **Mn-Br·CHCl$_3$** and **Mn-I·1.5CHCl$_3$** were conducted at the Center for Nanophase Materials Sciences (CNMS), Oak Ridge National Laboratory (ORNL) on a Quantum Design Magnetic Property Measurement System XL (MPMS-XL) magnetometer with a 7-T magnet. AC susceptibility measurements were

performed at 2.2-7.7 K for **Mn-Br·CHCl$_3$** and **Mn-I·1.5CHCl$_3$** under vacuum with a bias DC field of 0.14 T and 2.74 Oe driving amplitude.

4.3.6. HFEPR Studies of Mn-Br·CDCl$_3$ and Mn-I·CDCl$_3$

HFEPR measurements were made using a spectrometer described elsewhere[134], with the exception of a solid-state source from Virginia Diodes (Charlottesville, VA). The samples were investigated as pellets mixed with *n*-eicosane. HFEPR spectra were simulated, and computer fits performed, with the program SPIN from A. Ozarowski, using a standard spin-Hamiltonian for $S = 2$, with only second-order ZFS terms included.

4.3.7. INS Studies of Mn-Br·CDCl$_3$ and Mn-I·CDCl$_3$

INS measurements were carried out on Cold Neutron Chopper Spectrometer (CNCS), Spallation Neutron Source (SNS) at ORNL. CNCS is a direct geometry, time-of-flight spectrometer that receives a beam from a coupled cryogenic H_2 moderator.[62] Four chopper assemblies were used to select energy of neutrons at CNCS. The speeds and slit widths of the choppers can be varied, allowing adjustments in the instrumental resolution and intensity of the incident beam.

Approximately 500 mg of each sample of **Mn-Br·CDCl$_3$** and **Mn-I·CDCl$_3$** was loaded into a 1.27-cm-thick aluminum tube which was mounted on a sample holder mounted in a standard liquid helium cryostat with a base temperature of T = 1.7 K. An oscillating radial collimator was used to reduce background scattering form the tail of the cryostat. Vanadium was used as a standard for the detector efficiency correction.

Measurements were performed at 1.7, 10, and 25 K with incident neutron beam energy $E_i = 8.07$ cm^{-1}. E_i was chosen to cover the anticipated region of interest in both the

energy *E* and scattering-vector *Q* space.[152, 154] The small incident energy is especially important to observe excitations near the elastic peak (at energy transfer close to 0 cm^{-1}) as the full-width-at-half-maximum (FWHM) of the elastic peak, which is typically 1.5-2% of the incident energy, would be narrow, giving better energy resolution. It took approximately 20 h to run the two samples at various temperatures. Data were then reduced and analyzed using the DAVE (Data Analysis and Visualization Environment) program package.[90]

CHAPTER V

STUDIES OF MAGNETIC AND PHONON MODES OF METALLOPORPHYRINATES Fe(TPP)X (X = F, Cl, Br, I) VIA INELASTIC NEUTRON SCATTERING

5.1. Abstract

Vibrational spectra of *meso*-tetraphenylporphyrinates Fe(TPP)X (X = F, **Fe-F**; Cl, **Fe-Cl**; Br, **Fe-Br**; I, **Fe-I**; TPP^{2-} = *meso*-tetraphenylporphyrinate) have been collected on the VISION spectrometer at Spallation Neutron Source (SNS) at Oak Ridge National Laboratory (ORNL) and are presented here. In addition, INS of Fe(TPP-d_{28})Cl (**Fe-Cl-*d*$_{28}$**) has been collected to determine the degree of signal enhancement due to deuteration compared to protio **Fe-Cl**, affording a 3.4(2)-fold increase in the $M_S = \pm 1/2 \rightarrow \pm 3/2$ transition peak intensity. Phonon symmetries, phonon movies, and spin densities are presented for **Fe-Cl** and **Fe-Cl-*d*$_{28}$** for comparison.

5.2. Results and Discussion

meso-Tetraphenylporphyrinates Fe(TPP)X (X = F, **Fe-F**; Cl, **Fe-Cl**; Br, **Fe-Br**; I, **Fe-I**; TPP^{2-} = *meso*-tetraphenylporphyrinate) are d^5 square pyramidal complexes with S = 5/2 that can serve as models for hemes. Neutron scattering is a unique technique to probe magnetic properties, as spins of neutrons interact with spins of electrons in molecules during the scattering processes.[62] Inelastic neutron scattering (INS), leading to magnetic excitations, has been used to study paramagnetic compounds and single-molecule magnets.[62, 154, 163] However, use of neutron scattering in the studies of magnetic properties of biological or biomimetic systems is limited.[7, 9, 19]

Inelastic neutron scattering spectra were collected for the **Fe-X** series to fully characterize the phonon modes at varying temperatures from 5-125 K and determine magnitudes of ZFS splittings. Phonons refer to both external (intermolecular) and internal (intramolecular) vibrational modes in the solid. Internal modes are molecular

vibrations,[164] while external modes are lattice vibrations.[84] Internal and external modes often couple as they originate from the same governing equations.[84, 164] Thus, both external and internal modes are referred to as phonons.

5.2.1. INS, Phonon Animations, and Spin Densities of Fe-Cl and Fe-Cl-d_{28}

5.2.1.1. INS of **Fe-Cl** and **Fe-Cl-d_{28}**

To supplement understanding of **Fe-Cl** in the **Fe-X** series, INS was used to study the magnetic and phonon features of fully deuterated Fe(TPP-d_{28})Cl (**Fe-Cl-d_{28}**), as **Fe-Cl** and **Fe-Cl-d_{28}** are an ideal pair to compare magnetic peaks in the INS spectra. Additionally, the substitution of protons for heavier deuterium atoms in **Fe-Cl-d_{28}** is expected to change the frequencies of many phonon peaks.

Variable-temperature, indirect geometry INS results for **Fe-Cl** are given in Figure 5.1. **Fe-Cl** has been studied extensively via direct-geometry INS (Figure 1.8b) to directly observe ZFS[9] and, in Chapter II of this dissertation, to reveal intramolecular spin-spin interactions among Fe^{3+} metal centers. The axial ZFS parameter D has been previously measured via magnetic susceptibility,[165-168] far-IR,[169] NMR,[170] Mössbauer,[171] magnetic circular dichroism,[172] and EPR spectroscopies,[173] with results varying from D = 3.2 to 11.9 cm^{-1}. In 2014, D was determined to be +6.33(8) cm^{-1} by direct geometry INS at 20 K. With S = 5/2 and $D > 0$, magnetic ZFS transitions occur between (a) the ground M_S = ±1/2 and first excited M_S = ±3/2 states, separated by 2D and (b) the first and second excited M_S = ±3/2 and M_S = ±5/2 states, respectively, separated by 4D (Figure 1.2b). At 20 K, both the ground and first excited states are partially populated, allowing for observation of two magnetic peaks at 12.65(8) cm^{-1} (= 2D) and 25.60 cm^{-1} (= 4D).

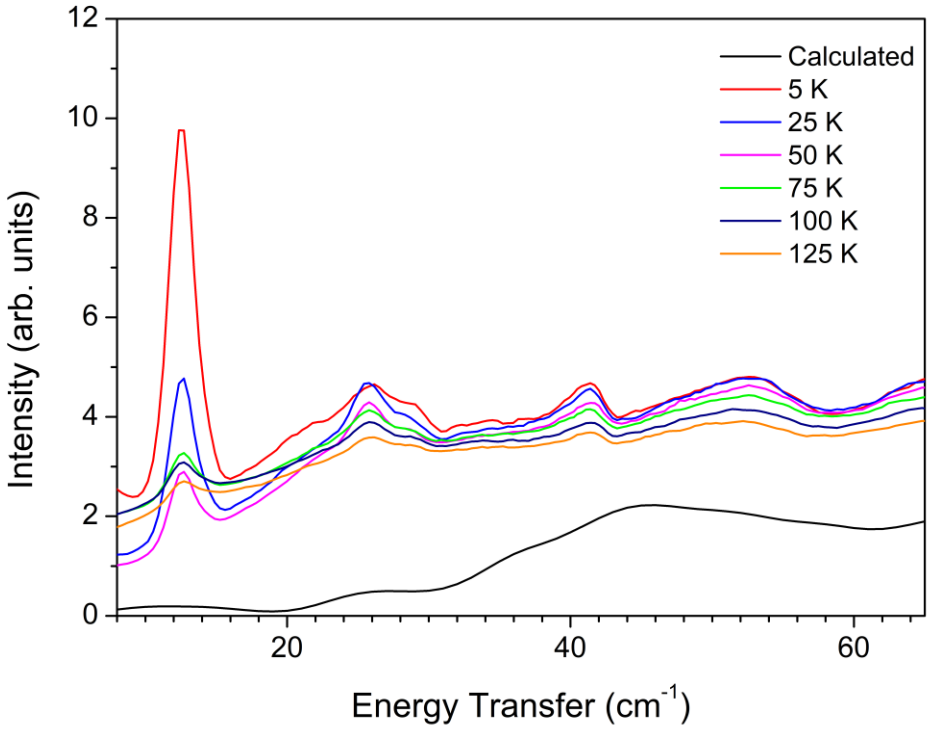


Figure 5.1. VT-INS forward-scattered spectra of **Fe-Cl** with VASP-calculated phonon spectrum (black). The full phonon spectrum (10-1600 cm^{-1}) is given in Figure D.1 in Appendix D. All spectra are Bose-corrected.

At 5 K, shown as a red line in Figure 5.1, both magnetic peaks appear in the Bose-corrected, forward-scattered INS data of **Fe-Cl**, and the $M_S = \pm 1/2 \rightarrow \pm 3/2$ transition at 12.55 cm^{-1} is roughly two times the intensity of the $M_S = \pm 3/2 \rightarrow \pm 5/2$ transition at ~25.76 cm^{-1} due to the relative Boltzmann distributions of the initial states. As these Gaussian peaks are magnetic in nature, they are not represented in the VASP-calculated phonon spectrum (black line in Figure 5.1). For the full phonon spectrum, particularly above 100 cm^{-1} (Figure D.1), VASP recreates the experimental phonon spectrum, though these modes are slightly shifted to lower energies from the experimental results.

Variable-temperature INS data for **Fe-Cl-*d*$_{28}$** is given in Figure 5.2. At 5 K, only the $M_S = \pm 1/2 \rightarrow \pm 3/2$ transition at 12.49 cm^{-1} is visible; this disparity compared to **Fe-Cl** could be due to a difference in sample mass (~0.20 g of **Fe-Cl-*d*$_{28}$** compared to ~0.50 g of **Fe-Cl**). However, relative to the intensities of the magnetic peaks, the spectra of **Fe-Cl** show much more intense background noise than **Fe-Cl-*d*$_{28}$**, in part due to the incoherent neutron scattering of its H atoms. At 25-125 K, the $M_S = \pm 3/2 \rightarrow \pm 5/2$ peak appears at 25.51 cm^{-1}, though it decreases in intensity at temperatures higher than 50 K due to a decreasing Boltzmann population as higher energy states are occupied.

When the spectrum of **Fe-Cl-*d*$_{28}$** is scaled to account for the difference in sample masses, a comparison of the first transition ($M_S = \pm 1/2 \rightarrow \pm 3/2$) at ~12.7 cm^{-1} shows that the peak in the perdeuterated **Fe-Cl-*d*$_{28}$** is 3.2(2) times stronger than that in protio **Fe-Cl**. No phonons are observed near the peaks at ~12.7 cm^{-1} in either spectrum. This is, to our knowledge, a rare comparison of a magnetic transition in INS between protio and perdeutero isotopologues, showing the degree of the enhancement through deuteration.

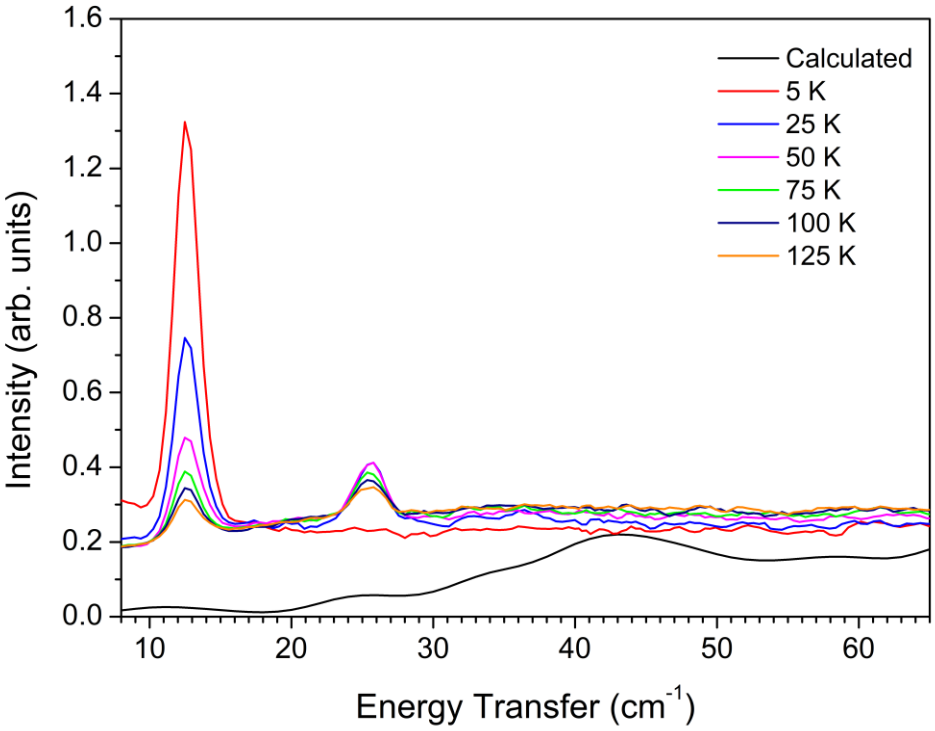


Figure 5.2. VT-INS forward-scattered spectra of **Fe-Cl-*d*$_{28}$** with VASP-calculated phonon spectrum (black). The full phonon spectrum (10-1600 cm^{-1}) is given in Figure D.2 in Appendix D. All spectra are Bose-corrected.

5.2.1.2. Calculated Phonon Symmetries and Energies of **Fe-Cl** and **Fe-Cl-*d*$_{28}$**

VASP-calculated phonon symmetries and energies <75 cm^{-1} of **Fe-Cl** and **Fe-Cl-*d*$_{28}$** are listed in Table 5.1. The full lists of calculated phonon energies/symmetries are included in Tables D.1-D.2 in Appendix D. It is apparent in Table 5.1 that phonons of **Fe-Cl** are shifted towards higher energies compared to corresponding **Fe-Cl-*d*$_{28}$** phonons, as the vibrational frequency of two bonded atoms is inversely proportional to their reduced mass μ, and the heavier deuterium atoms of **Fe-Cl-*d*$_{28}$** give a greater μ than protons of **Fe-Cl**. As such, the phonons of **Fe-Cl-*d*$_{28}$** are 4.5-9.0% lower in energy than the phonons of **Fe-Cl** in Table 5.1. It perhaps should be noted that, in Figure 5.2 of **Fe-Cl-*d*$_{28}$**, none of the calculated phonons in Table 5.1 are readily apparent in the spectrum. This is likely due to a combination of (a) the low sample mass and (b) a lack of incoherent neutron scattering from vibrations involving H atoms. However, strong phonon features of **Fe-Cl-*d*$_{28}$** are present at higher energies in the full vibrational spectrum (Figure D.2) and are sufficiently reproduced by VASP calculations.

In **Fe-Cl** and **Fe-Cl-*d*$_{28}$**, both ZFS transitions ($M_S = \pm1/2 \rightarrow \pm3/2$ and $M_S = \pm3/2 \rightarrow \pm5/2$) are fairly isolated from nearby phonons, reducing the potential for spin-phonon coupling. However, the deuteration of **Fe-Cl** shifts the lowest-energy phonons towards the magnetic peaks—particularly the $M_S = \pm3/2 \rightarrow \pm5/2$ peak at 25.76 cm^{-1} for **Fe-Cl** and at 25.11 cm^{-1} for **Fe-Cl-*d*$_{28}$**—suggesting that full or partial deuteration is a potential technique to reduce or promote potential spin-phonon coupling interactions in compounds exhibiting superparamagnetism.

Table 5.1. Select calculated phonon energies and symmetries for **Fe-Cl** and **Fe-Cl-d_{28}**

Phonon ID	Energy of Phonon of Fe-Cl (cm^{-1})	Energy of Phonon of Fe-Cl-d_{28} (cm^{-1})	Symmetry
1	31.497	29.821	*B*
2	42.599	40.450	*E*
3	47.146	43.457	*B*
4	49.740	45.268	*A*
5	62.471	59.654	*A*
6	68.903	64.518	*E*
7	70.293	67.127	*B*

5.2.1.3. Phonon Movies of **Fe-Cl** and **Fe-Cl-d_{28}**

The phonon movies of **Fe-Cl** and **Fe-Cl-d_{28}** in Appendix D give visualizations of how atoms in the molecule vibrate at different phonon frequencies. Figure 5.3 gives a labeled representation of a molecule of **Fe-Cl** for ease of discussion. As is expected, the atomic motions shown in the movies are directly analogous for corresponding phonons of **Fe-Cl** and **Fe-Cl-d_{28}**, with larger vectors representing the magnitude of vibrational motion for **Fe-Cl** than for **Fe-Cl-d_{28}**. It should be noted that some modes captured by the phonon movies are absent in Table 5.1 and Tables D.1-D.2, since the symmetry analysis is with respect to the primitive cell, whereas the phonon calculations and visualizations are performed with the unit cell of the crystal structure (twice the size of the primitive cell). Only modes in the low energy regions near the respective magnetic peaks of **Fe-Cl** and **Fe-Cl-d_{28}** (within 24-75 cm^{-1}) are visualized as movies, because changes in the bond lengths and angles via atomic displacement from vibrational motion can engender changes in the electronic and magnetic structures.

Phonon A in Appendix D is characterized by a cyclical rocking of the C−H bonds on the *meso* phenyl rings (carbons 7-11, 18-22, 29-33, and 40-44 in Figure 5.3), in a direction towards the "top" of the porphyrin backbone (*i.e.*, the face with the Fe−Cl bond in the non-disordered structure). Phonon A also shows simultaneous symmetrical wagging of the C−H bonds of the β-carbons (carbons 2-3, 13-14, 24-25, and 35-36) towards the "bottom" of the porphyrin. Doubly degenerate Phonon B exhibits similar rocking of two phenyls (opposite one another on the porphyrin backbone, carbons 7-11 and 29-33), while the other two phenyl rings (carbons 18-22 and 40-44) undergo twisting motions. Additionally, the entire porphyrin backbone exhibits a weak twisting motion in

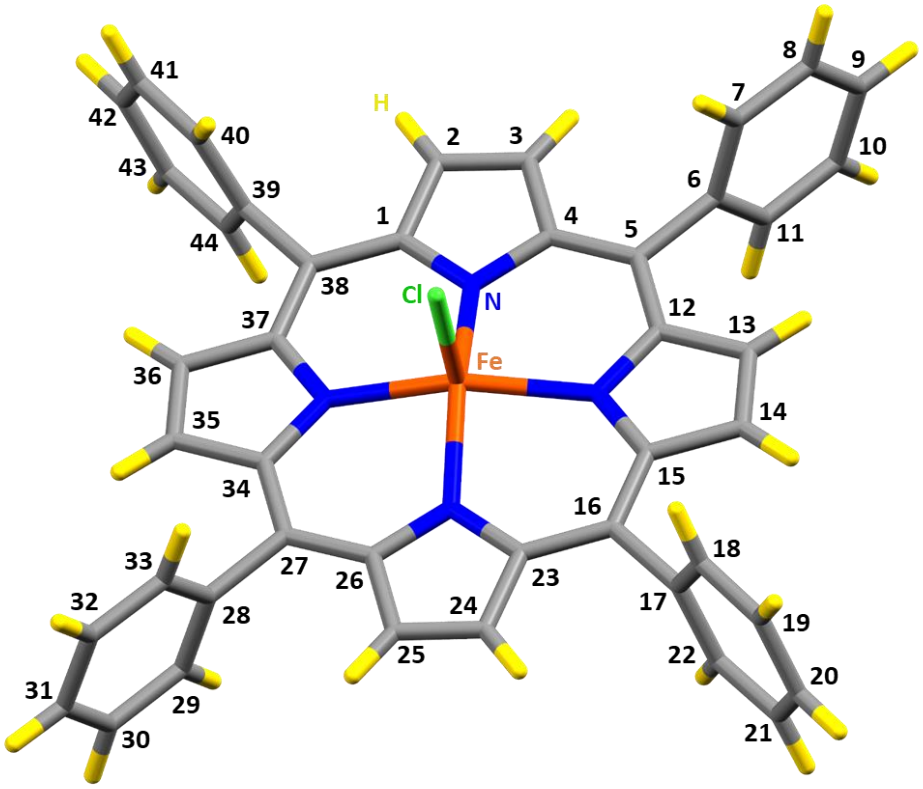


Figure 5.3. Molecular structure of **Fe-Cl** with numbered carbon atoms (shown in grey) for discussion of phonon movies. Select iron (orange), nitrogen (blue), chlorine (green), and hydrogen (yellow) atoms are labeled for clarity.

Phonon B due to vibrations of the β-carbons 2-3 and 24-25. Phonon C is characterized by strong twisting of all four phenyl rings, as well as weak twisting of the porphyrin backbone due to wagging of β-carbons 2-3 and 24-25 in the opposite direction of the wagging β-carbons 13-14 and 35-36.

For Phonons A-C, very little distortion of the first coordination sphere around Fe^{3+} is observed. However, Phonon D exhibits greater distortion of the Fe–N bonds due to stronger wagging vibrations of the β-carbons, which reflect Phonon C in character but are larger in magnitude. It is uncertain whether greater distortion of the first coordination sphere of the metal center is associated with stronger spin-phonon couplings, though this is possible due to the localization of unpaired electron density on the Fe^{3+} ion (see the discussion of spin densities below). It is possible that the difference in energy between Phonon D and the ZFS transitions is great enough to suppress any apparent spin-phonon coupling interactions.

Phonon E is characterized by moderate rocking of the phenyl rings with carbons 7-11 and 29-33, along with stronger cyclic rocking of the other two phenyls (carbons 18-22 and 40-44). β-Carbons 13-14 and 35-36 exhibit moderate wagging, whereas carbons 13-14 wag in the opposite direction than carbons 35-36. β-Carbons 2-3 wag weakly in the same direction as carbons 35-36, whereas β-carbons 24-25 wag weakly in the same direction as carbons 13-14.

For Phonon F, carbons 18-22 and 40-44 on the phenyl rings exhibit strong wagging vibrations, coupled with comparatively very weak wagging of carbons 7-11 and 29-33. This disparity in motion promotes distortion of the Fe–Cl bond, and Phonon F is one of the only phonon movies that shows visibly discernible motion of the Cl atom. As

Cl is the atom with the second-most unpaired electron density (after Fe^{3+}), it is possible that this motion could induce spin-phonon coupling interactions. As Phonon G shows very strong wagging of all four phenyl rings, the distortion of the porphyrin backbone is minimal, and Phonon G may be expected to couple less with the magnetic transition(s).

5.2.1.4. Spin Densities of **Fe-Cl** and **Fe-Cl-d_{28}**

Spin densities on different atoms in **Fe-Cl** have shown to lead to paramagnetic shifts in ^{1}H and ^{13}C NMR spectra.[174] We have directly calculated spin densities, ρ_s, of atoms in **Fe-Cl**, as summarized in Table 5.2 with detailed lists for each atom in Table D.3. The spin densities, calculated by the DFT-based program VASP, provide a quantitative scale to determine how spins from unpaired electrons are dispersed to individual atoms in **Fe-Cl**. VASP partitions electrons according to the Wigner-Seitz radius a_e by:

$$a_e = (3/4\pi n_e)^{1/3} \qquad \text{(Eq. 5.1)}$$

where n_e is the particle density of electrons; a_e is the radius "occupied" by one atom in a sample, and each atom is considered as a sphere.

VASP does not account for spin densities in bonds between atoms. Thus, the calculated ρ_s across all atoms in **Fe-Cl** is 4.789, slightly smaller than the expected value of 5 (for 5 unpaired electrons or $S = 5/2$). A large majority (~88%) of the molecular ρ_s is localized on the Fe^{3+} center, retaining 4.223 unpaired electrons. Axial Cl^- ligand has the greatest contribution (0.175) of the non-metal ligand atoms. These results are consistent with previously reported ρ_s distributions in paramagnetic compounds $Co(PPh_3)_2X_2$ (X =

Table 5.2. Calculated spin densities ρ_s in **Fe-Cl** and **Fe-Cl-d_{28}**

Atom	ρ_s
Fe	4.223
Cl	0.175
N	7.42×10^{-2}
C	-1.40×10^{-4} to 9.75×10^{-3}
H	-6.00×10^{-7} to 3.42×10^{-4}
Total	4.789

Cl, Br, I)[113] and a Co^{2+} coordination polymer.[175] Each N atom carries a small spin density of 7.42×10^{2}, and the *meso*-C5 atoms (shown in Figure D.3 to supplement Table D.3) exhibit a greater $\boldsymbol{\rho_s}$ (9.75×10^{-3}) than C_α (C1 and C4 in Figure D.3; ~1.52×10^{-3}) and C_β (C2 and C3 in Figure D.3; 4.00×10^{-3}) atoms on the TPP^{2-} ligand. Contributions from other C atoms on the phenyl groups (-1.40×10^{-4} to 6.66×10^{-4}) and H atoms (-6.00×10^{-7} to 3.42×10^{-4}) are comparatively minor. The calculated $\boldsymbol{\rho_s}$ values on the C6 and C7 atoms in Figure D.3 are negative, indicating opposite polarization compared to other atoms in the molecule.

5.2.2. INS of Fe-F, Fe-Br, and Fe-I

Variable-temperature INS data of **Fe-F**, **Fe-Br**, and **Fe-I** are given in Figures 5.4-5.7. INS of **Fe-F** by the direct-geometry Cold Neutron Chopper Spectrometer (CNCS) at Oak Ridge National Laboratory (ORNL) was reported in 2015 to show ZFS transitions; $D = 4.49$ cm^{-1} and magnetic peaks are observed at 8.99 cm^{-1} ($M_S = \pm 1/2 \rightarrow \pm 3/2$) and 18.05 cm^{-1} ($M_S = \pm 3/2 \rightarrow \pm 5/2$) in that work.[7] However, to our knowledge, INS of **Fe-F** has not been conducted on an indirect geometry INS spectrometer such as VISION. It is of interest to compare INS spectra from the two types of instruments. For **Fe-F** at 5 K on VISION in the current work, magnetic peaks arise at 8.92 cm^{-1} ($M_S = \pm 1/2 \rightarrow \pm 3/2$) and weakly at 18.2 cm^{-1} ($M_S = \pm 3/2 \rightarrow \pm 5/2$) in Figure 5.4-Top. The latter feature increases in intensity as the temperature is increased to 25 K. Interestingly, an additional peak at 12.7 cm^{-1}, which has not previously been observed, appears. While the origin of this peak is unknown, its variable-temperature properties in INS (Figure 5.4-Top) suggest that it is magnetic. It is possible that this additional peak is indicative of a cluster excitation, where

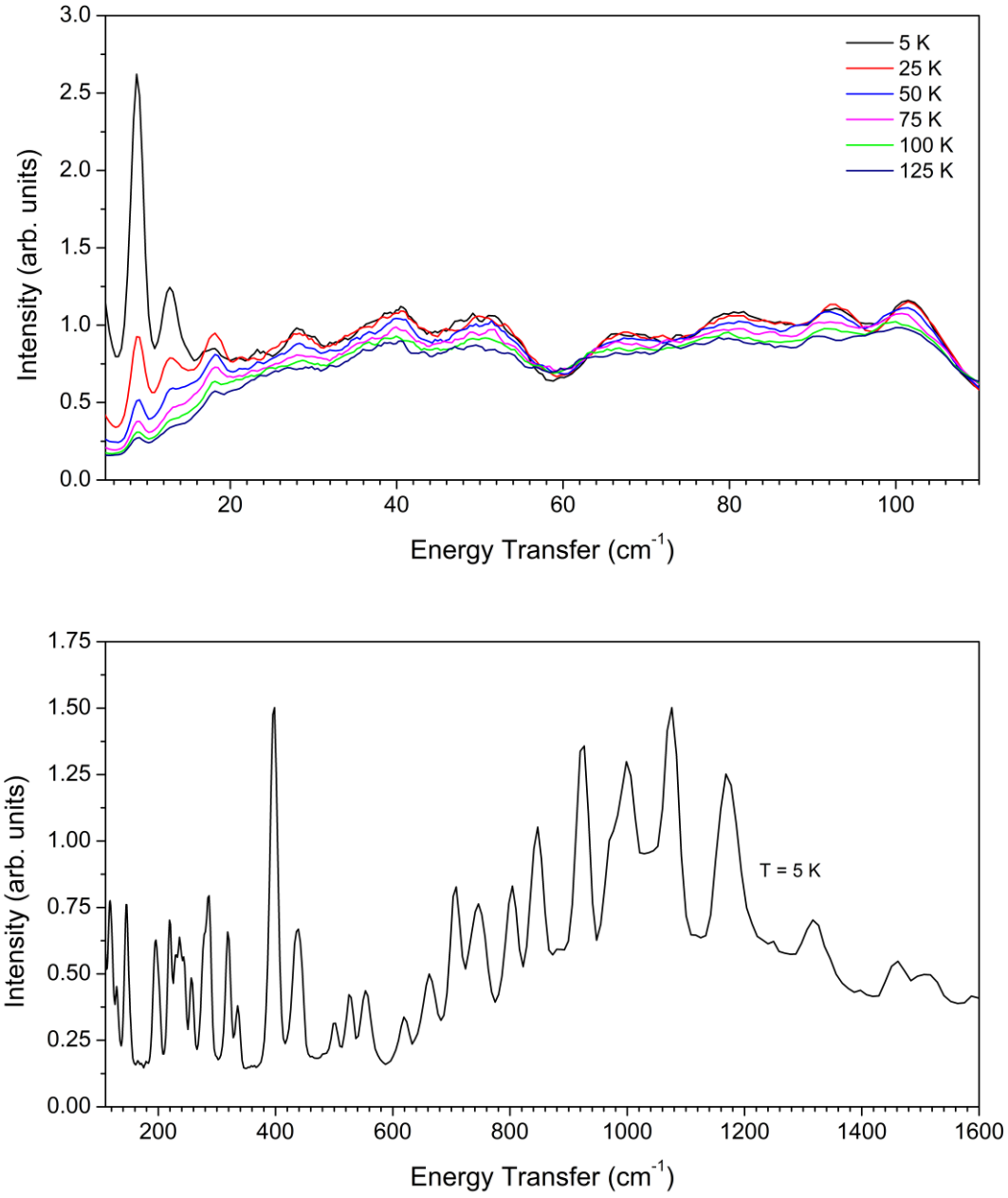


Figure 5.4. Forward-scattered, Bose-corrected INS spectra of **Fe-F** showing magnetic transitions at 5-125 K (Top) and the full phonon spectrum at 5 K (Bottom).

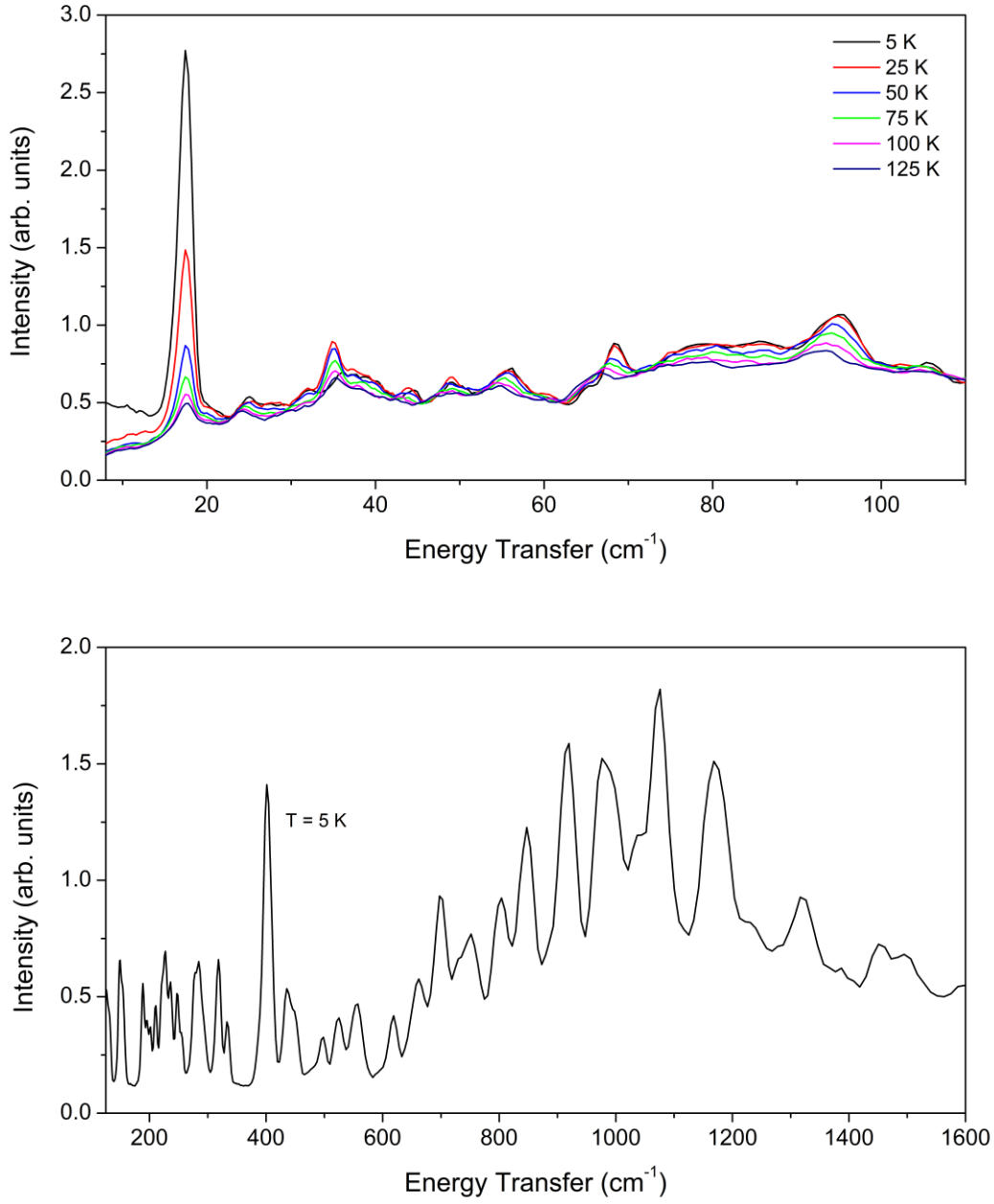


Figure 5.5. Forward-scattered, Bose-corrected INS spectra of **Fe-Br** showing magnetic transitions at 5-125 K (Top) and the full phonon spectrum at 5 K (Bottom).

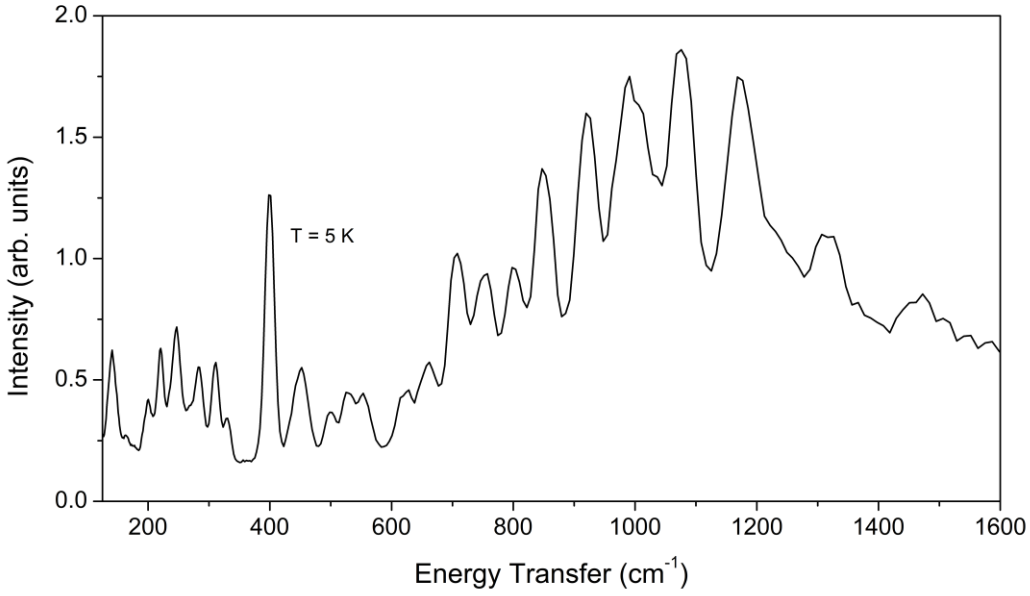


Figure 5.6. Forward-scattered, Bose-corrected INS spectrum of **Fe-I** at 5 K.

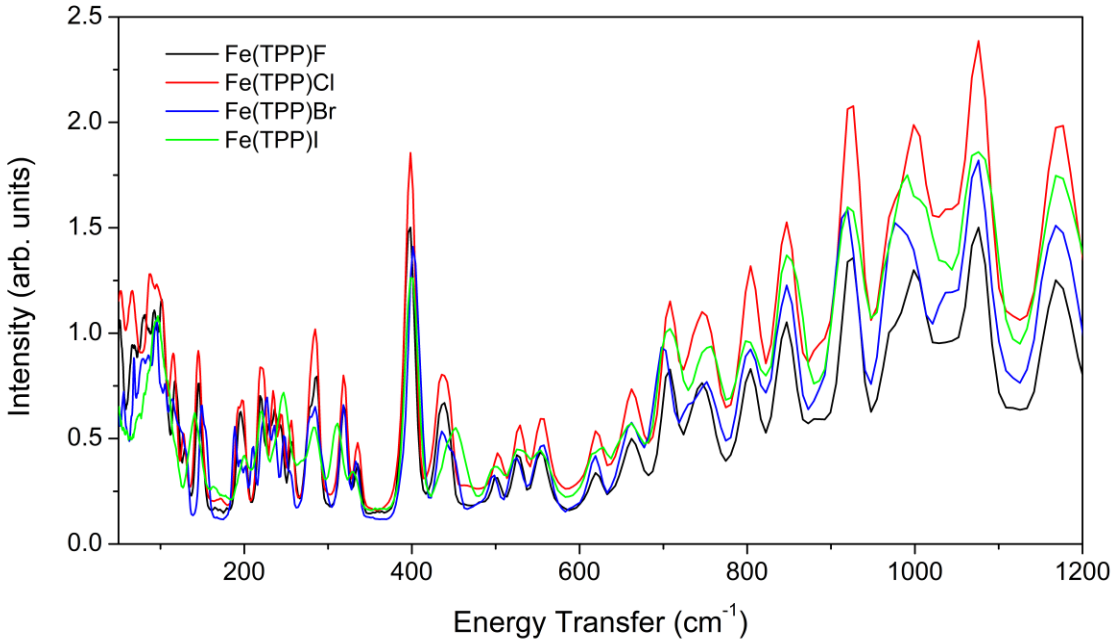


Figure 5.7. Forward-scattered, Bose-corrected INS spectra of **Fe-X** series: X = F (black), Cl (red), Br (blue), and I (green). **Fe-Cl** has been scaled by a factor of 0.25 to match the intensity of the other spectra.

multiple Fe^{3+} centers interact as an assembly to give rise to this additional peak. This phenomenon was observed for **Fe-Cl** as described in Chapter II of this dissertation, where the magnetic assembly excitation appears as a shoulder peak [11.8(1) cm^{-1}] off of the single-molecule magnetic peak [12.7(1) cm^{-1}]. However, additional studies are necessary to determine the nature of the peak at 12.7 cm^{-1} for **Fe-F**. An expanded phonon spectrum of **Fe-F** at 5 K is given in Figure 5.4-Bottom.

Fe-Br does not have crystallographic four-fold symmetry as **Fe-F** and **Fe-Cl** do, introducing a small E parameter that modifies the $2D$ and $4D$ splittings for the $M_S = \pm 1/2 \rightarrow \pm 3/2$ and $M_S = \pm 3/2 \rightarrow \pm 5/2$ transitions, respectively. Magnetic peaks of **Fe-Br** were observed at 17.5 cm^{-1} and 35.04 cm^{-1} in 2015, with $D = 8.8(2)$ cm^{-1} and $E = 0.1(2)$ cm^{-1}.[7] In Figure 5.5-Top, magnetic features of **Fe-Br** appear at 17.39 and 35.02 cm^{-1}, in good agreement with those in the 2015 paper.[7] It is unclear whether the minor temperature dependences of other peaks from 20-100 cm^{-1} indicate that they are magnetic in nature. However, they appear as phonon-like background peaks in the 2015 paper. It is possible that these peaks are phonons that undergo spin-phonon coupling with the magnetic transitions, displaying a minor temperature dependence. These could, in theory, also be due to assembly excitations as observed in **Fe-Cl** and postulated for **Fe-F**. An expanded phonon spectrum of **Fe-Br** at 5 K is given in Figure 5.5-Bottom.

When collecting the INS data for **Fe-I**, the SNS source had to be shut down during the experiment. Thus, there was a limited collection time for **Fe-I**. Probably due to the incomplete data collection, no strong magnetic excitations of **Fe-I** were observed on VISION. However, an expanded phonon spectrum is given in Figure 5.6 and again in Figure 5.7 (compared to **Fe-F**, **Fe-Cl**, and **Fe-Br**). Due to their similar coordination

environments, the expanded phonon spectra of **Fe-X** at 110-1200 cm^{-1} are very similar in nature, particularly above ~275 cm^{-1}, with multiple overlapping peaks. Further symmetry analysis is required via the VASP program to determine the symmetries of phonons in **Fe-F**, **Fe-Br**, and **Fe-I**.[120]

5.3. Experimental Methods

Fe(TPP)Cl (**Fe-Cl**, ≥98%) was purchased from Arctom (Westlake Village, California, USA) and used as received. **Fe-F**, **Fe-Br**, and **Fe-I** were synthesized using previously reported methods.[7] The synthesis of **Fe-Cl-d_{28}** by Dr. Brenda Smith is described in her Ph.D. dissertation.[176] Powder X-ray diffraction (PXRD) of the **Fe-X** series at 296 K was obtained on a Malvern Panalytical Empyrean powder diffractometer with a Cu source (λ = 1.54 Å). The PXRD patterns are given in Appendix D.

For variable-temperature INS at VISION, the samples (0.50 g on average) were sealed in aluminum containers and placed inside the neutron beam at Vibrational Spectrometer (VISION) at Spallation Neutron Source (SNS), ORNL. INS spectra of the **Fe-X** series were measured at 5, 25, 50, 75, 100, and 125 K. The design at VISION offers two banks of detectors for both forward (low $|\boldsymbol{Q}|$) and back (high $|\boldsymbol{Q}|$) scattering of neutrons.[177] The phonon population effect was corrected by normalizing the INS intensity at energy transfer ω with $\coth\left(\frac{\hbar\omega}{2k_BT}\right)$.[84]

The phonon calculations of **Fe-Cl** and **Fe-Cl-d_{28}** were performed by the Vienna Ab initio Simulation Package (VASP) program.[178] for **Fe-Cl**, the geometry optimizations were performed on its single-crystal X-ray diffraction structure.[8] The optimized structures completed at 0 T were used for the phonon calculations. Spin-polarized,

periodic DFT calculations were performed using VASP with the Projector Augmented Wave (PAW) method[136-137] and Perdew-Burke-Ernzerhof (PBE)[138] implementation implementation of the Generalized Gradient Approximation (GGA) for the exchange-correlation functional, with a Hubbard U term of 5.37 eV.[179] Energy cut off was 900 eV for the plane-wave basis of the valence electrons. Total energy tolerance for electronic structure minimization was 10^{-8} eV. The optB86b-vdW, a non-local correlation functional that roughly accounts for dispersion interactions,[141] was applied. The INS spectrum and peak intensities for both forward and backscattering were calculated using OCLIMAX, a versatile INS simulation program developed at ORNL.[135] Phonopy, an open source phonon analyzer,[120] was used to create a $1 \times 1 \times 1$ supercell structure, extract force constants and phonon symmetries, and perform the calculations of phonon frequencies and modes. For **2**-$\boldsymbol{d_{28}}$, H atoms in the structure of **2** were replaced by D atoms in Phonopy and OCLIMAX calculations.

CHAPTER VI

CONCLUSION AND RECOMMENDATIONS

This dissertation primarily focuses on the study of magnetic and vibrational modes as well as spin-phonon couplings in transition metal complexes via spectroscopic techniques such as inelastic neutron scattering (INS), far-IR magneto-spectroscopy (FIRMS), and high-field, high-frequency EPR (HFEPR). For the **Co-X** and **Mn-X** series, this dissertation provides the first examples of direct observation of ZFS transitions arising from the quenched orbital motion of the *d*-electrons. Additionally, for **Fe-Cl** and **Mn-Cl**, a novel propagation of an assembly excitation has been directly revealed via direct-geometry INS, providing insight towards potential relaxation mechanisms in SMMs and corresponding design considerations. Additional phonon characterization has been performed for many compounds described in the dissertation, including calculations of phonon symmetries and representations of the phonons via movies.

Chapter II investigates intermolecular spin-spin interactions from magnetic dipole-dipole and electric multipole interactions in solids of single molecules that can induce relaxation in SMMs. The work reveals that the intermolecular magnetic interaction leads to an assembly behavior of a molecule of **Fe-Cl** with its neighboring molecules, giving rise to a magnetic transition from the assembly at an energy different from the transition of a single molecule of **Fe-Cl** itself in the INS spectra. In addition, intensities of magnetic transitions in **Fe-Cl** and **Mn-Cl** show the oscillatory *Q*-dependence. To our knowledge, both the assembly magnetic transition and the oscillatory *Q*-dependence are observed for the first time for molecular compounds. The results demonstrate the INS is a suitable zero-field technique for revealing intermolecular magnetic interactions among metal centers in single molecules via Heisenberg spin-spin exchange. Analyses by the effective-field model developed in the dissertation give

reasonable exchange distances (R_{eff}) of 11.84 Å for **Fe-Cl** and 13.20 Å for **Mn-Cl** and reveal the nature of the intermolecular interactions. These studies show that INS may be used as a direct probe to study the nature of intermolecular interactions causing the collapse of magnetic memories in SMMs and molecular qubits.

The work in Chapter III on the $Co(PPh_3)_2X_2$ (X = Cl, Br, I; **Co-X**) series demonstrates that FIRMS is a powerful technique to determine magnetic excited levels in the complexes and probe spin-phonon coupling in SMMs, giving the intensity of these interactions. Additionally, it shows that INS spectroscopy is a unique, zero-field technique to identify both magnetic transitions in the molecules, providing an insight as to the phonons involved in these couplings, when combined with DFT phonon and INS calculations. For **Co-X** with centrosymmetric, C_{2h} crystallographic symmetry, INS spectra, showing all phonons, in combination with far-IR and Raman spectra showing *u*- and *g*-symmetry phonons, respectively, give a comprehensive characterization of phonons in the region of interest. The determination of complete spin-Hamiltonian parameters of **Co-X** by a combination of spectroscopies provides a rare view of the magnetic separations in these complexes from different spectroscopic perspectives. Ligand-field work calculates the *D*, *E* parameters and points to the origin of the ZFS for the three complexes. These studies of spin-phonon coupling will contribute to the understanding of magnetic relaxation in SMMs and molecular qubits, helping develop guidance to reduce or avoid the couplings.

It should be noted that the work in Chapter III experimentally determines the magnetic excited levels and degrees of their couplings with nearby phonons (as coupling constants). Additional studies, especially those with computation or modeling as recently

reported for other compounds,[121-125] are needed to provide an insight into the spin-phonon coupling. Such investigations are expected to correlate the magnetic and phonon properties of the compounds, including why only *u*-symmetry phonons in **Co-X** are involved in spin-phonon coupling, how the coupling phonons impact the ZFS parameters and spin densities, and how the intensity of this coupling affects other interactions such as crystal field, ZFS, and Zeeman splittings.

The work described in Chapter IV on Mn(TPP)X (X = Br, I) shows that the Mn(TPP)X complexes may accommodate different solvents in the lattice. The Mn(III)—Br and Mn(III)—I bonds in $S = 2$ Mn(TPP)X are unexpectedly longer than Fe(III)—Br and Fe(III)—I bonds in $S = 5/2$ Fe(TPP)X (X = Br, I). HFEPR and INS studies show that the axial ZFS parameter (D) decreases from Mn(TPP)Cl to Mn(TPP)Br, likely as a result of a weaker axial (Mn—Br) ligand field in **Mn-Br** than that (Mn—Cl) in **Mn-Cl**. Unlike **Mn-Cl** and **Mn-Br**, **Mn-I** has easy-plane anisotropy, presumably as a result of [I^- to Mn(III)] LMCT.

Chapter V provides a rare, direct comparison of magnetic transitions in INS of **Fe-Cl** and deuterated **Fe-Cl-d_{28}** isotopologues. Phonon properties and calculated INS spectra of **Fe-Cl** and **Fe-Cl-d_{28}** have been systematically analyzed. In addition, INS spectra of **Fe-F**, **Fe-Br**, and **Fe-I** have been collected across a broad energy spectrum for comparison. This work demonstrates that INS at VISION (SNS, ORNL) is a powerful technique for observing both magnetic peaks and phonon modes without a symmetry-based selection rule.

REFERENCES

1. Sessoli, R.; Gatteschi, D.; Caneschi, A.; Novak, M. A., Magnetic Bistability in a Metal-Ion Cluster. *Nature* **1993,** *365* (6442), 141-143.
2. Ishikawa, N.; Sugita, M.; Ishikawa, T.; Koshihara, S.; Kaizu, Y., Lanthanide double-decker complexes functioning as magnets at the single-molecular level. *J Am Chem Soc* **2003,** *125* (29), 8694-8695.
3. Woodruff, D. N.; Winpenny, R. E. P.; Layfield, R. A., Lanthanide Single-Molecule Magnets. *Chem Rev* **2013,** *113* (7), 5110-5148.
4. Gupta, S. K.; Murugavel, R., Enriching lanthanide single-ion magnetism through symmetry and axiality. *Chem Commun* **2018,** *54* (30), 3685-3696.
5. Liddle, S. T.; van Slageren, J., Improving f-element single molecule magnets. *Chem Soc Rev* **2015,** *44* (19), 6655-6669.
6. Moseley, D. H.; Stavretis, S. E.; Thirunavukkuarasu, K.; Ozerov, M.; Cheng, Y.; Daemen, L. L.; Ludwig, J.; Lu, Z.; Smirnov, D.; Brown, C. M.; Pandey, A.; Ramirez-Cuesta, A. J.; Lamb, A. C.; Atanasov, M.; Bill, E.; Neese, F.; Xue, Z.-L., Spin–phonon couplings in transition metal complexes with slow magnetic relaxation. *Nat. Commun.* **2018,** *9*, 2572.
7. Stavretis, S. E.; Atanasov, M.; Podlesnyak, A. A.; Hunter, S. C.; Neese, F.; Xue, Z.-L., Magnetic Transitions in Iron Porphyrin Halides by Inelastic Neutron Scattering and Ab Initio Studies of Zero-Field Splittings. *Inorg. Chem.* **2015,** *54*, 9790-9801.
8. Hunter, S. C.; Smith, B. A.; Hoffmann, C. M.; Wang, X.; Chen, Y.-S.; McIntyre, G. J.; Xue, Z.-L., Intermolecular Interactions in Solid-State

Metalloporphyrins and Their Impacts on Crystal and Molecular Structures. *Inorg. Chem.* **2014,** *53*, 11552-11562.

9. Hunter, S. C.; Podlesnyak, A. A.; Xue, Z.-L., Magnetic Excitations in Metalloporphyrins by Inelastic Neutron Scattering: Determination of Zero-Field Splittings in Iron, Manganese, and Chromium Complexes. *Inorg. Chem.* **2014,** *53* (4), 1955-1961.

10. Tin, P.; Stavretis, S. E.; Ozerov, M.; Krzystek, J.; Ponomaryov, A. N.; Zvyagin, S. A.; Wosnitza, J.; Chen, C.-C.; Chen, P. P. Y.; Telser, J.; Xue, Z.-L., Advanced Magnetic Resonance Studies of Tetraphenylporphyrinatoiron(III) Halides. *Appl. Magn. Reson.* **2020,** *51* (11), 1411-1432.

11. Skelton, B.; White, A., Crystal structure of Bromo(tetraphenylporphyrin)iron(III). *Aus. J. Chem.* **1977,** *30*, 2655-2660.

12. Hatano, K.; Scheidt, W. R., Molecular stereochemistry of iodo(meso-tetraphenylporphinato)iron(III). *Inorg. Chem.* **1979,** *18*, 877-879.

13. Feng, X.; Hwang, S. J.; Liu, J.-L.; Chen, Y.-C.; Tong, M.-L.; Nocera, D. G., Slow magnetic relaxation in intermediate spin (S = 3/2) mononuclear Fe(III) complexes. *J. Am. Chem. Soc.* **2017,** *139* (46), 16474-16477.

14. Wang, L.; Zlatar, M.; Vlahović, F.; Demeshko, S.; Philouze, C.; Molton, F.; Gennari, M.; Meyer, F.; Duboc, C.; Gruden, M., Experimental and theoretical identification of the origin of magnetic anisotropy in intermediate spin iron(III) complexes. *Chem. Eur. J.* **2018,** *24* (20), 5091-5094.

15. Mossin, S.; Tran, B. L.; Adhikari, D.; Pink, M.; Heinemann, F. W.; Sutter, J.; Szilagyi, R.; Meyer, K.; Mindiola, D. J., A mononuclear Fe(III) single molecule

magnet with a 3/2 <--> 5/2 spin crossover. *J. Am. Chem. Soc.* **2012,** *134* (33), 13651-13661.

16. Cheng, B.; Scheidt, W. R., Chloro(5,10,15,20-tetraphenylporphyrinato)manganese(III) with 4/m Symmetry. *Acta Cryst. C* **1996,** *52*, 361-363.

17. Armstrong, R. S.; Foran, G. J.; Hambley, T. W., Structure of chloro(α,β,γ,δ-tetra-phenylporphinato)manganese(III) toluene solvate. *Acta Cryst. C* **1993,** *49*, 236-238.

18. Tulinsky, A.; Chen, B. M. L., The crystal and molecular structure of chloro-α,β,γ,δ-tetraphenylporphinatomanganese(III). *J. Am. Chem. Soc.* **1977,** *99*, 3647-3651.

19. Bone, A. N.; Stavretis, S. E.; Krzystek, J.; Liu, Z.; Chen, Q.; Gai, Z.; Wang, X.; Steren, C. A.; Powers, X. B.; Podlesnyak, A. A.; Chen, X.-T.; Telser, J.; Zhou, H.; Xue, Z.-L., Manganese tetraphenylporphyrin bromide and iodide. Studies of structures and magnetic properties. *Polyhedron* **2020,** *184*, 114488.

20. Campbell, K. A.; Lashley, M. R.; Wyatt, J. K.; Nantz, M. H.; Britt, R. D., Dual-Mode EPR Study of Mn(III) Salen and the Mn(III) Salen-Catalyzed Epoxidation of cis-β-Methylstyrene. *J. Am. Chem. Soc.* **2001,** *123*, 5710-5719.

21. Krzystek, J.; Telser, J., High frequency and field EPR spectroscopy of Mn(III) complexes in frozen solutions. *J. Magn. Reson.* **2003,** *162*, 454-465.

22. Krzystek, J.; Yeagle, G. J.; Park, J.-H.; Britt, R. D.; Meisel, M. W.; Brunel, L.-C.; Telser, J., High-Frequency and -Field EPR Spectroscopy of Tris(2,4-

pentanedionato)manganese(III): Investigation of Solid-State versus Solution Jahn−Teller Effects. *Inorg. Chem.* **2003,** *42*, 4610-4618.

23. Krzystek, J.; Schnegg, A.; Aliabadi, A.; Holldack, K.; Stoian, S. A.; Ozarowski, A.; Hicks, S. D.; Abu-Omar, M. M.; Thomas, K. E.; Ghosh, A.; Caulfield, K. P.; Tonzetich, Z. J.; Telser, J., Advanced Paramagnetic Resonance Studies on Manganese and Iron Corroles with a Formal d4 Electron Count. *Inorg. Chem.* **2020,** *59*, 1075-1090.

24. Goldberg, D. P.; Telser, J.; Krzystek, J.; Montalban, A. G.; Brunel, L.-C.; Barrett, A. G. M.; Hoffman, B. M., EPR Spectra from "EPR-Silent" Species: High-Field EPR Spectroscopy of Manganese(III) Porphyrins. *J. Am. Chem. Soc.* **1997,** *119*, 8722-8723.

25. Krzystek, J.; Telser, J.; Pardi, L. A.; Goldberg, D. P.; Hoffman, B. M.; Brunel, L.-C., High-Frequency and -Field Electron Paramagnetic Resonance of High-Spin Manganese(III) in Porphyrinic Complexes. *Inorg. Chem.* **1999,** *38*, 6121-6129.

26. Krzystek, J.; Pardi, L. A.; Brunel, L.-C.; Goldberg, D. P.; Hoffman, B. M.; Licoccia, S.; Telser, J., High-frequency and -field electron paramagnetic resonance of high-spin manganese(III) in tetrapyrrole complexes. *Spectrochim. Acta A* **2002,** *58*, 1113-1127.

27. Kennedy, B. J.; Murray, K. S., Magnetic properties and zero-field splitting in high-spin manganese(III) complexes. 2. Axially ligated manganese(III) porphyrin complexes. *Inorg. Chem.* **1985,** *24*, 1557-1560.

28. Pascual-Álvarez, A.; Vallejo, J.; Pardo, E.; Julve, M.; Lloret, F.; Krzystek, J.; Armentano, D.; Wernsdorfer, W.; Cano, J., Field-Induced Slow Magnetic

Relaxation in a Mononuclear Manganese(III)–Porphyrin Complex. *Chem. Eur. J.* **2015,** *21*, 17299-17307.

29. Benelli, C.; Gatteschi, D., *Introduction to Molecular Magnetism*. Wiley-VCH: 2015.

30. Frost, J. M.; Harriman, K. L. M.; Murugesu, M., The rise of 3-*d* single-ion magnets in molecular magnetism: towards materials from molecules? *Chem. Sci.* **2016,** *7*, 2470-2491.

31. Layfield, R. A., Organometallic single-molecule magnets. *Organometallics* **2014,** *33*, 1084-1099.

32. Krzystek, J.; Telser, J., Measuring giant anisotropy in paramagnetic transition metal complexes with relevance to single-ion magnetism. *Dalton Trans.* **2016,** *45*, 16751-16763.

33. McInnes, E. J. L.; Winpenny, R. E. P., Molecular Magnets. In *Comprehensive Inorganic Chemistry II*, Poeppelmeier, K., Ed. Elsevier: Amsterdam, 2013; pp 371-395.

34. Neese, F.; Pantazis, D. A., What is not required to make a single molecule magnet. *Faraday Discuss.* **2011,** *148*, 229-238.

35. Gao, S., Ed., *Molecular Nanomagnets and Related Phenomena*. Springer: 2015.

36. Zhang, P.; Zhang, L.; Tang, J., Lanthanide single molecule magnets: Progress and perspective. *Dalton Trans.* **2015,** *44*, 3923-3929.

37. Liu, J.-L.; Chen, Y.-C.; Tong, M.-L., Symmetry strategies for high performance lanthanide-based single-molecule magnets. *Chem. Soc. Rev.* **2018,** *47*, 2431-2453.

38. Craig, G. A.; Murrie, M., 3d single-ion magnets. *Chem. Soc. Rev.* **2015,** *44*, 2135-2147.

39. Rinehart, J. D.; Long, J. R., Exploiting single-ion anisotropy in the design of *f*-element single-molecule magnets. *Chem. Sci.* **2011,** *2*, 2078-2085.

40. Gatteschi, D.; Sessoli, R., Quantum tunneling of magnetization and related phenomena in molecular materials. *Angew. Chem. Int. Ed.* **2003,** *42*, 268-297.

41. Demir, S.; Jeon, I.-R.; Long, J. R.; Harris, T. D., Radical ligand-containing single-molecule magnets. *Coord. Chem. Rev.* **2015,** *289*, 149-176.

42. Boca, R., Zero-field splitting in metal complexes. *Coordin Chem Rev* **2004,** *248* (9-10), 757-815.

43. Shatruk, M.; Gómez-Coca, S.; Dunbar, K. R., Molecular Magnetism. In *Molecular Magnetic Materials: Concepts and Applications*, Sieklucka, B.; Pinkowicz, D., Eds. Wiley-VCH: 2017; pp 29-77.

44. Yamashita, M.; Katoh, K., Single Molecule Magnets. In *Molecular Magnetic Materials: Concepts and Applications*, Sieklucka, B.; Pinkowicz, D., Eds. Wiley-VCH: 2017; pp 79-101.

45. Dey, M.; Gogoi, N., Geometry-mediated enhancement of single-ion anisotropy: A route to single-molecule magnets with a high blocking temperature. *Angew. Chem. Int. Ed.* **2013,** *52*, 12780-12782.

46. Pilbrow, J. R., Effective *g* values for $S = 3/2$ and $S = 5/2$. *J. Magn. Reson.* **1978,** *31*, 479-490.

47. Gast, P.; Groenen, E. J. J., *EPR Interactions - g-Anisotropy*. In *eMagRes*, 2016; pp 1435-1444.

48. Krzystek, J.; Park, J.-H.; Meisel, M. W.; Hitchman, M. A.; Stratemeier, H.; Brunel, L.-C.; Telser, J., EPR Spectra from "EPR-Silent" Species: High-Frequency and High-Field EPR Spectroscopy of Pseudotetrahedral Complexes of Nickel(II). *Inorg. Chem.* **2002,** *41*, 4478-4487.

49. Tomlinson, A. A. G.; Bellitto, C.; Piovesana, O.; Furlani, C., Crystal polarised spectra, and electronic structures, of some pseudotetrahedral cobalt(II) complexes with 'soft' bonding ligands. *J. Chem. Soc. Dalton Trans.* **1972**, 350-354.

50. Horrocks, W. D.; Burlone, D. A., Toward a theory of the spectral and magnetic properties of transition metal ions occupying low-symmetry sites in metalloproteins. Application of the angular overlap model to distorted tetrahedral tetrachlorocobaltate(2-) ions. *J. Am. Chem. Soc.* **1976,** *98* (21), 6512-6516.

51. Stapele, R. P. v.; Beljers, H. G.; Bongers, P. F.; Zijlstra, H., Ground State of Divalent Co Ions in Cs_3CoCl_5 and Cs_3CoBr_5. *J. Chem. Phys.* **1966,** *44*, 3719-3725.

52. Sundararajan, M.; Ganyushin, D.; Ye, S.; Neese, F., Multireference ab initio studies of zero-field splitting and magnetic circular dichroism spectra of tetrahedral Co(II) complexes. *Dalton Trans.* **2009,** (30), 6021-6036.

53. Lu, J.; Ozel, I. O.; Belvin, C. A.; Li, X.; Skorupskii, G.; Sun, L.; Ofori-Okai, B. K.; Dincă, M.; Gedik, N.; Nelson, K. A., Rapid and precise determination of zero-field splittings by terahertz time-domain electron paramagnetic resonance spectroscopy. *Chem. Sci.* **2017,** *8* (11), 7312-7323.

54. Krzystek, J.; Zvyagin, S. A.; Ozarowski, A.; Fiedler, A. T.; Brunold, T. C.; Telser, J., Definitive Spectroscopic Determination of Zero-Field Splitting in High-Spin Cobalt(II). *J. Am. Chem. Soc.* **2004,** *126*, 2148.

55. Saber, M. R.; Dunbar, K. R., Ligands effects on the magnetic anisotropy of tetrahedral cobalt complexes. *Chem. Commun.* **2014,** *50*, 12266.

56. Titiš, J.; Miklovič, J.; Boča, R., Magnetostructural study of tetracoordinate cobalt(II) complexes. *Inorg. Chem. Commun.* **2013,** *35*, 72-75.

57. Yang, F.; Zhou, Q.; Zhang, Y.-Q.; Zeng, G.; Li, G.; Shi, Z.; Wang, B.; Feng, S., Inspiration from old molecules: field-induced slow magnetic relaxation in three air-stable tetrahedral cobalt(II) compounds. *Chem. Commun.* **2013,** *49*, 5289.

58. Boča, R.; Miklovič, J.; Titiš, J., Simple Mononuclear Cobalt(II) Complex: A Single-Molecule Magnet Showing Two Slow Relaxation Processes. *Inorg. Chem.* **2014,** *53*, 2367-2369.

59. Swain, A.; Sharma, T.; Rajaraman, G., Strategies to quench quantum tunneling of magnetization in lanthanide single molecule magnets. *Chem. Commun.* **2023,** *59*, 3206-3228.

60. Sorace, L.; Gatteschi, D., Chapter 1 - Electronic Structure and Magnetic Properties of Lanthanide Molecular Complexes. In *Lanthanides and Actinides in Molecular Magnetism*, Layfield, R. A.; Murugesu, M., Eds. Wiley-VCH: Weinheim, 2015.

61. Bartolome, E.; Arauzo, A.; Luzon, J.; Bartolome, J.; Bartolome, F., Magnetic Relaxation of Lanthanide-Based Molecular Magnets. In *Handbook of Magnetic Materials*, Bruck, E., Ed. Elsevier: 2017; Vol. 26, pp 1-289.

62. Xue, Z.-L.; Ramirez-Cuesta, A. J.; Brown, C. M.; Calder, S.; Cao, H.; Chakoumakos, B. C.; Daemen, L. L.; Huq, A.; Kolesnikov, A. I.; Mamontov, E.; Podlesnyak, A. A.; Wang, X., Neutron Instruments for Research in Coordination Chemistry. *Eur. J. Inorg. Chem.* **2019,** (8), 1065-1089.

63. Baltzer, P.; Furrer, A.; Hullinger, J.; Stebler, A., Magnetic properties of nickelocene. A reinvestigation using inelastic neutron scattering and magnetic susceptibility. *Inorg. Chem.* **1988,** *27*, 1543-1548.

64. Furrer, A.; Güdel, H. U., Interference effects in neutron scattering from magnetic clusters. *Phys. Rev. Lett.* **1977,** *39*, 657-660.

65. Güdel, H. U.; Furrer, A., Neutron inelastic scattering study of exchange interactions in a chromium(III) dimer: μ-hydroxo-bis[pentaamminechromium-(III)] chloride monohydrate. *Mole. Phys.* **1977,** (33), 1334-1344.

66. Furrer, A.; Waldmann, O., Magnetic cluster excitations. *Rev. Mod. Phys.* **2013,** *85* (1), 367-420.

67. Dianoux, A.-J.; Lander, G., *Neutron Data Booklet, 2nd Ed.* OCP Science: Philadelphia, 2003.

68. Güdel, H. U.; Furrer, A.; Bührer, W.; Hälg, B., Exchange interactions in clusters of paramagnetic transition metal ions; inelastic neutron scattering studies. *Surf. Sci.* **1981,** *106*, 432-437.

69. Houchins, G.; Haraldsen, J. T., Generalization of polarized spin excitations for asymmetric dimeric systems. *Phys. Rev. B* **2015,** *91*, 014422.

70. Brackett, G. C.; Richards, P. L.; Caughey, W. S., Far-infrared magnetic resonance in Fe(III) and Mn(III) porphyrins, myoglobin, hemoglobin, ferrichrome A, and Fe(III) dithioncarbamates. *J. Chem. Phys.* **1971,** *54*, 4383-4401.

71. Brackett, G. C. Far-Infrared Magnetic Resonance in Fe(III) and Mn(III) Porphyrins, Myoglobin, Hemoglobin, Ferrichrome A, and Fe(III) Dithiocarbamates. Ph.D. dissertation, University of California, Berkeley, 1970.

72. Gnezdilov, V. P.; Eremenko, V. V.; Peschansky, A. V.; Fomin, V. I., Raman scattering by low-energy electronic excitations of Fe^{2+} ions in ferrous fluosilicate. *Fiz. Nizk. Temp. (Low Temp. Phys.)* **1991,** *17*, 253-258.

73. Clark, R. J. H.; Dines, T. J., Electronic Raman spectroscopy. In *Advances in Infrared and Raman Spectroscopy, Vol. 9*, Clark, R. J. H.; Hester, R. E., Eds. Heyden & Son: London, 1982; pp 282-360.

74. Podlesnyak, A. A.; Russina, M.; Furrer, A.; Alfonsov, A.; Vavilova, E.; Kataev, V.; Büchner, B.; Strässle, T.; Pomjakushina, E.; Conder, K.; Khomskii, D. I., Spin-state polarons in lightly hole-doped $LaCoO_3$. *Phys. Rev. Lett.* **2008,** *101*, 247603.

75. Haraldsen, J. T.; Barnes, T.; Musfeldt, J. L., Neutron scattering and magnetic observables for $S = 1/2$ spin clusters and molecular magnets. *Phys. Rev. B* **2005,** *71*, 064403.

76. Stebler, A.; Guedel, H. U.; Furrer, A.; Kjems, J. K., Intra- and intermolecular interactions in $[Ni_2(ND_2C_2H_4ND_2)_4Br_2]Br_2$. Study by inelastic neutron scattering and magnetic measurements. *Inorg. Chem.* **1982,** *21*, 380-386.

77. Gransbury, G. K.; Boulon, M.-E.; Mole, R. A.; Gable, R. W.; Moubaraki, B.; Murray, K. S.; Sorace, L.; Soncini, A.; Boskovic, C., Single-ion anisotropy and exchange coupling in cobalt(II)-radical complexes: Insights from magnetic and ab initio studies. *Chem. Sci.* **2019,** *10*, 8855-8871.

78. Paulat, F.; Praneeth, V. K. K.; Näther, C.; Lehnert, N., Quantum Chemistry-Based Analysis of the Vibrational Spectra of Five-Coordinate Metalloporphyrins [M(TPP)Cl]. *Inorg. Chem.* **2006,** *45* (7), 2835-2856.

79. Nehrkorn, J.; Telser, J.; Holldack, K.; Stoll, S.; Schnegg, A., Simulating Frequency-Domain Electron Paramagnetic Resonance: Bridging the Gap between Experiment and Magnetic Parameters for High-Spin Transition-Metal Ion Complexes. *J. Phys. Chem. B* **2015,** *119* (43), 13816-13824.

80. Ryland, E. S.; Lin, M.-F.; Verkamp, M. A.; Zhang, K.; Benke, K.; Carlson, M.; Vura-Weis, J., Tabletop Femtosecond M-edge X-ray Absorption Near-Edge Structure of FeTPPCl: Metalloporphyrin Photophysics from the Perspective of the Metal. *J. Am. Chem. Soc.* **2018,** *140* (13), 4691-4696.

81. Römelt, C.; Ye, S.; Bill, E.; Weyhermüller, T.; van Gastel, M.; Neese, F., Electronic Structure and Spin Multiplicity of Iron Tetraphenylporphyrins in Their Reduced States as Determined by a Combination of Resonance Raman Spectroscopy and Quantum Chemistry. *Inorg. Chem.* **2018,** *57* (4), 2141-2148.

82. Krzystek, J.; Telser, J.; Pardi, L. A.; Goldberg, D. P.; Hoffman, B. M.; Brunel, L.-C., High-Frequency and -Field Electron Paramagnetic Resonance of High-Spin Manganese(III) in Porphyrinic Complexes. *Inorg. Chem.* **1999,** *38* (26), 6121-6129.

83. Pascual-Álvarez, A.; Vallejo, J.; Pardo, E.; Julve, M.; Lloret, F.; Krzystek, J.; Armentano, D.; Wernsdorfer, W.; Cano, J., Field-Induced Slow Magnetic Relaxation in a Mononuclear Manganese(III)–Porphyrin Complex. *Chem. Eur. J.* **2015,** *21* (48), 17299-17307.

84. Mitchell, P. C. H.; Parker, S. F.; Ramirez-Cuesta, A. J.; Tomkinson, J., *Vibrational Spectroscopy with Neutrons: With Applications in Chemistry, Biology, Materials Science and Catalysis*. World Scientific Publishing Company: 2005.

85. Ehlers, G.; Podlesnyak, A. A.; Niedziela, J. L.; Iverson, E. B.; Sokol, P. E., The new cold neutron chopper spectrometer at the Spallation Neutron Source: Design and performance. *Rev. Sci. Instrum.* **2011,** *82*, 085108.

86. Howell, M.; DeGraff, B.; Galambos, J.; Kim, S. H., SNS proton power upgrade. *IOP Conf. Ser.: Mater. Sci. Eng.* **2017,** *278*, 012185.

87. Ehlers, G.; Podlesnyak, A. A.; Kolesnikov, A. I., The cold neutron chopper spectrometer at the Spallation Neutron Source--A review of the first 8 years of operation. *Rev. Sci. Instrum.* **2016,** *87*.

88. Hoard, J. L.; Cohen, G. H.; Glick, M. D., The stereochemistry of the coordination group in an iron(III) derivative of tetraphenylporphine. *J. Am. Chem. Soc.* **1967,** *89*, 1992-1996.

89. Arnold, O.; Bilheux, J. C.; Borreguero, J. M.; Buts, A.; Campbell, S. I.; Chapon, L.; Doucet, M.; Draper, N.; Ferraz Leal, R.; Gigg, M. A.; Lynch, V. E.; Markvardsen, A.; Mikkelson, D. J.; Mikkelson, R. L.; Miller, R.; Palmen, K.; Parker, P.; Passos, G.; Perring, T. G.; Peterson, P. F.; Ren, S.; Reuter, M. A.; Savici, A. T.; Taylor, J. W.; Taylor, R. J.; Tolchenov, R.; Zhou, W.; Zikovsky, J., Mantid—Data analysis and visualization package for neutron scattering and μ SR experiments. *Nucl. Instrum. Methods Phys. Res. A* **2014,** *764*, 156-166.

90. Azuah, R. T.; Kneller, L. R.; Qiu, Y.; Tregenna-Piggott, P. L. W.; Brown, C. M.; Copley, J. R. D.; Dimeo, R. M., DAVE: A Comprehensive Software Suite for the Reduction, Visualization, and Analysis of Low Energy Neutron Spectroscopic Data. *J. Res. Natl. Inst. Stand. Technol.* **2009,** *114*, 341-358.

91. Jacobs, P. W. M., *Group Theory with Applications in Chemical Physics*. Cambridge University Press: Cambridge, UK, 2005.

92. Koster, G. F.; Dimmock, J. O.; Wheeler, R. G.; Statz, H., *Properties of the Thirty-Two Point Groups*. MIT Press: Cambridge, MA, 1963.

93. Rechkemmer, Y.; Breitgoff, F. D.; Meer, M. v. d.; Atanasov, M.; Hakl, M.; Orlita, M.; Neugebauer, P.; Neese, F.; Sarkar, B.; Slageren, J. v., A four-coordinate cobalt(II) single-ion magnet with coercivity and a very high energy barrier. *Nat. Commun.* **2016,** *7*, 10467.

94. Ray, K.; Begum, A.; Weyhermüller, T.; Piligkos, S.; Slageren, J. v.; Neese, F.; Weighardt, K., The electronic structure of the isoelectronic, square-planar complexes $[Fe^{II}(L)_2]^{2-}$ and $[Co^{III}(LBu)_2]^{-}$ (L^{2-} and $(LBu)^{2-}$ = benzene-1,2-

dithiolates): An experimental and density functional theoretical study. *J. Am. Chem. Soc.* **2005,** *127*, 4403-4415.

95. Stavretis, S. E.; Moseley, D. H.; Fei, F.; Cui, H.-H.; Cheng, Y.; Podlesnyak, A. A.; Wang, X.; Daemen, L. L.; Hoffmann, C. M.; Ozerov, M.; Lu, Z.; Thirunavukkuarasu, K.; Smirnov, D.; Chang, T.; Chen, Y.-S.; Ramirez-Cuesta, A. J.; Chen, X.-T.; Xue, Z.-L., Spectroscopic Studies of the Magnetic Excitation and Spin-Phonon Couplings in a Single-Molecule Magnet. *Chem. Eur. J.* **2019,** *25*, 15846-15857.

96. Świtlicka, A.; Machura, B.; Penkala, M.; Bieńko, A.; Bieńko, D. C.; Titiš, J.; Rajnák, C.; Boča, R.; Ozarowski, A.; Ozerov, M., Slow Magnetic Relaxation in Cobalt(II) Field-Induced Single-Ion Magnets with Positive Large Anisotropy. *Inorg. Chem.* **2018,** *57*, 12740-12755.

97. Bunting, P. C.; Atanasov, M.; Damgaard-Møller, E.; Perfetti, M.; Crassee, I.; Orlita, M.; Overgaard, J.; van Slageren, J.; Neese, F.; Long, J. R., A Linear Cobalt(II) Complex with Maximal Orbital Angular Momentum from a Non-Aufbau Ground State

Science **2018,** *362*, eaat7319.

98. Jiang, S.-D.; Maganas, D.; Levesanos, N.; Ferentinos, E.; Haas, S.; Thirunavukkuarasu, K.; Krzystek, J.; Dressel, M.; Bogani, L.; Neese, F.; Kyritsis, P., Direct Observation of Very Large Zero-Field Splitting in a Tetrahedral $Ni^{II}Se_4$ Coordination Complex. *J. Am. Chem. Soc.* **2015,** *137*, 12923-12928.

99. Liu, J.-J.; Meng, Y.-S.; Hlavička, I.; Orlita, M.; Jiang, S.-D.; Wang, B.-W.; Gao, S., Determination of zero-field splitting in Co^{2+} halide complexes with magnetic and far-IR measurements. *Dalton Trans.* **2017,** *46*, 7408-7411.

100. Hay, M. A.; Sarkar, A.; Craig, G. A.; Bhaskaran, L.; Nehrkorn, J.; Ozerov, M.; Marriott, K. E. R.; Wilson, C.; Rajaraman, G.; Hill, S.; Murrie, M., In-depth investigation of large axial magnetic anisotropy in monometallic 3d complexes using frequency domain magnetic resonance and ab initio methods: A study of trigonal bipyramidal Co(II). *Chem. Sci.* **2019,** *10*, 6354-6361.

101. Nehrkorn, J.; Holldack, K.; Bittl, R.; Schnegg, A., Recent progress in synchrotron-based frequency-domain Fourier-transform THz-EPR. *J. Magn. Reson.* **2017,** *280*, 10-19.

102. Schnegg, A.; Behrends, J.; Lips, K.; Bittl, R.; Holldack, K., Frequency domain Fourier transform THz-EPR on single molecule magnets using coherent synchrotron radiation. *Phys. Chem. Chem. Phys.* **2009,** *11*, 6820-6825.

103. Kumar, P.; SantaLucia, D. J.; Kaniewska-Laskowska, K.; Lindeman, S. V.; Ozarowski, A.; Krzystek, J.; Ozerov, M.; Telser, J.; Berry, J. F.; Fiedler, A. T., Probing the Magnetic Anisotropy of Co(II) Complexes Featuring Redox-Active Ligands. *Inorg. Chem.* **2020,** *59*, 16178-16193.

104. Pedersen, K. S.; Dreiser, J.; Nehrkorn, J.; Gysler, M.; Schau-Magnussen, M.; Schnegg, A.; Holldack, K.; Bittl, R.; Piligkos, S.; Weihe, H.; Tregenna-Piggott, P.; Waldmann, O.; Bendix, J., A linear single-molecule magnet based on $[RuIII(CN)_6]^{3-}$. *Chem. Commun.* **2011,** *47*, 6918-6920.

105. Ibers, J. A.; Swalen, J. D., Paramagnetic Resonance Line Shapes and Magnetic Parameters of Polycrystalline Substances. *Phys. Rev.* **1962,** *127*, 1914-1917.

106. Nehrkorn, J.; Telser, J.; Holldack, K.; Stoll, S.; Schnegg, A., Simulating Frequency-Domain Electron Paramagnetic Resonance: Bridging the Gap between Experiment and Magnetic Parameters for High-Spin Transition-Metal Ion Complexes. *J. Phys. Chem. B* **2015,** *119*, 13816-13824.

107. Simo, C.; Holt, S., Polarized spectrum of dichlorobis(triphenylphosphine)cobalt(II). *Inorg. Chem.* **1968,** *7*, 2655-2657.

108. Jesson, J. P.; Trofimenko, S.; Eaton, D. R., Spectra and structure of some transition metal poly(1-pyrazolyl) borates. *J. Am. Chem. Soc.* **1967,** *89*, 3148-3158.

109. In Cs_3CoCl_5, the $[CoCl_4]^{2-}$ unit has D_{2d} symmetry, but is tetragonally elongated: Cl-Co-Cl angle = 106°. The labels used are appropriate for each of T_d, D_{2d}, and C_{2v} point group symmetry. Horrocks and Barlone use a different convention that leads to the ground state being $^4A_1$ in all three point group symmetries, but gives non-standard symmetry labels to the T_d and D_{2d} cases, which we find to be confusing, even if technically correct.

110. Davies, J. E.; Gerloch, M.; Phillips, D. J., Phosphine π-acceptor properties in dihalogenobis(triphenylphosphine)-nickel(II) and -cobalt(II). *J. Am. Chem. Soc.* **1979**, 1836-1842.

111. Miessler, G.; Fischer, P. J.; Tarr, D. A., *Inorganic Chemistry*. Pearson: New York, 2013; Vol. 5.

112. Brorson, M.; Schaeffer, C. E., Orthonormal interelectronic repulsion operators in the parametrical d^q model. Application of the model to gaseous ions. *Inorg. Chem.* **1988,** *27*, 2522-2530.

113. Bone, A. N.; Widener, C. N.; Moseley, D. H.; Liu, Z.; Lu, Z.; Cheng, Y.; Daemen, L. L.; Ozerov, M.; Telser, J.; Thirunavukkuarasu, K.; Smirnov, D.; Greer, S. M.; Hill, S.; Krzystek, J.; Holldack, K.; Aliabadi, A.; Schnegg, A.; Dunbar, K. R.; Xue, Z.-L., Applying unconventional spectroscopies to the single-molecule magnets, $Co(PPh_3)_2X_2$ (X = Cl, Br, I): Unveiling magnetic transitions and spin-phonon coupling. *Chem. Eur. J.* **2021,** *27* (43), 11110-11125.

114. Bendix, J., 2.55 - Ligfield. In *Comprehensive Coordination Chemistry II*, McCleverty, J. A.; Meyer, T. J., Eds. Pergamon: Oxford, 2003; pp 673-676.

115. Bendix, J.; Brorson, M.; Schaffer, C. E., Accurate empirical spin-orbit coupling parameters ζ_{nd} for gaseous nd^q transition metal ions. The parametrical multiplet term model. *Inorg. Chem.* **1993,** *32* (13), 2838-2849.

116. Telser, J., EPR Interactions – Zero-Field Splittings. In *eMagRes*, 2017; Vol. 6, pp 207-234.

117. The upper doublet gives $g_x(\text{min}) = 2.28$, $g_y(\text{max}) = 4.98$, $g_z(\text{mid}) = 3.76$, which is typical of $D > 0$ ($\boldsymbol{g}_{\text{eff}} = [4, 4, 2]$ for intrinsic $g = 2.00$). Thus, LFT does give the right sign.

118. Carlin, R. L.; Chirico, R. D.; Sinn, E.; Mennenga, G.; De Jongh, L. J., Magnetic ordering in cobalt chloride-triphenylphosphine ($CoCl_2.2P(C_6H_5)_3$) and cobalt bromide-triphenylphosphine ($CoBr_2.2P(C_6H_5)_3$). *Inorg. Chem.* **1982,** *21*, 2218-2222.

119. Cotton, F. A., *Chemical Applications of Group Theory*. 3rd ed.; Wiley: New York, 1990.

120. Togo, A. *VASP and Phonopy Calculation*, https://phonopy.github.io/phonopy/vasp-dfpt.html, 2009.

121. Aravena, D.; Ruis, E., Spin dynamics in single-molecule magnets and molecular qubits. *Dalton Trans.* **2020,** *49*, 9916-9928.

122. Lunghi, A.; Totti, F.; Sessoli, R.; Sanvito, S., The role of anharmonic phonons in under-barrier spin relaxation of single molecule magnets. *Nat. Commun.* **2017,** *8*, 14620.

123. Escalera-Moreno, L.; Suaud, N.; Gaita-Ariño, A.; Coronado, E., Determining Key Local Vibrations in the Relaxation of Molecular Spin Qubits and Single-Molecule Magnets. *J. Phys. Chem. Lett.* **2017,** *8*, 1695-1700.

124. Mirzoyan, R.; Hadt, R. G., The dynamic ligand field of a molecular qubit: decoherence through spin–phonon coupling. *Phys. Chem. Chem. Phys.* **2020,** *22*, 11249-11265.

125. Czap, G.; Wagner, P. J.; Li, J.; Xue, F.; Yao, J.; Wu, R.; Ho, W., Detection of Spin-Vibration States in Single Magnetic Molecules. *Phys. Rev. Lett.* **2019,** *123*, 106803.

126. Cohen-Tannoudji, C.; Diu, B.; Laloë, F., *Quantum Mechanics*. Herman: Paris, 1977; Vol. 1.

127. Stavretis, S. E.; Mamontov, E.; Moseley, D. H.; Cheng, Y.; Daemen, L. L.; Ramirez-Cuesta, A. J.; Xue, Z.-L., Effect of magnetic fields on the methyl

rotation in a paramagnetic cobalt(II) complex. Quasielastic neutron scattering studies. *Phys. Chem. Chem. Phys.* **2018,** *20*, 21119-21126.

128. Reinhard, P.-G.; Suraud, E., Gross Properties and Trends. In *Introduction to Cluster Dynamics*, Wiley-VCH Verlag GmbH: 2008; pp 133-178.

129. Mossin, S.; Weihe, H.; Barra, A.-L., Is the Axial Zero-Field Splitting Parameter of Tetragonally Elongated High-Spin Manganese(III) Complexes Always Negative? *J. Am. Chem. Soc.* **2002,** *124* (30), 8764-8765.

130. La Mar, G. N., *NMR of Paramagnetic Molecules. Principles and Applications*. Academic Press: New York, 1973.

131. Bertini, I.; Luchinat, C.; Parigi, G.; Ravera, E., *NMR of Paramagnetic Molecules: Applications to Metallobiomolecules and Models*. 2nd ed.; Elsevier: 2017.

132. Walker, F. A., NMR and EPR Spectroscopy of Paramagnetic Metalloporphyrins and Heme Proteins. In *Handbook of Porphyrin Science*, Kadish, K. M.; Smith, K. M.; Guilard, R., Eds. World Scientific: 2010; Vol. 6, pp 1-337.

133. Stavretis, S. E.; Cheng, Y.; Daemen, L. L.; Brown, C. M.; Moseley, D. H.; Bill, E.; Atanasov, M.; Ramirez-Cuesta, A. J.; Neese, F.; Xue, Z.-L., Probing Magnetic Excitations in Co^{II} Single-Molecule Magnets by Inelastic Neutron Scattering. *Eur. J. Inorg. Chem.* **2019,** *2019* (8), 1119-1127.

134. Hassan, A. K.; Pardi, L. A.; Krzystek, J.; Sienkiewicz, A.; Goy, P.; Rohrer, M.; Brunel, L. C., Ultrawide Band Multifrequency High-Field EMR Technique: A Methodology for Increasing Spectroscopic Information. *J. Magn. Reson.* **2000,** *142* (2), 300-312.

135. Cheng, Y. Q.; Daemen, L. L.; Kolesnikov, A. I.; Ramirez-Cuesta, A. J., Simulation of Inelastic Neutron Scattering Spectra Using OCLIMAX. *J. Chem. Theory Comput.* **2019,** *15* (3), 1974-1982.

136. Kresse, G.; Joubert, D., From Ultrasoft Pseudopotentials to the Projector Augmented-wave Method. *Phys. Rev. B* **1999,** *59*, 1758-1775.

137. Blöchl, P. E., Projector Augmented-wave Method. *Phys. Rev. B* **1994,** *50*, 17953-17979.

138. Perdew, J. P.; Burke, K.; Ernzerhof, M., Generalized Gradient Approximation Made Simple. *Phys. Rev. Lett.* **1996,** *77*, 3865-3868.

139. Zhou, F.; Cococcioni, M.; Marianetti, C. A.; Morgan, D.; Ceder, G., First-principles prediction of redox potentials in transition-metal compounds with LDA + U. *Phys. Rev. B* **2004,** *70*, 235121.

140. Chen, J.; Wu, X.; Selloni, A., Electronic structure and bonding properties of cobalt oxide in the spinel structure. *Phys. Rev. B* **2011,** *83* (24), 245204.

141. Klimeš, J.; Bowler, D. R.; Michaelides, A., Chemical accuracy for the van der Waals density functional. *J. Phys. Condens. Matter* **2010,** *22*, 022201.

142. Alvarez, S.; Alemany, P.; Casanova, D.; Cirera, J.; Llunell, M.; Avnir, D., Shape maps and polyhedral interconversion paths in transition metal chemistry. *Coord. Chem. Rev.* **2005,** *249*, 1693-1708.

143. Cirera, J.; Ruiz, E.; Alvarez, S., Continuous Shape Measures as a Stereochemical Tool in Organometallic Chemistry. *Organometallics* **2005,** *24*, 1556-1562.

144. Turner, P.; Gunter, M. J.; Skelton, B. W.; White, A. H., Crystal Structures of the Pentacoordinate Bromo, Isocyanato, Iodo, Acetato and Isothiocyanato Complexes

of the meso-Tetraphenylporphyrinatomanganese Cation. *Aust. J. Chem.* **1998,** *51*, 835-852.

145. Shannon, R. D., Revised effective ionic radii and systematic studies of interatomic distances in halides and chalcogenides. *Acta Cryst. A* **1976,** *32*, 751-767.

146. Collet, E.; Guionneau, P., Structural analysis of spin-crossover materials: From molecules to materials. *C. R. Chimie* **2018,** *21*, 1133-1151.

147. Scheidt, W. R., Systematics of the Stereochemistry of Porphyrins and Metalloporphyrins. In *The Porphyrin Handbook*, Kadish, K. M.; Smith, K. M.; Guilard, R., Eds. Academic Press: 2000; Vol. 3, pp 49-112.

148. Spackman, M. A.; Jayatilaka, D., Hirshfeld surface analysis. *CrystEngComm* **2009,** *11*, 19-32.

149. Spackman, M. A.; McKinnon, J. J., Fingerprinting intermolecular interactions in molecular crystals. *CrystEngComm* **2002,** *4*, 378-392.

150. Krzystek, J.; Zvyagin, S. A.; Ozarowski, A.; Trofimenko, S.; Telser, J., Tunable-frequency high-field electron paramagnetic resonance. *J. Magn. Reson.* **2006,** *178* (2), 174-183.

151. Behere, D. V.; Mitra, S., Magnetic susceptibility study and ground-state zero-field splitting in manganese(III) porphyrins. *Inorg. Chem.* **1980,** *19*, 992-995.

152. Furrer, A.; Mesot, J.; Strässle, T., *Neutron Scattering in Condensed Matter Physics*. World Scientific Publishing Company: 2009.

153. Bacon, G. E., *Neutron Scattering in Chemistry*. Butterworth: London, 1977.

154. Basler, R.; Boskovic, C.; Chaboussant, G.; Güdel, H. U.; Murrie, M.; Ochsenbein, S. T.; Sieber, A., Molecular Spin Clusters: New Synthetic Approaches and Neutron Scattering Studies. *ChemPhysChem* **2003,** *4* (9), 910-926.

155. Carpenter, J. M.; Loong, C. K., *Elements of Slow-Neutron Scattering: Basics, Techniques, and Applications*. Cambridge University Press: Cambridge, 2015.

156. CNCS website: https://neutrons.ornl.gov/cncs.

157. Krzystek, J.; Telser, J.; Knapp, M. J.; Hendrickson, D. N.; Aromí, G.; Christou, G.; Angerhofer, A.; Brunel, L. C., High-frequency and -field electron paramagnetic resonance of high-spin manganese(III) in axially symmetric coordination complexes. *Appl. Magn. Reson.* **2001,** *21*, 571-585.

158. Dugad, L. B.; Behere, D. V.; Marathe, V. R.; Mitra, S., Magnetic properties and electronic structure of manganese(III) porphyrins. *Chem. Phys. Lett.* **1984,** *104*, 353-356.

159. Powell, M. F.; Pai, E. F.; Bruice, T. C., Study of (tetraphenylporphinato)manganese(III)-catalyzed epoxidation and demethylation using p-cyano-N,N-dimethylaniline N-oxide as oxygen donor in a homogeneous system. Kinetics, radiochemical ligation studies, and reaction mechanism for a model of cytochrome P-450. *J. Am. Chem. Soc.* **1984,** *106*, 3277-3285.

160. Pedersen, K. S.; Sørensen, M. A.; Bendix, J., Fluoride-coordination chemistry in molecular and low-dimensional magnetism. *Coord. Chem. Rev.* **2015,** *299*, 1-21.

161. Turner, M. J.; McKinnon, J. J.; Wolff, S. K.; Grimwood, D. J.; Spackman, P. R.; Jayatilaka, D.; Spackman, M. A. CrystalExplorer17.

162. Turner, M. J.; McKinnon, J. J.; Jayatilaka, D.; Spackman, M. A., Visualisation and characterisation of voids in crystalline materials. *CrystEngComm* **2011,** *13*, 1804-1813.

163. Dunstan, M. A.; Mole, R. A.; Boskovic, C., Inelastic Neutron Scattering of Lanthanoid Complexes and Single-Molecule Magnets. *Eur. J. Inorg. Chem.* **2019,** *2019* (8), 1090-1105.

164. Dove, M. T., *Introduction to Lattice Dynamics*. Cambridge University Press: 1993; Vol. Cambridge Topics in Mineral Physics and Chemistry.

165. Maricondi, C.; Swift, W.; Straub, D. K., Thermomagnetic analysis of hemin and related compounds. *J. Am. Chem. Soc.* **1969,** *91*, 5205-5210.

166. Behere, D. V.; Mitra, S., Low-temperature magnetisation study on tetraphenylporphyrin-iron(III) chloride. *Indian Journal of Chemistry* **1980,** *19A*, 505-507.

167. Behere, D. V.; Mitra, S., Low-temperature paramagnetic anisotropy and zero-field splitting in high-spin (tetraphenylporphyrinato)iron(III) chloride. *Inorg. Chem.* **1979,** *18* (6), 1723-1724.

168. Behere, D. V.; Marathe, V. R.; Mitra, S., Paramagnetic anisotropy and zero-field splitting in tetraphenylporphinatoiron(III) chloride. *J. Am. Chem. Soc.* **1977,** *99* (12), 4149-4150.

169. Uenoyama, H., Far-infrared studies on hemin and hemin-like complexes. *Biochimica et Biophysica Acta* **1971,** *230* (3), 479-481.

170. La Mar, G. N.; Eaton, G. R.; Holm, R. H.; Walker, F. A., Proton magnetic resonance investigation of antiferromagnetic oxo-bridged ferric dimers and

related high-spin monomeric ferric complexes. *J. Am. Chem. Soc.* **1973,** *95* (1), 63-75.

171. Dolphin, D. H.; Sams, J. R.; Tsin, T. B.; Wong, K. L., Moessbauer-Zeeman spectra of some octaethylporphyrinato- and tetraphenylporphinatoiron(III) complexes. *J. Am. Chem. Soc.* **1978,** *100* (6), 1711-1718.

172. Browett, W. R.; Fucaloro, A. F.; Morgan, T. V.; Stephens, P. J., Magnetic circular dichroism determination of zero-field splitting in chloro(meso-tetraphenylporphinato)iron(III). *J. Am. Chem. Soc.* **1983,** *105*, 1868-1872.

173. Sato, M.; Rispin, A. S.; Kon, H., EPR studies on high-spin Fe(III) tetraphenylporphine having rhombic character. Spin Hamiltonian and crystal field analysis of *g* values. *Chem Phys* **1976,** *18*, 211-224.

174. Behere, D. V.; Goff, H. M., High-affinity binding of quinine to iron(III) porphyrins: novel formation of alkoxide complexes from alcohols and amines. *J. Am. Chem. Soc.* **1984,** *106* (17), 4945-4950.

175. Tin, P.; Bone, A. N.; Bui, N. N.; Zhang, Y.-Q.; Chang, T.; Moseley, D. H.; Ozerov, M.; Krzystek, J.; Cheng, Y.; Daemen, L. L.; Wang, X.; Song, L.; Chen, Y.-S.; Shao, D.; Wang, X.-Y.; Chen, X.-T.; Xue, Z. L., Advanced spectroscopic and computational studies of a cobalt(II) coordination polymer with single-ion magnet properties. *J. Phys. Chem. C* **2022,** *126* (31), 13268-13283.

176. Smith, B. A. Studies of tungsten alkyl alkylidyne compounds and iron porphyrin derivatives. University of Tennessee, Knoxville, TN, 2009.

177. Seeger, P. A.; Daemen, L. L.; Larese, J. Z., Resolution of VISION, a crystal-analyzer spectrometer. *Nucl. Instr. Meth. Phys. Res. A* **2009,** *604*, 719-728.

178. Kresse, G.; Furthmuller, J., Efficient iterative schemes for ab initio total-energy calculations using a plane-wave basis set. *Phys Rev B* **1996,** *54* (16), 11169-11186.

179. Wang, L.; Maxisch, T.; Ceder, G., Oxidation energies of transition metal oxides within the GGA+U framework. *Phys. Rev. B* **2006,** *73*, 195107.

180. Stoll, S.; Schweiger, A., EasySpin, a comprehensive software package for spectral simulation and analysis in EPR. *J. Magn. Reson.* **2006,** *178* (1), 42-55.

181. Stoll, S. EasySpin - EPR spectrum simulation. https://www.easyspin.org/ (accessed October 25, 2020).

182. Liu, Z. Studies of Molecular Magnetism and Dynamics by Inelastic Neutron Scattering and Nuclear Magnetic Resonance. M.S. Thesis, University of Tennessee, Knoxville, TN, 2019. https://trace.tennessee.edu/utk_gradthes/5449/

APPENDIX

Appendix A. Supporting Information for Chapter II

An E_i = 42.3 cm^{-1} was chosen to access a larger Q-range for Q-dependence analysis, though the increase in background noise made this analysis challenging, particularly for the peak at 25.72(17) cm^{-1}. Additionally, with E_i = 42.3 cm^{-1}, the overlapping peaks at 11.78(8) cm^{-1} and 12.73(9) cm^{-1} could not be resolved.

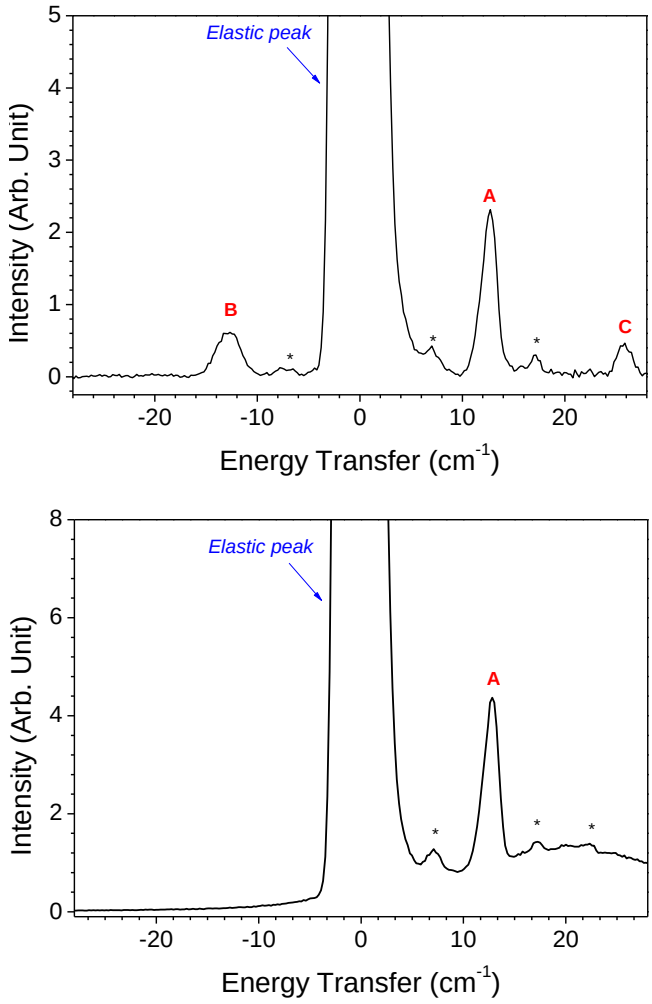


Figure A.1. INS spectra of **Fe-Cl** with incident neutron energy of E_i = 42.3 cm^{-1}: (Top) 20 K; (Bottom) 2 K. Each point in the plot contains the data over the entire available Q range. * Phonon modes.

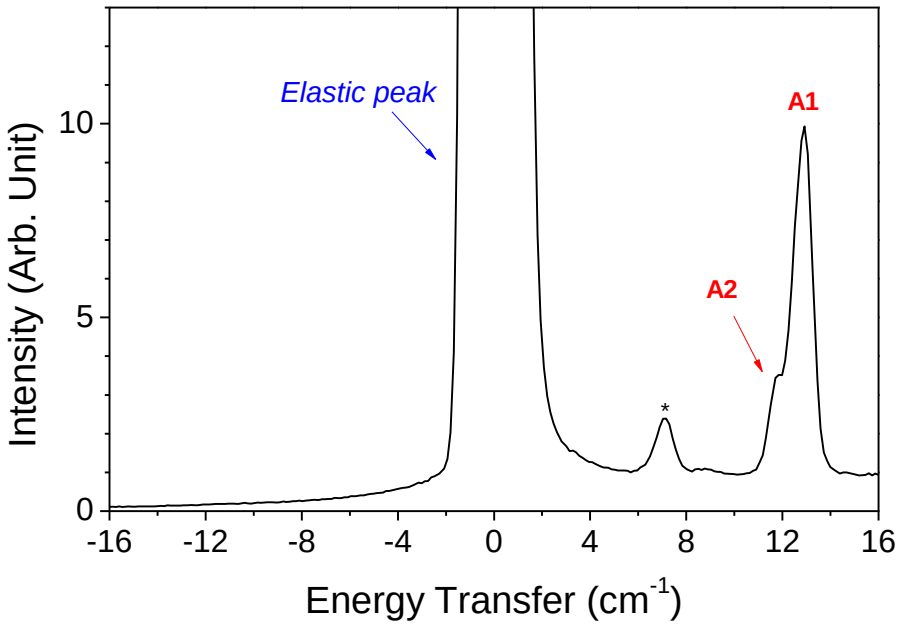


Figure A.2. INS spectrum of **Fe-Cl** at 2 K with incident energy E_i = 26.8 cm^{-1}. Each point in the plot contains the data over the entire available Q range. * Phonon modes.

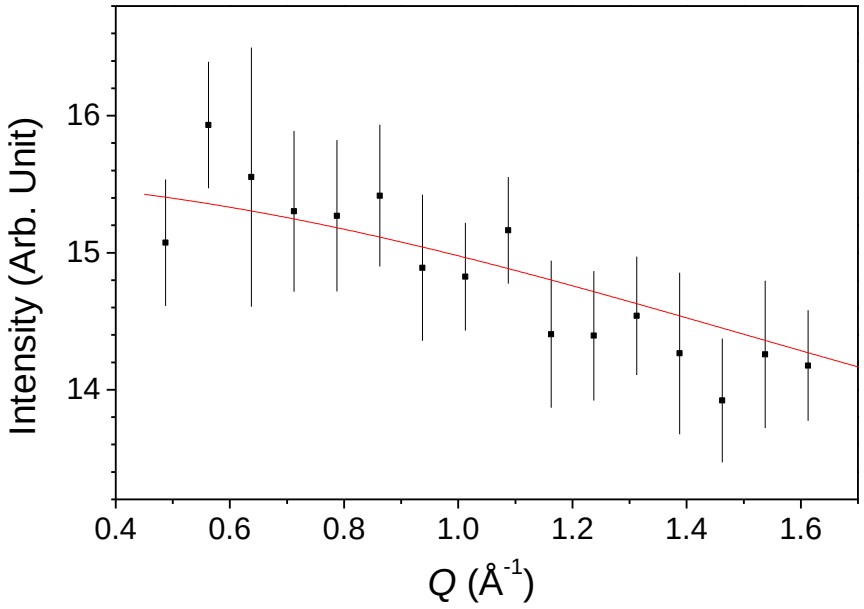


Figure A.3. *Q*-dependence plot of the overlapping magnetic Peak A at ~12.7(1) cm^{-1} for **Fe-Cl** at 2 K with E_i = 26.8 cm^{-1} in Figure A.2. Each point represents a *Q*-cut of 0.075 $Å^{-1}$. The red line is the fit from the single-molecule model which is in essence the intensity of the magnetic scattering factor $F^2(Q)$ in Eq. 2.1.

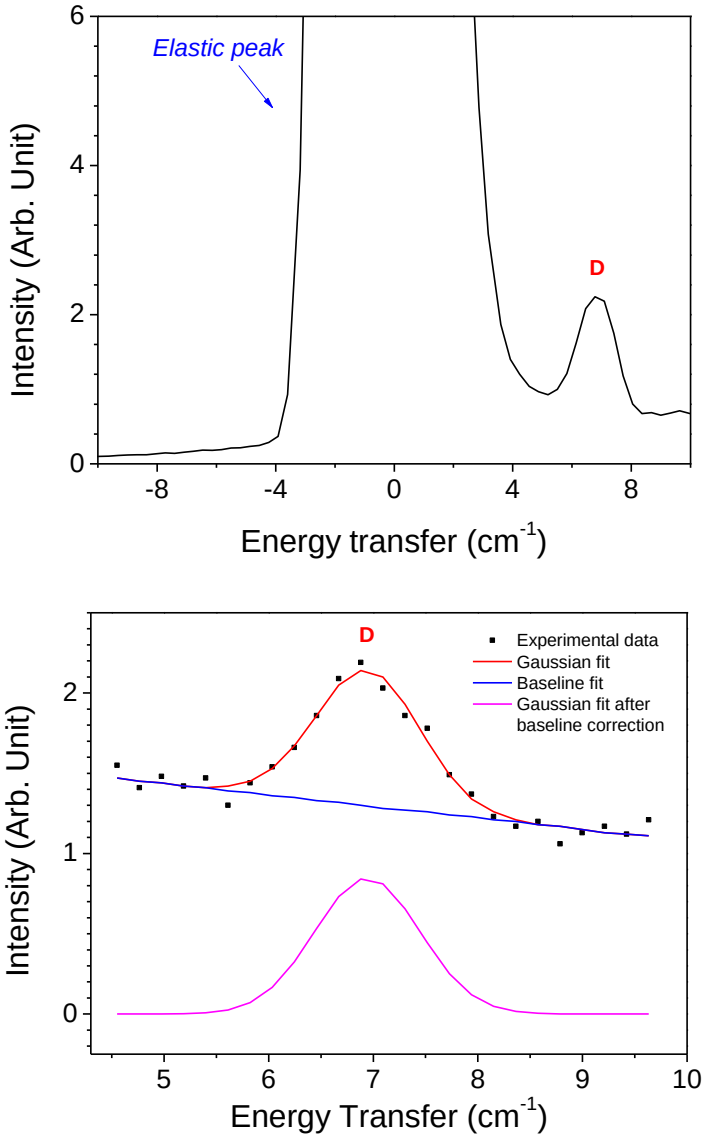


Figure A.4. (Top) INS spectrum of **Mn-Cl** at 2 K with E_i = 42.3 cm^{-1}. Each point in the plot contains the data over the entire available Q range. (Bottom) Peak **D** at Q = 1.7-1.8 Å^{-1} with a Gaussian fit and baseline. For the error bars of the experimental data, peak area, and estimated uncertainty of the Peak **D** energy, see Figure A.6 and Table A.2.

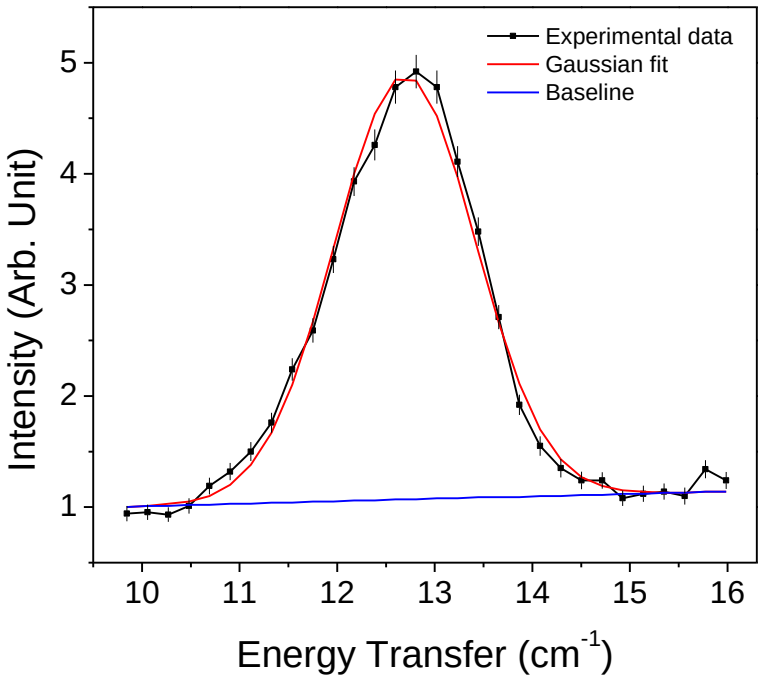


Figure A.5. Example of the fitting of the magnetic peaks in **Fe-Cl** to determine the intensity of the peak at a Q value. Temperature = 2 K; E_i = 42.3 cm^{-1}; Q = 1.5-1.6 Å^{-1}. The peak area of 6.896 is used as the intensity of the peak at Q = 1.55 Å^{-1}. Error associated with the peak position for respective E_i is estimated as 10% of the linewidth = 0.21 cm^{-1}. The step size in DAVE is 0.161 cm^{-1}.

Table A.1. Peak parameters for Figure A.5

Parameter	Value
Area	6.896(2)
Center	12.57(2) cm^{-1}
FWHM	2.10(3) cm^{-1}
Background	0.02369*x* + 0.7790

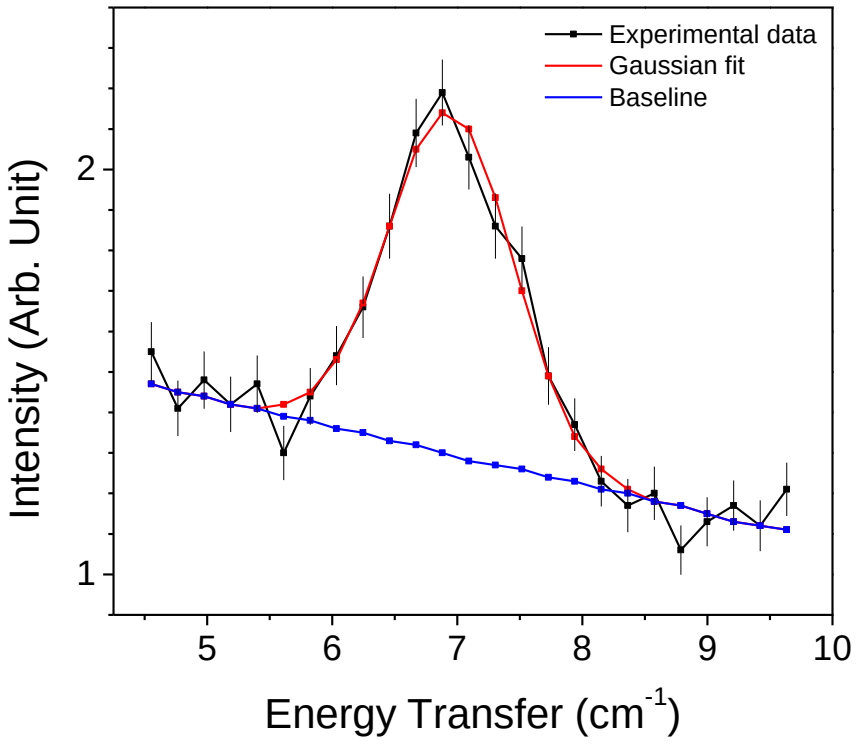


Figure A.6. Example of fitting of the magnetic peaks in **Mn-Cl** to determine *Q*-dependence. Temperature = 2 K, E_i = 42.3 cm^{-1}; *Q* = 1.7-1.8 Å^{-1}. The peak area of 1.070 is used as the intensity of the peak at *Q* = 1.7 Å^{-1} with a range of 0.1 Å^{-1}. Error associated with the peak positions for the respective E_i is estimated as 10% of the linewidth = 0.15 cm^{-1}. The step size in DAVE is 0.161 cm^{-1}.

Table A.2. Peak parameters for Figure A.6

Parameter	Value
Area	1.070(8)
Center	6.94(1) cm^{-1}
FWHM	1.46(3) cm^{-1}
Background	-0.07121*x* + 1.792

A.1. Fitting Using the Single-Molecule Model and the Average-Exchange Model

The single-molecule model is in essence the first part $\xi_0 F^2(Q)$ in Eq. 2.2 when f = 1.00. That is, there is *no* contribution from intermolecular interactions, and all contributions to the INS peak are from a single molecule. Since molecules of M(TPP)Cl (**Fe-Cl** and **Mn-Cl**) have just one magnetic center (*i.e.*, one metal ion with no *intra*molecular magnetic interactions), the fit by this model is expected to show the decrease in intensity I vs. Q increase but not the oscillation in the I vs. Q plot.

In the average-exchange model,[77] all intermolecular interactions are averaged. A basic version of this model was used by Gransbury and coworkers to fit the INS spectra of [Co(Me_3-tpa)(dbsq•)](PF_6) containing a semiquinonate radical ligand.[77] For our average-exchange model, $S(Q)_{eff}$ in the second part of Eq. 2.2 is replaced by $S(Q)_{av}$ in:

$$S(Q)_{av} = \xi_1{}' \left(1 - e^{-\frac{Q^2 R_{av}^2}{6}}\right) \qquad \text{(Eq. A.1)}$$

where R_{av} is the average distance between the central molecule and surrounding molecules.[77] ξ_1' is a fitting parameter for the average field model.

The parameter ξ_1' in Eq. A.1 indicates the amount of contributions from intermolecular interactions *other* than the average in the model. When ξ_1 = 1.00 (or 100%), all contributions are from the average. When ξ_1 < 1.00, interactions *not* represented by average in the model also make contributions to the intermolecular magnetic interactions.

One major feature of Eq. A.1 is that it does *not* mimic the $1 - \frac{\sin(QR)}{QR}$ part in Eq. 2.1 which leads to the oscillation when two magnetic centers with the distance of R

interact. That is, in the average-exchange model, the Q-dependent oscillatory nature of the intermolecular magnetic interactions is lost due to the average over all possible interactions. Therefore, the function in Eq. A.1 is dependent on the initial peak intensity at low Q. Since our data is not in the Q range of this downturn, we use the distance R_{eff} from the effective-field model here in the average-exchange model.

The fits by both the single-molecule model and the average-exchange model are given in Figure 2.4-Top. Indeed, the fits by the neither model show the oscillations, in contrast to the fits by the effective-field model. However, both models show the intensity decrease with Q increase. In addition, for **Fe-Cl**, the fits by single-molecule model and average-exchange model are close. This is also because of the separation of the single-molecule Peak **A1** and assembly Peak **A2** from intermolecular interactions. Q-dependence of the fit by the average-exchange model will collapse to the single-molecule model, as the contribution from the intermolecular interactions is reduced to zero, i.e., f = 1.00 in Eq. 2.2. For **Mn-Cl**, in contrast, there is large deviation between the fit by the single-molecule model and the fit by the average-exchange model in Figure 2.4-Top. This is consistent with the fact that, in the overlapping Peak **D** in Figure 2.3 containing excitations from both the single molecule and intermolecular interactions, the contribution from the latter is higher than that in **Fe-Cl**, leading to a larger deviation between the fits of the average-exchange model and the single-molecule model for **Mn-Cl**.

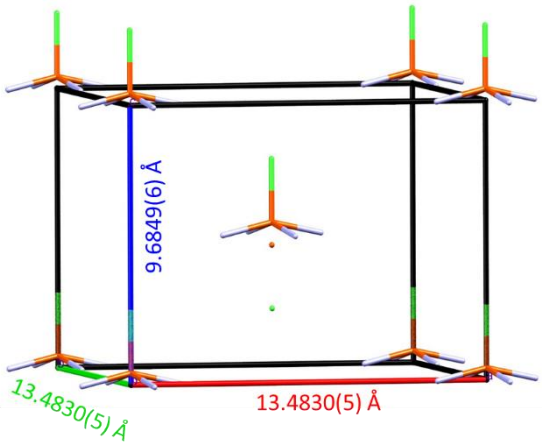
The ξ_1' value in Eq. A.1, indicating contributions by the average-exchange model and the exchange interactions *not* from the average, is significantly smaller for **Fe-Cl** (ξ_1'= 0.62) than for **Mn-Cl** (ξ_1' = 0.95). Thus, for **Mn-Cl**, both ξ_1 and ξ_1' values are

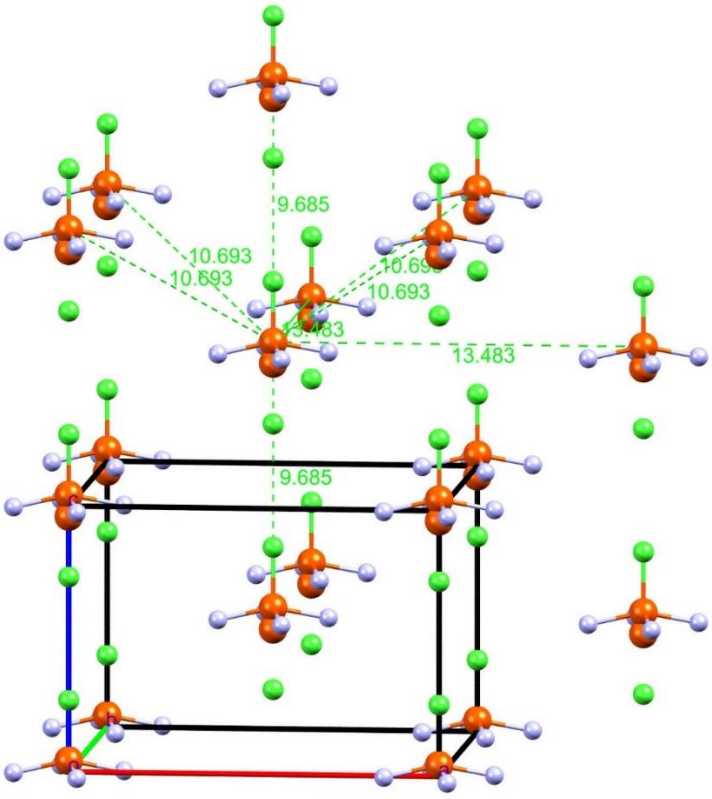
closer to 1.00, suggesting that the complex has more characteristics of either the effective-field model or the average-exchange model with little contributions not from the models. For **Fe-Cl**, both ξ_1 and ξ_1' values show larger deviations from 1.00, suggesting the presence of intermolecular magnetic interactions that the models do not represent. Overall, the parameters ξ_1 for **Fe-Cl** and **Mn-Cl** are reasonable, given the extra valence d electron in the $S = 3/2$, d^5 Fe^{3+} complex **Fe-Cl** than $S = 2$, d^4 Mn^{3+} complex **Mn-Cl**.

Table A.3. Fitting parameters for the effective-field and average-exchange models

	Fe(TPP)Cl (**Fe-Cl**)		Mn(TPP)Cl (**Mn-Cl**)	
Parameter	Effective-field model	Average-exchange model	Effective-field model	Average-exchange model
ξ_0	7.83	7.52	0.79	1.03
ξ_1 or ξ_1'	0.96 (ξ_1)	0.62 (ξ_1')	0.99 (ξ_1)	0.95 (ξ_1')
R_{eff} (Å)	11.84		13.22	
f	0.95	0.99	0.54	0.73

Figure A.7. Tetragonal crystal structure of **Fe-Cl** at 20 K.[8] (Top) Unit cell lengths. (Bottom) Relevant distances in the structure. Intermolecular (or Fe···Fe) distances are 10.693 Å and 13.483 Å. Crystal structures of **Fe-Cl** and Mn(TPP)Cl (**Mn-Cl**) are essentially isostructural.[8, 16]


9.6849(6) Å
13.4830(5) Å
13.4830(5) Å


9.685
10.693
10.693
10.693
10.693
13.483
13.483
9.685

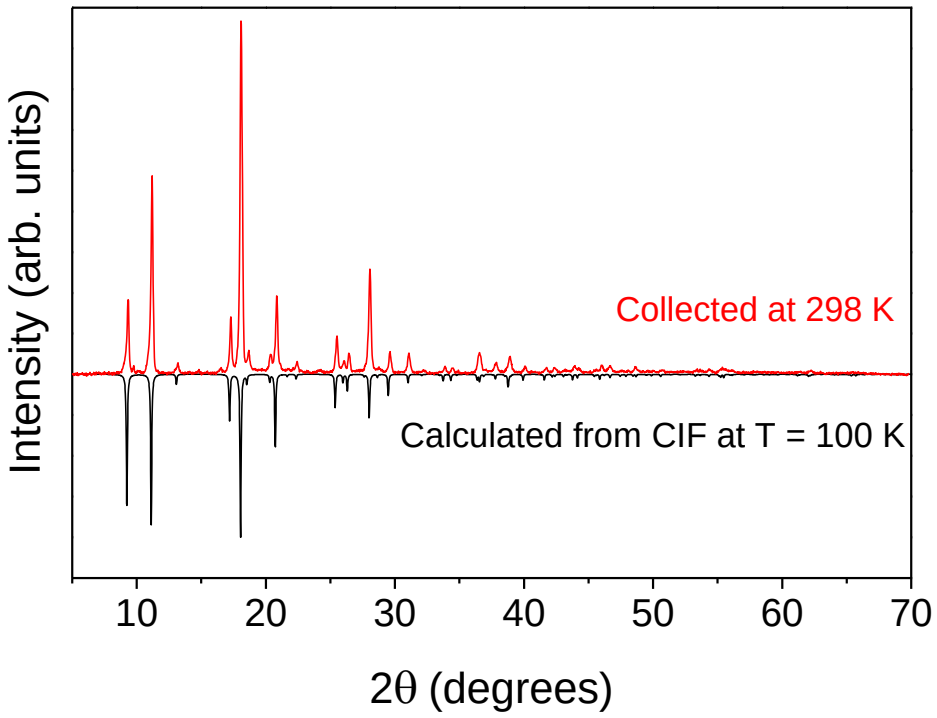


Figure A.8. Powder X-ray diffraction of **Fe-Cl** sample at 298 K (red) compared to pattern calculated from 100 K single-crystal X-ray data (black).

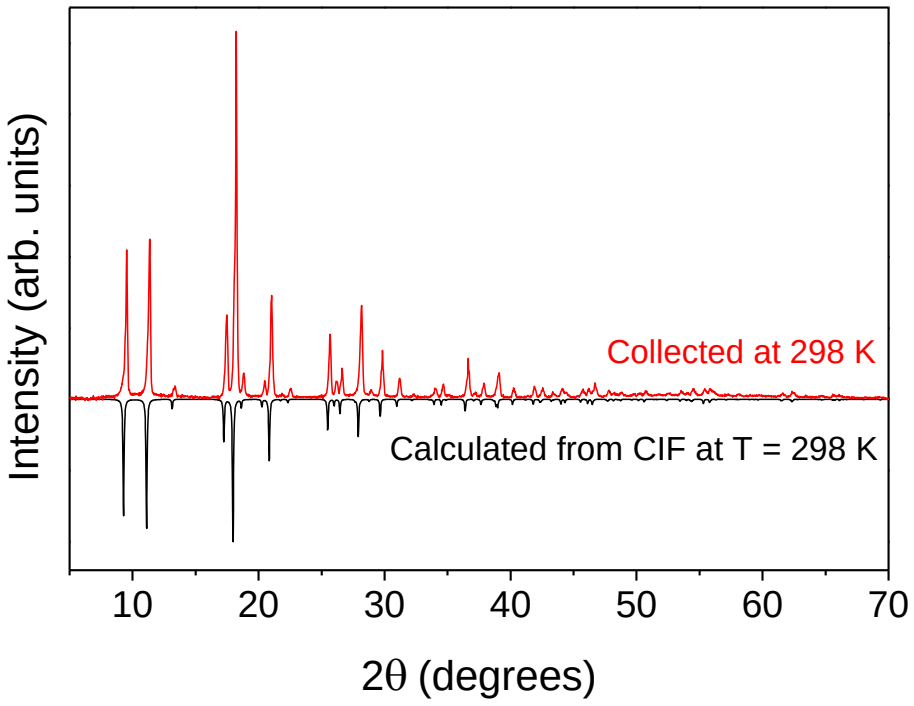


Figure A.9. Powder X-ray diffraction data of **Mn-Cl** sample at 298 K (red) compared to pattern calculated from 298 K single crystal X-ray data (black).

Appendix B. Supporting Information for Chapter III

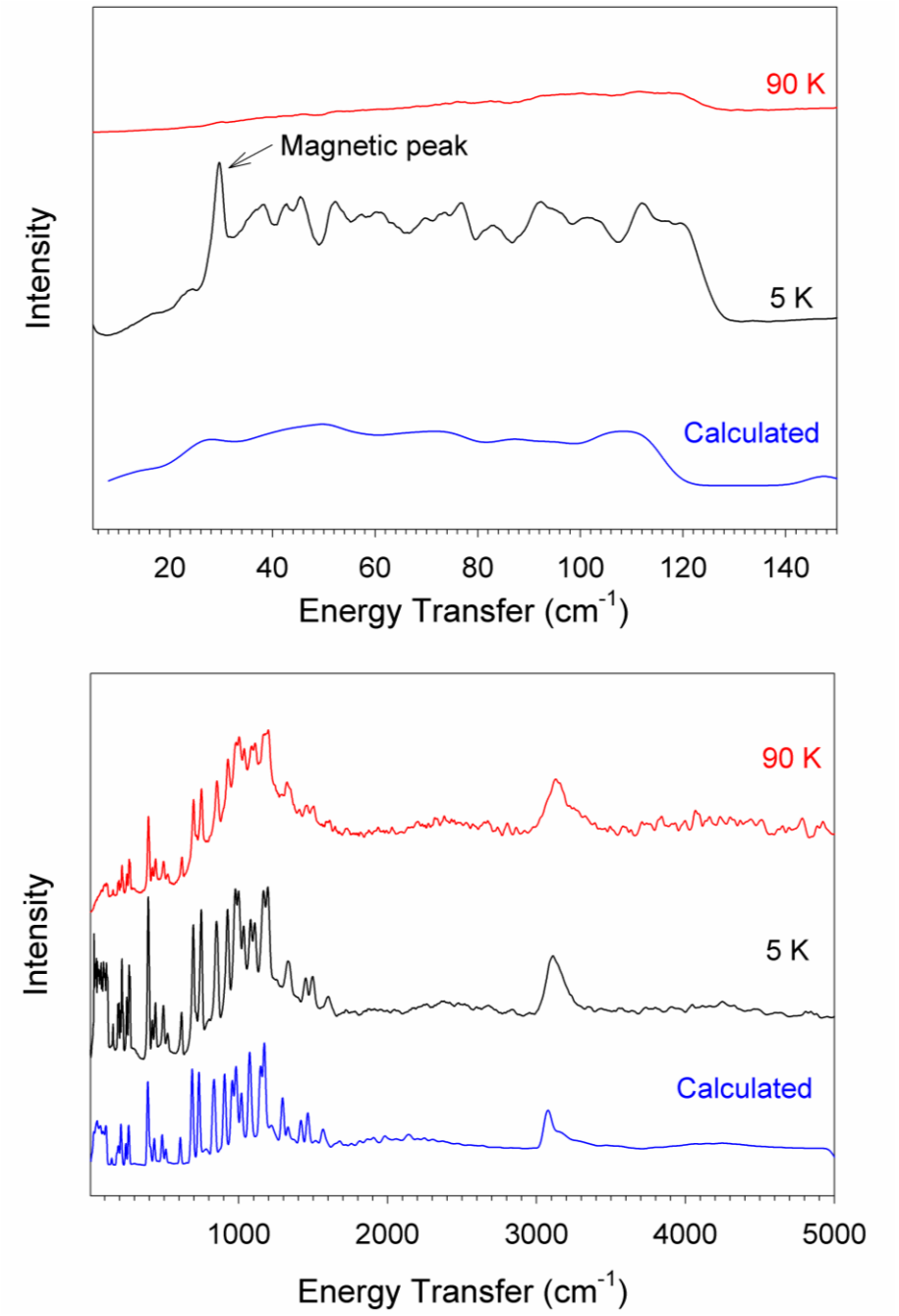


Figure B.1. Bose-corrected, forward-scattering variable-temperature INS spectra (5-5000 cm^{-1}) of **Co-Cl** (by VISION) with the VASP calculated INS spectrum.

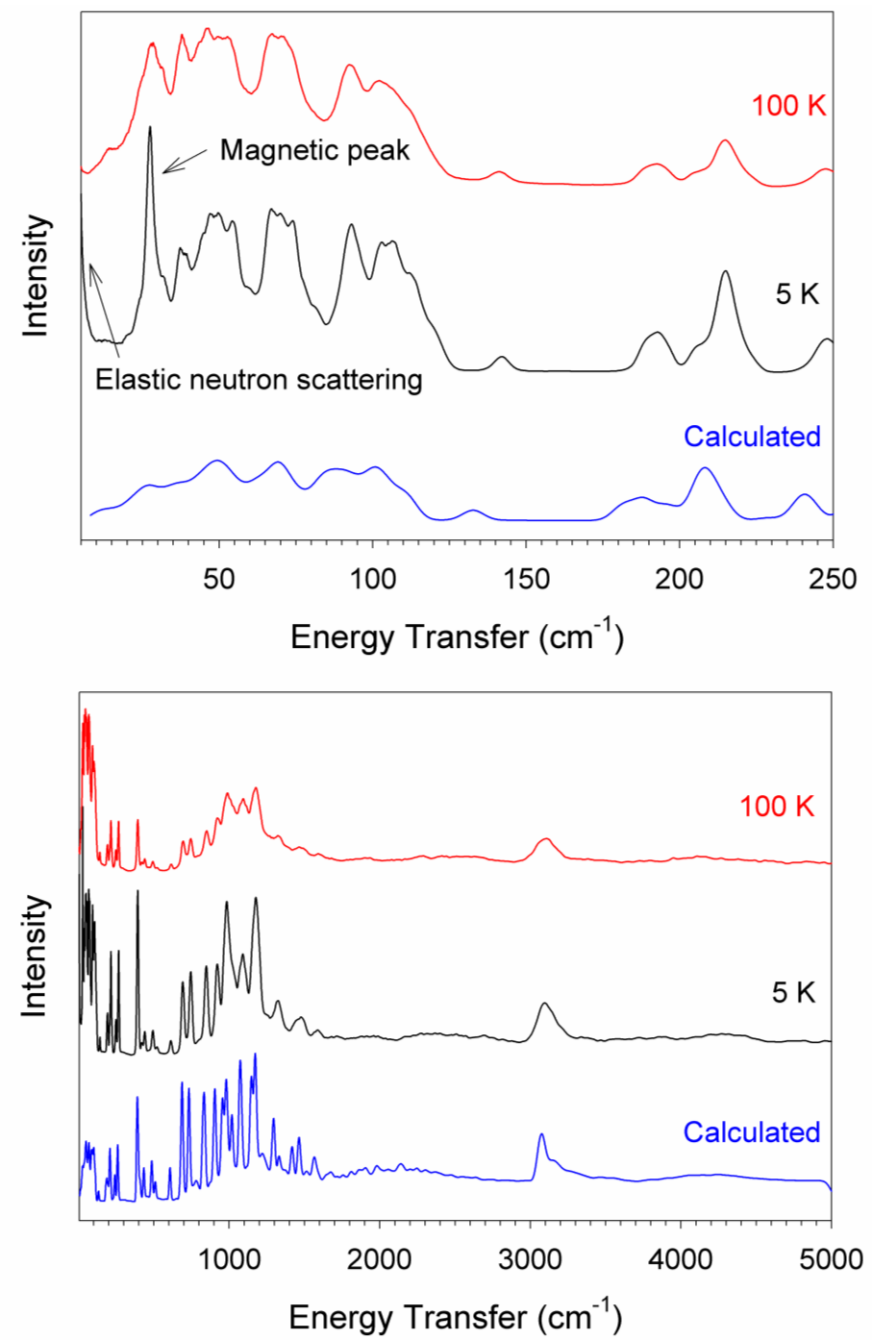


Figure B.2. Bose-corrected, forward-scattering variable-temperature INS spectra (5-5000 cm^{-1}) of **Co-Br** (by VISION) with the VASP calculated INS spectrum.

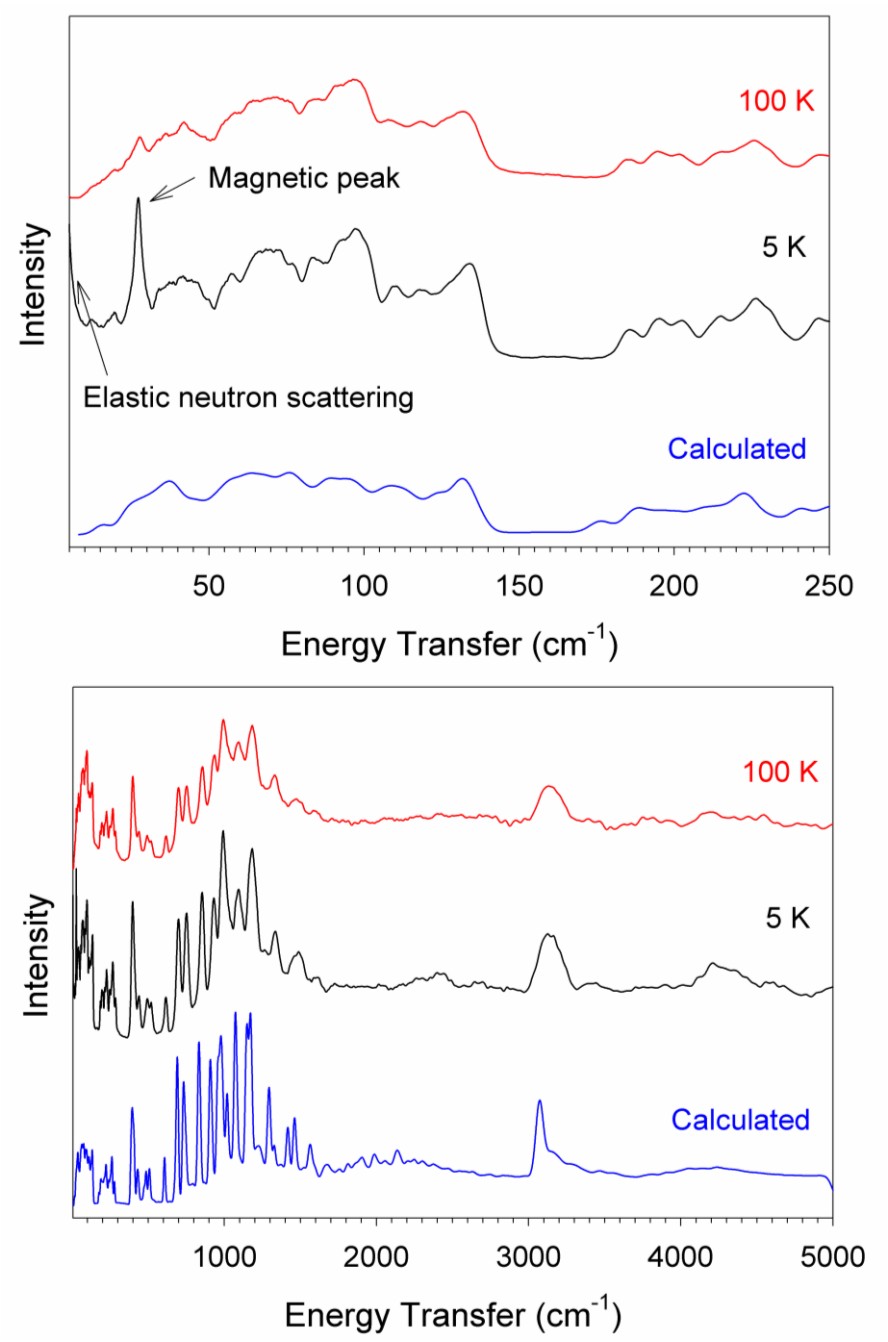


Figure B.3. Bose-corrected, forward-scattering variable-temperature INS spectra (5-5000 cm^{-1}) of **Co-I** (by VISION) with the VASP calculated INS spectrum.

B.1. Far-IR Magneto-Spectroscopy Studies

The spin-phonon coupling Hamiltonians for FIRMS spectra of **Co-Br** (Eq. B.1) in Figure 3.5-Top and for **Co-I** (Eq. B.2) in Figure 3.5-Bottom are as follows:

$$H = \begin{pmatrix} E_{sp} & \Lambda_1 & \Lambda_2 & \Lambda_3 & \Lambda_4 & \Lambda_5 & \Lambda_6 \\ \Lambda_1 & E_{ph1} & 0 & 0 & 0 & 0 & 0 \\ \Lambda_2 & 0 & E_{ph2} & 0 & 0 & 0 & 0 \\ \Lambda_3 & 0 & 0 & E_{ph3} & 0 & 0 & 0 \\ \Lambda_4 & 0 & 0 & 0 & E_{ph4} & 0 & 0 \\ \Lambda_5 & 0 & 0 & 0 & 0 & E_{ph5} & 0 \\ \Lambda_6 & 0 & 0 & 0 & 0 & 0 & E_{ph6} \end{pmatrix} \quad \text{(Eq. B.1)}$$

$$H = \begin{pmatrix} E_{sp} & \Lambda_1 & \Lambda_2 & \Lambda_3 & \Lambda_4 & \Lambda_5 & \Lambda_6 & \Lambda_7 & \Lambda_8 & \Lambda_9 \\ \Lambda_1 & E_{ph1} & 0 & 0 & 0 & 0 & 0 & 0 & 0 & 0 \\ \Lambda_2 & 0 & E_{ph2} & 0 & 0 & 0 & 0 & 0 & 0 & 0 \\ \Lambda_3 & 0 & 0 & E_{ph3} & 0 & 0 & 0 & 0 & 0 & 0 \\ \Lambda_4 & 0 & 0 & 0 & E_{ph4} & 0 & 0 & 0 & 0 & 0 \\ \Lambda_5 & 0 & 0 & 0 & 0 & E_{ph5} & 0 & 0 & 0 & 0 \\ \Lambda_6 & 0 & 0 & 0 & 0 & 0 & E_{ph6} & 0 & 0 & 0 \\ \Lambda_7 & 0 & 0 & 0 & 0 & 0 & 0 & E_{ph7} & 0 & 0 \\ \Lambda_8 & 0 & 0 & 0 & 0 & 0 & 0 & 0 & E_{ph8} & 0 \\ \Lambda_9 & 0 & 0 & 0 & 0 & 0 & 0 & 0 & 0 & E_{ph9} \end{pmatrix} \quad \text{(Eq. B.2)}$$

Figure B.4. (Top) Far-IR transmittance spectra of **Co-Cl** at 0 and 17 T with assignments of phonon peaks based on the calculated *u* phonons in Table B.4. A few calculated *u* phonons in the range were not assigned. (Bottom) Plot of spectra normalized by average, which minimizes phonon features that do not change with magnetic fields.

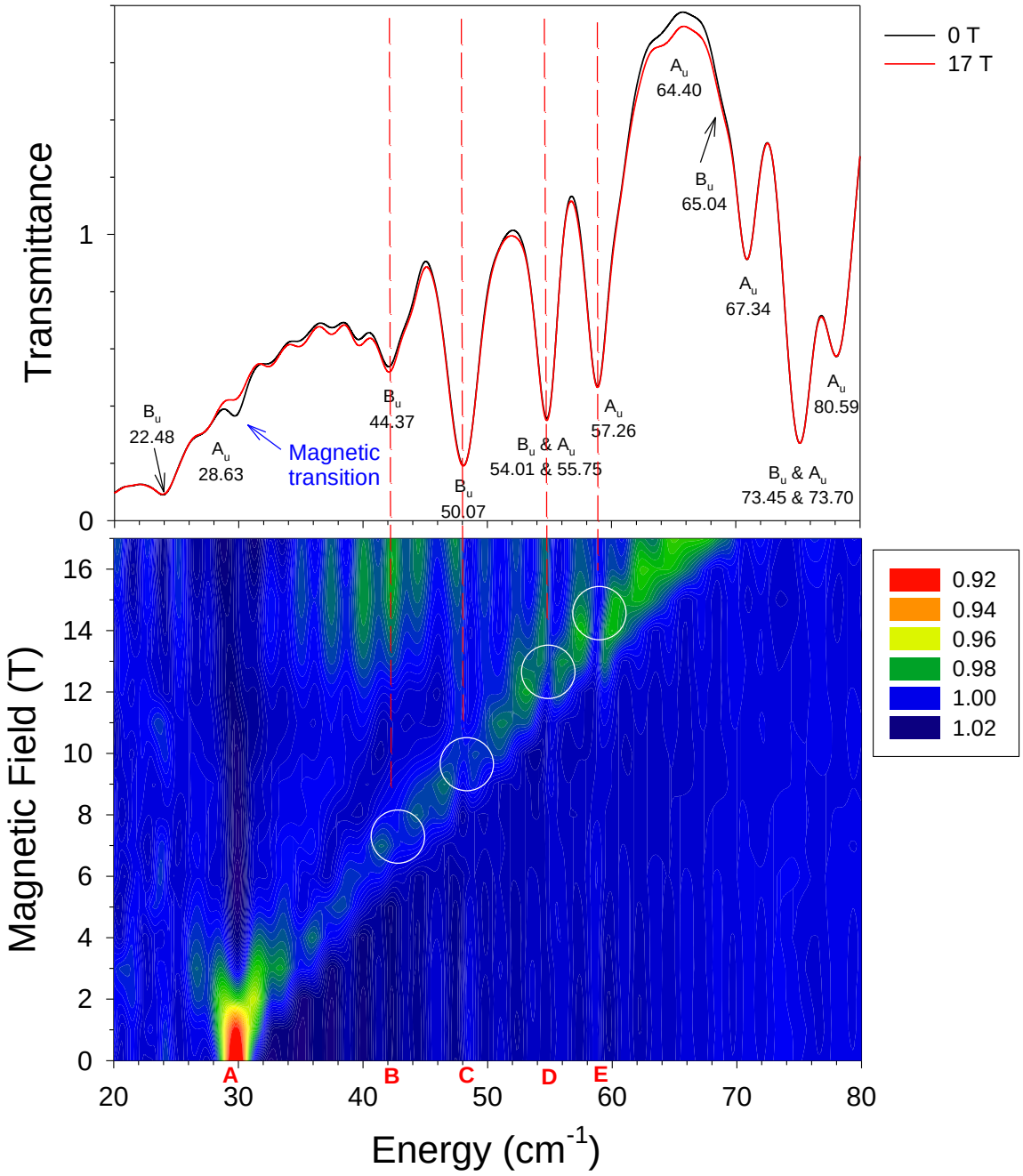

0 T
17 T
Transmittance
1
0
B_u 22.48
A_u 28.63
Magnetic transition
B_u 44.37
B_u 50.07
B_u & A_u 54.01 & 55.75
A_u 57.26
A_u 64.40
B_u 65.04
A_u 67.34
B_u & A_u 73.45 & 73.70
A_u 80.59
Magnetic Field (T)
16
14
12
10
8
6
4
2
0
A
B
C
D
E
20
30
40
50
60
70
80
Energy (cm^{-1})
0.92
0.94
0.96
0.98
1.00
1.02

Figure B.5. (Top) Far-IR transmittance spectra of **Co-Br** at 0 and 17 T with assignments of phonon peaks based on the calculated *u* phonons in Table B.5. A few calculated *u* phonons in the range were not assigned. (Bottom) Plot of spectra normalized by average, which minimizes phonon features that do not change with magnetic fields.

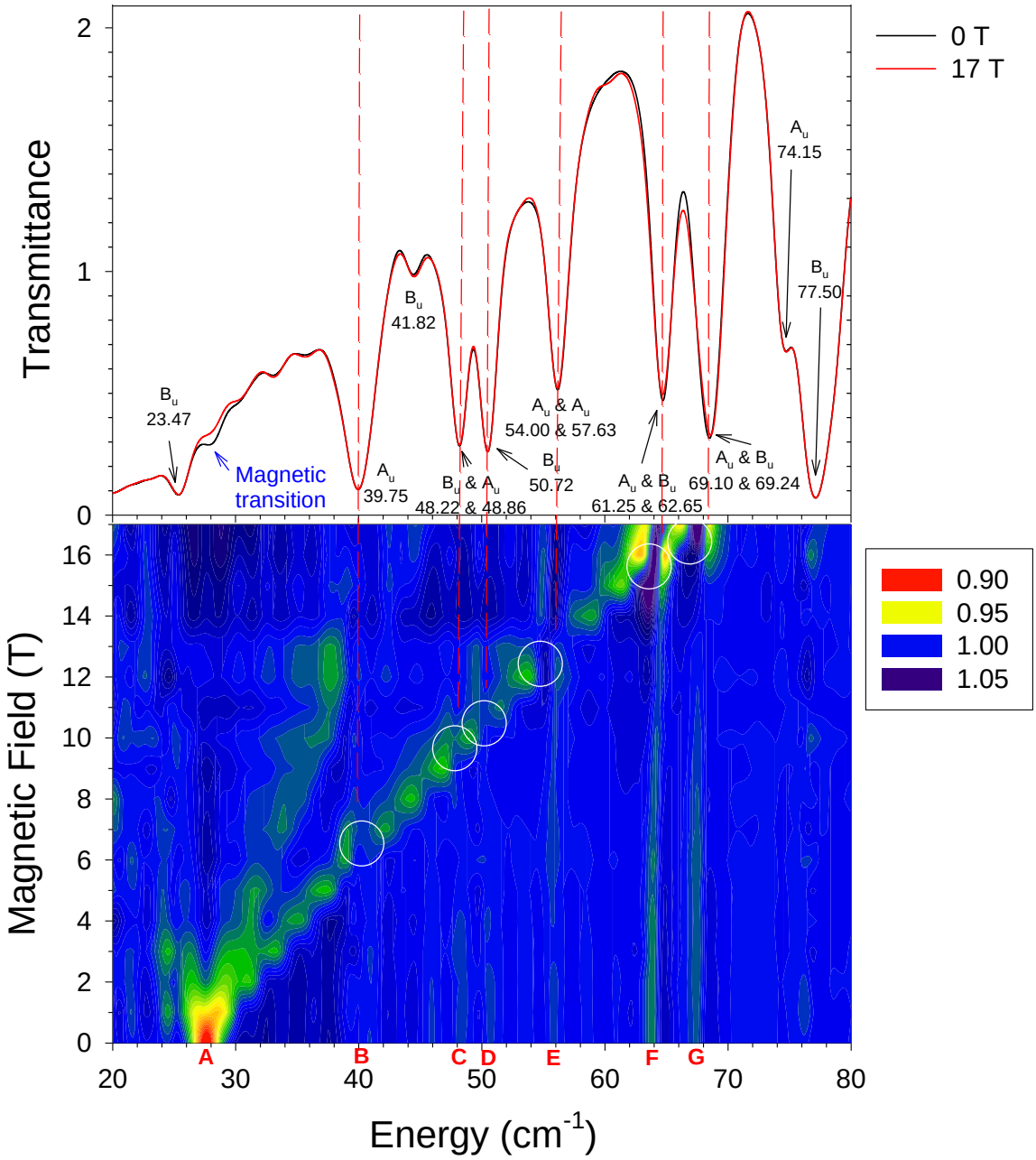
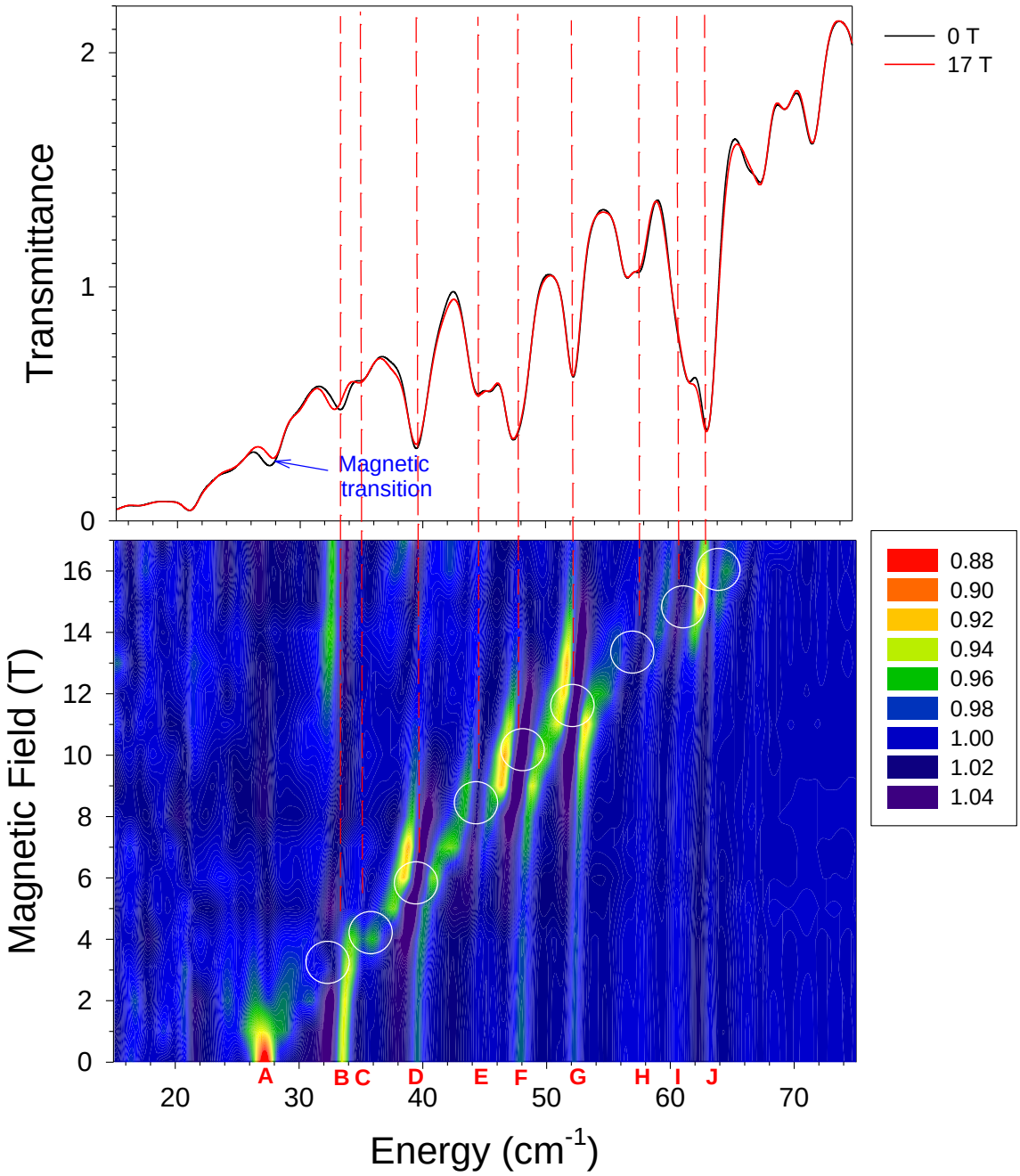

Transmittance
0 T
17 T
B_u 23.47
Magnetic transition
A_u 39.75
B_u 41.82
B_u & A_u 48.22 & 48.86
B_u 50.72
A_u & A_u 54.00 & 57.63
A_u & B_u 61.25 & 62.65
A_u & B_u 69.10 & 69.24
A_u 74.15
B_u 77.50
Magnetic Field (T)
0.90
0.95
1.00
1.05
A
B
C
D
E
F
G
Energy (cm^{-1})

Figure B.6. (Top) Transmittance far-IR spectra of **Co-I** at 0 and 17 T. We were not able to assign many *u* phonons in the 0 T spectrum based the calculated phonons in Table B.6 below–No calculated phonons were thus assigned to the spectrum. (Bottom) Plot of spectra normalized by average, which minimizes phonon features that do not change with magnetic fields.


Transmittance
0 T
17 T
Magnetic
transition
Magnetic Field (T)
Energy (cm-1)
A
B C
D
E
F
G
H
I
J
0.88
0.90
0.92
0.94
0.96
0.98
1.00
1.02
1.04

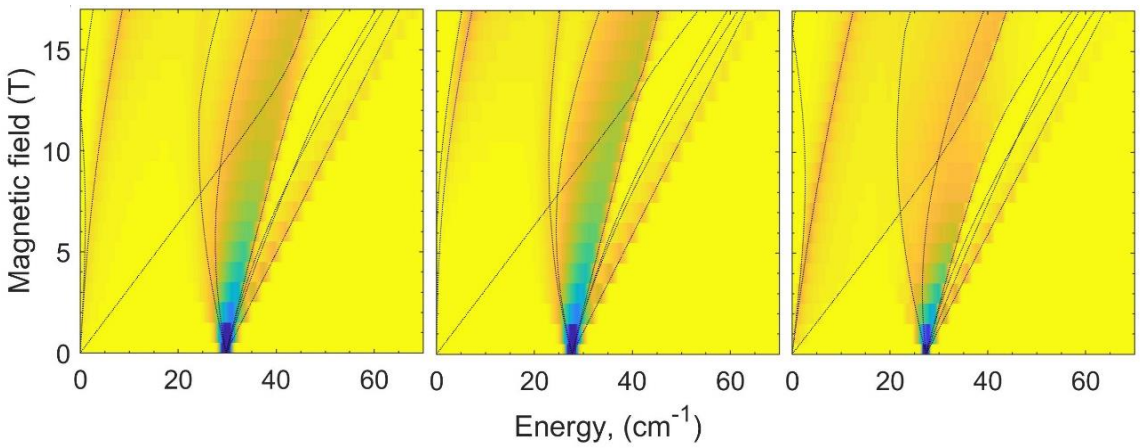


Figure B.7. Plots of magnetic resonance absorptions (intensity vs. field and energy) calculated for **Co-Cl** (left), **Co-Br** (middle), and **Co-I** (right). The *EasySpin* package[180-181] was used to simulate the powder spectrum in the frequency domain, while the spin-Hamiltonian parameters were taken from Tables 3.1-3.2 in the main text. The lines show turning points in the powder-patterned HFEPR spectra.

B.2. Magneto-Raman Studies

Raman spectroscopy, a light-scattering technique based upon exciting the molecule from the ground state to a higher virtual state, followed by the relaxation of the molecule back to a different state, can also be used to determine the energies of the excited states. Some of us have shown recently that spin-phonon couplings with Raman-active phonons in $Co(acac)_2(H_2O)_2$, $Co(acac)_2(D_2O)_2$, and $Co(acac\text{-}d_7)_2(D_2O)_2$ impart both spin and phonon features to the coupled peaks, leading to the observations of the coupled peaks and distinct spin-phonon couplings in the magneto-Raman spectra, even though the magnetic transitions between ground and excited states in the complexes are vanishingly weak in conventional Raman spectroscopy.

B.2.1. Experimental

Raman samples were prepared with unoriented single crystals of **Co-Cl**, **Co-Br**, and **Co-I**. Data were collected by a backscattering Faraday geometry using a 532 nm laser at a 14 T Superconducting Magnet (SCM) in the Electron Magnetic Resonance (EMR) facility. Crystals of samples were cooled at 5 K. Collected scattered light was guided via an optical fiber to a spectrometer equipped with a liquid nitrogen-cooled CCD camera.

B.2.2. Spectra

Magneto-Raman spectroscopy at 0-14 T magnetic fields was also used to characterize **Co-Cl**, **Co-Br**, and **Co-I**. The Raman spectra do not reveal the peak corresponding to the ZFS transitions in the complexes. The magneto-Raman spectra of **Co-Cl**, **Co-Br**, and **Co-I** in the 20-75 cm^{-1} are shown in Figures S5, S6, and S7,

respectively. Raman spectra of the three complexes at 0 T with an extended energy range are used below in the discussion of phonon spectra.

There are many VASP-calculated *g*, Raman-active modes in the 20-75 cm^{-1} range (Tables B.4-B.6 below). Attempts to assign them to the peaks in Figures B.8-B.10 were not successful.

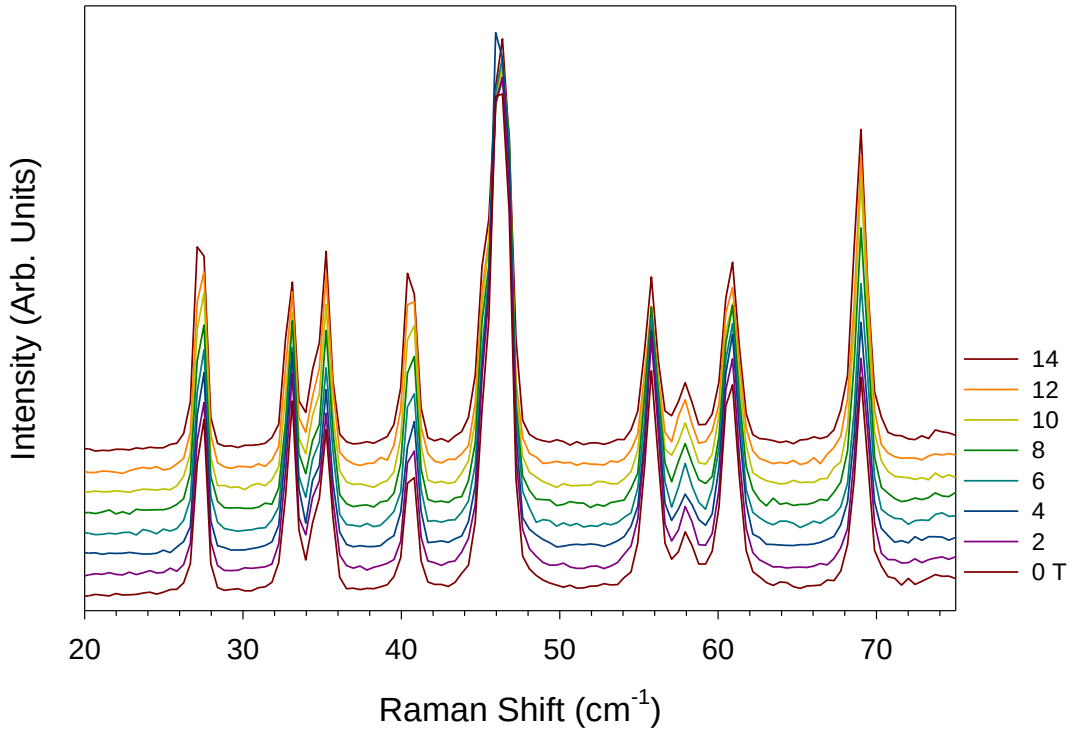


Figure B.8. Magneto-Raman spectra of **Co-Cl** at 5 K.

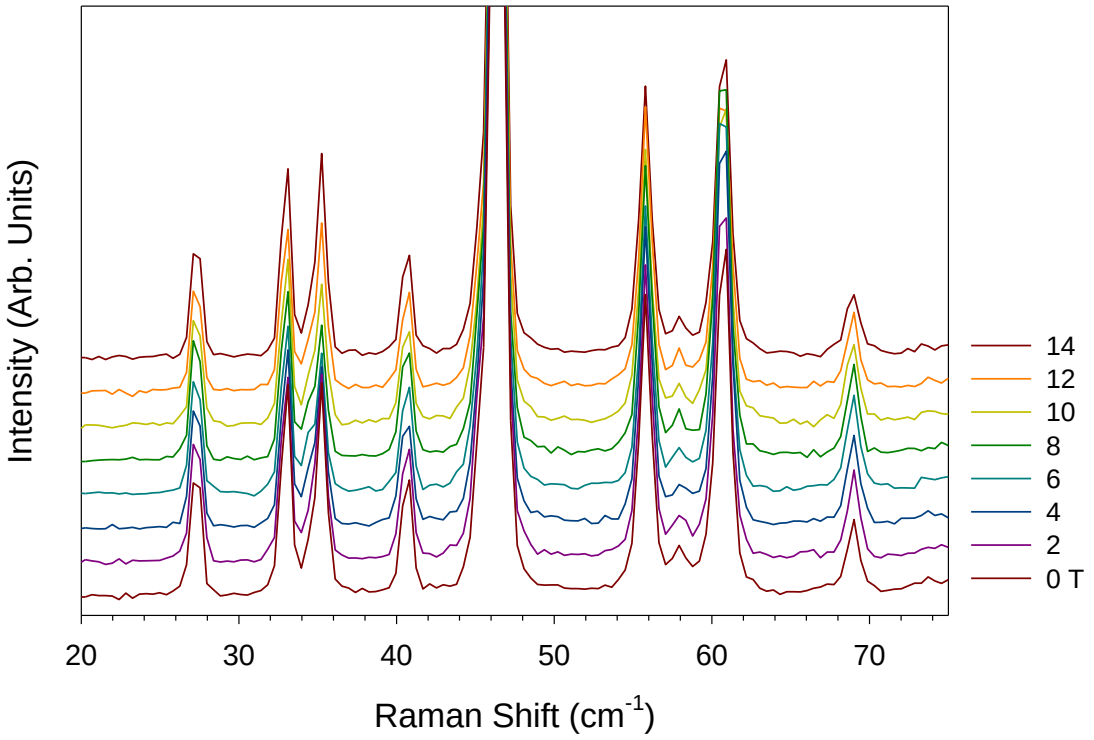


Figure B.9. Magneto-Raman spectra of **Co-Br** at 5 K.

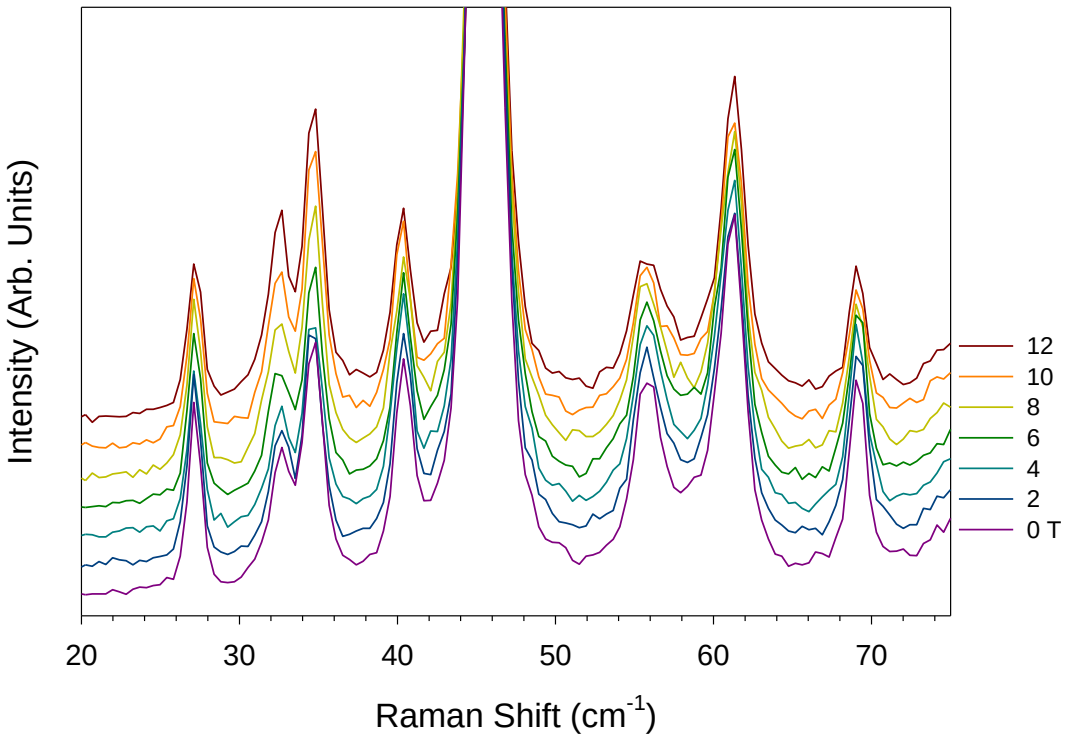


Figure B.10. Magneto-Raman spectra of **Co-I** at 5 K.

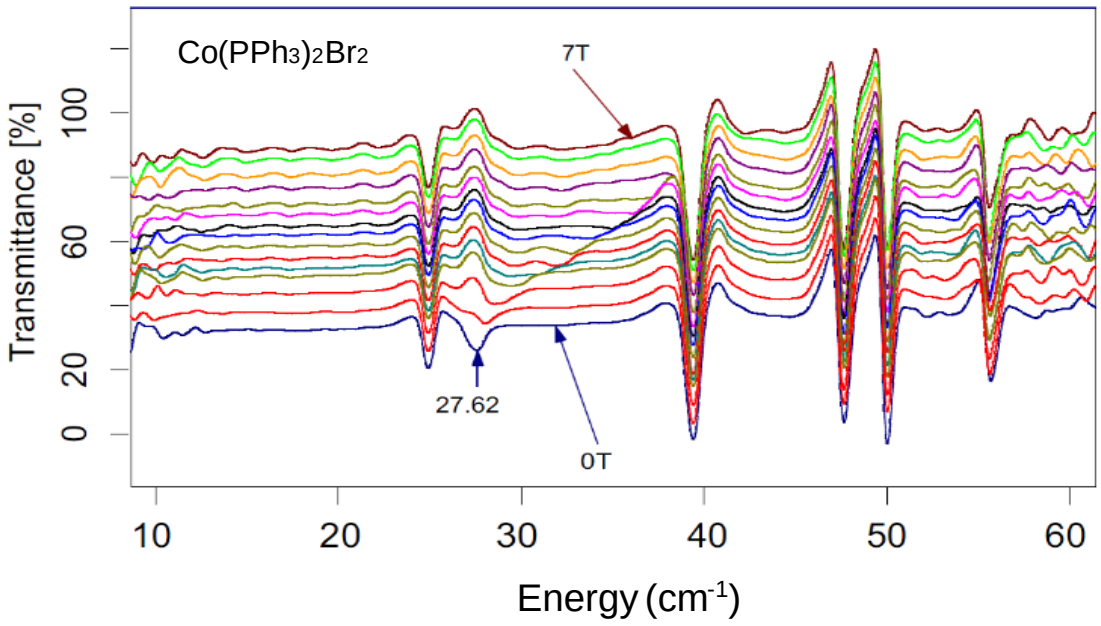


Figure B.11. Relative transmittance at 5 K in **Co-Br** upon changing the field from 0 to 7 T. The magnetic resonance at 27.62 cm^{-1} splits upon field change, while all other peaks are field-independent.

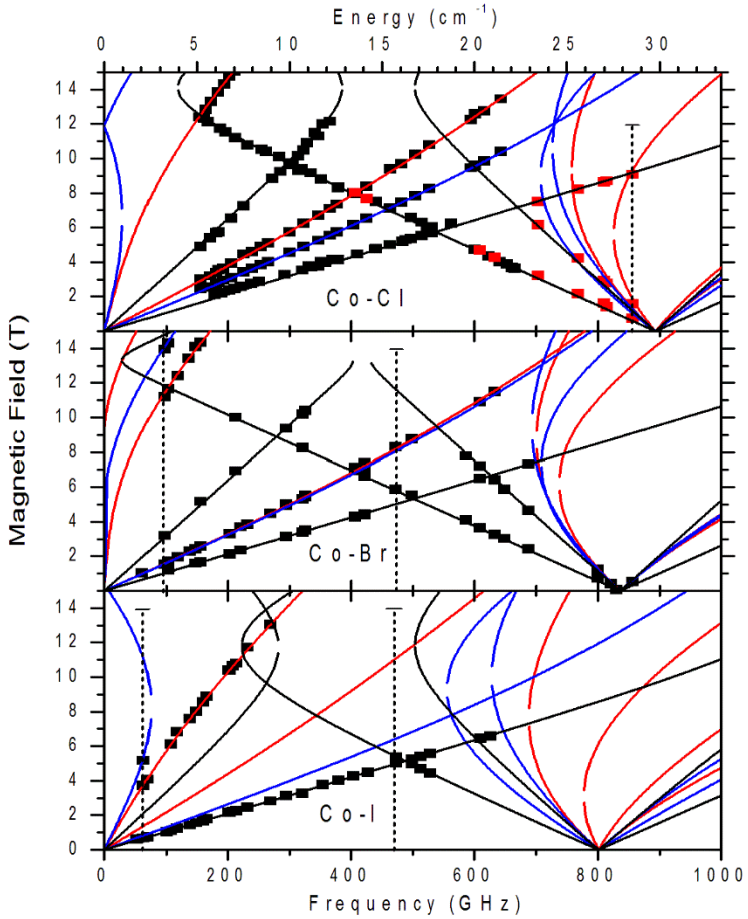


Figure B.12. Two-dimensional maps (field vs. frequency/energy) of turning points in the HFEPR spectra of **Co-Cl** (top), **Co-Br** (middle), and **Co-I** (bottom). The squares are experimental points. The red squares in the top window represent new data points obtained within this work. The curves were drawn using best-fitted spin-Hamiltonian parameters as in Tables 3.1-3.2. Red curves: resonances with $B||x$ axis of the ZFS tensor; blue: $B||y$, black: $B||z$. The dashed vertical lines represent the frequencies at which the spectra shown in Figures B.13-B.18 were recorded.

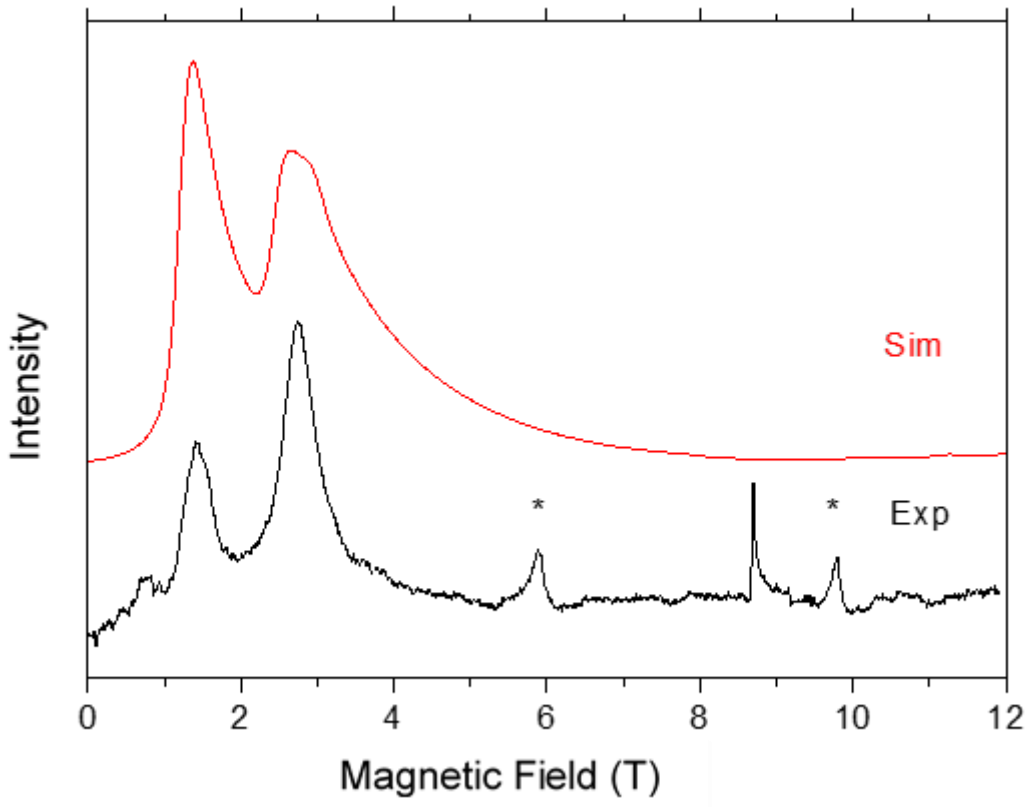


Figure B.13. HFEPR spectra of loose (unrestrained) sample of **Co-Cl** at 815 GHz and 10 K (black trace), accompanied by a powder-pattern simulation using spin-Hamiltonian parameters in Table 1 (red trace). The experimental spectrum was obtained using optical modulation (chopping) of the sub-THz wave beam and thus resulted in an absorptive shape. All the resonances are parallel ($B_0||z$) turning points due to field-induced alignment (torqueing) of the crystallites. The sharp resonance at ~8.7 T is the nominally forbidden intra-Kramers $M_S = -3/2 \rightarrow +3/2$ transition that particularly benefits from field torqueing and thus does not show up in the simulation. The two other resonances in the upper spectrum marked by asterisks originate from a Mn^{III} complex used to calibrate the frequency.

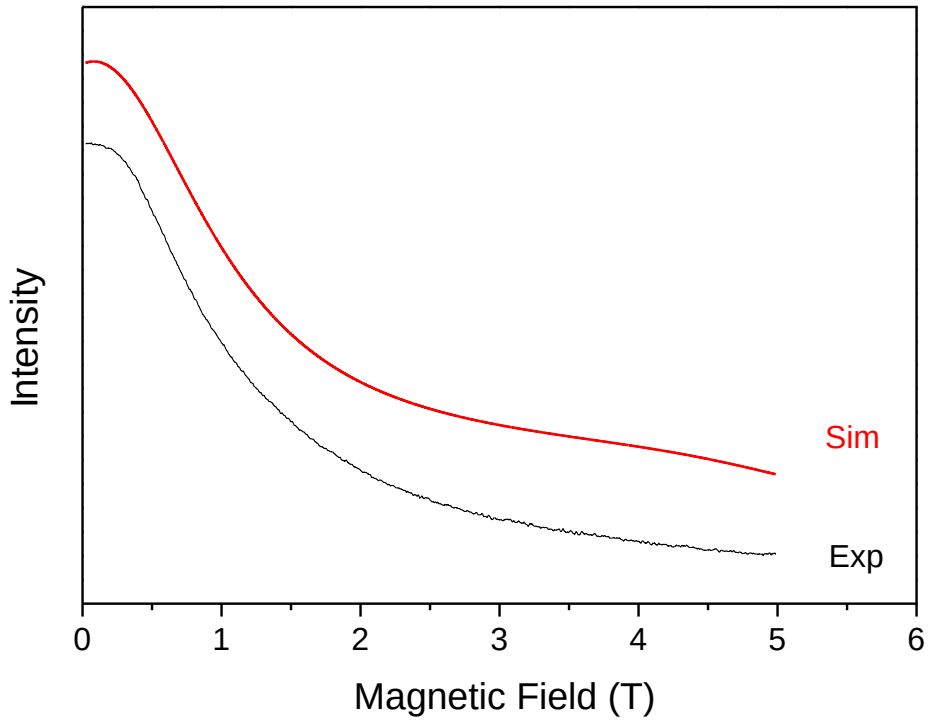


Figure B.14. Optically-modulated HFEPR spectrum of a loose (unrestrained) sample of **Co-Br** at 830 GHz and 10 K (black trace), accompanied by a simulation using spin-Hamiltonian parameters as in Table 1 (red trace). This frequency almost exactly matches the zero-field gap energy of this particular system (27.6 cm^{-1} = 828 GHz as obtained from both FIRMS and FD-FT THz-EPR) and results in a characteristic "half-dome" shape of the resonance recorded in the absorption mode.

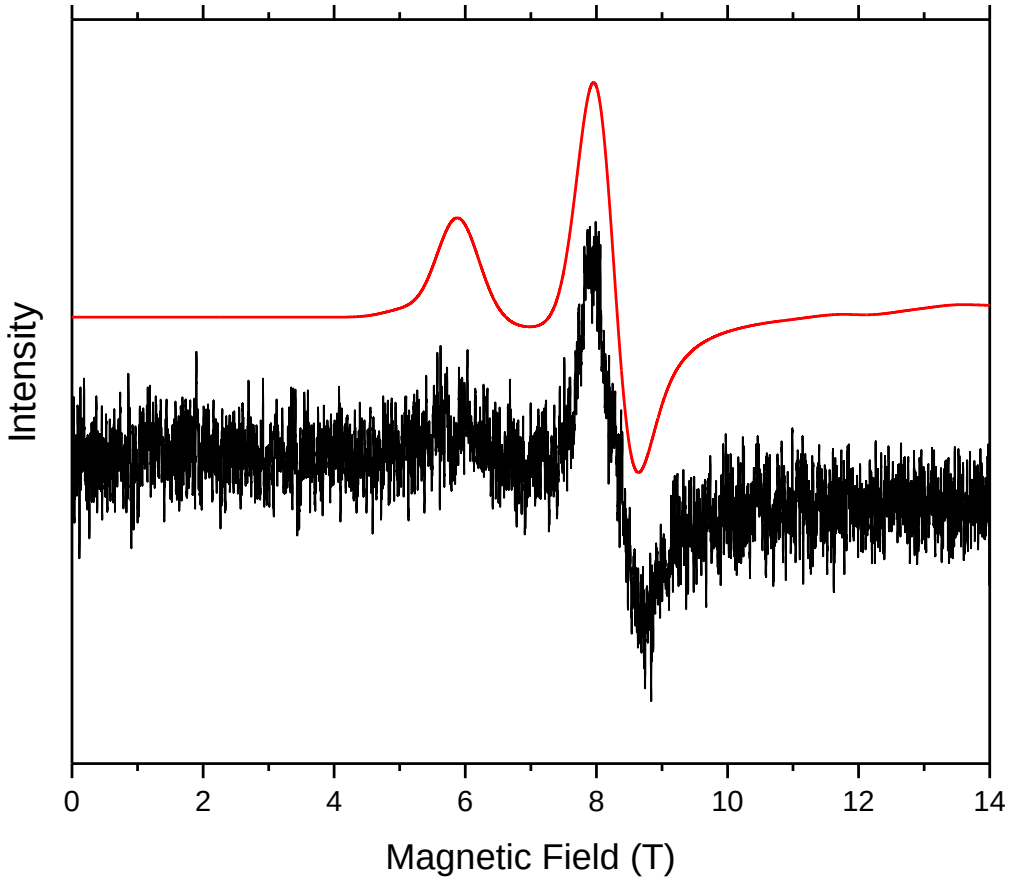


Figure B.15. Magnetically-modulated HFEPR spectrum of a **Co-Br** pellet at 473 GHz and 10 K, resulting in the conventional derivative shape of the resonances and its simulation using spin-Hamiltonian parameters as in Table 1 (red trace). The resonance at ~6 T is the parallel turning point of the $M_S = -3/2 \rightarrow +3/2$ transition. The stronger signal at ~8.3 T is the parallel turning point of the inter-Kramers $M_S = -3/2 \rightarrow +1/2$ transition and thus informative with regard to ZFS.

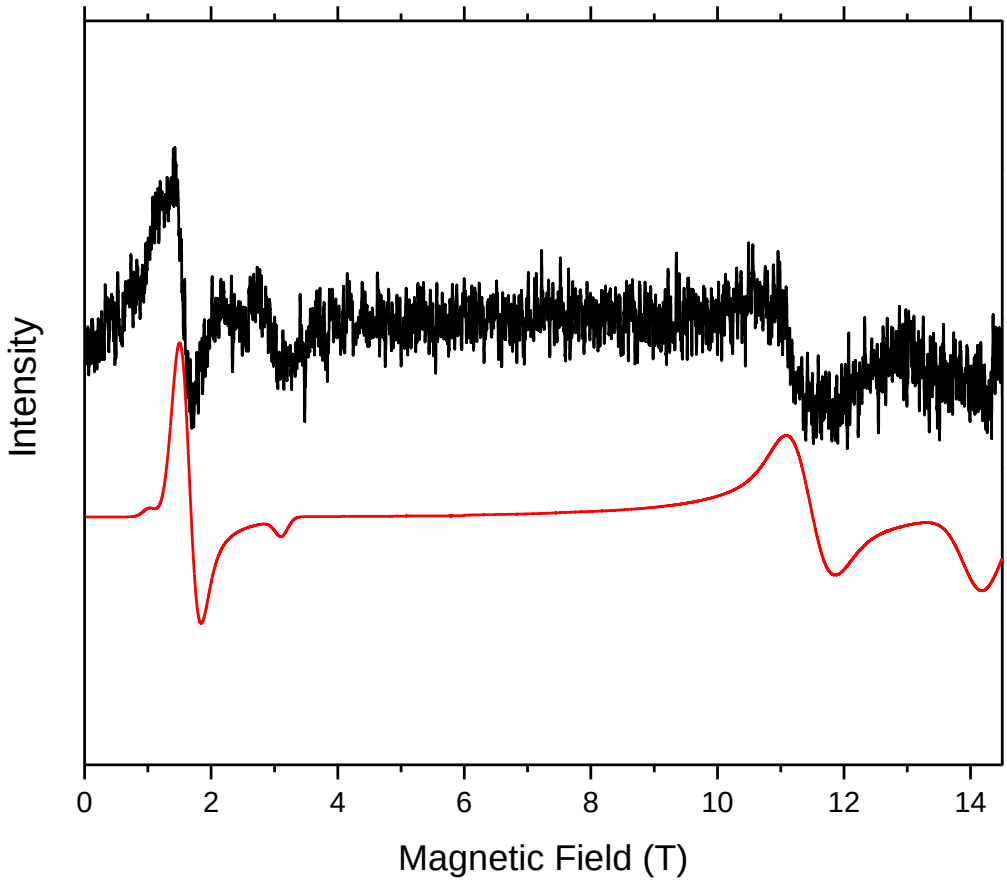


Figure B.16. Magnetically-modulated HFEPR spectrum of a **Co-Br** pellet at 98 GHz and 10 K, resulting in the conventional derivative shape of the resonances (black trace) and its simulation using spin-Hamiltonian parameters as in Table 1 (red trace). The signals at 3.0, 11.5 and 14.15 T represent the *z*, *y* and *x* turning points, respectively, of the nominally forbidden intra-Kramers $M_S = -3/2 \rightarrow +3/2$ transition. The resonance at 1.7 T is the perpendicular turning point of the $M_S = -1/2 \rightarrow +1/2$ transition in the excited Kramers doublet.

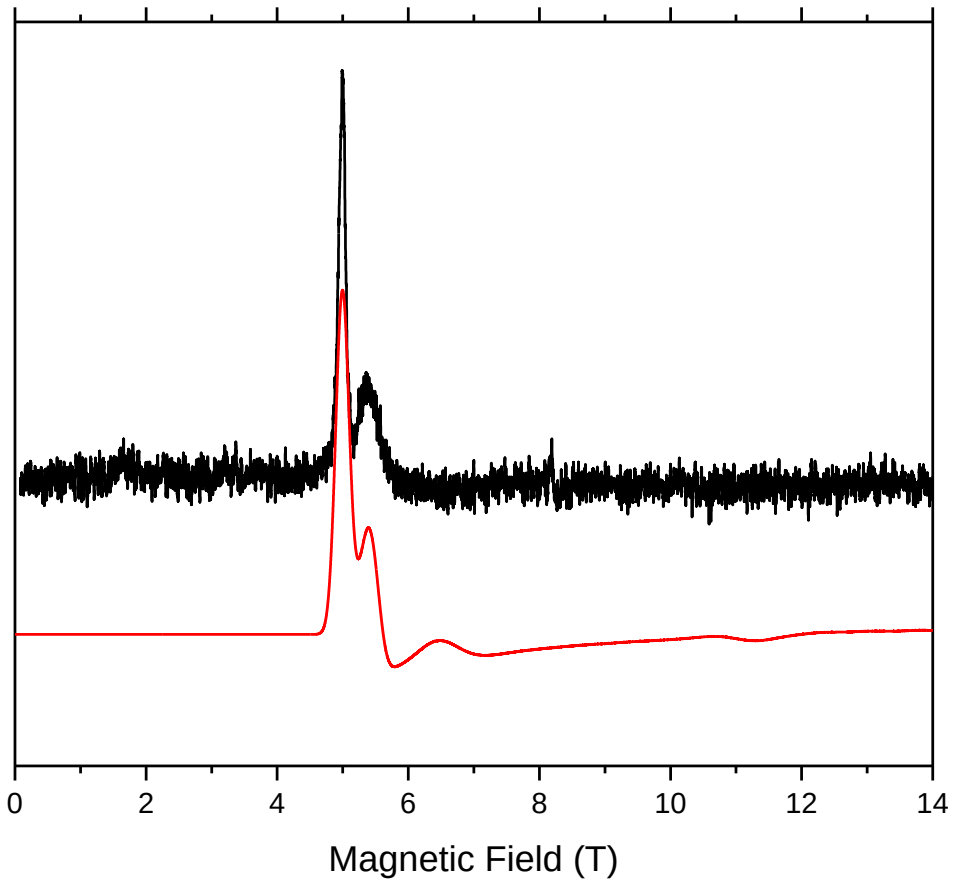


Figure B.17. Magnetically-modulated HFEPR spectrum of a **Co-I** pellet at 473 GHz and 10 K, resulting in the conventional derivative shape of the resonances and its simulation using spin-Hamiltonian parameters: $D = -13.0$ cm^{-1}, $E = -2.14$ cm^{-1}, $\boldsymbol{g} = [2.23, 2.23, 2.32]$. The stronger resonance at ~5 T is the parallel turning point of the $M_S = -3/2 \rightarrow +3/2$ transition. The weaker signal at ~5.4 T is the parallel turning point of the inter-Kramers $M_S = -3/2 \rightarrow +1/2$ transition and thus informative with regard to ZFS.

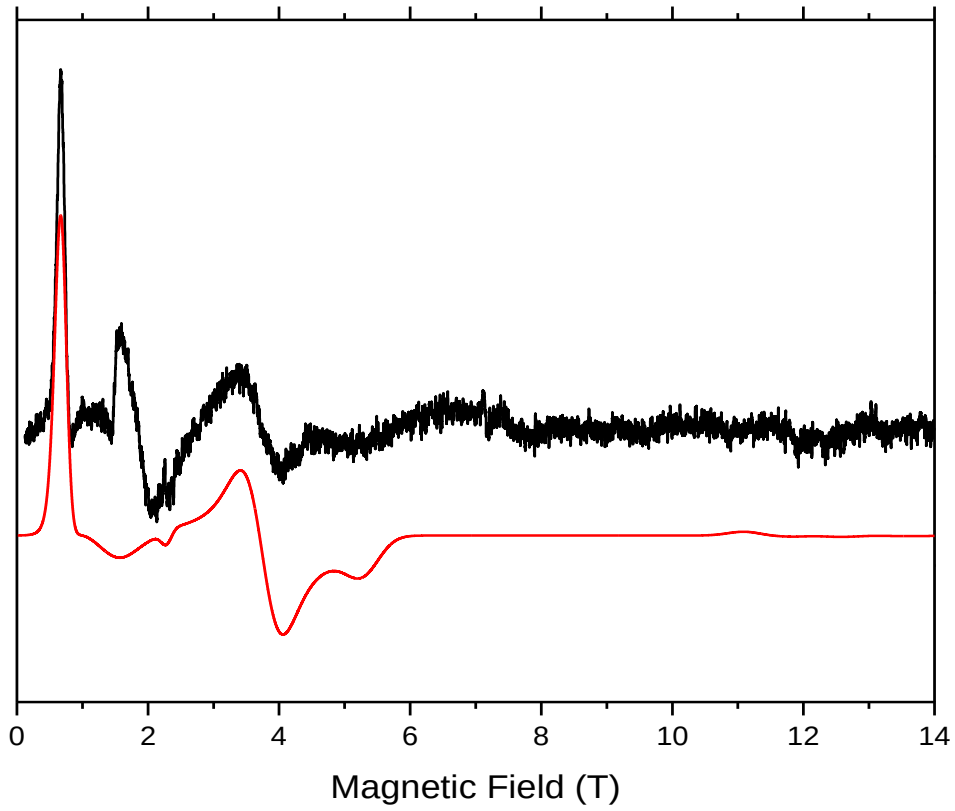


Figure B.18. Magnetically-modulated HFEPR spectrum of a **Co-I** pellet at 63 GHz and 10 K, resulting in the conventional derivative shape of the resonances and its simulation using spin-Hamiltonian parameters as in Table 1 except $g_z = 2.15$. The strong resonance at ~0.6 T is the parallel turning point of the intra-Kramers $M_S = -3/2 \rightarrow +3/2$ transition. The weaker and broader signals at ~3.75 and ~5.15 T are the perpendicular turning points of the same transition. The resonance at ~1.9 T is an impurity present in the probe and is thus not simulated.

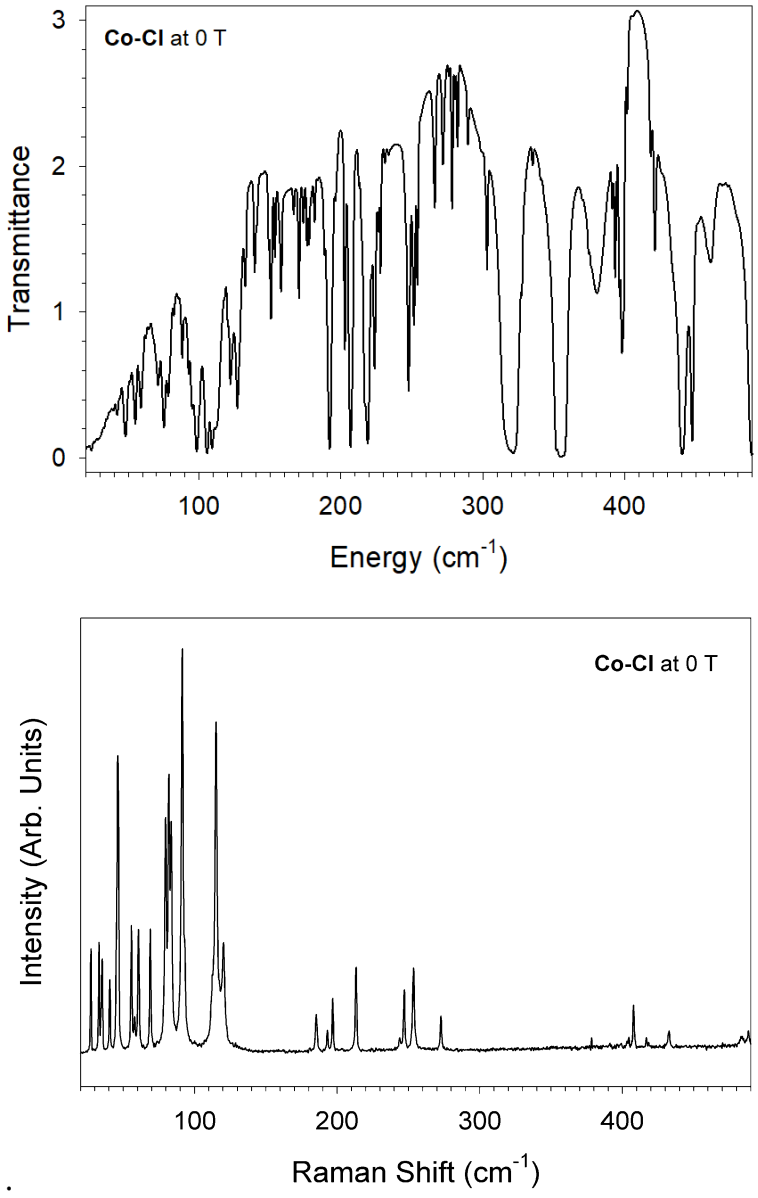


Figure B.19. (Top) Far-IR spectrum of **Co-Cl**. (Bottom) Raman spectrum of **Co-Cl**. Both spectra are at 0 T and 5 K in the 20-490 cm^{-1} spectral range.

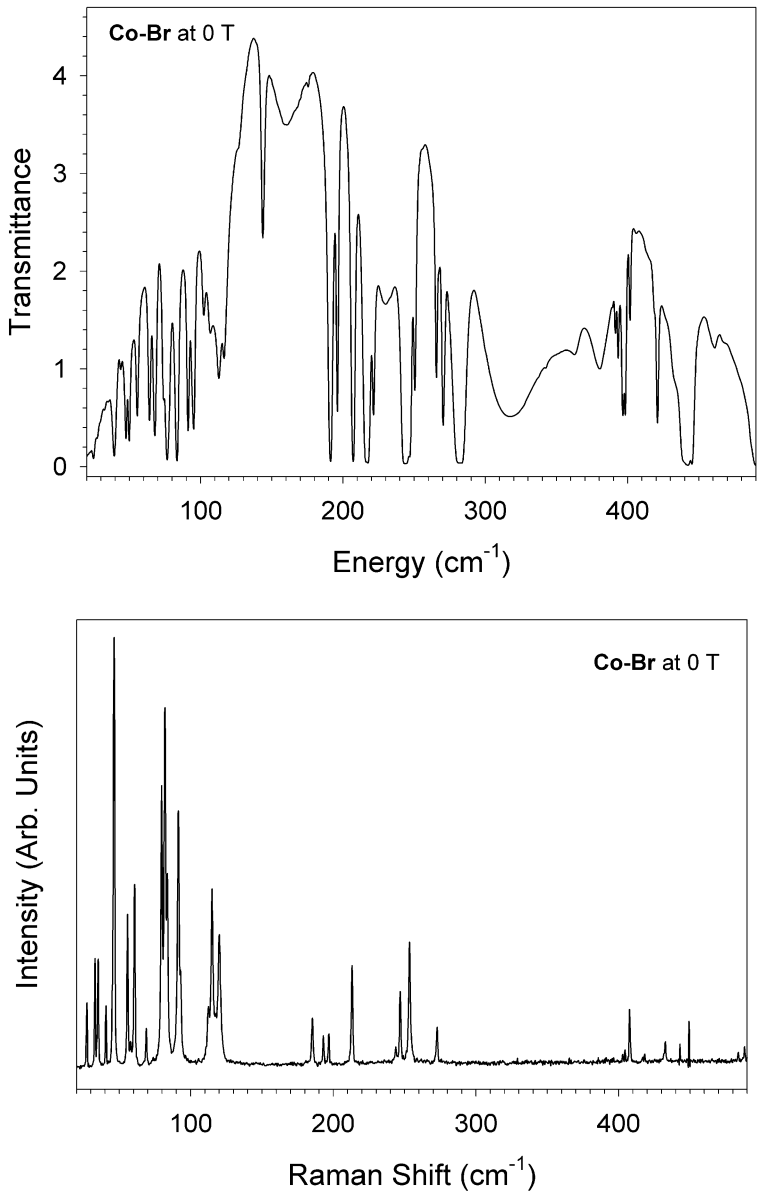


Figure B.20. (Top) Far-IR spectrum of **Co-Br**. (Bottom) Raman spectrum of **Co-Br**. Both spectra are at 0 T and 5 K in the 20-490 cm^{-1} spectral range.

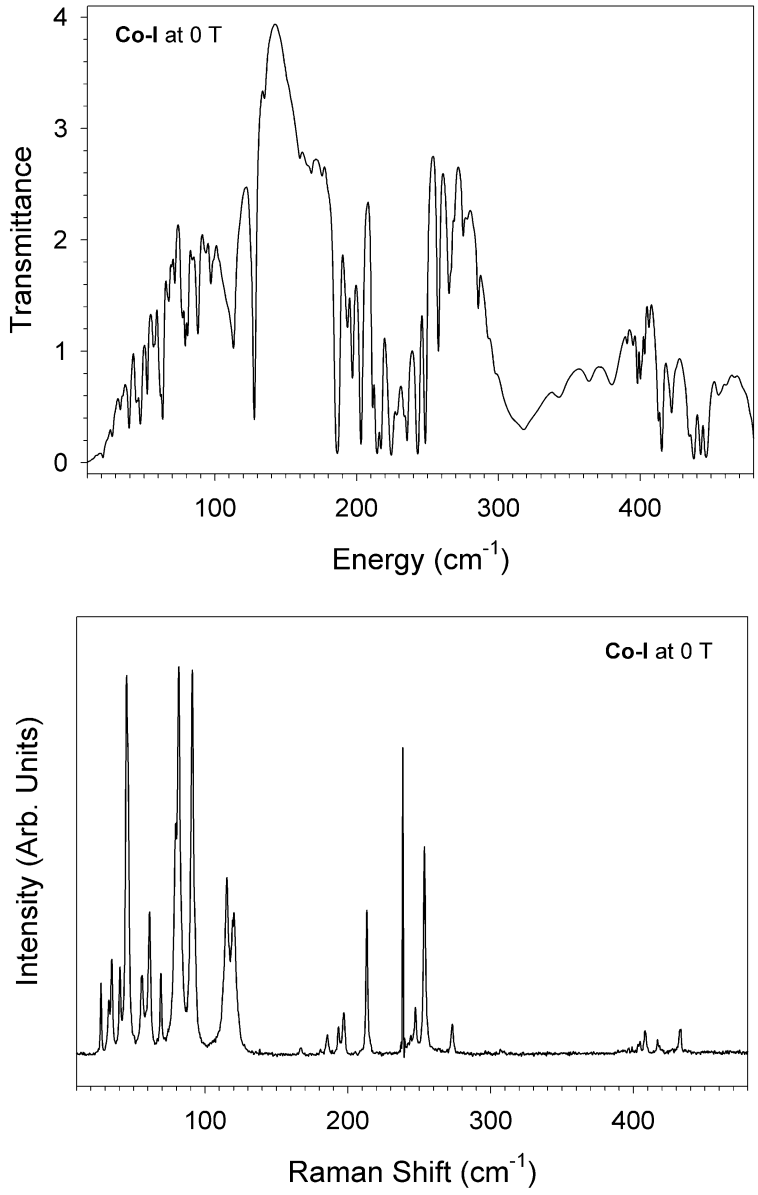


Figure B.21. (Top) Far-IR spectrum of **Co-I**. (Bottom) Raman spectrum of **Co-I**. Both spectra are at 0 T and 5 K in the 10-480 cm^{-1} spectral range.

Table B.1. Electronic Transitions (in cm^{-1}) for **Co-X** in Doped Single-Crystals of **Co/Zn-X** (X = Cl, Br, I)[49, 107] with Calculations from the AOM

Complexes				Molecular Polarization	Assignment $^4A_2[^4A_2(F)] \rightarrow$
Source	**Co-Cl**	**Co-Br**	**Co-I**		
calc [a]	3874	3695	3575	*y*	$^4B_1[^4T_2(F)]$
calc	4009	3951	3612	*x*	$^4B_2[^4T_2(F)]$
calc	5719	5506	4136	*forbidden*	$^4A_1[^4T_2(F)]$
expt	6400	6000	5800	*y*	$^4B_1[^4T_1(F)]$
calc	6378	6112	5816		
expt	8000	7600	7100	*z*	$^4A_2[^4T_1(F)]$
calc	8018	7476	7100		
expt	10 700	9700	9200	*x*	$^4B_2[^4T_1(F)]$
calc	10 699	9736	9189		
expt	13 550	13 500	12 800	*x*	$^4B_2[^4T_1(P)]$
calc	13 550	13 484	12 761		
expt	15 750	14 900	13 800	*z*	$^4A_2[^4T_1(P)]$
calc	15 759	14 884	13 884		
expt	17 000 [b]	15 900	14 700	*y*	$^4B_1[^4T_1(P)]$
calc	16 991	15 920	14 655		

[a] Calculations used (in cm^{-1}): B = 602.5 (Cl), 586.7 (Br), 559.7 (I); $\varepsilon_{\sigma(X)}$ = 3313.6 (Cl), 2560.7 (Br), 2177.2 (I); $\varepsilon_{\pi(X)}$ = 1818.6 (Cl), 1068.1 (Br), 633.1 (I); $\varepsilon_{\sigma(P)}$ = 3641.5 (Cl), 3089.7 (Br), 2501.6 (I); $\varepsilon_{\pi(P)}$ = -1635.4 (Cl), -1752.6 (Br), -1482.4 (I). These values are also given in Table B.3.

[b] This is the average of bands reported at 16 555, 16 778, 16 863, 17 065, 17 153, and 17 405 cm^{-1}. Bands were also reported at 17 645 and 18 315 cm^{-1}.[107]

Table B.2. Key Metrics for the AOM of the **Co-X** Series (X = Cl, Br, I)

Metric	**Co-Cl** [a]	**Co-Br** [b]	**Co-I** [c]
∠X-Co-X (deg)	117.27	115.23	111.44
∠P-Co-P (deg)	115.87	117.45	108.25
d(Co-X) (Å)	2.212	2.350	2.543, 2.558
d(Co-P) (Å)	2.384	2.385	2.390, 2.413

[a] These values are taken from the structure reported by Carlin et al.[118] (CSD code: BIHGEE); that reported by Yang et al.[57] (CSD code: BIHGEE01) is essentially the same: ∠Cl-Co-Cl = 117.12°, ∠P-Co-P = 115.86°; *d*(Co-Cl), 2.211 Å, *d*(Co-P), 2.386 Å. For comparison, in Cs_2CoCl_4, the two angles in the $[CoCl_4]^{2-}$ unit are: ∠Cl-Co-Cl = 107.5° and 116.1°.

[b] These values are taken from the structure reported by Carlin et al.[118] (CSD code: BIHGII).

[c] These values are taken from the structure reported by Saber and Dunbar[55] (CSD code: HONQOS). Note that this structure was determined at low temperature (110 K), and identified different Co-(X,P) bond distances, while the others (**Co-Cl** and **Co-Br**) were all recorded at room temperature.

Table B.3. LFT AOM parameters (in cm^{-1}) determined for the **Co-X** series (X = Cl, Br, I)

Complex			AOM parameter [a,b]
Co-Cl	**Co-Br**	**Co-I**	
602.5	586.7	559.7	*B*
575	575	---	
3313.6	2560.7	2177.2	$\varepsilon_{\sigma(X)}$
3500	3500	---	
1818.6	1068.1	633.1	$\varepsilon_{\pi(X)}$
2000	1500	---	
3641.5	3089.7	2501.6	$\varepsilon_{\sigma(P)}$
4000	3500	---	
–1635.4	–1752.6	–1482.4	$\varepsilon_{\pi(P)}$
–1000	–1000	---	

[a] The second row of values for each complex are taken from Davies *et al*.[110] There is a typo in their Table 7, as $\varepsilon_{\sigma(X)}$ is given twice, but we assume that the second entry is $\varepsilon_{\pi(X)}$.

[b] For comparison, Horrocks and Barlone found $B = 740$ cm^{-1}, $\varepsilon_{\sigma(Cl)} = 2300$ cm^{-1} for $[CoCl_4]^{2-}$ in both Cs_3CoCl_5 (elongated D_{2d} symmetry) and Cs_2CoCl_4 (compressed C_{2v} symmetry); π-interactions were considered, but not deemed necessary for adequate fitting of the optical and magnetic data.[50]

Table B.4. Calculated phonon modes in **Co-Cl** and their symmetries

Wavenumber (cm^{-1})	**Symmetries of the modes**	**Wavenumber (cm^{-1})**	**Symmetries of the modes**
22.477	B_u	74.967	A_g
26.403	B_g	80.587	A_u
26.519	A_g	81.475	B_g
28.631	A_u	84.099	A_g
35.094	B_g	86.054	B_u
36.292	A_u	86.650	A_u
37.241	B_g	89.197	A_u
37.585	A_g	89.412	B_g
37.757	B_u	89.526	A_g
41.586	A_g	91.469	B_u
41.634	B_g	92.788	B_g
44.374	B_u	94.726	A_g
48.076	B_g	97.033	B_u
48.336	A_g	98.739	B_g
48.690	B_g	99.320	A_g
50.068	B_u	102.344	B_u
54.005	B_u	103.361	B_u
55.750	A_u	103.550	A_u
57.264	A_u	104.457	B_g
57.531	A_g	105.962	A_g
60.219	B_g	112.119	B_u
62.816	A_g	113.792	A_g
64.402	A_u	114.192	B_g
65.035	B_u	115.896	A_u
67.336	A_u	116.986	A_u
69.660	A_g	148.151	A_u
72.266	B_g	149.834	A_g
73.451	B_u	181.226	B_g
73.695	A_u	183.362	B_u
73.926	B_g	190.666	A_u

Table B.4 (Continued). Calculated phonon modes in **Co-Cl** and their symmetries

Wavenumber (cm^{-1})	**Symmetries of the modes**	**Wavenumber (cm^{-1})**	**Symmetries of the modes**
193.102	A_g	388.548	B_u
196.193	B_g	390.097	B_g
197.329	B_u	392.008	B_u
206.130	B_g	392.967	B_g
206.441	A_g	393.081	B_u
208.710	A_u	393.183	A_g
209.217	B_u	393.901	A_u
210.384	A_u	396.293	A_g
212.888	A_g	396.814	A_u
214.516	B_u	406.636	A_u
217.503	B_g	408.423	A_g
239.626	B_g	408.567	B_g
240.365	B_u	409.205	B_u
243.543	A_u	431.646	B_g
246.273	A_g	431.916	A_g
258.147	B_g	431.968	A_u
259.063	B_u	432.515	B_u
259.465	A_u	432.667	B_u
259.484	A_g	434.507	B_g
264.235	A_g	437.537	A_g
264.625	B_u	437.772	A_u
265.256	A_u	481.108	B_u
265.867	B_g	484.139	B_g
299.849	A_g	485.348	A_g
299.961	A_u	486.663	A_u
337.225	B_u	488.148	A_g
340.923	B_g	489.347	B_u
385.858	A_g	490.530	A_u
387.005	A_u	490.673	B_g
388.134	B_g	508.240	B_g

Table B.4 (Continued). Calculated phonon modes in **Co-Cl** and their symmetries

Wavenumber (cm^{-1})	**Symmetries of the modes**	**Wavenumber (cm^{-1})**	**Symmetries of the modes**
509.477	B_u	694.830	A_g
513.638	A_u	695.300	B_g
514.975	A_g	695.425	A_u
607.654	B_u	695.895	B_u
607.671	B_g	696.856	A_u
607.997	B_g	697.224	B_u
608.178	A_g	697.513	A_g
608.666	A_u	698.009	B_g
608.674	B_g	728.907	B_u
608.805	A_g	730.217	B_g
609.135	A_u	731.659	A_u
609.162	B_u	731.747	A_g
609.759	B_u	731.899	B_u
610.451	A_u	733.696	B_g
674.828	B_u	734.912	A_u
675.660	A_g	735.022	A_g
675.909	B_g	735.479	B_u
676.211	A_u	737.415	B_g
684.151	B_u	738.216	A_u
685.220	B_u	741.093	A_g
685.508	B_g	823.775	B_g
686.069	A_u	824.534	B_u
686.889	B_g	827.893	A_g
686.948	A_g	827.920	A_u
688.826	A_g	831.707	B_u
688.988	A_u	834.018	A_u
689.384	B_g	835.381	B_g
689.713	B_u	837.895	A_g
690.894	A_u	838.918	B_g
692.219	A_g	841.283	B_u

Table B.4 (Continued). Calculated phonon modes in **Co-Cl** and their symmetries

Wavenumber (cm^{-1})	Symmetries of the modes	Wavenumber (cm^{-1})	Symmetries of the modes
842.016	A_g	978.746	B_g
844.551	A_u	979.519	B_u
899.954	B_g	981.067	B_g
900.073	B_u	981.213	A_g
901.287	A_u	982.765	A_g
902.048	A_g	982.847	A_u
906.017	A_u	985.107	B_u
906.443	B_u	985.386	A_u
907.604	A_g	986.142	B_u
907.626	B_g	986.326	A_g
910.918	A_g	986.657	B_g
911.356	B_u	987.109	A_u
911.918	A_u	988.140	B_g
912.223	B_g	988.376	B_u
951.960	B_g	989.796	A_u
952.253	A_u	990.153	B_g
952.472	B_u	990.168	A_g
952.536	A_g	990.375	B_u
956.173	A_g	990.874	A_g
956.572	B_g	990.949	A_u
958.144	B_u	1016.923	B_u
959.023	A_u	1016.982	B_g
961.387	B_g	1017.949	A_g
961.979	B_u	1018.176	A_u
962.513	A_g	1019.828	A_g
962.852	A_u	1020.066	A_u
976.071	A_g	1020.080	B_g
976.079	B_g	1020.162	B_u
976.898	B_u	1020.370	A_g
977.302	A_u	1020.436	B_g

Table B.4 (Continued). Calculated phonon modes in **Co-Cl** and their symmetries

Wavenumber (cm^{-1})	Symmetries of the modes	Wavenumber (cm^{-1})	Symmetries of the modes
1021.162	A_u	1145.993	A_u
1021.233	B_u	1146.467	B_u
1068.627	B_u	1147.192	A_g
1069.960	B_g	1147.929	B_g
1070.111	A_u	1153.989	B_g
1071.108	A_g	1154.067	B_u
1071.485	B_g	1154.935	A_u
1071.743	B_u	1155.135	A_g
1072.078	B_u	1169.187	B_u
1072.087	A_u	1169.438	A_u
1072.408	A_g	1170.424	B_g
1072.420	B_g	1171.619	A_g
1072.735	A_u	1171.974	B_u
1073.027	A_g	1173.658	A_u
1078.966	B_g	1173.921	B_u
1079.405	B_u	1174.430	B_g
1079.633	A_u	1174.987	A_g
1080.124	A_g	1175.024	A_u
1081.484	B_g	1176.608	B_g
1081.682	B_u	1177.000	A_g
1081.789	A_u	1289.357	B_g
1082.369	A_g	1289.990	B_u
1083.881	A_g	1292.336	A_u
1084.200	B_u	1292.813	A_g
1085.295	B_g	1295.755	B_u
1086.418	A_u	1296.208	B_g
1142.040	B_g	1297.015	A_g
1142.196	B_u	1297.623	A_u
1142.465	A_u	1299.237	A_g
1142.630	A_g	1299.267	B_u

Table B.4 (Continued). Calculated phonon modes in **Co-Cl** and their symmetries

Wavenumber (cm^{-1})	**Symmetries of the modes**	**Wavenumber (cm^{-1})**	**Symmetries of the modes**
1299.366	B_g	1463.675	A_u
1299.406	A_u	1463.811	B_g
1326.794	B_g	1464.123	B_u
1326.833	B_u	1464.331	A_u
1327.938	A_u	1465.112	B_g
1328.040	A_g	1465.231	B_u
1328.939	A_u	1465.535	A_g
1329.206	B_u	1465.591	A_u
1330.029	B_g	1558.178	A_g
1330.059	A_g	1558.487	B_u
1331.755	A_u	1559.278	B_g
1331.890	B_g	1560.092	A_u
1332.077	B_u	1560.527	B_g
1332.148	A_g	1560.872	B_u
1416.311	B_u	1560.994	A_g
1416.318	A_u	1561.046	A_u
1416.375	B_g	1561.377	B_g
1417.030	A_g	1561.733	A_g
1419.131	B_u	1561.846	A_u
1419.290	B_g	1562.052	B_u
1419.416	A_g	1571.838	B_g
1419.903	B_u	1572.191	B_u
1420.083	A_u	1572.248	A_g
1420.555	A_u	1572.652	A_u
1420.645	B_g	1573.182	A_u
1421.420	A_g	1573.604	B_u
1461.541	B_g	1573.779	B_g
1461.759	B_u	1573.832	A_g
1463.196	A_g	1574.102	B_u
1463.639	A_g	1574.449	A_u

Table B.4 (Continued). Calculated phonon modes in **Co-Cl** and their symmetries

Wavenumber (cm^{-1})	**Symmetries of the modes**	**Wavenumber (cm^{-1})**	**Symmetries of the modes**
1575.137	A_g	3072.911	B_u
1575.537	B_g	3072.952	B_g
3045.541	B_u	3072.954	A_u
3045.551	B_g	3073.125	A_g
3046.108	A_u	3073.735	B_u
3046.118	A_g	3073.843	A_u
3054.838	B_g	3074.732	B_g
3054.877	B_u	3074.785	A_g
3054.940	A_g	3080.633	B_g
3054.973	A_u	3080.634	B_u
3058.373	B_g	3081.612	B_u
3058.409	A_g	3081.618	A_u
3058.458	B_u	3081.999	B_g
3058.506	A_u	3082.036	A_g
3059.662	B_g	3083.329	A_u
3059.824	A_g	3083.349	A_g
3060.867	B_u	3088.955	A_u
3061.191	A_u	3089.023	B_u
3062.562	B_g	3089.036	B_g
3062.671	B_u	3089.154	A_g
3064.940	A_u	3091.363	B_u
3064.978	A_g	3091.413	A_u
3064.997	B_u	3091.587	B_g
3065.012	B_g	3091.686	A_g
3065.361	A_u	3091.834	A_g
3065.380	A_g	3091.892	B_g
3071.585	B_u	3091.932	A_u
3071.823	A_u	3091.941	B_u
3071.847	B_g	3093.559	A_g
3071.899	A_g	3093.623	B_u

Table B.4 (Continued). Calculated phonon modes in **Co-Cl** and their symmetries

Wavenumber (cm^{-1})	**Symmetries of the modes**	**Wavenumber (cm^{-1})**	**Symmetries of the modes**
3093.653	B_g	3093.690	A_u

Table B.5. Calculated phonon modes in **Co-Br** and their symmetries

Wavenumber (cm^{-1})	**Symmetries of the modes**	**Wavenumber (cm^{-1})**	**Symmetries of the modes**
23.470	B_u	70.128	B_g
25.376	A_g	70.934	A_u
25.610	B_g	72.467	A_g
28.146	A_u	72.643	B_g
31.389	B_g	74.152	A_u
34.545	B_g	77.501	B_u
35.977	A_g	82.429	B_g
36.494	B_u	84.616	A_g
38.867	B_g	84.619	B_u
38.880	A_g	84.743	A_u
39.747	A_u	85.818	B_u
41.818	B_u	86.817	B_g
46.113	A_g	87.279	A_g
47.175	B_g	90.532	B_g
48.215	B_u	90.863	A_g
48.412	B_g	92.312	B_g
48.855	A_u	95.884	B_u
50.715	B_u	96.396	A_u
52.561	A_g	98.787	A_g
54.000	A_u	101.126	B_u
56.005	B_g	102.283	B_u
56.449	A_g	105.683	A_u
57.631	A_u	107.974	B_g
61.248	A_u	111.669	A_g
62.652	B_u	114.415	A_u
62.657	A_g	134.448	A_u
66.271	B_g	134.601	A_g
67.731	A_g	181.273	B_g
69.102	A_u	182.433	B_u
69.244	B_u	188.690	A_u

Table B.5 (Continued). Calculated phonon modes in **Co-Br** and their symmetries

Wavenumber (cm^{-1})	Symmetries of the modes	Wavenumber (cm^{-1})	Symmetries of the modes
190.311	A_g	389.092	B_u
195.520	B_g	390.500	B_g
195.924	B_u	391.870	B_u
205.631	B_g	392.920	B_u
206.291	A_g	393.057	B_g
207.653	A_u	393.475	A_u
208.380	B_u	393.541	A_g
208.476	A_u	396.769	A_g
210.165	A_g	397.228	A_u
212.100	B_u	406.235	A_u
215.223	B_g	408.183	A_g
228.156	A_u	408.577	B_g
228.187	A_g	408.743	B_u
238.880	B_u	431.134	B_g
239.365	B_g	431.487	B_u
242.032	A_u	432.760	A_g
244.247	A_g	433.219	A_u
257.516	B_g	433.805	B_u
257.911	B_u	435.088	B_g
259.239	A_g	435.461	A_g
259.692	A_u	435.901	A_u
261.641	A_g	481.936	B_u
261.945	B_u	484.730	B_g
262.406	A_u	485.499	A_g
262.433	B_g	487.100	A_u
266.817	B_u	487.368	A_g
268.875	B_g	488.303	B_u
386.448	A_g	489.241	B_g
387.475	A_u	489.317	A_u
388.782	B_g	507.154	B_g

Table B.5 (Continued). Calculated phonon modes in **Co-Br** and their symmetries

Wavenumber (cm^{-1})	**Symmetries of the modes**	**Wavenumber (cm^{-1})**	**Symmetries of the modes**
508.360	B_u	690.877	A_g
511.710	A_u	693.454	A_g
514.003	A_g	694.142	B_g
606.803	B_u	694.455	A_u
606.944	A_g	694.671	B_u
607.011	B_g	695.612	A_u
607.392	B_g	695.911	B_u
607.656	B_g	695.917	A_g
607.758	A_g	696.420	B_g
607.855	A_u	728.563	B_u
608.061	A_u	729.599	B_g
608.124	B_u	730.694	A_g
608.360	A_g	731.404	A_u
609.106	B_u	731.649	B_u
609.944	A_u	733.295	B_g
674.017	B_u	734.179	A_u
674.279	A_g	734.511	B_u
674.913	B_g	734.583	A_g
674.949	A_u	736.592	B_g
683.487	B_u	738.004	A_u
684.315	B_u	741.029	A_g
684.855	B_g	822.528	B_g
685.031	A_u	823.149	B_u
686.182	A_g	826.396	A_g
686.342	B_g	826.655	A_u
688.124	A_u	830.680	B_u
688.132	A_g	833.092	A_u
688.553	B_g	834.172	B_g
689.183	B_u	835.826	A_g
690.452	A_u	836.498	B_g

Table B.5 (Continued). Calculated phonon modes in **Co-Br** and their symmetries

Wavenumber (cm^{-1})	**Symmetries of the modes**	**Wavenumber (cm^{-1})**	**Symmetries of the modes**
839.488	B_u	976.741	A_u
840.744	A_g	977.148	B_g
842.853	A_u	978.381	B_u
899.266	B_g	980.070	A_g
899.270	B_u	980.145	B_g
900.550	A_u	981.524	A_u
900.916	A_g	981.788	A_g
905.037	A_u	983.232	B_u
905.269	B_u	983.994	A_u
906.430	B_g	986.138	B_u
906.601	A_g	986.384	A_g
909.730	A_g	986.445	B_g
910.359	B_u	987.346	A_u
910.468	A_u	987.865	B_g
910.970	B_g	988.085	B_u
951.188	B_g	989.022	A_u
951.325	A_u	989.407	B_u
951.437	A_g	989.613	B_g
951.583	B_u	989.982	A_g
955.572	A_g	990.506	A_u
955.914	B_g	990.647	A_g
957.185	B_u	1016.396	B_g
957.838	A_u	1016.518	B_u
960.305	B_g	1018.016	A_u
961.075	B_u	1018.185	A_g
961.682	A_g	1019.326	A_u
962.573	A_u	1019.432	B_g
975.703	A_g	1019.635	B_u
975.752	B_g	1019.976	A_g
976.402	B_u	1020.228	B_g

Table B.5 (Continued). Calculated phonon modes in **Co-Br** and their symmetries

Wavenumber (cm^{-1})	Symmetries of the modes	Wavenumber (cm^{-1})	Symmetries of the modes
1021.011	A_u	1144.083	A_g
1021.082	B_u	1146.118	A_u
1021.103	A_g	1146.645	B_u
1069.258	B_u	1147.286	A_g
1070.195	B_g	1147.808	B_g
1070.555	A_u	1153.531	B_u
1070.838	B_u	1153.590	B_g
1071.335	A_g	1154.359	A_u
1071.385	B_g	1154.716	A_g
1071.496	A_u	1170.217	B_u
1071.747	B_g	1170.302	B_g
1072.065	B_u	1170.498	A_u
1072.155	A_g	1172.063	B_u
1072.545	A_g	1172.925	A_g
1072.643	A_u	1174.221	B_u
1078.766	B_g	1174.230	A_u
1079.065	B_u	1174.809	B_g
1079.522	A_u	1174.809	A_u
1079.914	A_g	1175.947	A_g
1080.352	B_g	1177.606	B_g
1080.563	B_u	1178.723	A_g
1080.675	A_u	1289.898	B_g
1081.958	A_g	1290.427	B_u
1083.231	B_u	1292.791	A_g
1083.917	B_g	1292.815	A_u
1084.744	A_g	1295.856	B_u
1085.147	A_u	1296.366	B_g
1143.223	B_g	1296.931	A_g
1143.300	B_u	1298.149	A_u
1143.595	A_u	1298.753	A_g

Table B.5 (Continued). Calculated phonon modes in **Co-Br** and their symmetries

Wavenumber (cm^{-1})	Symmetries of the modes	Wavenumber (cm^{-1})	Symmetries of the modes
1299.124	B_u	1463.415	A_g
1299.155	B_g	1463.537	A_u
1299.219	A_u	1463.542	B_g
1326.846	B_u	1463.879	B_u
1326.895	B_g	1464.061	A_u
1327.969	A_g	1465.030	B_g
1328.126	A_u	1465.192	B_u
1329.273	A_u	1465.414	A_g
1329.636	B_u	1465.581	A_u
1330.072	A_g	1558.008	B_u
1330.470	B_g	1558.128	A_g
1331.681	A_u	1558.602	B_g
1331.850	B_g	1559.309	A_u
1331.961	B_u	1560.208	B_g
1332.002	A_g	1560.350	A_u
1415.807	B_u	1560.532	B_u
1416.523	A_u	1560.968	B_g
1416.546	A_g	1561.121	A_u
1416.984	B_g	1561.341	B_u
1418.974	B_g	1561.701	A_g
1419.077	B_u	1562.318	A_g
1419.443	A_g	1571.218	B_g
1419.597	A_u	1571.492	B_u
1419.726	B_u	1571.751	A_g
1419.851	B_g	1572.014	A_u
1420.356	A_u	1572.358	A_u
1421.098	A_g	1572.968	B_g
1461.391	B_g	1572.975	B_u
1461.452	B_u	1573.689	A_g
1463.101	A_g	1573.713	B_u

Table B.5 (Continued). Calculated phonon modes in **Co-Br** and their symmetries

Wavenumber (cm^{-1})	Symmetries of the modes	Wavenumber (cm^{-1})	Symmetries of the modes
1573.886	A_u	3069.647	B_g
1574.904	A_g	3069.703	A_u
1575.374	B_g	3070.105	B_g
3045.475	B_u	3070.173	B_u
3045.577	B_g	3070.301	A_u
3045.602	A_g	3075.071	A_u
3045.990	A_u	3075.232	B_u
3052.366	A_g	3075.366	A_g
3052.728	B_g	3076.052	B_g
3052.833	A_u	3079.219	A_g
3052.964	B_u	3079.511	B_u
3054.847	A_g	3079.521	A_u
3055.394	B_g	3079.659	B_g
3055.415	A_u	3080.676	B_g
3055.449	B_u	3080.864	B_u
3060.675	B_g	3082.490	A_g
3060.845	A_g	3083.592	A_u
3061.361	B_u	3084.195	A_g
3062.437	A_u	3084.800	B_g
3063.155	B_g	3084.943	B_u
3063.274	A_g	3085.003	A_u
3063.673	B_u	3086.625	A_g
3063.826	A_u	3087.598	B_u
3063.861	B_g	3087.708	A_u
3064.035	B_u	3087.834	B_g
3064.501	A_g	3088.772	A_g
3065.832	A_u	3089.989	B_g
3069.082	A_g	3090.030	A_u
3069.464	B_u	3090.031	B_u
3069.584	A_g	3090.280	A_g

Table B.5 (Continued). Calculated phonon modes in **Co-Br** and their symmetries

Wavenumber (cm^{-1})	**Symmetries of the modes**	**Wavenumber (cm^{-1})**	**Symmetries of the modes**
3091.646	A_u	3091.838	B_u
3091.772	B_g		

Table B.6. Calculated phonon modes in **Co-I** and their symmetries

Wavenumber (cm^{-1})	**Symmetries of the modes**	**Wavenumber (cm^{-1})**	**Symmetries of the modes**
15.994	B_g	47.516	B_g
24.197	A_u	49.422	A_u
24.672	A_g	50.532	A_g
25.028	B_u	51.978	B_g
25.157	B_g	51.994	B_u
25.412	A_g	53.610	A_g
26.923	B_g	53.711	A_u
27.698	A_u	56.144	B_u
28.216	A_g	56.293	B_g
28.490	B_u	56.959	A_g
30.730	A_u	57.544	A_g
32.387	B_g	58.209	A_u
32.499	A_g	58.755	B_u
33.370	B_u	60.235	A_u
34.739	A_u	61.113	B_g
34.860	B_g	61.512	B_u
35.326	A_g	62.326	A_g
36.626	B_g	62.826	B_g
36.684	B_u	63.634	A_u
38.376	A_g	63.729	A_g
38.548	A_u	63.876	B_u
38.908	B_g	64.399	B_u
39.169	A_u	65.224	A_u
39.242	A_g	65.960	B_g
40.571	B_u	67.976	B_g
41.490	B_u	68.619	A_u
42.263	A_u	68.679	B_u
44.451	B_g	69.705	A_g
46.337	A_g	70.459	B_g
46.644	B_u	71.320	A_u

Table B.6 (Continued). Calculated phonon modes in **Co-I** and their symmetries

Wavenumber (cm^{-1})	**Symmetries of the modes**	**Wavenumber (cm^{-1})**	**Symmetries of the modes**
72.902	A_u	100.817	B_u
73.064	B_u	104.575	A_u
73.314	A_g	106.944	B_u
75.497	A_g	107.555	A_g
75.519	B_g	108.190	B_g
75.956	A_u	108.377	A_g
77.562	B_u	109.536	B_g
77.581	A_g	110.720	A_g
77.734	B_g	110.723	A_u
79.318	A_u	112.281	B_u
79.739	B_u	115.036	B_g
80.066	B_g	115.909	A_u
80.152	A_u	118.116	B_u
80.543	A_g	118.188	A_g
82.853	B_g	121.069	A_u
83.187	B_u	121.953	B_g
85.283	A_g	123.445	B_u
86.172	A_u	125.082	B_u
87.343	B_g	125.816	B_g
88.812	B_u	126.815	A_g
89.105	A_u	130.186	A_g
89.300	A_g	131.537	A_u
92.243	A_u	132.628	B_u
93.036	B_g	133.245	B_g
93.160	A_g	134.329	A_u
94.335	B_u	134.703	B_g
96.667	A_g	136.505	A_g
96.710	B_u	175.928	A_g
97.131	A_u	176.699	B_u
97.849	B_g	177.099	A_u

Table B.6 (Continued). Calculated phonon modes in **Co-I** and their symmetries

Wavenumber (cm^{-1})	**Symmetries of the modes**	**Wavenumber (cm^{-1})**	**Symmetries of the modes**
178.179	B_g	231.670	A_g
185.969	A_u	231.799	A_u
187.990	B_g	232.161	B_g
189.204	B_u	240.364	A_u
189.731	A_g	240.729	B_g
193.780	A_g	241.122	A_g
194.848	A_u	241.185	B_u
196.514	B_g	249.689	A_g
197.206	B_u	250.090	A_u
200.751	B_u	250.373	B_g
201.133	B_g	250.426	B_u
202.455	A_g	256.094	A_g
202.682	A_u	256.352	B_g
208.011	B_u	256.462	B_u
208.608	B_g	256.565	A_u
208.843	A_g	260.106	A_u
209.348	A_u	260.250	A_g
214.940	B_u	262.519	B_g
215.619	A_g	262.560	B_u
215.984	B_g	264.814	A_u
216.869	A_u	264.901	A_g
220.892	A_u	265.829	B_g
221.846	B_g	265.899	B_u
222.115	B_u	277.922	A_g
222.201	A_g	278.014	B_u
224.835	B_u	278.742	A_u
224.958	B_g	278.770	B_g
226.154	A_u	385.325	A_g
226.594	A_g	386.054	A_u
231.116	B_u	386.689	B_u

Table B.6 (Continued). Calculated phonon modes in **Co-I** and their symmetries

Wavenumber (cm^{-1})	**Symmetries of the modes**	**Wavenumber (cm^{-1})**	**Symmetries of the modes**
386.934	B_g	427.113	B_g
389.845	A_g	427.187	B_u
389.930	A_u	427.605	A_u
390.224	B_u	428.793	A_u
390.870	B_g	428.833	A_g
393.683	B_g	429.623	B_u
394.182	A_u	429.665	B_g
395.581	A_g	433.907	B_u
396.474	B_u	434.342	B_g
396.947	B_u	434.508	A_u
398.158	A_g	434.942	A_g
398.656	B_g	437.952	A_u
398.849	A_u	438.371	B_u
401.623	A_u	438.405	B_g
402.421	B_u	438.484	A_g
402.830	B_g	472.982	A_u
403.266	A_g	473.136	B_u
405.927	B_u	473.163	A_g
406.351	B_g	473.397	B_g
406.803	A_g	484.966	B_u
406.900	A_u	484.997	A_u
407.862	B_g	485.479	B_g
408.056	A_u	485.718	A_g
408.193	B_u	486.605	B_u
408.252	A_g	487.283	A_u
410.627	B_u	487.803	A_g
410.714	A_u	488.336	B_g
411.546	B_g	502.974	A_g
411.761	A_g	503.337	B_g
426.306	A_g	503.495	B_u

Table B.6 (Continued). Calculated phonon modes in **Co-I** and their symmetries

Wavenumber (cm^{-1})	**Symmetries of the modes**	**Wavenumber (cm^{-1})**	**Symmetries of the modes**
504.059	A_u	689.749	A_u
506.762	B_u	690.613	A_u
507.320	A_g	690.668	A_g
509.019	A_u	691.937	B_g
509.839	B_g	691.984	B_u
511.635	B_g	692.050	A_g
511.776	A_u	692.192	A_u
512.293	A_g	692.510	A_g
512.519	B_u	692.581	B_u
605.453	B_u	693.156	B_g
605.542	A_u	693.190	A_u
605.682	A_g	693.440	A_g
605.736	B_g	693.724	B_g
606.517	A_g	693.821	A_u
606.764	A_u	693.893	B_u
606.888	B_g	694.791	B_u
610.540	A_u	695.056	B_g
674.340	B_u	695.377	A_u
675.167	B_u	695.680	B_u
685.421	A_g	696.264	A_u
685.582	A_u	696.294	A_g
685.710	B_u	696.390	B_g
687.066	B_g	696.725	A_g
687.377	B_g	696.842	B_g
687.403	A_u	697.568	B_u
687.622	A_g	697.974	A_u
687.727	B_u	698.649	A_g
688.074	B_u	726.568	B_u
688.953	B_g	727.428	B_u
689.279	A_g	727.765	B_g

Table B.6 (Continued). Calculated phonon modes in **Co-I** and their symmetries

Wavenumber (cm^{-1})	**Symmetries of the modes**	**Wavenumber (cm^{-1})**	**Symmetries of the modes**
727.772	A_u	833.196	A_g
729.822	A_g	833.829	B_g
729.891	B_g	834.311	A_g
730.100	B_u	834.612	B_u
730.920	B_g	835.260	A_u
732.386	A_u	835.290	B_g
732.860	A_g	835.961	B_u
734.723	A_u	839.605	B_u
734.838	A_g	840.205	A_u
736.178	A_g	840.704	B_g
736.835	B_g	841.099	A_g
737.398	A_u	842.073	B_u
737.476	B_u	842.347	A_u
740.045	A_u	846.666	A_g
742.092	B_u	847.169	B_g
745.629	A_g	898.757	A_u
745.750	A_u	898.926	A_g
746.563	B_g	904.379	A_g
746.676	B_u	904.647	B_u
751.480	A_g	904.995	B_g
751.649	B_g	905.088	A_u
826.291	A_g	906.385	A_u
826.584	A_u	906.412	A_g
827.905	A_u	907.174	B_u
827.946	B_u	907.427	B_g
828.692	A_g	908.783	B_u
828.795	B_g	909.033	A_u
830.496	B_u	909.854	B_g
830.636	B_g	910.206	B_u
832.430	A_u	910.307	B_g

Table B.6 (Continued). Calculated phonon modes in **Co-I** and their symmetries

Wavenumber (cm^{-1})	**Symmetries of the modes**	**Wavenumber (cm^{-1})**	**Symmetries of the modes**
911.634	A_g	969.796	B_u
915.954	A_g	970.173	B_g
916.285	B_g	970.519	A_g
916.834	B_u	973.005	B_u
916.908	A_u	973.202	B_g
920.067	A_u	974.725	B_g
920.242	A_g	974.939	A_g
921.128	B_g	975.185	A_u
921.150	B_u	975.391	B_u
952.355	A_g	977.248	A_g
952.751	A_u	977.957	B_u
953.842	B_u	978.006	A_u
954.754	B_g	978.142	B_g
955.619	A_u	978.271	A_g
955.648	B_g	978.321	A_u
956.145	B_u	978.825	B_g
956.217	A_g	979.520	B_u
956.579	A_g	980.354	A_u
957.057	A_u	980.459	A_g
958.075	B_g	982.743	A_g
958.740	B_u	982.970	B_g
959.264	A_g	983.942	A_u
959.322	B_u	984.028	B_u
959.619	B_g	984.471	A_g
959.901	A_u	984.525	B_g
965.971	B_g	985.127	B_u
966.410	A_g	985.283	A_u
966.779	A_u	985.312	B_g
966.811	B_u	985.580	B_u
969.235	A_u	985.680	A_g

Table B.6 (Continued). Calculated phonon modes in **Co-I** and their symmetries

Wavenumber (cm^{-1})	**Symmetries of the modes**	**Wavenumber (cm^{-1})**	**Symmetries of the modes**
985.792	B_g	1019.061	A_g
985.803	B_u	1019.118	A_u
986.205	A_g	1019.317	B_u
986.741	A_u	1019.406	A_u
986.874	A_u	1019.451	B_u
986.987	B_g	1019.756	B_g
987.950	B_u	1019.993	B_u
988.075	A_g	1020.041	A_g
988.132	B_g	1020.062	A_u
988.444	B_u	1020.352	B_g
988.468	A_u	1021.086	A_g
988.619	A_u	1022.384	A_u
988.701	B_g	1022.814	A_g
988.860	A_g	1022.924	B_g
989.054	B_u	1022.990	B_u
991.021	A_u	1065.802	A_u
991.337	A_g	1066.324	B_g
993.812	B_u	1066.744	B_u
993.986	A_u	1066.959	A_g
995.365	A_g	1068.726	A_g
995.410	B_g	1068.813	A_u
1014.667	B_u	1068.906	B_g
1014.710	B_g	1069.132	A_u
1014.815	A_u	1069.275	B_u
1015.104	A_g	1069.449	A_g
1016.448	B_u	1070.305	B_u
1016.471	A_u	1070.697	A_g
1016.764	B_g	1071.001	B_g
1017.136	A_g	1071.191	B_u
1019.045	B_g	1071.432	A_u

Table B.6 (Continued). Calculated phonon modes in **Co-I** and their symmetries

Wavenumber (cm^{-1})	**Symmetries of the modes**	**Wavenumber (cm^{-1})**	**Symmetries of the modes**
1071.529	B_g	1084.302	B_g
1073.236	A_g	1084.315	B_u
1073.372	B_g	1085.366	A_g
1073.513	A_u	1142.619	B_g
1073.753	B_u	1142.823	B_u
1074.478	A_u	1143.352	A_g
1075.009	B_g	1143.668	B_g
1075.084	B_u	1143.745	A_u
1075.251	B_u	1144.647	B_u
1075.322	B_g	1145.028	B_g
1075.330	A_u	1145.257	A_u
1075.410	A_g	1145.440	A_g
1075.681	A_g	1145.520	B_u
1078.530	B_u	1146.141	A_u
1078.540	A_g	1146.492	A_g
1078.717	A_u	1148.947	A_u
1078.907	B_g	1149.133	B_u
1078.946	A_g	1149.335	B_g
1078.974	A_u	1149.414	A_g
1079.312	B_u	1153.048	B_u
1079.369	B_g	1153.668	B_g
1079.584	B_u	1153.843	A_u
1079.974	A_g	1153.850	A_g
1080.075	A_u	1155.551	B_u
1080.736	B_g	1155.948	A_u
1082.488	A_u	1156.145	B_g
1082.893	B_u	1156.263	A_g
1082.918	B_g	1167.171	A_g
1083.858	A_g	1167.243	B_g
1084.242	A_u	1167.266	A_u

Table B.6 (Continued). Calculated phonon modes in **Co-I** and their symmetries

Wavenumber (cm^{-1})	**Symmetries of the modes**	**Wavenumber (cm^{-1})**	**Symmetries of the modes**
1167.340	B_u	1293.011	B_u
1167.599	B_g	1293.173	A_g
1168.183	B_u	1293.297	B_g
1168.363	A_u	1296.699	A_g
1169.888	A_g	1297.141	B_u
1170.526	B_u	1297.377	A_u
1170.819	A_u	1297.448	B_g
1170.938	B_g	1297.580	B_g
1171.078	A_g	1297.585	B_u
1174.643	B_u	1297.803	A_g
1174.798	A_u	1297.976	A_u
1174.897	A_g	1301.858	A_g
1176.442	B_g	1302.017	B_u
1176.735	A_u	1302.125	B_g
1177.379	B_g	1302.128	A_u
1178.274	B_u	1323.647	B_g
1178.669	A_g	1323.728	A_g
1178.866	A_u	1323.822	B_u
1179.422	B_u	1323.831	A_u
1179.509	B_g	1326.302	B_g
1180.093	A_g	1326.352	A_u
1287.079	A_g	1326.669	B_u
1287.216	A_u	1327.045	B_g
1287.323	B_g	1327.100	A_g
1287.373	B_u	1327.217	B_u
1288.841	A_u	1327.258	A_u
1289.071	B_u	1327.405	A_g
1289.119	A_g	1328.543	B_u
1289.502	B_g	1328.585	B_g
1292.825	A_u	1329.306	A_u

Table B.6 (Continued). Calculated phonon modes in **Co-I** and their symmetries

Wavenumber (cm^{-1})	**Symmetries of the modes**	**Wavenumber (cm^{-1})**	**Symmetries of the modes**
1329.331	A_g	1422.214	B_u
1329.837	B_g	1423.417	A_u
1329.918	A_u	1423.616	B_g
1330.090	B_u	1458.647	A_g
1330.204	A_g	1458.746	B_g
1330.261	B_u	1458.776	B_u
1330.308	A_g	1458.920	A_u
1331.074	A_u	1460.189	A_u
1331.530	B_g	1460.195	B_u
1412.601	B_g	1460.724	A_g
1413.142	A_g	1460.728	B_g
1413.345	A_u	1460.926	B_u
1413.429	B_u	1461.062	A_u
1413.760	B_g	1461.255	B_g
1414.016	A_u	1461.310	A_g
1414.754	B_u	1462.621	A_u
1415.068	A_g	1462.714	A_g
1417.558	B_g	1463.022	B_g
1417.779	A_g	1463.049	B_u
1418.081	B_u	1464.269	A_u
1418.263	B_u	1464.324	A_g
1418.275	A_u	1464.679	B_g
1418.395	A_g	1464.869	B_u
1418.675	A_u	1465.178	A_g
1418.726	B_g	1465.350	A_u
1420.299	A_g	1465.540	B_u
1420.353	A_u	1465.670	B_g
1420.623	B_u	1554.276	A_u
1420.752	B_g	1554.494	B_g
1421.936	A_g	1554.850	A_u

Table B.6 (Continued). Calculated phonon modes in **Co-I** and their symmetries

Wavenumber (cm^{-1})	Symmetries of the modes	Wavenumber (cm^{-1})	Symmetries of the modes
1555.075	B_u	1569.660	B_g
1555.089	A_g	1569.811	A_u
1555.113	B_g	1570.380	A_g
1555.420	A_g	1570.507	B_g
1555.487	B_u	1570.548	B_u
1557.365	B_u	1570.783	A_u
1557.408	B_g	1570.925	A_g
1557.494	A_u	1571.373	B_g
1558.091	A_g	1571.529	B_u
1559.403	B_g	1571.542	A_u
1559.516	A_u	1571.967	A_g
1559.870	B_u	1572.149	A_u
1559.945	A_g	1572.533	B_g
1560.900	A_u	1572.584	A_g
1561.013	A_g	1572.701	B_u
1561.321	B_u	3035.359	A_g
1561.600	B_g	3035.649	B_u
1561.684	A_g	3035.659	A_u
1561.825	B_g	3035.685	B_g
1561.867	B_u	3045.959	A_g
1561.967	A_u	3046.088	B_u
1565.825	A_g	3046.105	A_u
1565.933	B_g	3046.267	B_g
1566.137	B_u	3052.328	A_g
1566.347	A_u	3052.703	A_u
1568.523	B_g	3052.708	B_u
1568.606	B_u	3052.748	B_g
1568.622	A_u	3053.772	A_g
1568.716	A_g	3053.875	B_u
1569.576	B_u	3053.926	A_u

Table B.6 (Continued). Calculated phonon modes in **Co-I** and their symmetries

Wavenumber (cm^{-1})	**Symmetries of the modes**	**Wavenumber (cm^{-1})**	**Symmetries of the modes**
3053.928	B_g	3066.434	A_u
3055.229	A_g	3066.474	B_u
3055.638	B_u	3066.808	B_g
3055.667	A_u	3067.925	A_g
3055.809	B_g	3068.130	B_u
3058.895	A_g	3068.174	B_g
3059.201	B_g	3068.252	A_u
3059.262	A_u	3069.371	A_u
3059.281	B_u	3069.427	A_g
3060.117	A_g	3069.436	B_u
3060.721	B_g	3069.616	B_g
3060.781	B_u	3070.008	B_u
3060.898	A_u	3070.084	B_g
3062.069	A_g	3071.760	A_g
3062.420	A_u	3072.089	A_u
3062.483	A_g	3072.355	A_g
3062.513	B_u	3072.602	A_g
3062.576	B_g	3072.629	A_u
3062.628	B_u	3072.828	B_g
3062.650	B_g	3073.076	B_u
3062.722	A_u	3073.253	A_u
3064.033	A_g	3073.692	B_g
3064.321	B_g	3073.716	B_u
3064.475	A_u	3073.721	A_g
3064.535	B_u	3074.490	A_u
3065.363	B_u	3074.673	A_g
3065.368	A_u	3074.974	B_u
3065.444	A_g	3075.089	B_g
3066.128	B_g	3075.214	A_u
3066.133	A_g	3075.308	B_u

Table B.6 (Continued). Calculated phonon modes in **Co-I** and their symmetries

Wavenumber (cm^{-1})	**Symmetries of the modes**	**Wavenumber (cm^{-1})**	**Symmetries of the modes**
3075.495	A_g	3088.617	A_u
3075.758	B_g	3088.643	B_g
3075.867	A_g	3088.742	B_u
3075.878	B_u	3090.177	A_g
3075.894	B_g	3090.534	B_u
3076.297	A_u	3090.658	B_g
3076.667	B_g	3091.143	A_u
3076.965	A_u	3092.382	A_g
3076.982	B_u	3093.499	B_g
3078.001	A_u	3093.527	A_u
3078.148	B_u	3093.935	B_u
3078.744	A_g	3096.187	A_g
3079.085	B_g	3096.970	B_u
3080.071	A_g	3097.040	B_g
3080.231	B_g	3097.042	A_u
3080.250	B_u		
3080.261	A_u		
3083.114	A_g		
3083.409	A_u		
3084.337	B_u		
3084.340	B_g		
3086.675	A_g		
3087.665	A_g		
3087.712	A_u		
3087.975	B_u		
3088.003	B_g		
3088.072	A_g		
3088.228	A_u		
3088.237	B_g		
3088.387	B_u		

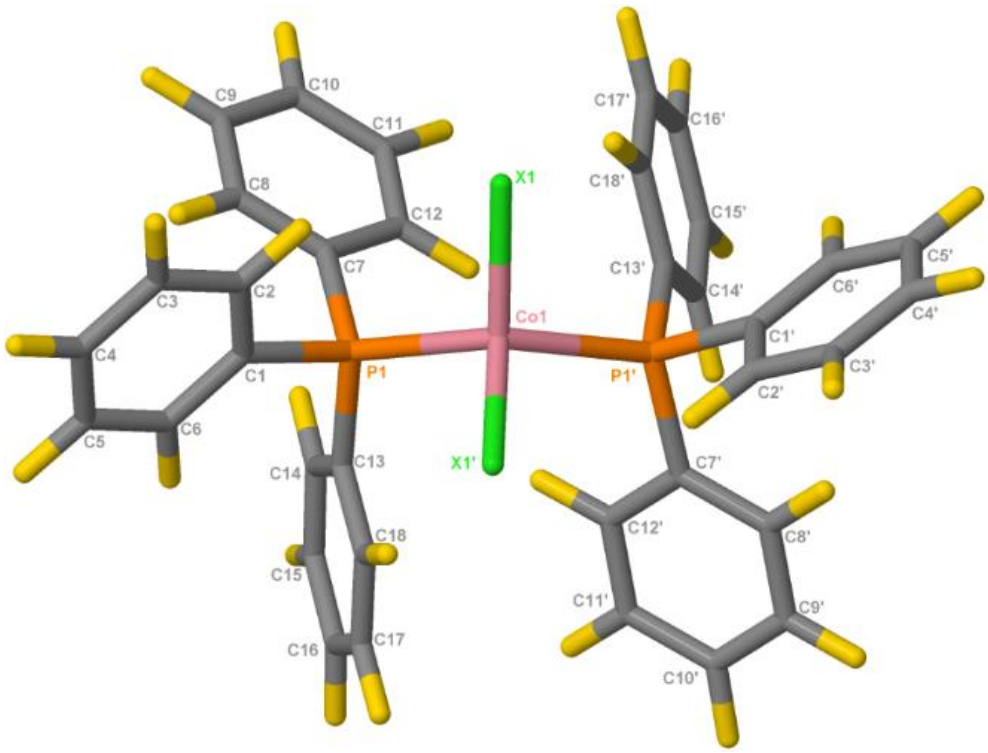


Figure B.22. Capped stick molecular structure representing **Co-Cl** and **Co-Br**. Atom labels correspond to the labels in Table B.7. Yellow caps represent H-atoms.

Table B.7. Calculated spin densities of atoms in **Co-Cl** and **Co-Br**

Atom	Co-Cl	Co-Br
Co	2.585	2.570
X1, X1′	6.69×10^{-2}	6.85×10^{-2}
P1, P1′	2.06×10^{-2}	1.92×10^{-2}
C1, C1′	1.21×10^{-4}	3.90×10^{-4}
C2, C2′	1.37×10^{-3}	1.91×10^{-3}
C3, C3′	-5.05×10^{-4}	-2.07×10^{-4}
C4, C4′	1.45×10^{-3}	1.50×10^{-3}
C5, C5′	-2.02×10^{-4}	-5.36×10^{-4}
C6, C6′	1.89×10^{-3}	1.37×10^{-3}
C7, C7′	1.03×10^{-3}	8.55×10^{-4}
C8, C8′	2.37×10^{-3}	2.93×10^{-3}
C9, C9’	-2.40×10^{-4}	-2.92×10^{-4}
C10, C10′	1.91×10^{-3}	2.73×10^{-3}
C11, C11′	-4.18×10^{-4}	-5.34×10^{-4}
C12, C12′	1.85×10^{-3}	2.18×10^{-3}
C13, C13′	6.96×10^{-4}	1.15×10^{-3}
C14, C14′	2.98×10^{-3}	2.14×10^{-3}
C15, C15′	-3.78×10^{-4}	-1.50×10^{-4}
C16, C16′	2.73×10^{-3}	1.70×10^{-3}
C17, C17′	-6.38×10^{-4}	-2.08×10^{-4}
C18, C18′	2.20×10^{-3}	1.69×10^{-3}
H2, H2′	-3.19×10^{-5}	-2.12×10^{-5}
H3, H3′	2.40×10^{-7}	5.47×10^{-5}
H4, H4′	-1.77×10^{-5}	-1.89×10^{-5}
H5, H5′	5.10×10^{-5}	1.21×10^{-6}
H6, H6′	-1.84×10^{-5}	-3.61×10^{-5}
H8, H8′	1.57×10^{-5}	-3.49×10^{-5}
H9, H9′	7.25×10^{-5}	9.47×10^{-5}
H10, H10′	-2.50×10^{-5}	1.78×10^{-5}
H11, H11′	5.57×10^{-5}	3.83×10^{-5}
H12, H12′	-5.65×10^{-5}	-2.74×10^{-5}
H14, H14′	-3.45×10^{-5}	2.03×10^{-5}
H15, H15′	8.40×10^{-5}	7.09×10^{-5}
H16, H16′	1.28×10^{-5}	-2.02×10^{-5}
H17, H17′	2.50×10^{-5}	8.60×10^{-5}
H18, H18′	-3.27×10^{-5}	-4.92×10^{-5}
Total	**2.797**	**2.783**

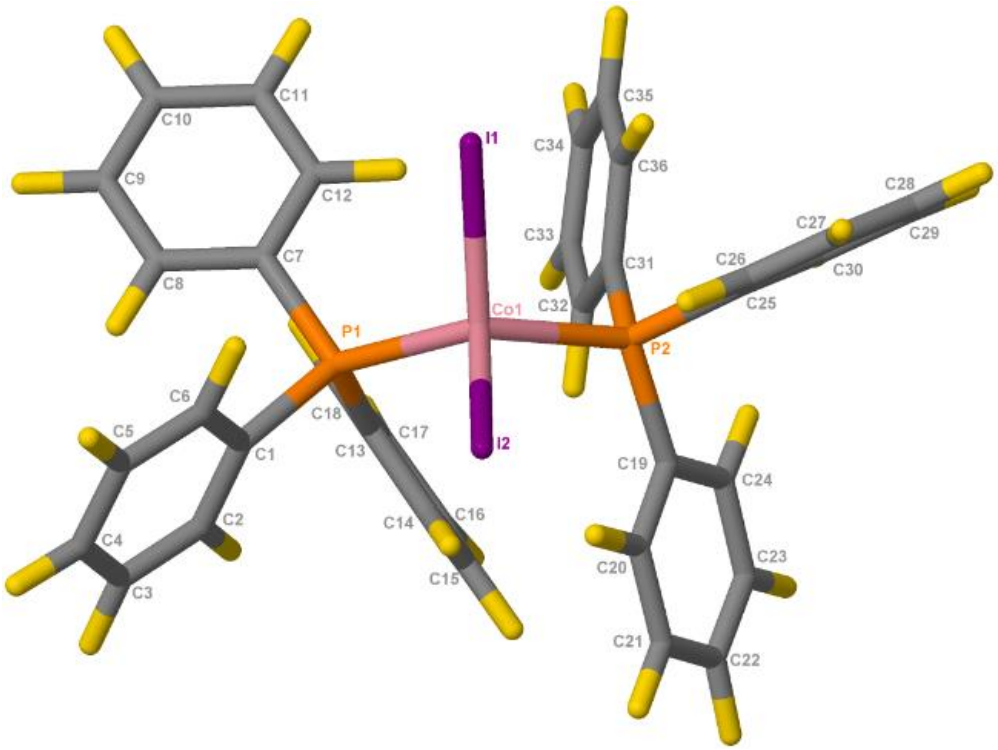


Figure B.23. Capped stick molecular structure of **Co-I**. Atom labels correspond to the labels in Table B.8. Yellow caps represent H-atoms.

Table B.8. Calculated spin densities of atoms in **Co-I**

Atoms	Spin density	Atoms	Spin density
Co	2.553		
I1	6.39×10^{-2}	I2	6.01×10^{-2}
P1	1.55×10^{-2}	P2	1.94×10^{-2}
C1	1.15×10^{-3}	C2	1.55×10^{-3}
C3	-6.62×10^{-6}	C4	1.32×10^{-3}
C5	-2.46×10^{-4}	C6	8.09×10^{-4}
C7	1.30×10^{-3}	C8	1.68×10^{-3}
C9	1.55×10^{-4}	C10	1.34×10^{-3}
C11	7.71×10^{-6}	C12	6.40×10^{-4}
C13	1.86×10^{-4}	C14	2.12×10^{-3}
C15	-3.41×10^{-4}	C16	2.15×10^{-3}
C17	-4.38×10^{-4}	C18	2.06×10^{-3}
C19	2.28×10^{-3}	C20	3.76×10^{-4}
C21	-2.12×10^{-4}	C22	4.51×10^{-4}
C23	4.68×10^{-4}	C24	2.06×10^{-3}
C25	9.47×10^{-4}	C26	4.26×10^{-4}
C27	4.00×10^{-8}	C28	5.54×10^{-4}
C29	4.33×10^{-4}	C30	1.07×10^{-3}
C31	5.39×10^{-4}	C32	2.75×10^{-3}
C33	-1.04×10^{-3}	C34	5.07×10^{-3}
C35	-9.95×10^{-4}	C36	4.31×10^{-3}
H2	1.68×10^{-5}	H3	5.87×10^{-5}
H4	-2.70×10^{-6}	H5	8.21×10^{-6}
H6	-1.74×10^{-5}	H8	4.45×10^{-5}
H9	7.86×10^{-5}	H10	3.97×10^{-5}
H11	6.44×10^{-5}	H12	-2.65×10^{-5}
H14	-2.29×10^{-5}	H15	2.74×10^{-5}
H16	4.78×10^{-5}	H17	4.49×10^{-5}
H18	1.42×10^{-5}	H20	-2.49×10^{-5}
H21	9.52×10^{-6}	H22	5.85×10^{-6}
H23	8.85×10^{-5}	H24	-1.66×10^{-5}
H26	1.68×10^{-5}	H27	1.34×10^{-5}
H28	4.74×10^{-5}	H29	7.52×10^{-5}
H30	3.13×10^{-5}	H32	-3.17×10^{-5}
H33	6.75×10^{-6}	H34	-4.10×10^{-5}
H35	6.21×10^{-5}	H36	3.32×10^{-5}
Total	**2.747**		

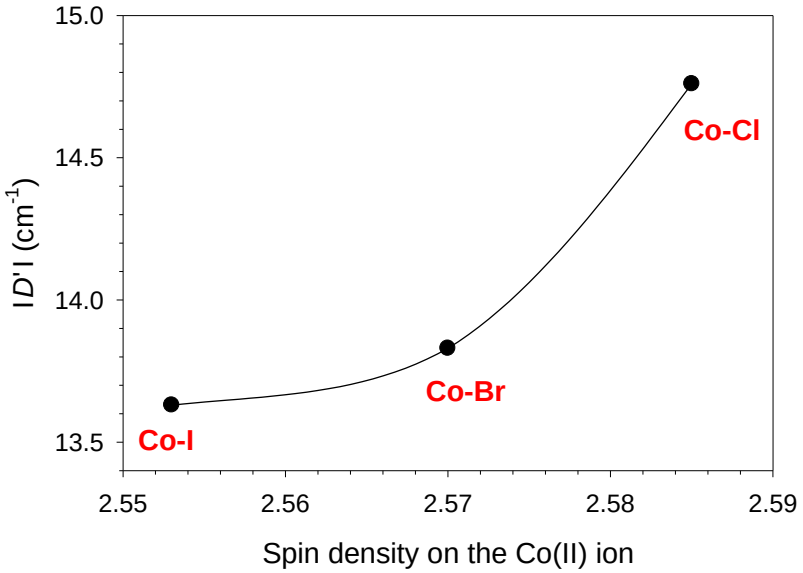


Figure B.24. Correlation between the calculated spin densities on the Co(II) ions in **Co-X** and the ZFS *D*' parameters.

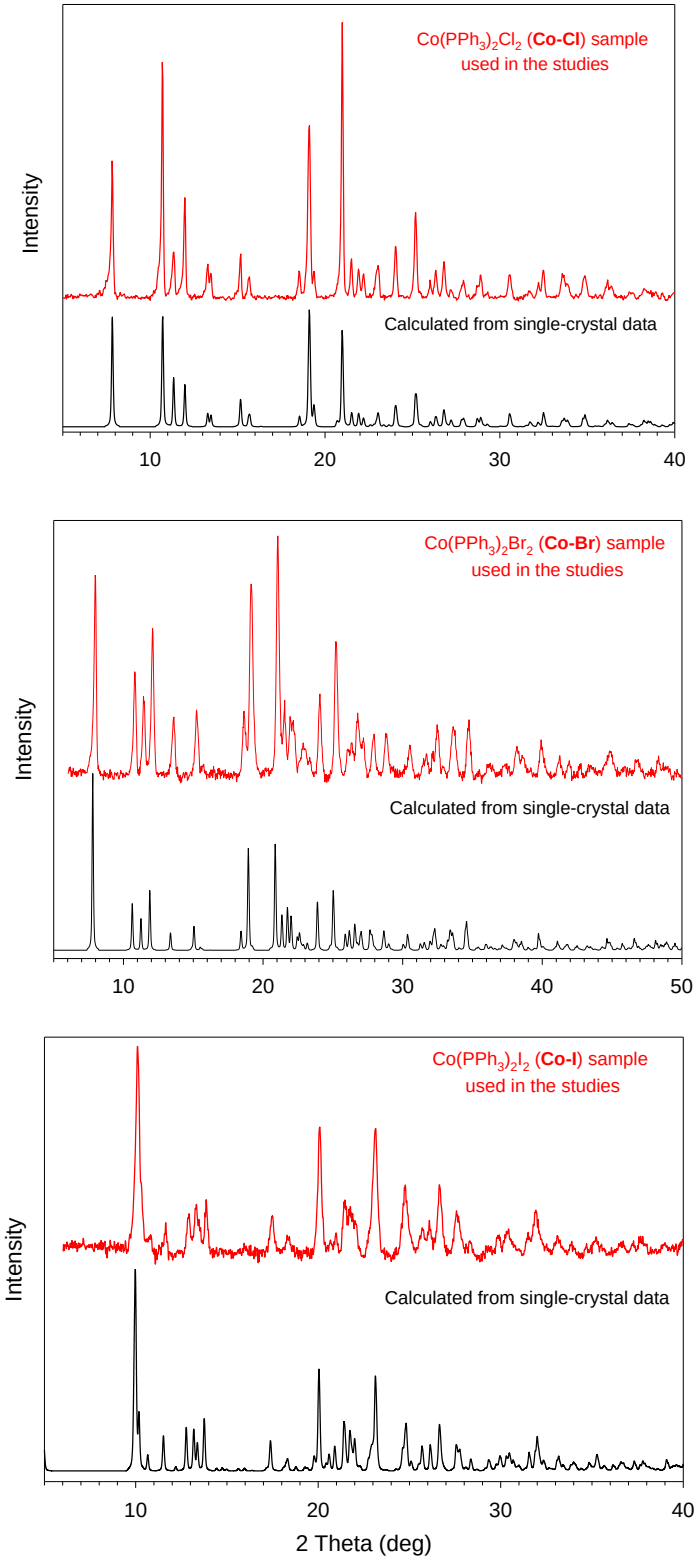


Figure B.25. Powder X-ray diffraction of typical **Co-Cl**, **Co-Br**, and **Co-I** samples.

Appendix C. Supporting Information for Chapter IV

C.1. Crystallographic Data, Figures, Tables, and CShM Calculations

C.1.1. Crystallographic Data, Figures, and Tables

Table C.1. Crystallographic data for **Mn-Br·CHCl$_3$** and **Mn-Br·CH$_2$Cl$_2$**

	Mn(TPP)Br·CHCl$_3$ (**Mn-Br·CHCl3**)	Mn(TPP)Br·CH$_2$Cl$_2$ (**Mn-Br·CH$_2$Cl$_2$**)
Molecular formula	$C_{45}H_{29}BrCl_3MnN_4$	$C_{45}H_{30}BrCl_2MnN_4$
CCDC No.	1977356	1977357
Formula weight	866.92	832.48
Temperature	100(2) K	100(2) K
Crystal system	Monoclinic	Monoclinic
Space group	$P2_1/n$	$P2_1/n$
a (Å)	12.1478(5)	11.9351(5)
b (Å)	21.9344(9)	45.8490(19)
c (Å)	14.4549(6)	14.3311(6)
α (°)	90	90
β (°)	101.521(2)	104.5960(10)
γ (°)	90	90
V (Å^3)	3774.0(3)	7589.1(5)
Z	4	8
D_{calc} (g/cm^3)	1.526	1.457
μ (mm^{-1})	1.661	1.580
F(000)	1752	3376
θ range (°)	2.21-31.51	2.18-25.68
Reflns collected	36191	75086
R_{int}	0.0365	0.0882
Indep. reflns	12271	14431
[$I > 2\sigma(I)$]	9694	10839
Data/restr./paras	12271/0/487	14431/25/966
Goodness-of-fit on F^2	1.039	1.119
R_1, wR_2 [$I > 2\sigma(I)$]	0.0527/0.1296	0.0817/0.1704

Table C.1. Continued

	Mn(TPP)Br·$CHCl_3$ (**Mn-Br·CHCl3**)	Mn(TPP)Br·CH_2Cl_2 (**2·CH_2Cl_2**)
R_1, wR_2 [all data]	0.0720/0.1393	0.1105/0.1830

Table C.2. Crystallographic data for **Mn-I·CHCl$_3$, Mn-I·CDCl$_3$** and **Mn-I·1.5CHCl$_3$**

	Mn(TPP)I·CHCl$_3$ (**Mn-I·CHCl$_3$**)	Mn(TPP)I·CDCl$_3$ (**Mn-I·CDCl$_3$**)	Mn(TPP)I·1.5CHCl$_3$ (**Mn-I·1.5CHCl$_3$**)
Molecular formula	$C_{45}H_{29}Cl_3IMnN_4$	$C_{45}H_{28}DCl_3IMnN_4$	$C_{45.50}H_{29.50}Cl_{4.5}IMnN_4$
CCDC No.	1977355	1977353	1977354
Formula weight	913.91	914.91	973.59
Temperature	100(2) K	293(2) K	100(2) K
Crystal system	Monoclinic	Monoclinic	Triclinic
Space group	$P2_1/n$	$P2_1/c$	$P\bar{1}$
a (Å)	13.5192(8)	17.310(4)	13.0316(12)
b (Å)	18.0774(11)	22.039(4)	15.3967(14)
c (Å)	15.9581(9)	20.706(4)	20.7018(19)
α (°)	90	90	77.333(2)
β (°)	91.221(2)	99.07(3)	88.214(2)
γ (°)	90	90	85.568(2)
V (Å^3)	3899.1(4)	7800.(3)	4040.0(6)
Z	4	8	4
D_{calc} (g/cm^3)	1.557	1.556	1.601
μ (mm^{-1})	1.374	1.374	1.428
F(000)	1824	3648	1940
θ range (°)	2.25-28.28	1.19-26.02	2.09-31.51
Reflns collected	39482	59507	148051
R_{int}	0.0406	0.0261	0.0374
Indep. reflns	9666	15364	26930
[$I > 2\sigma(I)$]	7939	12527	23364
Data/restr./paras	9666/0/487	15364/1/1007	26930/127/1053
Goodness-of-fit on F^2	0.974	1.074	1.012
R_1, wR_2 [$I > 2\sigma(I)$]	0.0302/0.0690	0.0442/0.1070	0.0426/0.1006
R_1, wR_2 [all data]	0.0421/0.0764	0.0559/0.1141	0.0510/0.1077

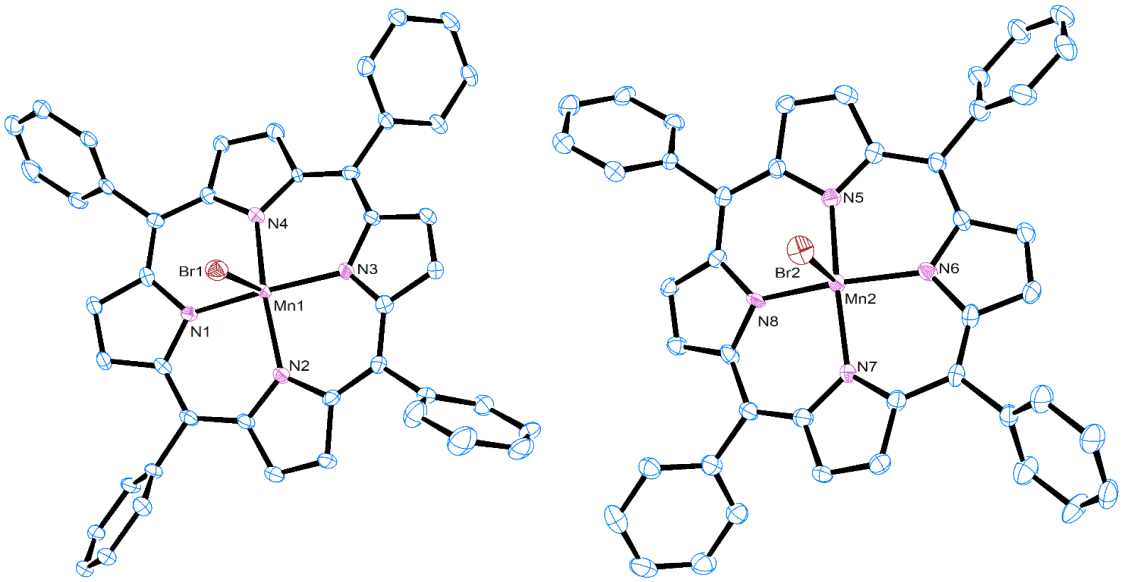


Figure C.1. ORTEP diagrams of the two independent Mn(TPP)Br molecules in **Mn-Br·CH_2Cl_2**. CH_2Cl_2 and H atoms are omitted. One CH_2Cl_2 molecule is disordered, as discussed in Experimental.

Table C.3. Selected bond lengths (Å) and angles (°) for **Mn-Br·CH_2Cl_2**

Atoms	Length (Å) or angle (°)	Atoms	Length (Å) or angle (°)
Mn1—Br1	2.5247(12)	Mn2—Br2	2.5200(13)
Mn1—N1	1.999(5)	Mn2—N5	2.000(5)
Mn1—N2	2.017(5)	Mn2—N6	2.011(5)
Mn1—N3	2.008(5)	Mn2—N7	2.006(5)
Mn1—N4	2.008(5)	Mn2—N8	2.004(5)
N1—Mn1—N2	89.8(2)	N5—Mn2—N6	89.0(2)
N2—Mn1—N3	89.1(2)	N6—Mn2—N7	89.0(2)
N3—Mn1—N4	88.9(2)	N7—Mn2—N8	88.3(2)
N1—Mn1—N4	88.9(2)	N5—Mn2—N8	89.9(2)
N1—Mn1—Br1	92.42(16)	N5—Mn2—Br2	91.31(16)
N2—Mn1—Br1	95.59(15)	N6—Mn2—Br2	98.89(17)
N3—Mn1—Br1	98.52(16)	N7—Mn2—Br2	101.06(17)
N4—Mn1—Br1	101.40(16)	N8—MN2—Br2	98.99(16)
N1—Mn1—N3	169.1(2)	N5—Mn2—N7	167.6(2)
N2—Mn1—N4	163.0(2)	N6—Mn2—N8	162.1(2)

Mn(TPP)I (**Mn-I**) crystallized in deuterated chloroform at 23 °C into **Mn-I·CDCl$_3$** with the monoclinic space group $P2_1/c$. Using $CHCl_3$ alone as solvent at either 23 or -33 °C, crystallization gave **Mn-I·1.5CHCl$_3$** (triclinic space group $P\bar{1}$, SM). As indicated in the main text, **Mn-I** in layered pentane/$CHCl_3$ gave **Mn-I·CDCl$_3$**.

Mn-I·CDCl$_3$ and **Mn-I·1.5CHCl$_3$** each have two crystallographically distinct Mn(TPP)I (**3**) molecules in the unit cells, while there is only one Mn(TPP)I molecule in the unit cell of **Mn-I·CHCl$_3$**. ORTEP diagrams of one molecule of **Mn-I** in **Mn-I·CDCl$_3$** and **Mn-I·1.5CHCl$_3$** are given in Figs. C.2 and C.3, respectively.

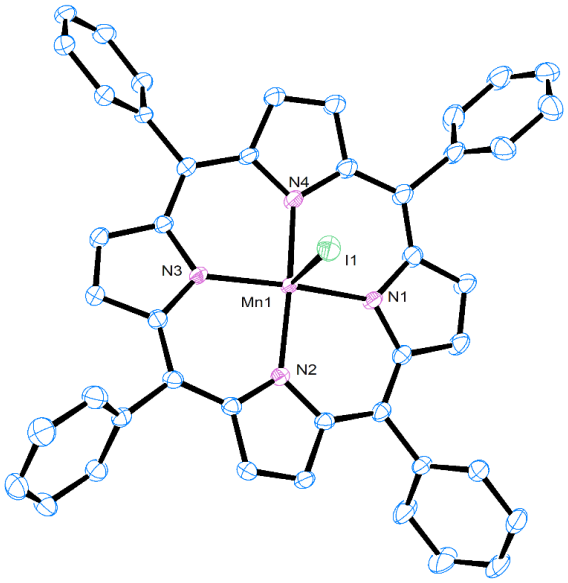


Figure C.2. ORTEP diagram of the structure of one molecule of Mn(TPP)I in the crystal of **Mn-I·CDCl$_3$**. $CDCl_3$ in the lattice and H atoms are omitted.

Table C.4. Selected bond lengths (Å) and angles (°) for one molecule of **Mn-I** in **Mn-I·$CDCl_3$**

Atoms	Length (Å) or angle (°)	Atoms	Length (Å) or angle (°)
Mn1—I1	2.7437(9)	Mn1—N1	2.013(3)
Mn1—N2	2.007(3)	Mn1—N3	2.006(3)
Mn1—N4	2.006(3)		
N1—Mn1—N2	89.2(1)	N2—Mn1—N3	89.1(1)
N3—Mn1—N4	89.3(1)	N1—Mn1—N4	89.5(1)
N1—Mn1—I1	96.65(9)	N2—Mn1—I1	99.88(8)
N3—Mn1—I1	98.25(9)	N4—Mn1—I1	91.80(9)
N1—Mn1—N3	165.1(1)	N2—Mn1—N4	168.3(1)

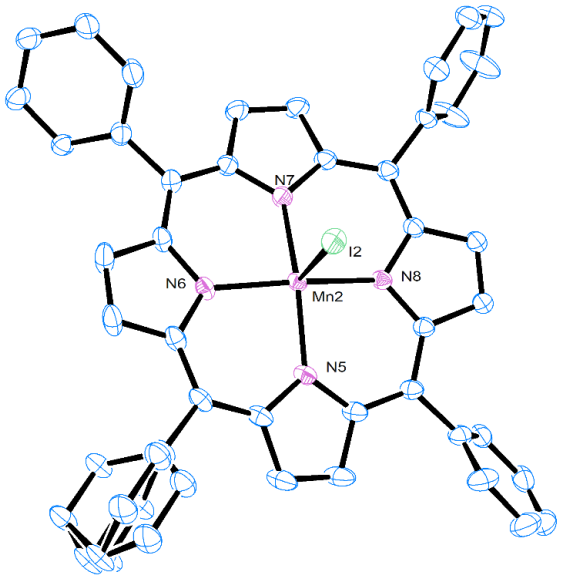


Figure C.3. ORTEP diagram of the structure of the molecule containing Mn2 in the crystal of Mn(TPP)I·1.5$CHCl_3$ (**Mn-I·1.5$CHCl_3$**). $CHCl_3$ and H atoms are omitted. The structure was disordered, as discussed in the main text.

Table C.5. Selected bond lengths (Å) and angles (°) for **Mn-I·1.5CHCl$_3$**

Atoms	Length (Å) or angle (°)	Atoms	Length (Å) or angle (°)
Mn1—I1	2.7423(4)	Mn2—I2	2.7843(4)
Mn1—N1	2.0179(19)	Mn2—N5	2.007(2)
Mn1—N2	2.0041(18)	Mn2—N6	2.0084(19)
Mn1—N3	2.018(2)	Mn2—N7	2.006(2)
Mn1—N4	2.0000(19)	Mn2—N8	2.0109(19)
N1—Mn1—N2	89.22(7)	N5—Mn2—N6	89.65(8)
N2—Mn1—N3	89.76(8)	N6—Mn2—N7	88.69(8)
N3—Mn1—N4	89.17(8)	N7—Mn2—N8	89.26(8)
N1—Mn1—N4	89.58(8)	N5—Mn2—N8	88.66(8)
N1—Mn1—I1	96.92(5)	N5—Mn2—I2	100.97(6)
N2—Mn1—I1	93.44(5)	N6—Mn2—I2	95.81(6)
N3—Mn1—I1	99.37(6)	N7—Mn2—I2	96.05(6)
N4—Mn1—I1	94.56(6)	N8—Mn2—I2	96.82(6)
N1—Mn1—N3	163.71(8)	N5—Mn2—N7	162.98(8)
N2—Mn1—N4	172.00(8)	N6—Mn2—N8	167.35(8)

C.1.2. Results of the CShM Calculations by the SHAPE Program

CShM calculations were performed on the solvent-containing structures of Mn(TPP)Br [**Mn-Br·CHCl$_3$**, **Mn-Br·toluene** and two independent Mn(TPP)Br molecules in **Mn-Br·CH$_2$Cl$_2$** (Table C.6)] show that Mn(TPP)Br molecules in all three analogs exhibit only slight distortion from square pyramidal geometry. However, distortion value of **Mn-Br·toluene** (0.448) is lower than those of both the chloroform analog **Mn-Br·CHCl$_3$** (0.645) and **Mn-Br·CH$_2$Cl$_2$** (0.593-0.597). The Mn−Br bond lengths of 2.5363(5) Å in **Mn-Br·CHCl$_3$** and 2.5200(13)-2.5247(12) Å of two Mn(TPP)Br molecules in **Mn-Br·CH$_2$Cl$_2$** are all longer than 2.490(1) Å in **Mn-Br·toluene**.[144]

Table C.6. CShM results for **Mn-Br·$CHCl_3$**, **Mn-Br·CH_2Cl_2**, and **Mn-Br·toluene**

CSM	Mn-Br·$CHCl_3$	Mn-Br·CH_2Cl_2		Mn-Br·toluene[144]
		Mn1	Mn2	
Pentagon	31.067	31.846	32.256	34.068
Vacant octahedron (Johnson square pyramid)	2.003	1.986	2.117	2.085
Trigonal bipyramid	5.300	4.855	4.933	4.720
Square pyramid	0.645	0.593	0.597	0.448
Johnson trigonal bipyramid	8.796	8.380	8.472	8.420

Table C.7. CShM results for **Mn-I·CHCl$_3$**, **Mn-I·CDCl$_3$**, **Mn-I·1.5CHCl$_3$** and **Mn-I·toluene**

CSM	**Mn-I·CHCl$_3$**	**Mn-I·CDCl$_3$**		**Mn-I·1.5CHCl$_3$**		**Mn-I·toluene**[144]	
		Mn1	Mn2	Mn1	Mn2	Mn1	Mn2
Pentagon	33.706	33.029	33.621	34.242	34.082	34.167	33.746
Vacant octahedron (Johnson square pyramid)	2.851	2.876	2.879	2.759	3.233	3.037	2.817
Trigonal bipyramid	5.339	5.596	5.025	4.808	5.447	5.617	5.589
Square pyramid	0.938	0.978	0.998	0.986	1.062	1.002	0.871
Johnson trigonal bipyramid	9.279	9.535	9.098	8.847	9.525	9.658	9.619

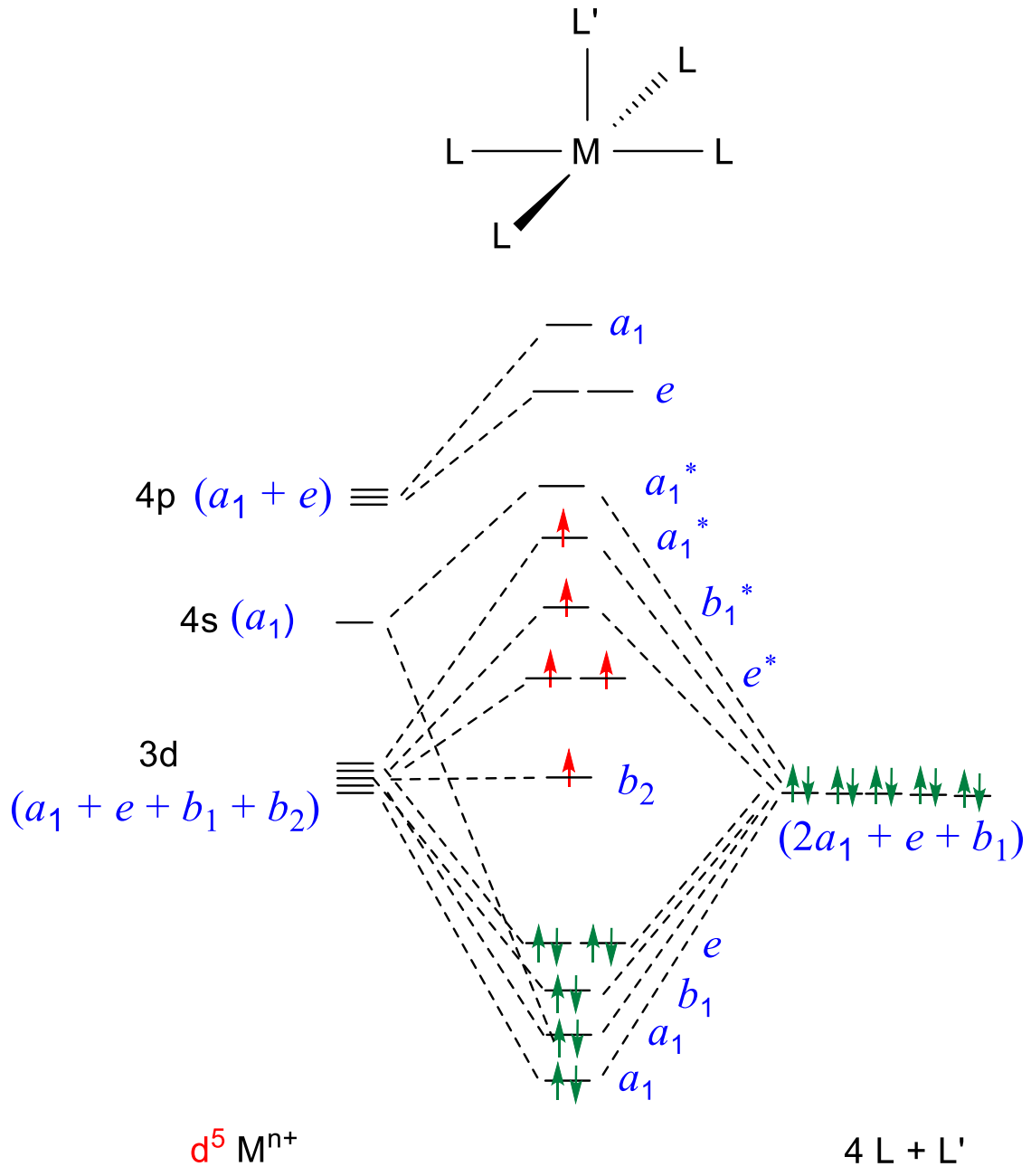
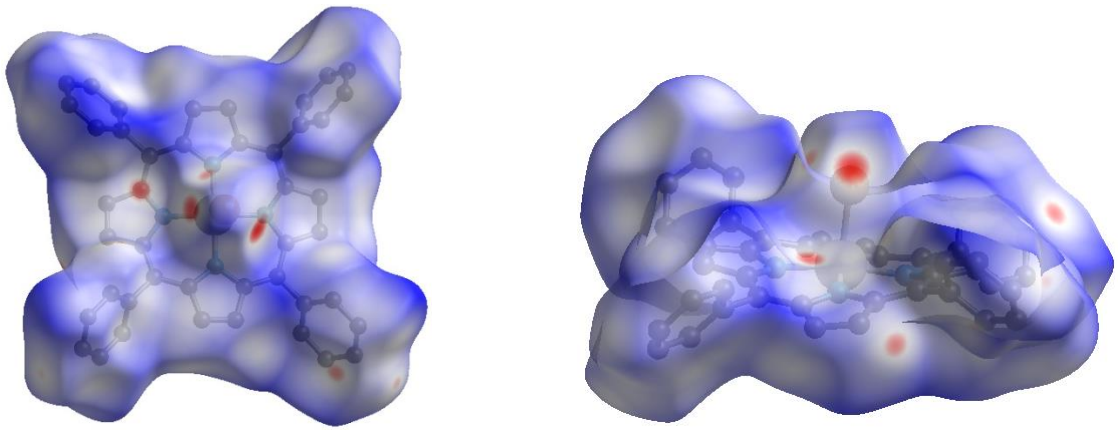


Figure C.4. Qualitative MO diagram in a d^5 square pyramid complex with C_{4v} symmetry.

Mn1 Molecule



Mn2 Molecule

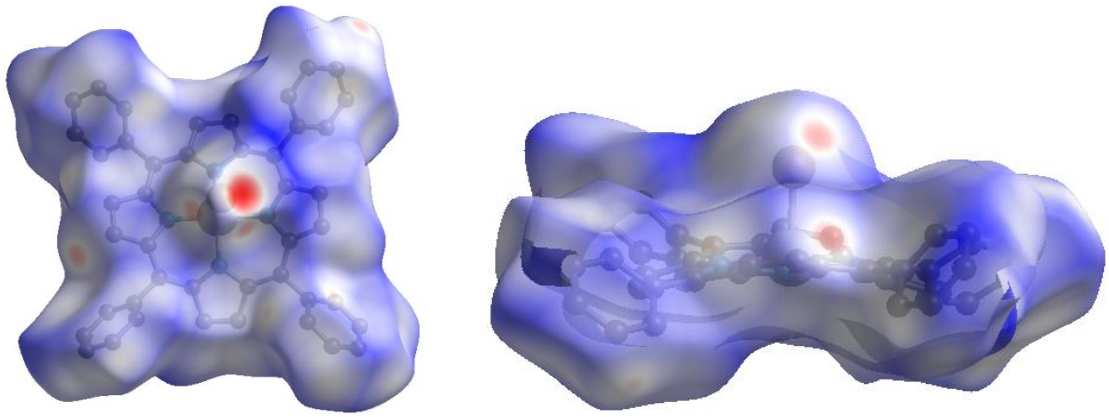
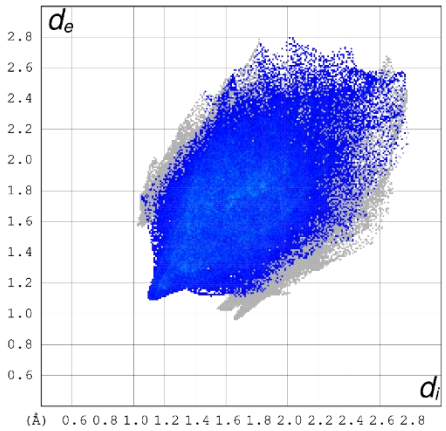


Figure C.5. Two views of the Hirshfeld surface of the Mn1 (Top) and Mn2 (Bottom) molecules Mn(TPP)Br·CH_2Cl_2 (**Mn-Br·CH_2Cl_2**) showing normalized close distances of the pro-molecule and neighboring molecules at 100(2) K.[148] The red-white-blue coloring scheme demonstrates decreasing contacts. Sites of close contacts are shown in red dots. Semi-transparent view reveals the enclosed molecule. Hereafter the same below for the coloring scheme, sites of close contacts and semi-transparent view.

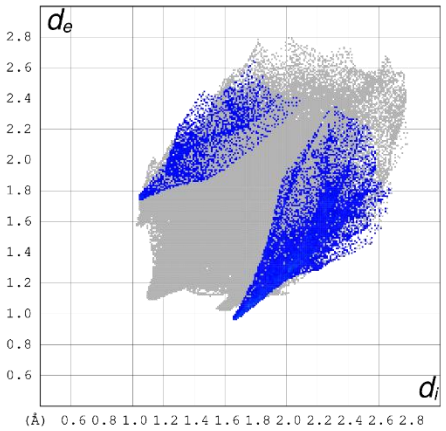
Figure C.6. Hirshfeld fingerprint plots for **Mn-Br·CH_2Cl_2**: (Top) Molecule containing Mn1 atom; (Bottom) Molecule containing Mn2 atom**.** The closest contacts correspond to the minimum $d_i + d_e$ values in each plot, hereafter the same below. d_i and d_e are distances from the Hirshfeld surface to the nearest atom *interior* and *exterior* to the surface, respectively.[149]

Molecule of Mn1

H···H close contact (blue) below

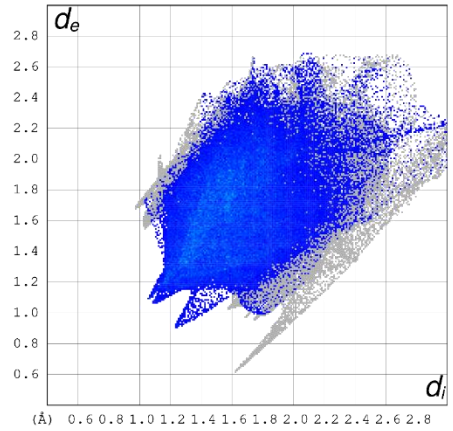


Br···H close contact (blue) below

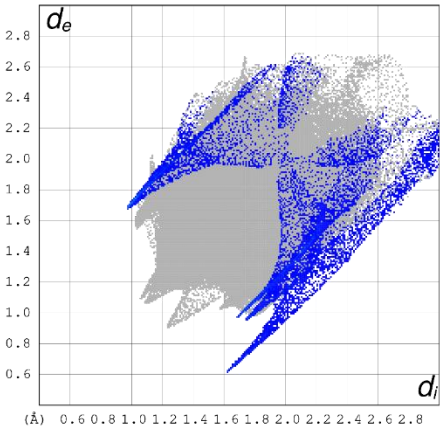


Molecule of Mn2

H···H close contact (blue) below



Br···H close contact (blue) below



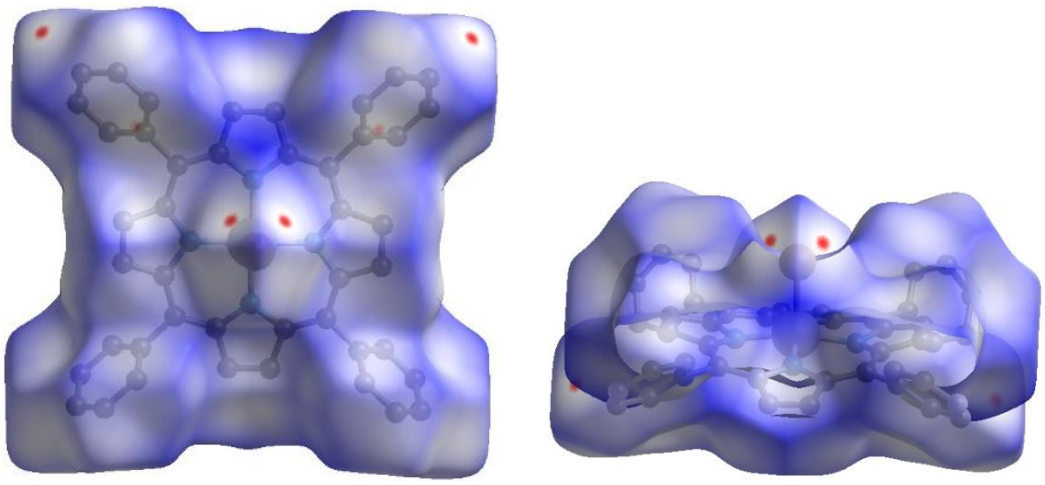


Figure C.7. Hirshfeld surface of Mn(TPP)Br·toluene (**Mn-Br·toluene**) showing normalized close distances of the pro-molecule and neighboring molecules at 100(2) K.[148]

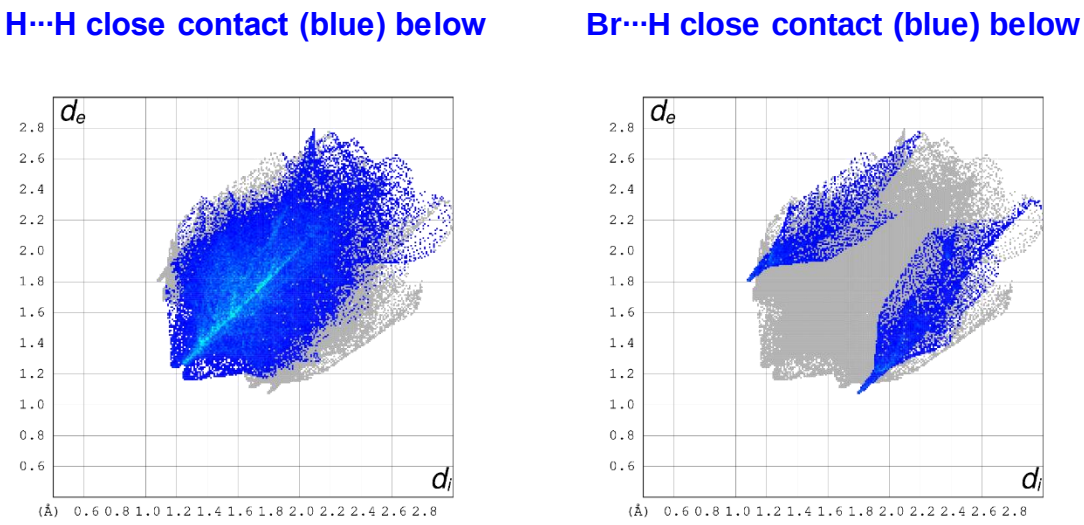


Figure C.8. Hirshfeld fingerprint plots for **Mn-Br·toluene**.

C.1.3. Comparison of Contributions to the Hirshfeld Surface Areas for Mn(TPP)Br (Mn-Br) Molecules in Various Crystal Structures

The contributions to the Hirshfeld surface areas for various intermolecular close contacts for Mn(TPP)Br (**Mn-Br**) molecules in various crystal structures are compared in Figure C.9.

The percentage contributions of the intermolecular H···H (46.0%-48.9%) and C···H (24.9%-28.5%) close contacts to the Hirshfeld surface area for **Mn-Br** molecules in **Mn-Br·$CHCl_3$** and **Mn-Br·CH_2Cl_2** (Figure C.9) are similar but lower than those (54.7% and 31.3% for H···H and C···H close contacts, respectively) in **Mn-Br·toluene** likely because the solvent toluene in the latter, containing eight H atoms, increases the percentage.

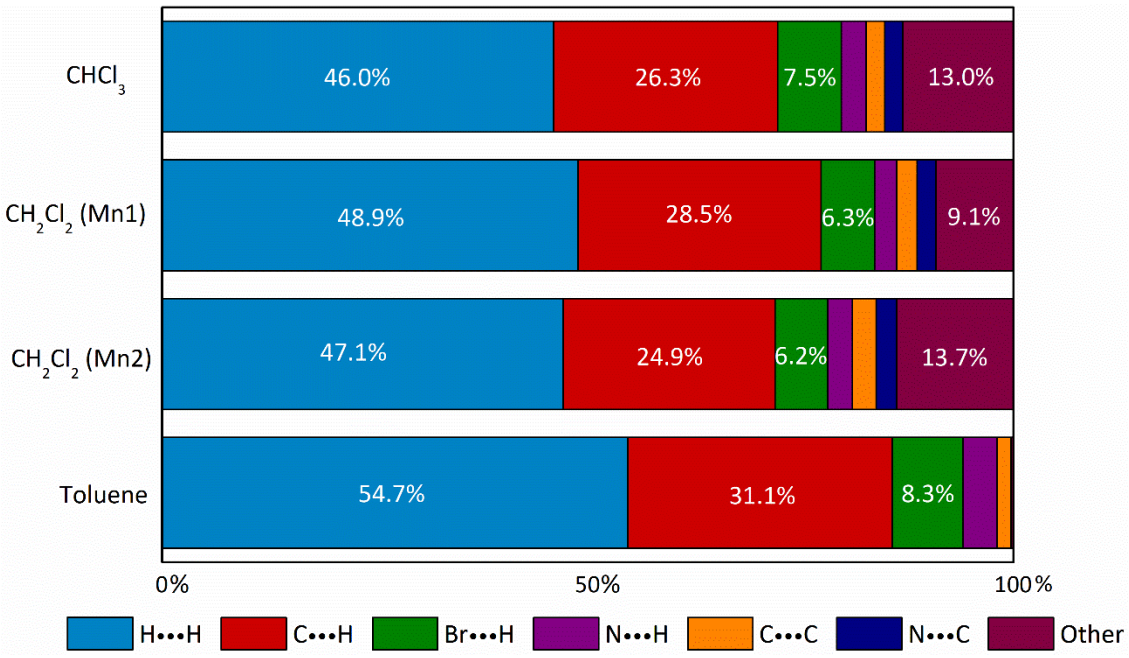
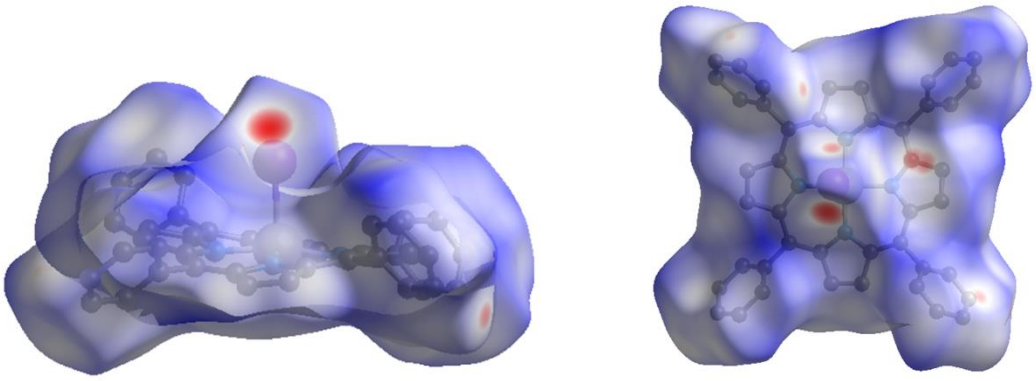


Figure C.9. Percentage contributions to the Hirshfeld surface areas for various intermolecular close contacts for Mn(TPP)Br (**Mn-Br**) molecules in various crystal structures.

Mn1 Molecule



Mn2 Molecule

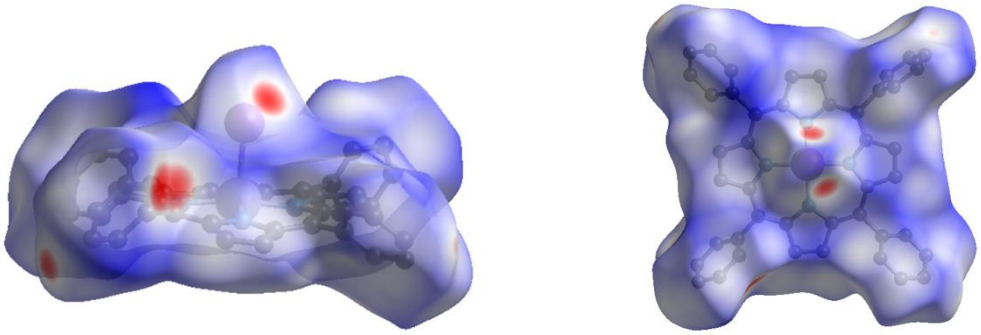
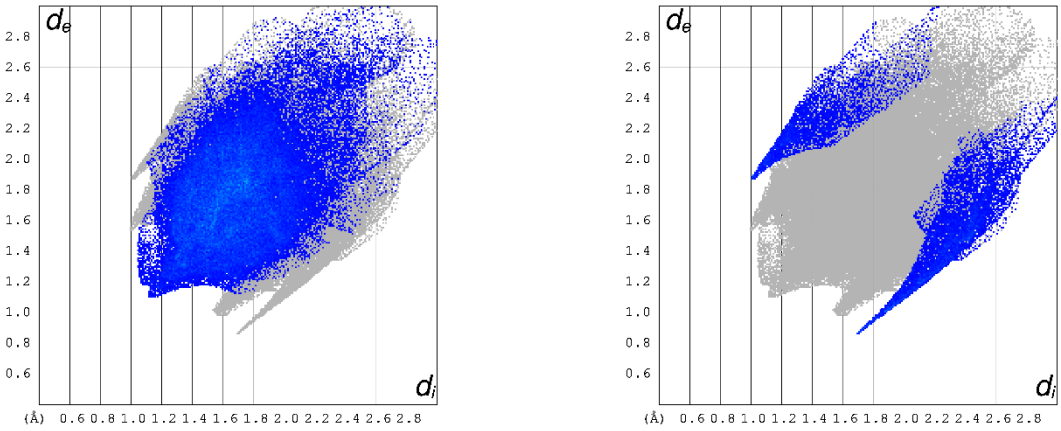


Figure C.10. Two views of the Hirshfeld surfaces of the Mn1 (Top) and Mn2 (Bottom) molecules **Mn-I·CDCl$_3$** showing normalized close distances of the pro-molecule and neighboring molecules at 100(2) K.[148]

Mn1 Molecule

H/D···H/D close contact (blue) below **I···H/D close contact (blue) below**



Mn2 Molecule

H/D···H/D close contact (blue) below **I···H/D close contact (blue) below**

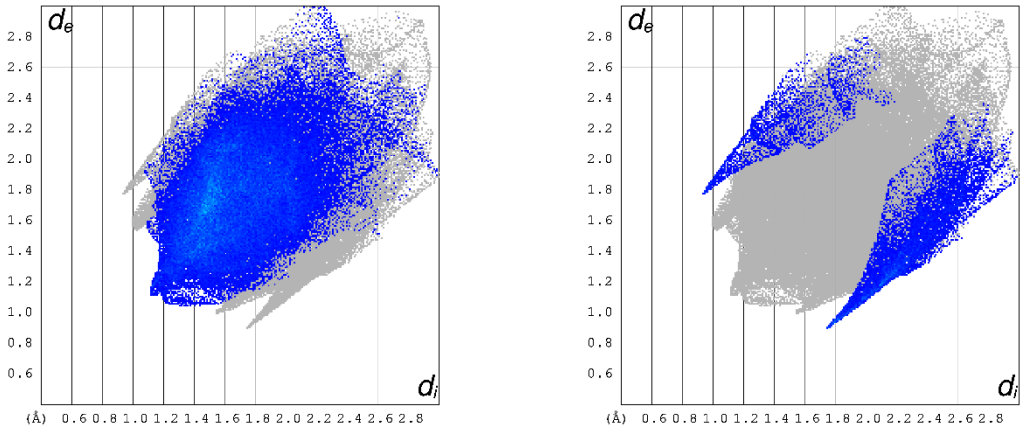


Figure C.11. Hirshfeld fingerprint plots for **Mn-I·CDCl$_3$**: (Top) Molecule containing the Mn1 atom; (Bottom) Molecule containing the Mn2 atom.

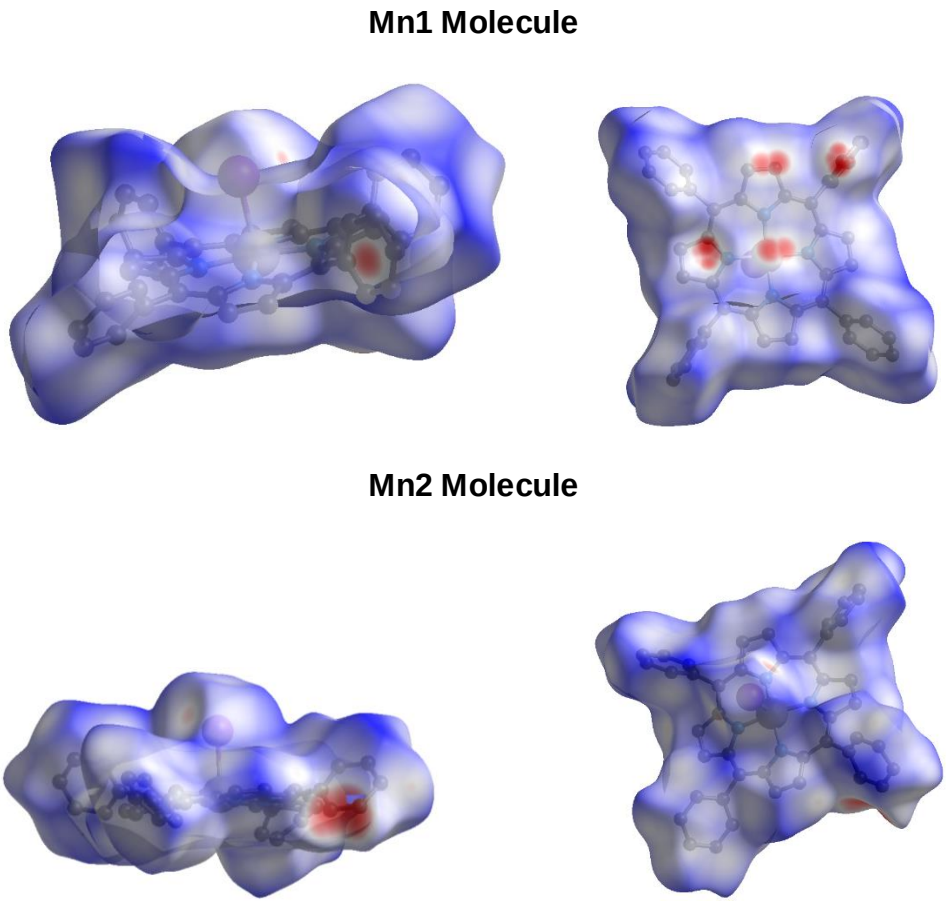
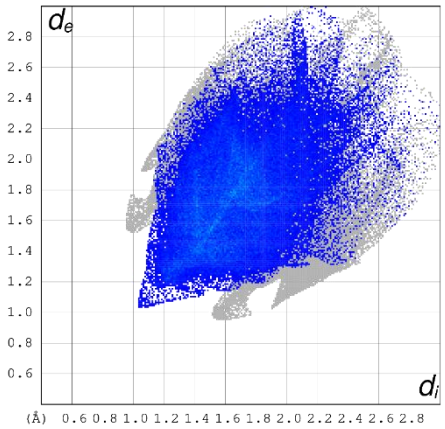


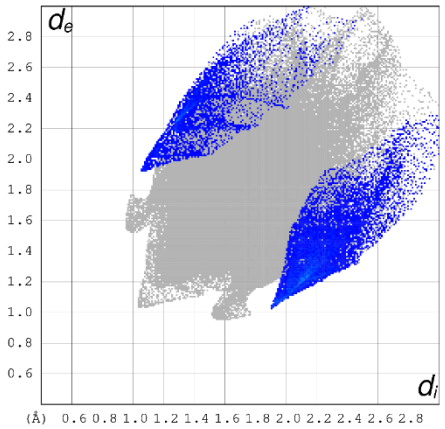
Figure C.12. Two views of the Hirshfeld surfaces of the Mn1 (Top) and Mn2 (Bottom) molecules **Mn-I·1.5CHCl$_3$** showing normalized close distances of the pro-molecule and neighboring molecules at 100(2) K.[148]

Mn1 Molecule

H···H close contact (blue) below

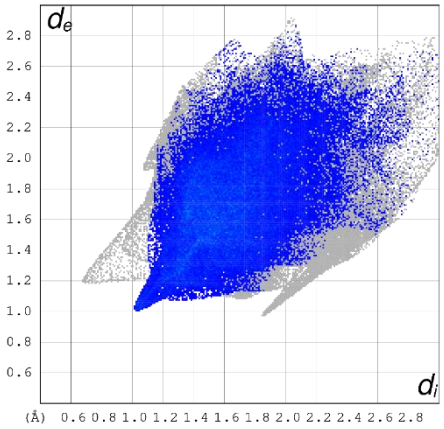


I···H close contact (blue) below



Mn2 Molecule

H···H close contact (blue) below



I···H close contact (blue) below

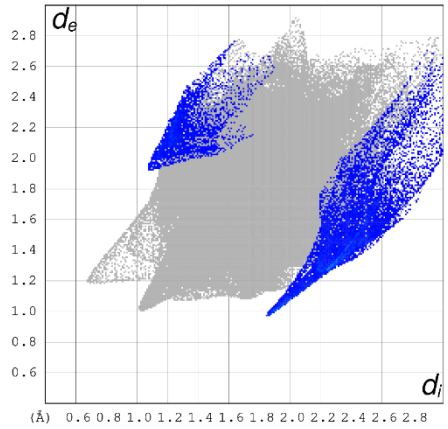
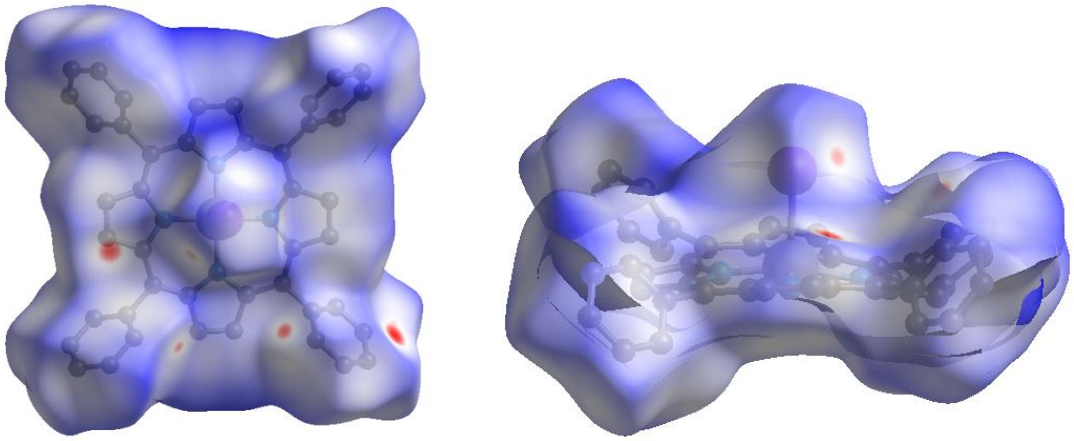


Figure C.13. Hirshfeld fingerprint plots for **Mn-I·1.5CHCl$_3$**: (Top) Molecule containing the Mn1 atom; (Bottom) Molecule containing the Mn2 atom.

Mn1 Molecule



Mn2 Molecule

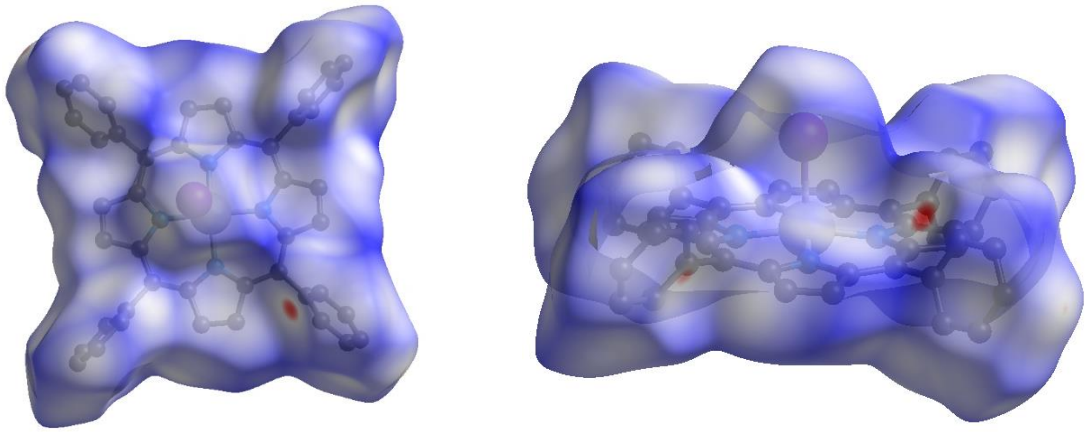
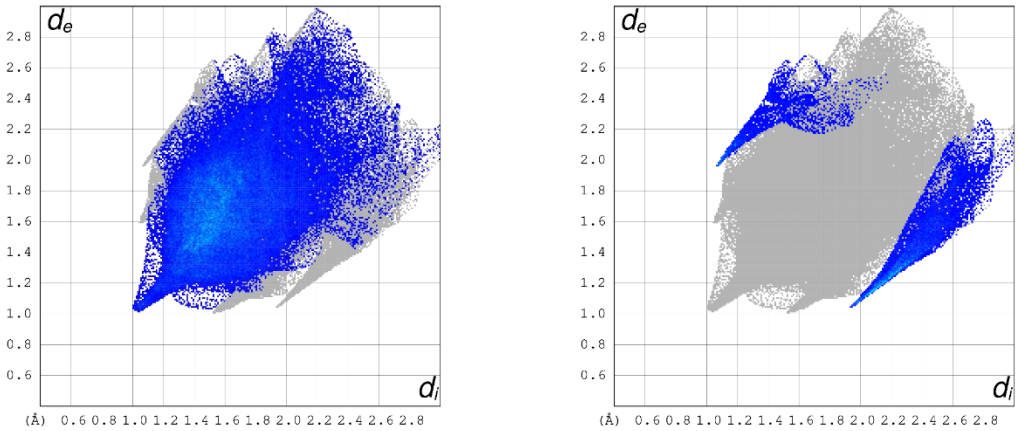


Figure C.14. Two views of the Hirshfeld surface of the Mn1 (Top) and Mn2 (Bottom) molecules of Mn(TPP)I·toluene (**Mn-I·toluene**) showing normalized close distances of the pro-molecule and neighboring molecules at 100(2) K.[148]

Mn1 Molecule

H···H close contact (blue) below **I···H close contact (blue) below**



Mn2 Molecule

H···H close contact (blue) below **I···H close contact (blue) below**

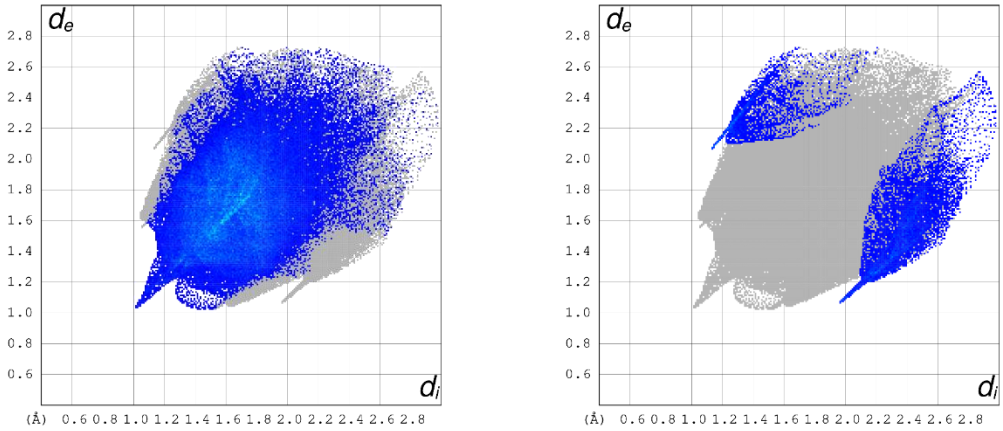


Figure C.15. Hirshfeld fingerprint plots for Mn(TPP)I·toluene (**Mn-I·toluene**): (Top) Molecule containing Mn1 atom; (Bottom) Molecule containing Mn2 atom**.**

C.1.4. Comparison of Contributions to the Hirshfeld Surface Areas for Mn(TPP)I (Mn-I) Molecules in Various Crystal Structures

The contributions to the Hirshfeld surface areas for various intermolecular close contacts for Mn(TPP)I (**Mn-I**) molecules in various crystal structures are compared in Figure C.16.

Comparison of percentage contributions to the Hirshfeld surface area for different intermolecular close contacts for **Mn-I** molecules in various crystal structures (Fig. C.15) shows that **Mn-I·toluene** has the highest contributions from close H···H and C···H contacts likely as a result of the toluene solvent in the lattice.

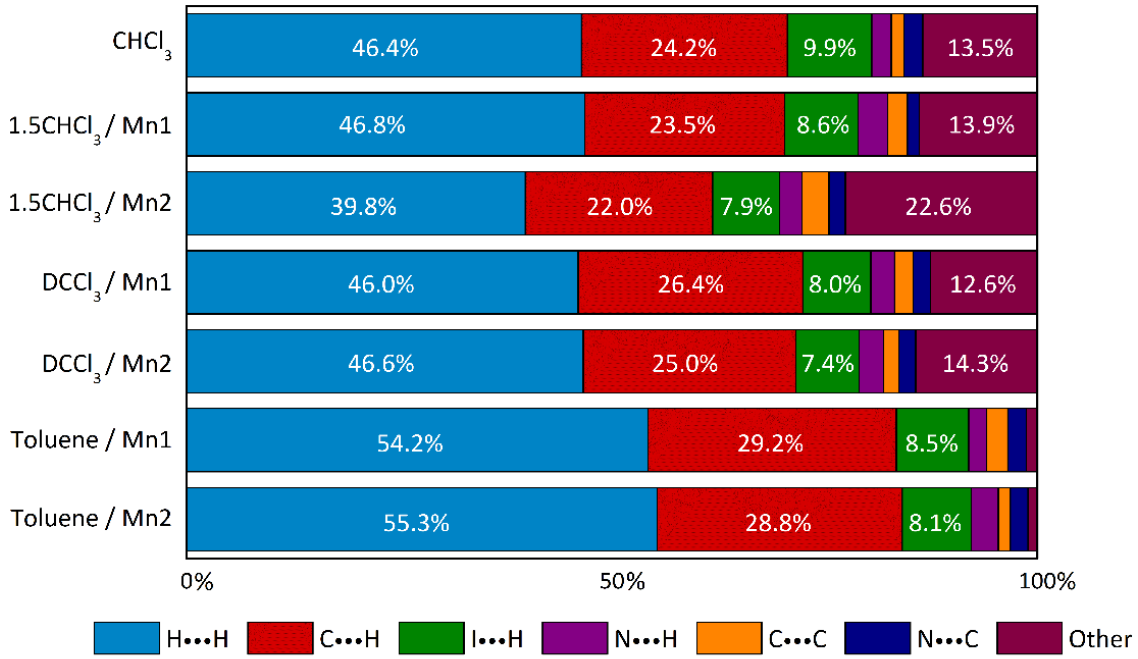


Figure C.16. Percentage contributions to the Hirshfeld surface areas for various intermolecular close contacts for Mn(TPP)I (**Mn-I**) molecules in various crystal structures.

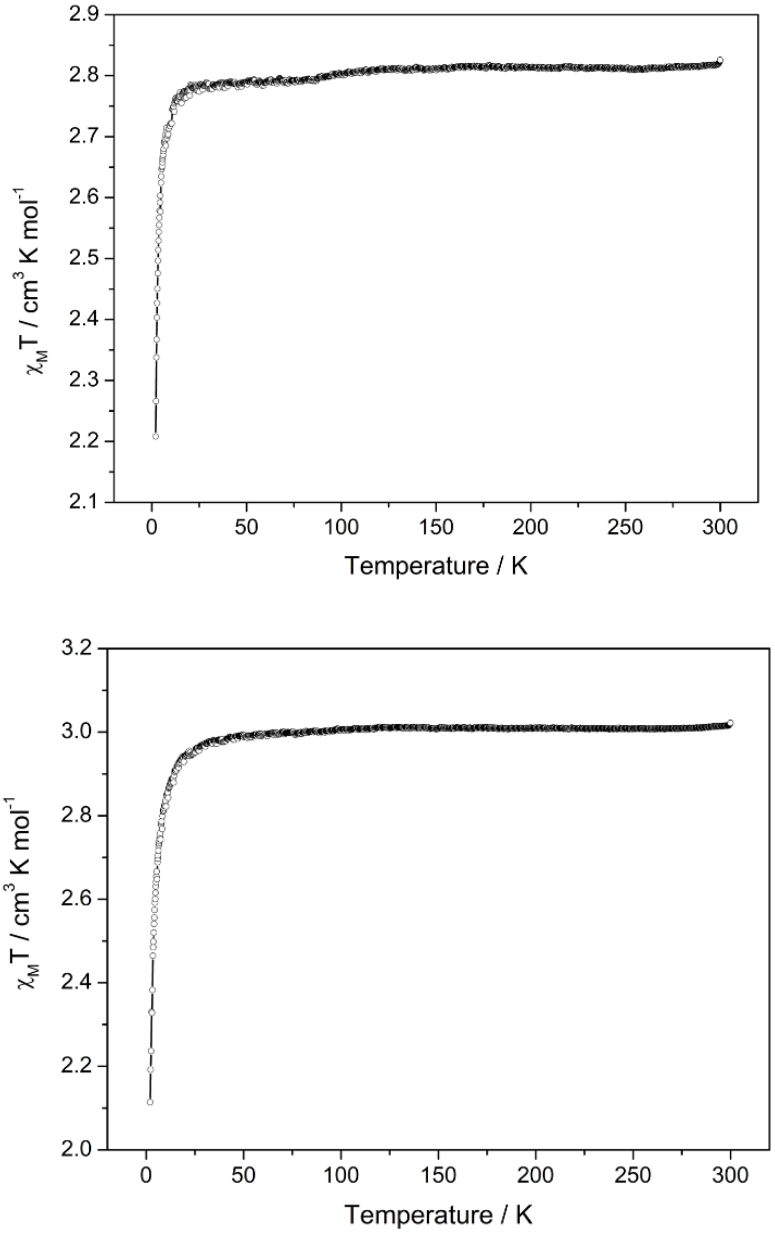
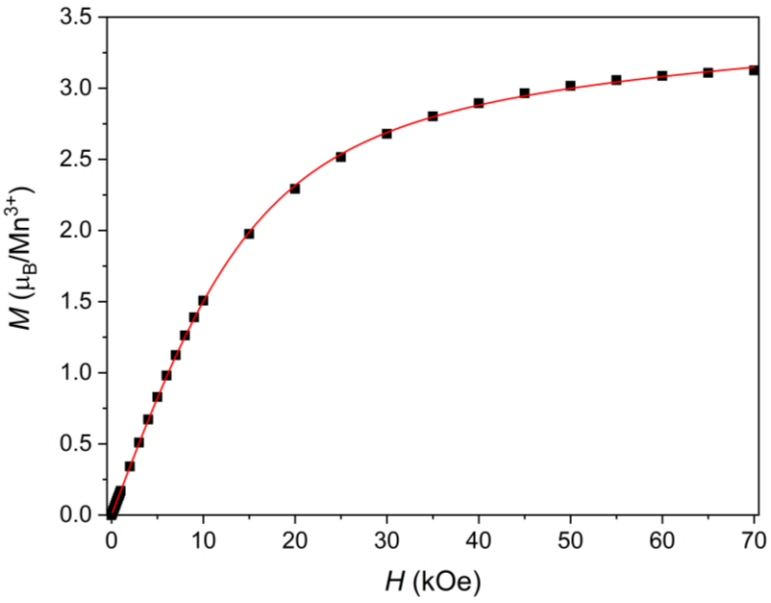


Figure C.17. Variable-temperature DC susceptibility data under applied DC field of 0.5 T fitted for solvent-free samples: (Top) Mn(TPP)Br (**Mn-Br**). (Bottom) Mn(TPP)I (**Mn-I**). Fits are included to guide the eye.

Figure C.18. (Top) M-H plot for **Mn-Br·CHCl$_3$** at 1.8 K. The red line indicates the Brillouin function for a system with S = 2.0 and g = 1.42. The M-H plot shows deviation from the Brillouin function for spin state S = 2.0 (with g = 2.0 and no ZFS). Since HFEPR of **Mn-Br·CDCl$_3$** gives g = 1.99-2.00, using the M-H plot to yield the g value was not pursued further. (Bottom) AC susceptibility data (χ_M' = filled circles, χ_M'' = empty circles) for Mn(TPP)Br·CHCl$_3$ (**Mn-Br·CHCl$_3$**) with a DC field of 0.14 T and 2.74 Oe driving amplitude.


3.5
3.0
2.5
2.0
1.5
1.0
0.5
0.0
M (μB/Mn3+)
0
10
20
30
40
50
60
70
H (kOe)

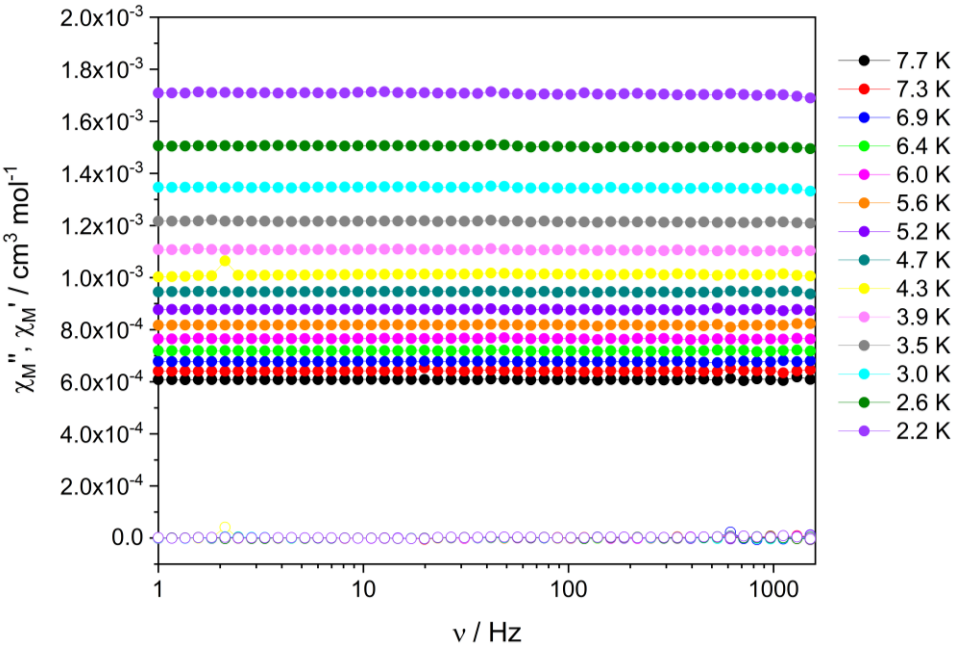
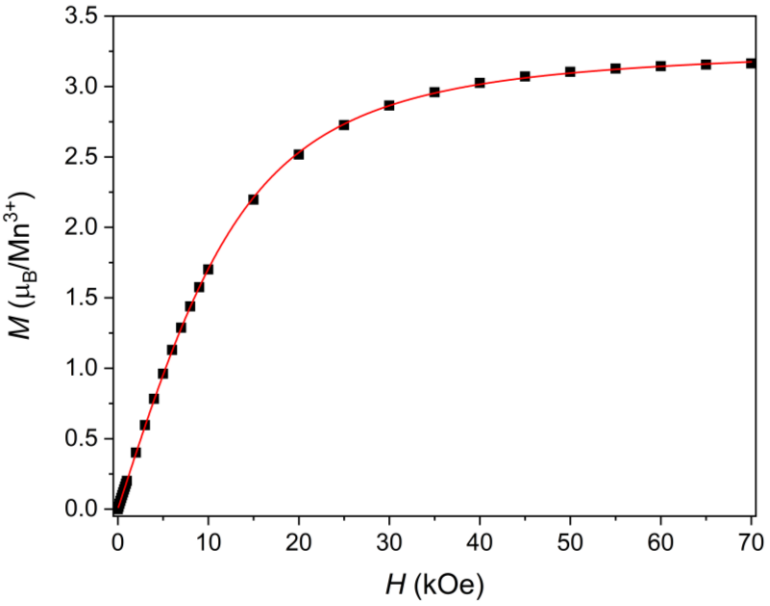
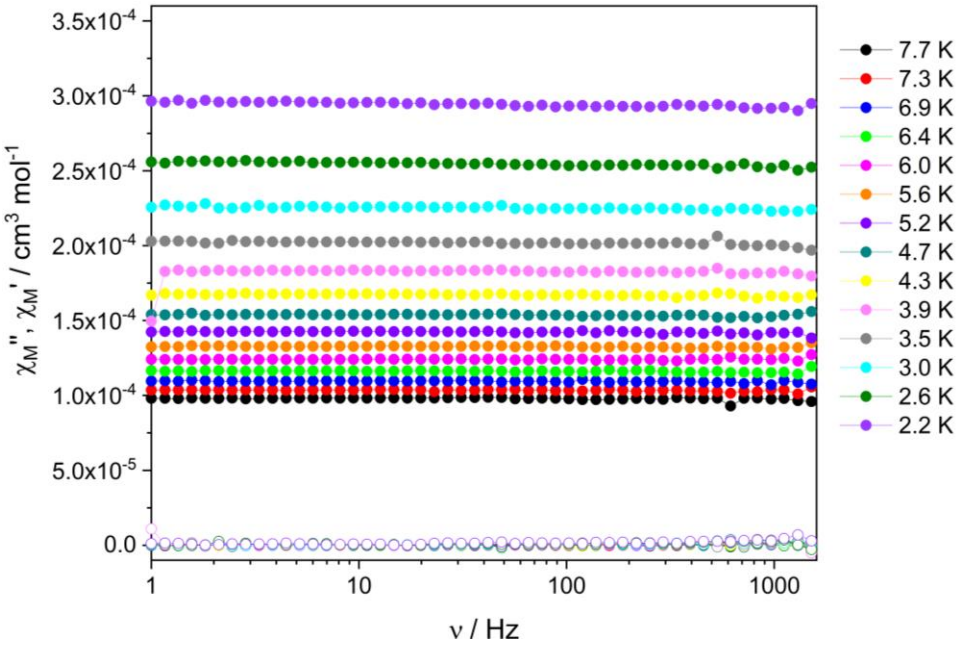

2.0x10-3
1.8x10-3
1.6x10-3
1.4x10-3
1.2x10-3
1.0x10-3
8.0x10-4
6.0x10-4
4.0x10-4
2.0x10-4
0.0
χM", χM' / cm3 mol-1
1
10
100
1000
ν / Hz
7.7 K
7.3 K
6.9 K
6.4 K
6.0 K
5.6 K
5.2 K
4.7 K
4.3 K
3.9 K
3.5 K
3.0 K
2.6 K
2.2 K

Figure C.19. (Top) M-H plot for **Mn-I·1.5CHCl$_3$** at 1.8 K. The red line indicates the Brillouin function for a system with S = 2.0 and g = 1.54. The M-H plot shows deviation from the Brillouin function for spin state S = 2.0 (with g = 2.0 and no ZFS). Since HFEPR of **Mn-I·CDCl$_3$** gives g = 1.93-1.97, using the M-H plot to yield the g value was not pursued further. (Bottom) AC susceptibility data (χ_M' = filled circles, χ_M'' = empty circles) for Mn(TPP)I·1.5CHCl$_3$ (**Mn-I·1.5CHCl$_3$**) with a DC field of 0.14 T and 2.74 Oe driving amplitude.


M (μB/Mn3+)
H (kOe)
0.0
0.5
1.0
1.5
2.0
2.5
3.0
3.5
0
10
20
30
40
50
60
70


χM'' , χM' / cm3 mol-1
ν / Hz
3.5x10-4
3.0x10-4
2.5x10-4
2.0x10-4
1.5x10-4
1.0x10-4
5.0x10-5
0.0
1
10
100
1000
7.7 K
7.3 K
6.9 K
6.4 K
6.0 K
5.6 K
5.2 K
4.7 K
4.3 K
3.9 K
3.5 K
3.0 K
2.6 K
2.2 K

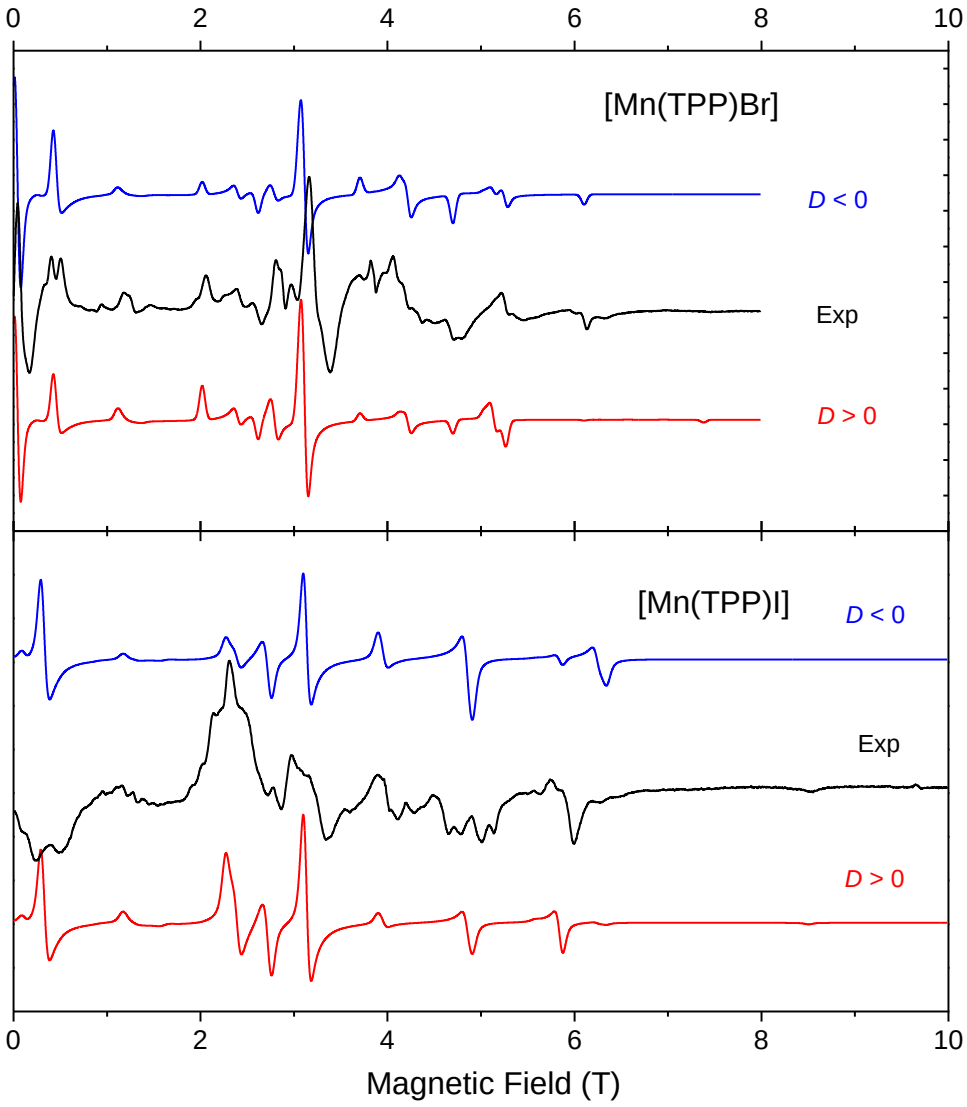


Figure C.20. HFEPR spectra of **Mn-Br·CDCl$_3$** (Top) and **Mn-I·CDCl$_3$** (Bottom) at 10 K and 108 GHz and 112 GHz, respectively (black traces) and their powder-pattern simulations (colored traces). The spin-Hamiltonian parameters used in simulations were the same as in Table 4.4. Blue traces: $D < 0$; red traces: $D > 0$.

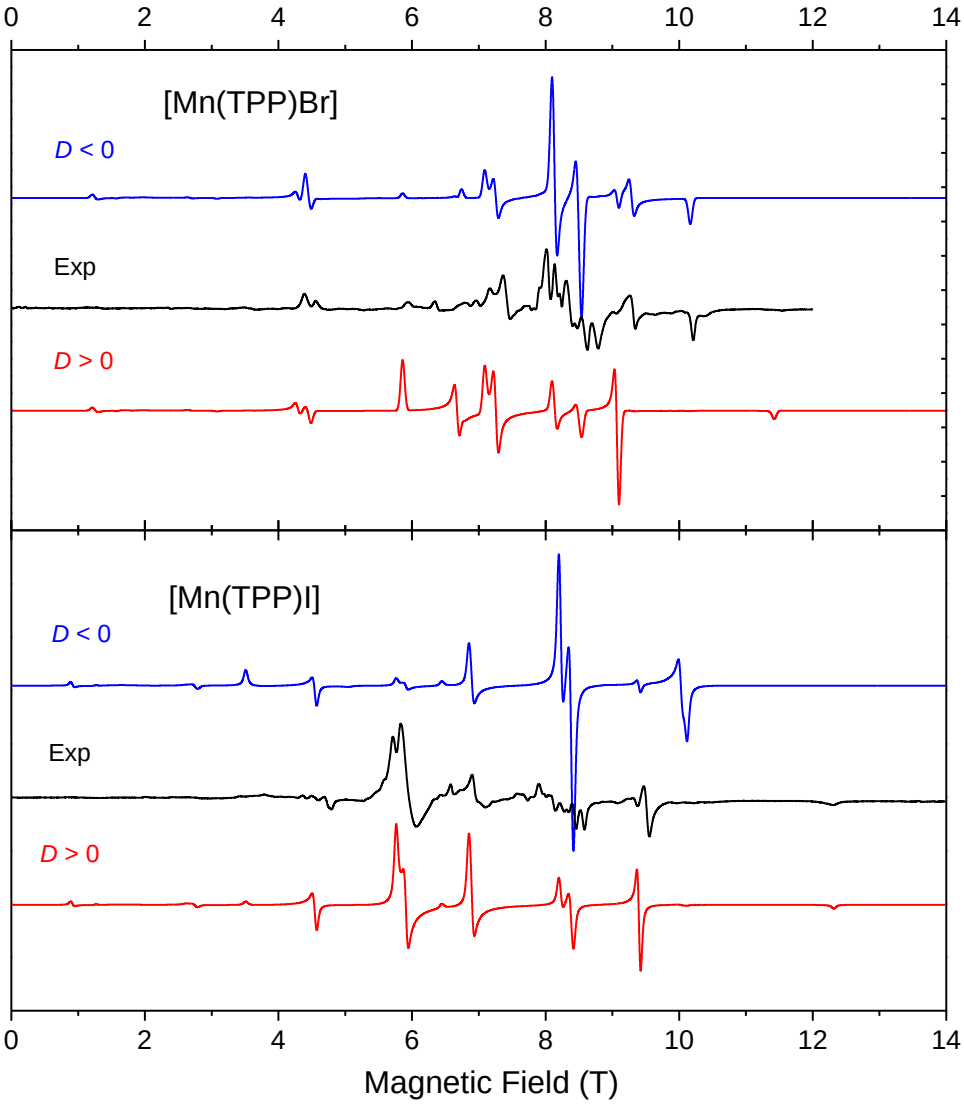


Figure C.21. HFEPR spectra of **Mn-Br·CDCl$_3$** (Top) and **Mn-I·CDCl$_3$** (Bottom) at 10 K and 216 GHz and 220.8 GHz, respectively (black traces) and their powder-pattern simulations (colored traces). The spin-Hamiltonian parameters used in simulations were the same as in Table 4.4. Blue traces: $D < 0$; red traces: $D > 0$.

Appendix D. Supporting Information for Chapter V

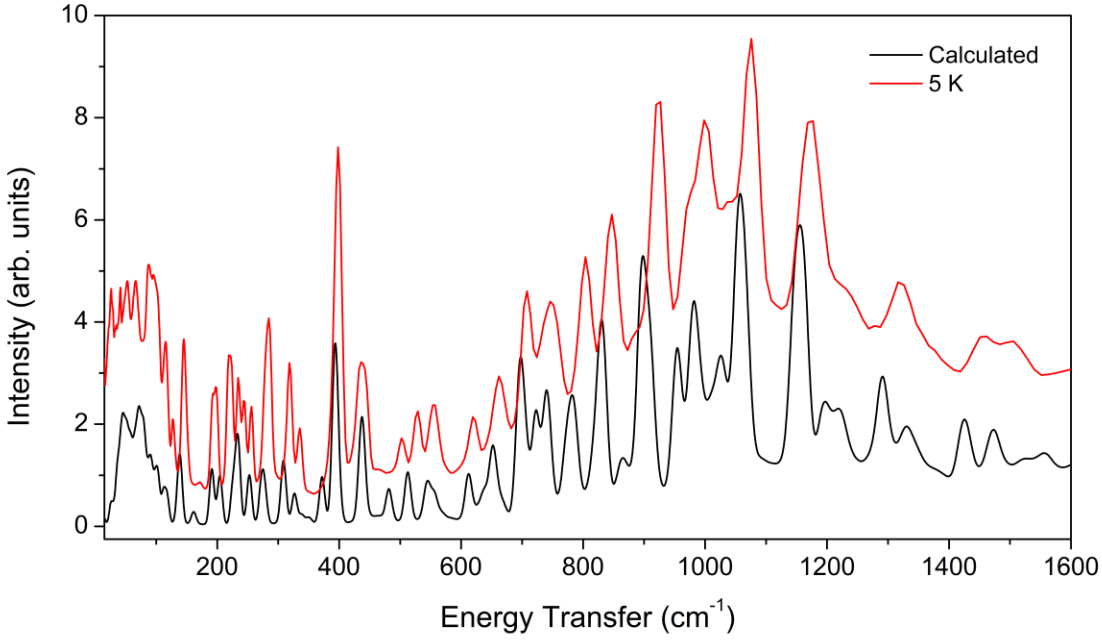


Figure D.1. INS forward-scattered, Bose-corrected spectra of **Fe-Cl** at 5 K with VASP-calculated phonon spectrum (black).

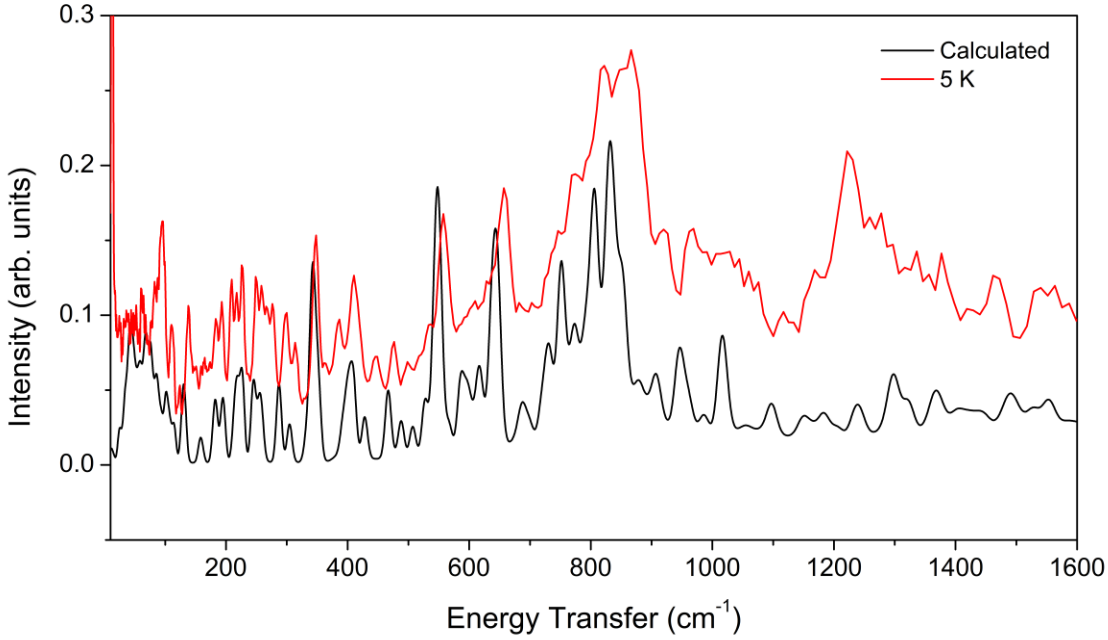


Figure D.2. INS forward-scattered, Bose-corrected spectra of **Fe-Cl-*d*$_{28}$** at 5 K with VASP-calculated phonon spectrum (black).

Table D.1. Calculated phonon modes of **Fe-Cl** and their symmetries

Energy (cm^{-1})	**Symmetry**	**Energy (cm^{-1})**	**Symmetry**
31.497	*B*	396.688	*E*
42.599	*E*	401.510	*B*
47.146	*B*	435.637	*B*
49.740	*A*	437.710	*E*
62.471	*A*	439.317	*A*
68.903	*E*	482.814	*B*
70.293	*B*	512.141	*E*
79.915	*E*	543.324	*A*
84.241	*E*	546.682	*B*
88.072	*B*	557.173	*E*
96.477	*A*	569.085	*A*
97.682	*B*	611.379	*B*
103.917	*E*	612.738	*E*
110.384	*A*	614.876	*A*
117.524	*B*	629.995	*A*
138.128	*E*	640.027	*B*
164.678	*B*	650.467	*E*
191.640	*A*	654.006	*E*
197.135	*A*	661.718	*A*
202.911	*E*	670.269	*B*
224.745	*E*	692.154	*E*
231.422	*B*	698.455	*B*
232.295	*E*	703.789	*A*
236.127	*B*	708.967	*A*
250.397	*A*	721.941	*B*
254.228	*E*	722.483	*E*
272.337	*A*	738.234	*E*
281.681	*A*	744.752	*B*
306.498	*E*	746.018	*A*
330.717	*B*	775.088	*B*
339.850	*A*	782.458	*E*
358.376	*A*	788.610	*A*
372.891	*E*	812.202	*A*
390.229	*B*	818.150	*E*
392.486	*A*	821.836	*B*

Table D.1 (Continued). Calculated phonon modes of **Fe-Cl** and their symmetries

Energy (cm^{-1})	Symmetry	Energy (cm^{-1})	Symmetry
824.556	*A*	1068.047	*A*
831.454	*B*	1147.454	*B*
835.758	*E*	1147.684	*E*
857.778	*B*	1149.125	*A*
863.069	*E*	1160.016	*B*
872.041	*A*	1160.612	*A*
895.580	*E*	1162.151	*E*
895.877	*A*	1166.324	*B*
896.214	*B*	1193.410	*E*
905.472	*E*	1201.719	*A*
914.406	*B*	1218.576	*A*
915.264	*A*	1223.706	*E*
949.495	*B*	1241.691	*B*
953.486	*A*	1250.984	*B*
957.472	*E*	1272.037	*E*
968.778	*A*	1290.912	*E*
975.181	*E*	1291.429	*A*
979.491	*E*	1291.666	*B*
980.413	*B*	1312.309	*A*
982.244	*A*	1324.897	*E*
988.098	*A*	1325.924	*B*
989.226	*E*	1326.168	*A*
989.789	*B*	1330.872	*E*
995.712	*A*	1335.324	*A*
996.480	*B*	1345.256	*B*
1009.624	*B*	1423.059	*A*
1010.438	*E*	1423.818	*E*
1021.986	*A*	1425.686	*B*
1026.962	*E*	1430.497	*E*
1036.991	*B*	1436.087	*A*
1052.978	*E*	1455.420	*B*
1054.180	*A*	1472.911	*A*
1058.571	*B*	1472.930	*E*
1066.490	*E*	1475.213	*B*
1067.246	*B*	1479.636	*B*

Table D.1 (Continued). Calculated phonon modes of **Fe-Cl** and their symmetries

Energy (cm^{-1})	Symmetry	Energy (cm^{-1})	Symmetry
1490.427	*A*	3063.540	*E*
1501.189	*E*	3073.862	*E*
1515.909	*E*	3074.327	*A*
1535.794	*A*	3074.346	*B*
1552.934	*B*	3078.644	*B*
1562.717	*A*	3078.795	*A*
1562.994	*E*	3078.886	*E*
1564.697	*B*	3089.388	*E*
1583.794	*A*	3089.407	*A*
1584.052	*B*	3089.438	*B*
1584.077	*E*	3135.412	*E*
3058.970	*E*	3136.963	*A*
3059.533	*B*	3137.305	*B*
3059.845	*A*	3155.027	*E*
3062.518	*B*	3155.254	*B*
3062.634	*A*	3155.327	*A*

Table D.2. Calculated phonon modes of **Fe-Cl-d_{28}** and their symmetries

Energy (cm^{-1})	Symmetry	Energy (cm^{-1})	Symmetry
29.821	*B*	355.816	*A*
40.450	*E*	392.758	*B*
43.547	*B*	399.588	*B*
45.268	*A*	404.854	*A*
59.654	*A*	407.638	*E*
64.518	*E*	429.193	*B*
67.127	*B*	465.994	*E*
76.232	*E*	490.473	*A*
80.027	*E*	507.797	*B*
83.576	*B*	527.319	*E*
91.082	*A*	544.565	*E*
92.899	*B*	544.669	*B*
102.102	*E*	545.750	*B*
105.705	*A*	550.904	*E*
113.875	*B*	551.572	*A*
130.097	*E*	555.183	*A*
161.582	*B*	568.098	*A*
184.480	*A*	585.381	*B*
186.246	*A*	586.349	*E*
193.180	*E*	594.950	*A*
215.352	*B*	597.880	*A*
217.495	*E*	604.599	*A*
225.005	*E*	614.498	*E*
228.199	*B*	622.342	*B*
243.336	*A*	636.301	*E*
246.848	*E*	638.086	*A*
254.845	*A*	639.521	*B*
262.581	*A*	642.538	*A*
284.864	*E*	644.791	*B*
308.663	*B*	646.596	*E*
333.283	*A*	649.145	*E*
339.363	*B*	687.292	*B*
341.025	*A*	699.510	*B*
345.523	*E*	720.010	*B*
352.509	*E*	728.802	*E*

Table D.2 (Continued). Calculated phonon modes of **Fe-Cl-d_{28}** and their symmetries

Energy (cm^{-1})	Symmetry	Energy (cm^{-1})	Symmetry
734.992	*E*	994.100	*B*
747.446	*A*	944.955	*A*
750.594	*A*	946.286	*E*
751.772	*B*	948.117	*B*
751.832	*E*	958.588	*A*
753.490	*A*	961.558	*E*
762.777	*A*	986.014	*B*
767.007	*E*	1015.820	*E*
768.748	*B*	1016.665	*A*
772.877	*B*	1016.777	*B*
775.140	*A*	1023.811	*B*
776.741	*E*	1098.685	*E*
788.032	*B*	1150.259	*A*
791.041	*E*	1164.480	*A*
793.476	*A*	1182.285	*E*
799.286	*A*	1209.104	*B*
805.815	*E*	1232.049	*A*
805.879	*A*	1238.258	*B*
807.380	*B*	1243.643	*E*
809.156	*E*	1293.557	*E*
810.589	*B*	1296.842	*A*
818.466	*A*	1299.123	*B*
825.633	*E*	1300.549	*E*
825.671	*B*	1301.332	*B*
830.124	*B*	1320.479	*A*
831.678	*E*	1323.766	*E*
834.375	*A*	1323.911	*A*
836.991	*E*	1324.183	*B*
839.786	*A*	1363.387	*A*
841.405	*A*	1367.354	*E*
850.080	*B*	1380.897	*B*
852.454	*E*	1401.416	*E*
857.560	*B*	1419.966	*A*
880.841	*A*	1435.006	*B*
908.186	*E*	1444.480	*B*

Table D.2 (Continued). Calculated phonon modes of **Fe-Cl-d_{28}** and their symmetries

Energy (cm^{-1})	Symmetry	Energy (cm^{-1})	Symmetry
1483.664	*A*	2260.092	*E*
1487.139	*E*	2271.506	*E*
1498.537	*E*	2272.157	*B*
1514.052	*A*	2272.387	*A*
1528.157	*B*	2277.561	*B*
1528.961	*A*	2277.660	*A*
1529.059	*E*	2277.955	*E*
1550.788	*B*	2289.623	*B*
1552.831	*A*	2289.748	*E*
1552.983	*E*	2290.040	*A*
1553.166	*B*	2314.291	*E*
2255.608	*E*	2314.767	*A*
2255.936	*B*	2315.382	*B*
2256.044	*A*	2348.211	*E*
2259.213	*B*	2348.271	*B*
2259.442	*A*	2348.387	*A*

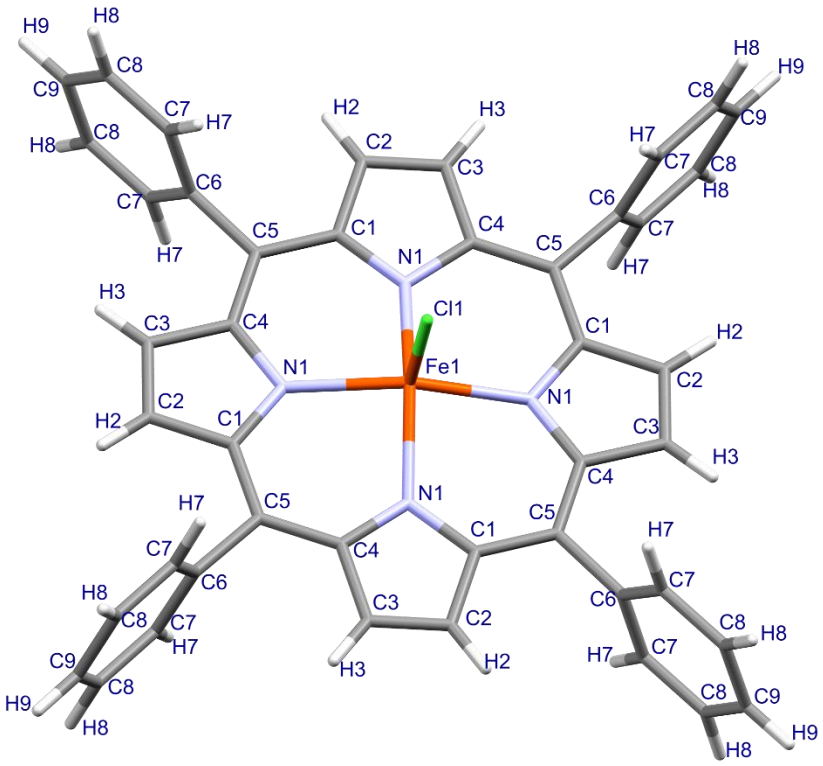


Figure D.3. Molecular structure of **Fe-Cl** with labeled atoms to accompany Table D.3.

Table D.3. Spin densities, ρ_s, of individual atoms in **Fe-Cl**. Labels correspond to atoms labeled in Figure D.3.

Atom	ρ_s	**Atom**	ρ_s
Fe1	4.223	C7	6.66×10^{-4}
Cl1	0.175	C8	2.15×10^{-4}
N1	7.42×10^{-2}	C9	4.20×10^{-4}
C1	1.53×10^{-3}	H2	3.38×10^{-4}
C2	4.01×10^{-3}	H3	3.42×10^{-4}
C3	3.99×10^{-3}	H7	-6.00×10^{-7}
C4	1.50×10^{-3}	H8	2.41×10^{-5}
C5	9.75×10^{-3}	H9	7.46×10^{-5}
C6	-1.40×10^{-4}	**Total**	4.789

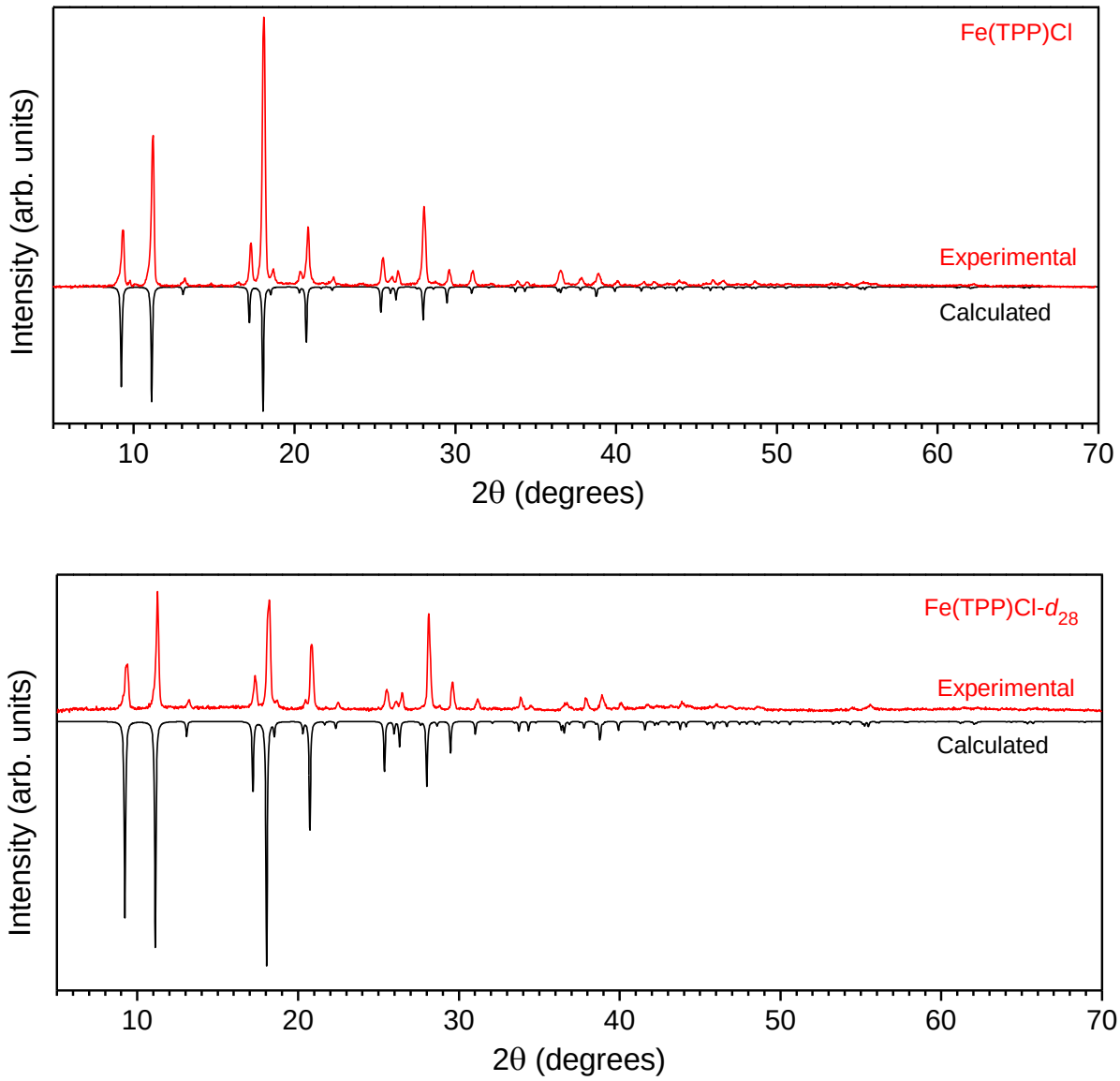


Figure D.4. PXRD at 296 K of the samples of **Fe-Cl** (Top) and **Fe-Cl-*d*$_{28}$** (Bottom) used in INS and comparisons with that of calculated from single-crystal structure of **Fe-Cl**. For the X-ray diffraction, no distinction is made for the H and D isotopes in **Fe-Cl** and **Fe-Cl-*d*$_{28}$**. X-ray wavelength: 1.54 Å.

VITA

Alexandria N. Bone was born in Knoxville, TN to Michael and Jeanie Bone. She attended public school in Anderson County, TN before graduating with a B.S. in Chemistry from Maryville College in Maryville, TN. During her undergraduate studies, Alexandria completed several internships at the National Transportation Research Center in Hardin Valley, TN, and at Oak Ridge National Laboratory in Oak Ridge, TN, producing an undergraduate thesis on the optimization of storage phosphors. In 2018, Alexandria entered the graduate program at the University of Tennessee, where she studied molecular magnetism in the group of Zi-Ling (Ben) Xue. In graduate school, Alexandria received the Second-Year Ph.D. Candidacy Award and an Outstanding Teaching Award from the Department of Chemistry. As of December 2023, Alexandria has co-authored the following publications with several additional manuscripts in preparation for submission:

(1) Moseley, D. H.; Liu, Z.; **Bone, A. N**.; Stavretis, S. E.; Singh, S. K.; Atanasov, M.; Lu, Z.; Ozerov, M.; Thirunavukkuarasu, K.; Cheng, Y.; Daemen, L. L.; Lubert-Perquel, D.; Smirnov, D.; Neese, F.; Ramirez-Cuesta, A. J.; Hill, S.; Dunbar, K. R.; Xue, Z.-L. Comprehensive studies of magnetic transitions and spin-phonon couplings in the tetrahedral cobalt complex $Co(AsPh_3)I_2$. *Inorg. Chem.* **2022**, *61*, 17123. DOI: 10.1021/acs.inorgchem.2c02604

(2) Tin, P.; **Bone, A. N**.; Bui, N. N.; Zhang, Y.-Q.; Chang, T.; Moseley, D. H.; Ozerov, M.; Krzystek, J.; Cheng. Y.; Daemen, L. L.; Wang, X.; Song, L.; Chen, Y.-S.; Shao, D.; Wang, X.-Y.; Chen, X.-T.; Xue, Z.- L. Advanced spectroscopic and

computational studies of a cobalt(II) coordination polymer with single-ion magnet properties. *J. Phys. Chem. C* **2022**, *126*, 13268. DOI: 10.1021/acs.jpcc.2c03083

(3) **Bone, A. N.**; Widener, C. N.; Moseley, D. H.; Liu, Z.; Lu, Z.; Cheng, Y.; Daemen, L. L.; Ozerov, M.; Telser, J.; Thirunavukkuarasu, K.; Smirnov, D.; Greer, S. M.; Hill, S.; Krzystek, J.; Holldack, K.; Aliabadi, A.; Schnegg, A.; Dunbar, K. R.; Xue, Z.-L. Applying unconventional spectroscopies to the single-molecule magnets, $Co(PPh_3)_2X_2$ (X = Cl, Br, I): Unveiling magnetic transitions and spin-phonon coupling. *Chem. Eur. J.* **2021**, *27*, 11110. DOI: 10.1002/chem.202100705

(4) **Bone, A. N.**; Stavretis, S. E.; Krzystek, J.; Liu, Z.; Chen, Q.; Gai, Z.; Wang, X.; Steren, C. A.; Powers, X. B.; Podlesnyak, A. A.; Chen, X.-T.; Telser, J.; Zhou, H.; Xue, Z.-L. Manganese tetraphenylporphyrin bromide and iodide. Studies of structures and magnetic properties. *Polyhedron* **2020**, *184*, 114488. DOI: 10.1016/j.poly.2020.114488

(5) Widener, C. N.; **Bone, A. N.**; Ozerov, M.; Richardson, R.; Lu, Z.; Thirunavukkuarasu, K.; Smirnov, D.; Chen, X.-T.; Xue, Z. L. Direct observation of magnetic transitions in a nickel (II) complex with large anisotropy. *Chin. J. Inorg. Chem.* **2020**, *6*, 1149.